Imperial College
London

Extending HHG Spectroscopy to new molecular species

Felicity C. McGrath

June 2015

Thesis submitted in partial fulfilment of the
requirements for the degree of
Doctor of Philosophy of Imperial College London
and the Diploma of Imperial College

Laser Consortium
Quantum Optics and Laser Science Group
Department of Physics
Imperial College London
London, SW7 2BW
United Kingdom

Abstract

HHG spectroscopy is a powerful tool for observing electronic structure along with electronic and nuclear dynamics with state of the art resolution on the attosecond (10^{-18} s = 1 as) timescale and angstrom (10^{-10} m = 1 Å). Thus far, HHG spectroscopy has been applied to small hydrocarbons such as ethylene and methane using an 800 nm drive laser field wherein dynamics can only be measured in a $0.9 - 1.6$ fs time window. This PhD has two primary aims: 1) to extend the time window over which we can make measurement up to ≈ 4 fs using an ≈ 2 μm drive laser field and 2) to perform HHG spectroscopy on molecules which are in the liquid phase at room temperature. The molecules at the focus of this thesis are benzene and substituted benzenes. The design and development of an apparatus to generate a stable vapour jet from a thin continuous nozzle is presented. The completed and tested apparatus has demonstrated that stable and reproducible spectra can be acquired with no contamination between different samples as they are switched over. Comparison of methylated benzene to benzene harmonic spectra show good agreement with theoretical results on coupled electron-nuclear dynamics developed by our collaborators. We also compare HHG spectra acquired under similar generating conditions from deuterated and protonated benzene which enables us to track nuclear dynamics and to determine the origin of the ionized electron in benzene. HHG spectra from the halogenated benzenes, in particular fluorobenzene, seem to illustrate the contribution of more tightly bound orbitals to the HHG signal which is indicative of dynamical interferences.

Contents

Abstract **1**

Declaration **7**

Dissemination of Results **8**

Contributions to the work presented in this thesis **9**

Acknowledgements **11**

List of Figures **16**

1 Background **25**

1.1 Introduction 25

1.1.1 Introduction to the thesis 25

1.1.2 The evolution of attosecond and angstrom resolution experiments 27

1.1.3 Introduction to strong field physics 31

1.2 Ionization processes 37

1.2.1 Multiphoton ionisation 39

1.2.2 Above threshold ionisation 40

1.2.3 Tunnel ionisation 40

1.2.4 Over the barrier ionisation 41

1.3 Ponderomotive energy 42

1.4 The Keldysh parameter 43

1.5 High harmonic generation 45

1.5.1 Step 1: Ionisation 46

1.5.2 Step 2: Continuum propagation 51

1.5.3 Step 3: Recombination 55
1.6 Phasematching in HHG 60
1.6.1 Material Dispersion 61
1.6.2 Geometric Phase 62
1.6.3 Atomic Dipole Phase 63
1.7 Basic molecular physics 66
1.7.1 The electronic wavefunction 66
1.7.2 Energy spectrum 71
1.7.3 Molecular orbital theory: quantum mechanics of multiple electrons 73
1.7.4 Molecular orbital theory applied to benzene 77
1.7.5 Substituted benzene molecules 82
1.8 Modelling HHG in Molecules 83

2 Laser requirements for High Harmonic Generation 88
2.1 Laser parameters 88
2.1.1 Drive wavelength 88
2.1.2 Pulse duration 93
2.1.3 Laser intensity 96
2.1.4 Repetition rate 97
2.2 Fundamentals of laser physics for ultrashort pulses 97
2.2.1 Description of optical pulses 98
2.2.2 Nonlinear optics for ultrashort pulse generation 100
2.3 Ultrashort pulse production 107
2.4 Modelocking 108
2.5 Ultrashort pulse generation in a modelocked laser 112
2.5.1 Chirped Pulse Amplification 114
2.5.2 CPA laser system at Imperial College 115
2.6 Pulse characterisation 120
2.7 Generation and characterisation of the idler 123
2.7.1 Near-IR wavelength generation 123
2.7.2 Spectral broadening 125
2.7.3 NIR pulse characterisation methods 129
2.7.4 Frequency Resolved Optical Gating 133

3 HHG Spectroscopy **137**
3.1 Molecular alignment . . . 137
3.1.1 Static electric field alignment . . . 138
3.1.2 Laser induced alignment in the adiabatic limit . . . 139
3.1.3 Impulsive alignment . . . 140
3.1.4 Rotational cooling . . . 144
3.2 Charge coupled nuclear dynamics . . . 146
3.3 PACER on large organic molecules . . . 156
3.4 The origin and interpretation of minima in molecular HHG spectra . 165
3.4.1 Cooper minima in organic molecules . . . 165
3.4.2 Structural minima in HHG spectra . . . 168
3.4.3 Dynamical minima in HHG spectra . . . 170

4 Experimental methods and apparatus design and implementation **174**
4.1 Outline of existing HHG apparatus at the start of the project . . . 175
4.2 Vapour generation from organic molecules . . . 182
4.2.1 Evaporation of liquid phase organics at room temperature . . 183
4.2.2 Earlier heated gas jet for vapour phase molecular HHG . . . 191
4.2.3 Design and development of an apparatus for multi-source HHG in vapours . . . 193
4.3 Other modifications for working with organic molecules . . . 199
4.3.1 Pumping system . . . 200
4.3.2 Moving flange for MCP detector and CCD . . . 204
4.3.3 Jet orientation . . . 205
4.3.4 Cold traps on vacuum chamber . . . 206
4.3.5 Spectrometer chamber material . . . 206
4.4 Working apparatus for vapour phase molecular HHG . . . 207
4.5 Supplementary information on vacuum heater . . . 210

5 Methodology **213**
5.1 Safety . . . 213
5.2 2013 data run . . . 215
5.2.1 Spectral calibration . . . 215
5.2.2 2013 halogenated benzene data . . . 215
5.2.3 2013 PACER data . . . 220

5.2.4 Pacer 2013 discussion . . . 222
5.3 2013 data: Conclusions and actions taken . . . 224
5.4 2015 data run: benzene . . . 226
5.4.1 Intensity measurements . . . 227
5.4.2 Reproducibility of the spectra from benzene . . . 229
5.4.3 Pressure dependence of harmonic spectra in benzene and substituted benzenes . . . 236

6 Results **240**
6.1 Comparison of benzene to deuterated benzene HHG spectra: December 2013 data . . . 242
6.2 Comparison of benzene to methylated benzene HHG spectra: December 2013 data . . . 245
6.3 Intensity dependence of HHG in benzene and substituted benzenes . . . 248
6.3.1 Halogenated benzenes 2015 . . . 254
6.4 2015 PACER data . . . 259
6.5 Methylated benzene molecules . . . 263
6.6 Molecular SFA calculations . . . 272

7 Discussion of results **278**
7.1 Discussion of halogenated benzenes data . . . 278
7.2 PACER . . . 280
7.3 Methylated benzenes . . . 281
7.4 Linking photoelectron spectroscopy to high harmonic generation spectroscopy . . . 283
7.5 Future work: improvements to intensity scan method . . . 285
7.6 Conclusions and outlook . . . 287

Appendix A: Physical properties of the molecules studied **290**

Permissions **294**

Bibliography **294**

Butterflies and zebras
And moonbeams and fairy tales
That's all she ever thinks about
Riding with the wind.

- Jimi Hendrix, 1967

Declaration

I hereby certify that the material presented in this thesis, which I now submit for the award of Doctor of Philosophy of Imperial College London, is entirely my own work unless otherwise cited or acknowledged within the body of the text.

Felicity C. McGrath

The copyright of this thesis rests with the author and is made available under a Creative Commons Attribution Non-Commercial No Derivatives licence. Researchers are free to copy, distribute or transmit the thesis on the condition that they attribute it, that they do not use it for commercial purposes and that they do not alter, transform or build upon it. For any reuse or redistribution, researchers must make clear to others the licence terms of this work.

Dissemination of Results

Articles Published:

- McGrath, F *et al* "Extending HHG Spectroscopy to New Molecular Species", Proc. SPIE 8984, Ultrafast Phenomena and Nanophotonics XVIII, 89841B (March 7, 2014); doi:10.1117/12.2039123
- McGrath, F *et al* "Extending HHG Spectroscopy to New Molecular Species", Frontiers in Optics 2013/Laser Science XXIX ©OSA 2013; http://dx.doi.org/10.1364/LS.2013.LTh2I.3
- McGrath, F., Siegel T., Austin, D., Marangos, J.P. "Ultrafast lasers: High-harmonic-generation spectroscopy is extended to new types of molecules", Laser Focus World, February 2014.

Formal Presentation of Work:

- McGrath, F *et al* "High Harmonic Generation Spectroscopy and Ultrafast Measurements", Optics and Photonics, NUI Galway, April 2014 (invited talk)
- McGrath, F *et al* "Extending HHG Spectroscopy to New Molecular Species", Proc. SPIE 8984, Ultrafast Phenomena and Nanophotonics XVIII, 89841B (March 7, 2014) (oral presentation)
- McGrath, F *et al*, "Extending HHG Spectroscopy to New Molecular Species", Frontiers in Optics 2013/Laser Science XXIX © OSA 2013 (oral presentation)
- McGrath, F *et al*, "Extending HHG Spectroscopy to New Molecular Species", ATTO 2013 conference (poster presentation)

Contributions to the work presented in this thesis

The apparatus that has been designed in-house for generating stable vapours for the molecular HHG experiments has been primarily designed, built and tested by myself. I acknowledge the consistent input from our groups Electronics Technician, Mrs. Susan Parker, throughout this PhD project. Susan advised me on the the proposed designs of the vacuum heating system and taught me how to assemble and test the PID controller and resistive heaters. The apparatus vapour delivery lines were all designed, constructed and tested by myself. The preliminary experiments which focused around testing the capabilities of the apparatus as a whole were performed in the period of early 2012-mid 2013. PhD students Emma Simpson and Peter Hawkins, who joined the group in October 2012, assisted with the data taking, operation of the apparatus, general troubleshooting and data analysis. Postdoctoral researchers, Dr. Thomas Siegel and Dr. Zsolt Diveki, who joined the group in September 2012 also assisted in the day to day running of the apparatus. Dr. Siegel was also heavily involved in discussions on the adaptation of the apparatus to handle the VOC vapours.

From October 2011 to mid 2013 I was also working on the day to day maintenance and alignment of the laser system, both the 800 nm CPA laser system and the HE-TOPAS OP-CPA laser. Dr. Dane Austin became the primary laser maintenance team member so that I could focus on my own apparatus and experiment.

Peter Hawkins, Emma Simpson, David Wood (PhD student that joined the group in October 2014) and Dane Austin were the team members who performed the majority of the data analysis using Matlab. Allan Johnson and Lukas Miseikis (who both joined the group as PhD students in October 2013) have been key team members

in both the day to day running of the apparatus and the data acquisition. Morgane Vacher (PhD student that joined the Theoretical Chemistry group in October 2012) has also assisted with data taking in the laboratory.

Collaborations have also been established with Professor Marta Castillejo (CSIC Madrid, Spain), Dr Ravi Bhardwaj (University of Ottawa, Canada) - both have participated in experimental campaigns at Imperial College. Former group member Dr. Ricardo Torres has assisted with developments of molecular SFA codes.

The data presented in this thesis is that which was acquired with myself as the leader of the experiment and I shall not present any data which was recorded and processed once I left the laboratory to write up my PhD in April 2015.

Acknowledgements

Firstly, I would like to thank my wonderful supervisor Jon Marangos. Jon, I am indebted to you for having the faith in me to do this PhD and for allowing me to fulfil my heart's desire of working in ultrafast science. Your enthusiasm for my project has given me a sense of security during all the bleak times with experiments not working and equipment breaking. You have truly gone above and beyond the call of duty as a supervisor and I have enjoyed every moment of your company over the last 3 years.

I also want to thank John Tisch for all the support and advice he gave me during my PhD. Also for all of the quips, jokes and for having amazing hair. Amelle - thank you for always being supportive of my work and for being there for me when things used to go pear shaped.

Thank you to the QOLS group for all of the fun over the last 3 years. Many a good time was shared with Richard, Tom S, Zsolt and Simon over broken lasers or pints of cider. Emma, for being a great friend and so easy to work with - I am still really apologetic for going all silent when Labview decided to crash coincidentally to when you touched the computer! Pete (aka Petey, Sweetie, Petey pie) thanks for all the silly YouTube videos and for introducing me to some cool music. Allan - you rock!, do you have to align that rude spectrometer again anytime soon?! Lukas, for always coming out with the most bizarre statements and opinions - never change. Dave, for getting stuck in on the experiment and for keeping Pete sane with the "odd" game of FIFA. I also want to thank Daniel, Paloma, Chris B, Tobi, Tom B, Konstantin, Alvaro, Chris Price, Sid, Taran, Jon, Bridgette, Emilio, Marco and Martin for all the fun and jokes we have had in the group. I wish every success to the 2011 recruits, Steffen, Davide, Zara and Jon - we did it! Dane for being disturbingly good at Matlab and for all of the amazing work you have done helping me get the experiment going.

Also, best of luck to the new postdocs - Gediminas, Bernd, Christian and Peng - don't work too hard!

To the backbone of the group - Andy, Peter and Susan, thanks for turning all my rubbish or non-existent drawings into works of art. Susan, thank you for being a wonderful friend, I am wishing you and Ashley every happiness you deserve - sushi sometime soon perhaps? Judith, Marcia and Sanja - thank you for dealing with all my silly questions and for always being there for a natter.

I also want to thank all of those who have also helped out with the project - Ravi, Morgane, Mike B, Mike R, Vitali, Ricardo - I think we have all finally made benzene smile a little! Very special thanks to Marta Castillejo for being a pleasure to work with - thank you for always looking out for me and for really caring about my project, I am always delighted to see you and I am extremely grateful for all the support you have given me over the last three years. Also to those I have met from other groups on my journey including Helder, Inigo and Nacho - it has been great working with you and thank you for embracing my craziness with such politeness.

To all the great people I have met and friends I have made from my time at Imperial - Dylan, Emma A, Kwasi, Debra, Rob W, Khushi, Neil C, Jess W, Martin McCall, Geoff New, Jon Dyne, Brian Willey, Richard Thompson, Neil Powell, Malcolm, Simon G, Roger Smith, Vinita Hassard, Viv and Meilin - I appreciate all you have done for me and for always helping me out when I asked or going for tea with me when I really should have been working! I especially want to thank everyone who helped with events for the Imperial Optical Society - I was thinking of you all when I was on my funded conference trips to Florida and San Francisco! I also want to thank my new Imperial "family" of Stef, Julia and Anthony - I am extremely grateful to have the opportunity to work with such nice and enthusiastic people.

A special note of thanks to Chris Dainty, Tom Glynn and Gary Gillanders in the NUI Galway Physics department for recognising and encouraging my enthusiasm for physics - I think I owe you all a few pints next time I am back in Galway. I also want to thank the TOMI group members, especially Kai and Martin for being so open minded about the Imperial-NUI Galway student chapter collaborations and for

converting my brother back to doing physics!

Ricardo - thank you for keeping me sane (or driving me more insane, I actually can't tell anymore!). Your friendship means a lot to me. The "Cantina" at RAL almost seems like it was just yesterday. I wish you every success you deserve and thank you for your continued friendship. You always find a way to make me laugh when something is stressing me.

To my wonderful housemates - the Pembar Massive! Amy - you have become a very close friend and you are always there for me with a smile and a positive attitude and for getting into the most comical of situations - you have been a great Irish comfort to have whilst I have been away from home. Joe, I do not think I have ever met someone as funny as you, even your laugh makes me laugh uncontrollably. Showing me how to chop garlic while you were drunk and dancing to Leo Sayer are memories I will cherish! Helen, for being the life and soul of the house, you are a very strong woman and I am looking forward to spending more time with you as I get into "normal" working hours! To the alumni of the house - Mary, Aaron, Tristan and Kate - thank you for all the good times we have had.

To my mates Debbie, Brenda and Fiona, sorry for being so hard to get in touch with, this PhD has consumed me but you have always been there for me with a laugh and a word of encouragement on the rare occasions I have been back home. You are three amazing women with fantastic opportunities ahead; just don't forget to call me to help celebrate them over several glasses/bottles of bucky! Also to Michael Jordan for being a lifelong friend and always first to take the mick out of me. I think we really bonded over our loves of Kate Bush and Catchphase and our resentment of Irish Rail.

My best friend Shane, a truly beautiful soul - it has been a privilege growing up with you and sharing so much of our lives together. I have never met a more loving person with a wicked sense of humour and a wonderful outlook on life. You have no idea how much I appreciate you being there for me on this journey. Life has great things in store for you.

Zara, I always say to myself if only one good thing ever came out of moving to London

it would be our friendship. I feel like I have grown so much in the presence of such an intelligent and strong woman. Thank you for helping integrate me into London life, inviting me to your dance events, and for *always* being there for me when I needed a friend. Thank you to you and your mum Sandra for welcoming me into your home (oh and I must not forget Missy, Freddy and Princess!). Keep dancing and I expect to see you back in Ireland at another cow show soon - I really am proud of how much you have embraced my double life as a cow breeder - think I need to start working on my shimmies! Also for introducing me to Delia, Azin and Gintare, who have been great fun on nights out.

To my "girls" - Daisy, Davina, Colette, Gracie, Dinky, Honey, Baggy, Allie, Fran, Galaxee, Angela, Cinderella, Jean, Jane, Dolittle, Koka-Kola, Hazel, Beatrice, Benfada, Jessica and all those who have gone before and will come after. You have no idea how much you love and are loved. You never fail to make me smile and your affection has kept me going when times were at their toughest. I can only hope I make you as happy as you make me. While I am on the subject of Angus, I want to thank John McCabe for being a great friend and sharp mind and for teaching my mother and I so much about the business. I also want to thank Corinne Dainty for visiting the farm and for embracing my cows with such a great attitude and enthusiasm - they expect you to be back to carry on grooming them!

I dedicate the "Experimental methods and apparatus design and implementation" chapter of my thesis to Tommy and Pat Roche. Thank you for getting me started in science and for being some of the kindest, warm and generous people I have met. I am sad that you have both left us but I know being together in heaven is what brings you all the happiness you need.

Apologies to anyone I have omitted from my acknowledgements - I am writing this clutching a large cup of coffee to see me through the (hopefully) last of my sleep and fun deprived nights.

Finally I want to thank my *amazing* family for putting up with all the moods, missed calls and forgetfulness associated with doing a PhD. Firstly to Tom and Breda for being proud of me and always supporting me in what I have done at university (and

with cows!). I can't forget Ruby, Suzie, Tilly and Jessie for looking after my mum. Matt for being the joker of the pack and being afraid of nothing. James for always taking care of me and being my guide, I am here for you as you have always been for me. To my mother - thank you for giving me all you have and for being a wonderful role model and inspiration - this thesis is for you.

List of Figures

1.1 Experimental apparatus for Frankens SHG experiment 33
1.2 Reproduction of the spectrographic plate in which there was an indication of second harmonic generation. 34
1.3 Ionisation mechanisms that occur in the perturbative and the non perturbative regimes 39
1.4 Diagram of the 3−step model of HHG. 45
1.5 Dependence of the instantaneous ionization rate on the phase of the laser field. 48
1.6 Classical calculation of the short and long trajectories from an 800 nm field. 54
1.7 Diagram of the characteristic shape of a typical HHG spectrum. . . . 55
1.8 Ionization and recombination times for short and long trajectories from an 800 nm laser field. 56
1.9 Excursion time of an electron in the continuum as a function of drive wavelength. 58
1.10 Time−frequency mapping as a function of field intensity for the benzene molecule and a drive wavelength of 1800 nm. 59
1.11 Plot of the Gouy phase shift through the focus for two values of z_R. . 63
1.12 Phase matching maps for short and long trajectories of the 21st, 35th and 45th harmonics in neon driven by a 750 nm laser field. 65
1.13 The formation of a bonding molecular orbital. 68
1.14 The formation of an anti-bonding molecular orbital. 69
1.15 The gerade and ungerade character of σ bonding and antibonding orbitals. 70

1.16 Simplified schematic of a diatomic molecule consisting of two masses m_1 and m_2 rotating about their common centre of mass. 72
1.17 Schematic of the π and σ electron charge density on the benzene ring. 78
1.18 Photoelectron spectrum from benzene with a table showing the corresponding energies of the peaks. 79
1.19 Rotation and reflection symmetry operations for the D_{6h} benzene molecule. 81
1.20 Flow chart representing the different point groups a molecule can belong to based on decisions concerning its symmetry properties. 82
1.21 Structural isomers of xylene (C_8H_{10}) molecule. 83

2.1 The TOF-MS when benzene was irradiated with a wavelength of 395 nm and 790 nm. 92
2.2 Harmonic intensity as a function of laser intensity for xenon, cyclohexane and benzene with a 240 fs pulse and a 70 fs pulse. 94
2.3 Harmonic spectra in neon at 250 torr backing pressure for 30 fs and 7 fs pulse durations and an 0.8 μm drive wavelength. 95
2.4 Difference frequency generation. 102
2.5 Self focusing of light in a non−linear medium. 104
2.6 Self phase modulation. 106
2.7 Roadmap of the advancements in ultrashort pulse generation. 108
2.8 Schematic of a typical self−modelocked Ti:sapphire oscillator. 113
2.9 Schematic of a pulse stretcher employed in a CPA laser system. . . . 114
2.10 Schematic of a pulse compressor employed in a CPA laser system. . . 116
2.11 The complete layout of the CPA laser system - KM Labs Red Dragon - used in this thesis. 119
2.12 Schematic of a general SPIDER for pulse characterisation. 120
2.13 Typical SPIDER trace measured in the laboratory. 122
2.14 Layout of the main components and stages of the HE−TOPAS OP−CPA NIR wavelength generation system. 123
2.15 Layout of the spectral broadening beam line including the main components and stages of the HE−TOPAS OP−CPA NIR wavelength generation system and the hollow core fibre. 126
2.16 Broadened spectra as a function of pressure of argon in the hollow core fibre. 127

2.17 Concept of the mid-IR SPIDER apparatus. 129
2.18 SEA-SPIDER traces from a femtolasers oscillator. 131
2.19 SEA-SPIDER fringes. 132
2.20 Typical layout of a second harmonic generation FROG (SHG FROG). 135
2.21 Measured and reconstructed FROG traces acquired using the SHG FROG constructed in our laboratory. 136

3.1 Half revival obtained in benzene using an 800 nm-800 nm alignment-generation collinear interferometer. 142
3.2 Resonance structures of the benzene radical cation. 149
3.3 Simulation of the charge migration and charge transfer for the benzene radical cation with fixed nuclei. 151
3.4 Simulation of the charge migration and charge transfer for the benzene radical cation when nuclear motion is allowed. 152
3.5 Spin densities partitioned on the carbon atoms of benzene as a function of time after ionization. 153
3.6 Spin densities partitioned on carbon atoms in toluene as a function of time after ionization. 154
3.7 Spin densities partitioned on carbon atoms in p-xylene as a function of time after ionization. 155
3.8 Encoding of nuclear dynamics in HHG from exploiting the chirped nature of the electron wavepacket. 158
3.9 Ratio of harmonic peak intensities for D_2 to H_2. 160
3.10 Ratio of the harmonic signals for deuterated methane to methane. . . 161
3.11 Nuclear vibrational factors calculated for a range of polyatomic molecules. 162
3.12 Autocorrelation function calculations for the ratio of D_2 to H_2 and for the ratio of CD_4 to CH_4. 163
3.13 The shape of the HOMO and HOMO-1 orbitals in N_2 with respect to the internuclear axis. 171

4.1 The original HHG chamber at Imperial College London. 176
4.2 Schematic of the continuous flow gas jet used in the HHG chamber. . 178
4.3 Illustration of the Rowland circle concept showing the diffracted wavelengths focused at different points on the circle. 179
4.4 Alignment of the flat field XUV grating for HHG. 180

4.5 Avalanche amplification caused by secondary electrons in a microchannel plate pore. 181
4.6 Schematic of the most common types of gas cells used in HHG experiments. 185
4.7 Plots of XUV transmission in benzene for 500 μm and 1 mm medium lengths. 187
4.8 Simulation of a Gaussian pulse which propagates through a SIGC with 400 μm apertures and a 200 μm orifice continuous flow gas jet. 188
4.9 Intensity profile in space and time of a laser pulse at the beginning and the end of a 3 mm long neon gas cell. 190
4.10 Temperature controlled pulsed valve that was first used at Imperial College for molecular HHG experiments. 191
4.11 Layout of the mark I apparatus designed to perform molecular HHG experiments from a liquid phase target. 193
4.12 Layout of the Thermocoax heater used to heat the gas jet. 194
4.13 Block diagram of inhouse heating system mark II. 196
4.14 Stages of operation for a zero-crossing solid state relay. 197
4.15 The in-house designed heaters for the gas jet and the tubing to the gas jet as it is in the vacuum chamber. 198
4.16 The redesign of the mount to dampen vibrations and backlash arising from the translation of the gas jet. 199
4.17 Main components involved in the operation of a rotary vane pump. . 201
4.18 Moving MCP flange with main components labelled. 205
4.19 The complete apparatus that has been used for the experiments performed in this thesis. 209
4.20 Detailed wiring diagram of the vacuum heating system. 212

5.1 Results for the calibration of the energy scale of the spectrum. 215
5.2 Unscaled spectra for deuterated benzene, bromobenzene, chlorobenzene and benzene for the three different MCP flange positions. 216
5.3 Normalised plots for the data shown in Figure 5.2 as a function of beam energy per pulse. 217
5.4 Comparison of the spectra for benzene and fluorobenzene as a function of energy per pulse. 217

5.5 Intensity scans comparing the spectra from benzene and fluorobenzene under similar HHG conditions. 218
5.6 Pressure scan in benzene using spectra taken at different times during the data collection day. 219
5.7 Background subtracted peak heights plotted as a function of peak number for C_6D_6 and C_6H_6. 220
5.8 The average peak intensity as a function of peak number for C_6D_6 and C_6H_6. 221
5.9 Stability of the harmonic spatial mode for the data shown in Figure 5.7 222
5.10 Stability of the harmonic spatial mode for the data shown in Figure 5.8 223
5.11 Vapour pressure curve recorded for benzene 227
5.12 HHG spectra from benzene recorded with a backing pressure of 0.55 bar and a range of beam energies per pulse. 229
5.13 Spectra recorded in benzene for two different days where the generating conditions are not the same. 230
5.14 Unnormalised HHG spectra from benzene taken on three different days with similar backing pressures and laser parameters. 231
5.15 Ratios of fluorobenzene spectra for different runs to the first benzene run. 232
5.16 Ratios of benzene, fluorobenzene and deuterated benzene to benzene with associated errors. 233
5.17 Unnormalised plots of the HHG spectra from toluene recorded as a function of the vertical position of the gas−jet. 234
5.18 Normalised plots of the HHG spectra from toluene recorded as a function of the vertical position of the gas−jet. 235
5.19 Unnormalised plot of a pressure scan in benzene going from $0.83 - 0.1$ bar. 236
5.20 Harmonic peak intensities of the pressure scan shown in Figure 5.19 normalised to the maximum intensity peak of each spectrum. 237
5.21 Area normalised HHG spectra as a function of backing pressure. . . . 238
5.22 Unnormalized HHG spectra recorded as a function of backing pressure. 238
5.23 Spectra for benzene, toluene, fluorobenzene and the three xylene isomers are plotted unnormalised. 239

6.1 Raw harmonic spectra recorded in benzene, toluene, m-xylene and p-xylene. 241
6.2 Spectra recorded in benzene, deuterated benzene and all of the mono halo substituted benzenes. 242
6.3 Area normalised spectra for benzene and deuterated benzene. 243
6.4 Four pairs of C_6D_6 and C_6H_6 spectra plotted for three intensity values. 244
6.5 HHG spectra acquired in benzene, toluene, m−xylene and p−xylene. 245
6.6 Area normalised harmonic peak intensities for benzene, toluene, m−xylene and p−xylene. 246
6.7 This plot is identical to that of the bottom panel in Figure 6.5 but with the addition of the ratio of m−xylene to p−xylene. 247
6.8 Intensity scan in benzene. 248
6.9 Intensity dependence of the cut−off position in the HHG spectrum from benzene. 250
6.10 Intensity dependence of the cut−off position in the HHG spectrum from fluorobenzene. 250
6.11 Intensity scans recorded in benzene, deuterated benzene, toluene, fluorobenzene and m and p−xylene. 252
6.12 Normalized HHG spectra from toluene as a function of varying iris diameter. 253
6.13 Comparison of high harmonic spectra taken in benzene and fluorobenzene under identical conditions. 254
6.14 Unnormalised HHG spectra from fluorobenzene for three data runs. . 255
6.15 Unnormalised HHG spectra from benzene for two data runs. 255
6.16 Unnormalised HHG spectra recorded in benzene at a backing pressure of 0.48 bar. 256
6.17 Unnormalised HHG spectra recorded from fluorobenzene. 257
6.18 Area normalised HHG spectra recorded in benzene and the halogenated benzenes. 258
6.19 Area normalised HHG spectra from deuterated benzene. 259
6.20 Pressure scan recorded from deuterated benzene. 260
6.21 Comparison of HHG spectra in benzene and deuterated benzene under similar generating conditions. 261
6.22 Ratio of deuterated benzene to benzene. 262

6.23 Pressure scan recorded from toluene. 263
6.24 Comparison of HHG spectra recorded in benzene and toluene. 264
6.25 Ratio of toluene to benzene. 265
6.26 Ratios of toluene to benzene harmonics as a function of input beam power. 266
6.27 HHG spectra recorded in the para-xylene isomer to allow for a comparison of the differing shapes of the spectra between isomers. 267
6.28 HHG spectra recorded in the ortho-xylene isomer to allow for a comparison of the differing shapes of the spectra between isomers. 267
6.29 HHG spectra recorded in the meta-xylene isomer to allow for a comparison of the differing shapes of the spectra between isomers. 268
6.30 Ratios of p−xylene and o−xylene to m−xylene. 268
6.31 Ratios of toluene, m−xylene p−xylene and o−xylene to benzene. . . 269
6.32 Unnormalised HHG spectra from benzene, o−xylene and p−xylene plotted to facilitate a comparison of the shapes of the spectra between molecules. 270
6.33 Ratios of methylated benzene molecules to the reference benzene. . . 271
6.34 SFA simulation results of the harmonic intensity as a function of the relative phase between HOMO and HOMO-1, for different molecules. 273
6.35 SFA simulation results of the harmonic intensity as a function of the relative phase between HOMO and HOMO-1, for different molecules. 274
6.36 SFA simulation results of the harmonic intensity as a function of the relative phase between HOMO and HOMO-1, for different molecules. 275
6.37 SFA simulation results of the harmonic intensity as a function of the relative phase between HOMO and HOMO-1, for different molecules. 276

7.1 Estimation of widths of ground state photoelectron bands for benzene and fluoroebenzene. 284
7.2 Iris scan intensity adjustment set-up. 285
7.3 Intensity scan in toluene showing clear cut-off shift using new iris adjustment method. 286
7.4 Permission email response from the IOP for reference "A newcomers guide to ultrashort pulse shaping and characterization". 295

7.5 Permission email response from the OSA for reference "Generating single attosecond pulses via spatial filtering" 296
7.6 Permission email response from the OSA for reference "Characterization of high-intensity sub-4-fs laser pulses using spatially encoded spectral shearing interferometry" 297

List of Tables

3.1 Ionization potentials and Cooper Minima positions for the chloromethane molecules. 167

4.1 Outgassing rates of anodized aluminium and stainless steel after 1 hour and 10 hours of pumping under similar conditions. 207

5.1 Bath temperature and vapour pressure of molecules. WB stands for molecules that were heated using the waterbath. OB indicates those heated using the oil bath 226

7.1 Ionization potentials for substituted benzene 290
7.2 Other physical properties of substituted benzenes 291
7.3 Temperature and vapour pressures for substituted benzenes 291

Chapter 1

Background

1.1 Introduction

1.1.1 Introduction to the thesis

The work presented in this thesis seeks to further the understanding of electronic and nuclear dynamics in large organic molecules, such as benzene and substituted benzenes, with Angstrom (10^{-10} m) spatial and femto (10^{-15} s) to attosecond (10^{-18} s) temporal resolutions. The use of ultrashort, high intensity laser pulses has enabled the imaging of nuclear motion, structural deformations and charge motion in molecules which are the fundamental building blocks of matter. Using a process known as high harmonic generation (HHG), this technique can be employed to make movies of chemical processes at timescales that are almost incomprehensible to the human imagination. HHG bears similarities to strobe photography, wherein rapid motion can be freeze-framed by leaving the camera's shutter open in a darkened environment and then producing a bright flash of light. The shorter this flash, the faster the motion that can be recorded. Freezing the movement of a speeding bullet, for example, requires a flash of light no longer than 1 microsecond.

In HHG, ultrashort laser pulses are fired into a jet of gas or vapour or even a plasma plume, and the high intensity light tears an electron off each atom or molecule in the jet. The electron is quickly driven back to its parent ion. In this collision, the electron's kinetic energy is released in an extremely short, but very bright burst of x-ray radiation. These x-ray bursts can be squeezed down to a duration of 100 attoseconds.

Analysing certain characteristics of the x-ray beam, enables us to build up a movie of the molecule, for example how it structurally deforms after being ionised. The time interval between the individual "frames" in these movies is also $\approx$ 100 attoseconds - resulting in an effective framing-rate of 10 million billion frames per second.

An understanding of the complex processes in molecules could help to create quantum computers, faster electronics, designer materials or artificial photosynthesis.

High harmonic generation has already been employed in atoms and small diatomic molecules - most of which exist in the gaseous phase or as plasma plumes from solids. The motivation of this PhD work is to extend HHG spectroscopy to organic molecules which are in the liquid phase at room temperature. For example, benzene is a building block for making plastics, rubber, resins and synthetic fabrics like nylon and polyester in addition to being a fundamental constituent of DNA and is also a known carcinogen.

This thesis aims to develop and apparatus which can produce stable vapour jets from a range of substituted benzenes. A comparison between benzene and deuterated benzene harmonic spectra will give an insight into the origin of the electron wavepacket from the molecules as it can be ionised from the π or σ systems. Harmonic spectra from benzene and the substituted benzenes will provide a starting point for understanding charge transport in biomolecules. This PhD aims to give an insight into ultrafast structural deformations, contributions from lower lying orbitals and charge migration in substituted benzene aromatic molecules.

Organisation of thesis

This thesis is organised as follows. Chapter one introduces strong field physics before leading on to a detailed explanation of HHG on a macroscopic level. The chapter then leads on to basic molecular physics before concluding with an introduction to the theoretical modelling of HHG in molecules.

Chapter two focuses on the laser requirements for HHG and how the different laser parameters or pulse duration, wavelength, repetition rate and intensity affect the process. A detailed account of ultrashort pulse production is presented which develops

into an explanation of the laser systems used in this thesis and the pulse diagnostics used to characterize the laser pulses.

Chapter three presents HHG spectroscopy and the techniques that will be used in this thesis along with an explanation of the structural and dynamical information we can gain from molecules. Theoretical calculations made by the Quantum Chemistry group at Imperial College are also presented along with an interpretation of what we expect to detect experimentally.

Chapter four is concerned with the design and development of the apparatus used for vapour generation from the organic molecules. This chapter introduces the standard apparatus for HHG in gaseous molecules before detailing the modifications which need to be made for the vapour generation experiments.

Chapter five introduces the methodology of testing the apparatus to ensure stable and reproducible spectra are obtained. Chapter six presents the main results obtained in this thesis. The dependence of the HHG spectra on the backing pressure and the laser intensity are presented. Comparisons between HHG spectra from benzene and substituted benzenes are made to investigate charge transfer, structural and dynamical interferences in these molecules. Some basic strong field approximation (SFA) calculations are also presented to facilitate a basic interpretation of the data acquired.

Chapter seven discusses the results obtained along with conclusions made from the work presented and an outlook on future work.

1.1.2 The evolution of attosecond and angstrom resolution experiments

The advent of the laser in 1960 [1] soon led on to the development of short pulse, high power laser systems over the following decades. When a high power laser pulse of sufficient energy is focused into a gas of atoms/molecules, the laser electric field becomes comparable to that of the atomic field strength, E_{at}, enabling electrons to be liberated from the atoms. This section will briefly describe the interaction of atoms

with strong laser fields and the information that can be gained from these processes.

There are several potential outcomes from the interaction of a gas of atoms with an intense laser field (before the use of titanium-sapphire as a gain medium and chirped pulse amplification (CPA) became universal in the 1990s). As detailed in section 1.2.2, Above Threshold Ionisation (ATI) occurs when electrons that are initially in the parent atoms ground state absorb more photons than that required for ionization. These electrons are consequently ionised with a high kinetic energy. The introduction of high resolution time of flight (TOF) spectrometers in the early 1980s permitted ATI spectra to be recorded at higher laser intensities . This development resulted in the observation of a number of interesting characteristics of the ATI spectra. These include the influence of the ponderomotive potential, the transition from perturbative ATI to non perturbative and the effect of the laser field on the atomic bound states manifesting itself in the AC Stark shift [2].

Many electrons can also be ejected from atoms/molecules subject to strong laser fields. In one case, there may be a sequence of single electron ionization events: the atom is ionised, followed by the ionization of the singly charged ion then the doubly charged ion and so on. Another process may also occur, non-sequentially. In this case electrons can be emitted simultaneously; a liberated electron may scatter onto a parent ion and cause the ejection of a secondary electron.

Another outcome of the ionization of an atom was demonstrated for the first time in 1987 [3] when the XUV photon emission in the form of high order harmonics of a linearly polarized laser field was observed. High harmonic generation (HHG) has become a fundamental research area for scientists over the last three decades. The reasons for this lie in the unique properties of the radiation such as [4]:

- The HHG process is driven by the laser in a fully coherent manner; the generated harmonics have similar temporal and spatial coherence properties to the driving laser field
- The entire HHG process of tearing an electron from its parent atom, accelerating it in the continuum and its recollision and recombination with the parent ion occurs in only a fraction of a driving laser field cycle; e.g. 2.7 fs for an 800 nm

laser field. The duration of the electron probe pulse can be sub femtosecond, which leads to the generation of attosecond (10^{-18} s) pulses which can be used for imaging ultrafast dynamics in molecules

- An advantage of using electrons compared to X-rays is that the electron scattering cross-section is much higher ($\approx 4-6$ times larger than X-rays) as it is regulated by the Coulomb interaction with both electrons and nuclei [5]. The ratio of inelastic to elastic scattering cross sections for electrons is much lower than that of X-rays. The energy that is deposited into the target per elastic collision event is lower for electrons than for X-ray probes. However, the presence of a strong laser field can induce more damage on the target. Referring to the discussion on non-linear optics in section 1.1.2, laser fields of sufficient intensity can induce significant damage to the target it is focussed on to.

Electron energies, E, correspond to de-Broglie wavelengths in the Angstrom and sub-Angstrom range by the simple relation:

$$\lambda_e = \frac{h}{\sqrt{2Em}} \tag{1.1}$$

Obtaining the same wavelengths with photons for which $\lambda = \frac{hc}{E_{ph}}$, requires several keV of energy which corresponds to hard x-rays. To obtain 1 Å spatial resolution for the measurement of structural dynamics, a comparable or shorter wavelength is required. Photons with an energy in excess of 12 keV are required to achieve 1 Å wavelength for X-ray probes. For an electron to have a de Broglie wavelength of 1 Å, its kinetic energy must be > 150 eV. In essence, much lower electron energies are needed than photon energies to achieve the same spatial resolution.

Not only are hard x-rays of this kind hard to produce, which can be done using Free Electron Lasers (FELs) [6], but also they primarily interact with a systems core electrons as opposed to the valence electrons which are relevant for imaging dynamics in topical chemical and biological systems; i.e. DNA, carcinogens and semiconductor materials.

- The temporal resolution provided by the chirped electron wavepacket in HHG is on the attosecond timescale (≈ 100 as) which is ideally suited to the measuring ultrafast nuclear dynamics in molecules [7]. It should also be stressed that some structural changes in biomolecules such as protein folding take place on femtosecond to microsecond scales and are of much importance to understanding chemical dynamics as attosecond measurements. X-ray FELs are of importance to the measurements of longer timescale dynamics as they can provide time resolutions of up to 20 fs. Altucci *et.al* [5] has published a very accessible and comprehensive review of various methods for ultra-fast dynamic imaging in molecules for achieving atomic scale spatial resolution and femtosecond temporal resolution.

1.1.3 Introduction to strong field physics

When a light source of sufficient intensity is applied to a medium it can induce non-linear modifications of the optical properties of the material - this phenomenon is known as non-linear optics. To give the reader an appreciation for the maximum electric field strengths that can be used to induce non-linear effects in an optical material, mentioning the optical damage thresholds is useful. The efficiency of a non−linear process is limited by the maximum field strength at which the process can occur without damaging the material. Examples of damage include burns on optical surfaces which can reduce the reflectivity of certain optical elements, and overheating of the material which can caused thermal stress, chemical degradation of optical coatings and even fracturing of a material.

Linear absorption which leads to heating and cracking of materials is the dominant damage mechanism for continuous wave and long pulse ($\geq 1\mu$s) laser beams. Avalanche breakdown influences the onset of optical damage for pulsed lasers of durations $\leq 1\mu$s typically for intensities in the range $10^9 - 10^{12}$ W/cm^2. Multiphoton ionization/dissociation is the dominant mechanism for inducing optical damage for the intensities in the range $10^{12} - 10^{16}$ W/cm^2. Direct photoionization wherein the laser field strength is sufficient to rip electrons away from an atomic nucleus is the dominant mechanism for intensities $\geq 10^{20}$ W/cm^2. For laser pulses of typically < 100 fs duration these effects may occur at lower intensities [8]. It is worth noting that modern day laser technology can produce lasers of sufficient intensities to exceed the damage threshold of all known optical materials. Therefore, the optical damage threshold of a material provides us with a baseline for understanding the constraints of inducing non−linear effects.

Typically, only a laser can produce the intensities required to induce non-linear effects in a material. These effects are termed non-linear due to the fact that the electronic response of the medium depends non-linearly on the strength of the applied optical field. The birth of non-linear optics is credited as the discovery of second harmonic generation (SHG) by Franken *et.al* in 1961 [9], shortly after the demonstration of the first working laser by Maiman in 1960 [1]. Electro−optic effects such as the Kerr effect which was studied first in 1875 and the Pockels effect which was discovered

in 1893 are also two fundamental examples of non−linear effects which have become cornerstone to modern laser technology. The fusion of these two milestones has led to the availability of commercial lasers that can be operated at two wavelengths. For example the 1064 nm output from a Nd:YAG system can be frequency doubled to produce visible light at 532 nm. More commonly used in the field of strong field physics is the 800 nm output from a 1 kHz Ti:Sapphire laser system which can generate visible light at 400 nm when SHG is employed.

In order to define more precisely what is meant by an optical non-linearity it is useful to consider how the dipole moment per unit volume - the polarization - of a material depends upon the strength of an applied electric field. In the case of linear optics the polarization of a material varies linearly with the applied electric field strength as described by the relationship [10]:

$$P(t) = \epsilon_0 \chi^{(1)} E(t) \tag{1.2}$$

For non-linear optics we can generalize this equation by expressing the polarization as a power series in the applied electric field strength as:

$$P(t) = \epsilon_0 [\chi^{(1)} E(t) + \chi^{(2)} E^2(t) + \chi^{(3)} E^3(t) + \ldots] \tag{1.3}$$

The term $\chi^{(n)}$ is the n^{th} order non-linear susceptibility. For example, the corresponding non-linear susceptibility for second harmonic generation is $\chi^{(2)}$ whilst for self-phase modulation a susceptibility of $\chi^{(3)}$ is necessary. The first susceptibility term, $\chi^{(1)}$, which represents a linear response, is dimensionless. All higher order terms, $\chi^{(n)}$, have units of $(\mathrm{m/V})^{n-1}$. The electrons within a non−linear material are not uniformly distributed but are constrained in their motion by the potentials that confine them. In response to the electric field, the electrons may move a greater or smaller distance which is dependent upon the strength of their confinement in the applied field direction. Hence, the susceptibility and properties dependent upon it such as refractive index, are anisotropic cannot be defined by a single value but must be treated for the x, y and z axes depending on which axis the field is applied along. Thus, $\chi^{(n)}$ is a tensor of rank $n + 1$.

In a more general case, if an electron is not aligned along the co−ordinate axis then the resultant polarization may also have a component in one of the other directions. We can therefore write the susceptibility tensor as $P = \epsilon_0 \chi E$ where ϵ_0 is the permittivity of free space and E is the applied electric field strength. The susceptibility tensor is defined as:

$$\begin{bmatrix} \chi_{xx} & \chi_{xy} & \chi_{xz} \\ \chi_{yx} & \chi_{yy} & \chi_{yz} \\ \chi_{zx} & \chi_{zy} & \chi_{zz} \end{bmatrix}$$

The first term of equation 1.3 is linearly dependent on the electric field describes the dispersion and loss. As stated, the second term gives rises to SHG. Note that the second order susceptibility is only non-zero for non-centrosymmetric media such as Beta Barium Borate (BBO) and Potassium Dihydrogen Phosphate (KDP). The third term is responsible for effects such as third harmonic generation. Higher order terms can be neglected as their susceptibility decreases with increasing orders [8].

The first demonstration of a non-linear effect in a laser field was performed by Franken *et.al* in 1961. The experiment consisted of focusing a commercial ruby maser (Trion Instruments Inc.), which produces ≈ 3 mJ of 694.3 nm light in a 1 ms pulse, into a quartz crystal. The maser output passed through a red filter for filtering out the xenon flash background and was brought to a focus inside a crystalline quartz sample [9], as illustrated in Figure 1.1.

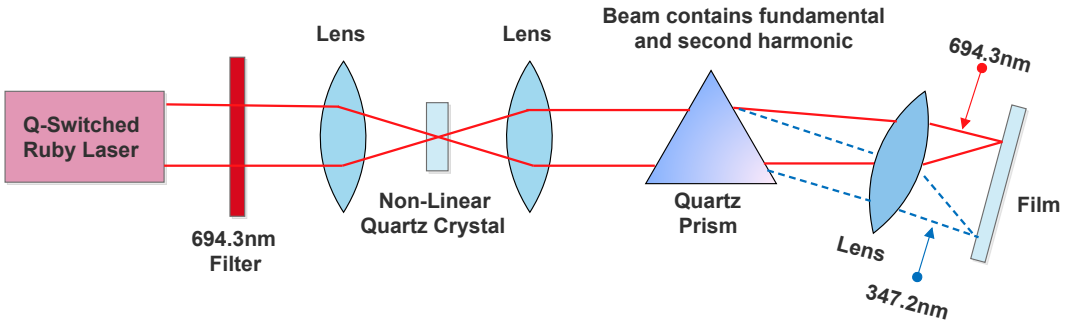


Figure 1.1: Experimental apparatus for Frankens SHG experiment [10]

The emergent beam was analysed by a quartz prism spectrometer which was equipped with red insensitive spectrographic plates. In this situation the electronic response of

the crystal scales not linearly but quadratically with the applied field which results in the generation of light with twice the frequency of the fundamental. Mathematically we can describe the polarization as follows: the electric field of the maser beam can be written as:

$$E = Acos(\omega t) \tag{1.4}$$

Substituting this equation into 1.2 the polarization now reads as:

$$P(t) = \epsilon_0 \underbrace{(\chi^{(1)} A\cos(\omega t)}_{\text{linear term}} + \underbrace{\frac{1}{2}\chi^{(2)} A^2(1+\cos(2\omega t))}_{\text{non-linear term}} \tag{1.5}$$

Figure 1.2 below illustrates the result of Franken's experiment - at first glance it appears as though the plate is blank at 3472 Å. What actually happened is that the journal copy editors assumed the mark on the image of the photographic plate was a speck of dirt and had it removed from the publication. In this case the energy conversion efficiency from the fundamental to the second harmonic was about 1 part in 10^8. This value is quite low considering that today, for example, SHG can be $> 40\%$ efficient. This is due to the phasematching not being optimised for this experiment. Phasematching shall be described in detail in section 1.6. This experiment is a clear demonstration that SHG is a real effect although at the time of its discovery it was more of a curiosity than a practical means of generating UV light.

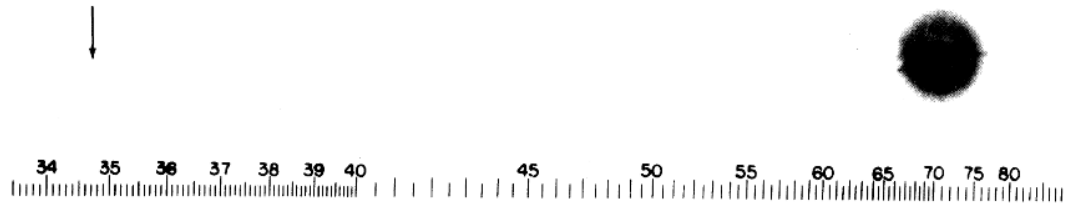


Figure 1.2: Reproduction of the first plate in which there was an indication of second harmonic generation. The wavelength scale is in units of 100 Å. The arrow at 3472 Å indicates the small but dense image produced by the second harmonic. The image of the primary beam at 6943 Å is very large due to halation. [9]

Now that the concept of non-linear optics has been introduced - albeit on a basic level - the discussion of other non-linear processes employed in laser technology for strong field physics will be simplified. Second harmonic generation is an example of a two photon non-linear effect and we can now introduce higher order n-photon non-linear effects that occur when the laser intensity is sufficiently strong.

Multiphoton ionization at relatively low laser intensities ($\leq 10^{13}$ W/cm^2) can be described by perturbation theory as a bound$-$free transition. The theory, low order perturbation theory (LOPT), treats the applied field as a small perturbation to the Coulomb potential of the atom/ molecule. LOPT predicts that the ionization rate for an $n-$photon process can be described by an intensity dependent power law:

$$\frac{dP_n}{dt} \propto I^n \tag{1.6}$$

where P_n is the ionization probability. Several experiments have been performed which have found significant discrepancies with this power law and has signalled a breakdown of LOPT [11]. Energy levels in atoms and molecules can be Stark shifted from their unperturbed positions which leads to intensity dependent corrections necessary for the generalised multiphoton absorption cross$-$sections. As the intensity is increased, population can be transferred between resonant levels via Rabi oscillations and the concept of a time dependent ionization rate becomes redundant. The non$-$perturbative nature of MPI at higher intensities manifests into ATI which is essentially MPI with more photons than the minimum required. ATI is a result from the absorption of photons by the ejected photoionizing electron while still under the influence of the atomic potential. The scaling law was verified in 1982 by Fabre *et.al* [12]. The advent of high resolution time of flight (TOF) spectrometers in 1983 [2] made it possible to obtain good ATI spectra with higher laser intensities. This development resulted in photoelectron spectra being acquired with characteristics different to those previously observed namely that the first peak of the ATI spectrum was missing and that the remaining peaks did not follow the power law in equation 1.6. The suppression of peaks in the ATI spectra can be attributed to AC Stark shifts of the bound states which is induced by the laser field.

An intense laser field will also have a significant effect on bound electrons. Since Rydberg levels are weakly bound their shifts will be close to the ponderomotive energy. Lower lying states are more tightly bound and have a much smaller polarizability so will experience a smaller shift. The shift induced on the Rydberg states is much greater than that of the lower states such that their shift can be neglected. This implies that the ionization potential increases by $\approx U_p$. This results in a reduction of the ejected electrons kinetic energy by the same amount:

$$E_{kin} \approx (n+s)\hbar\omega - (I_p + U_p) \tag{1.7}$$

Once $U_p > \hbar\omega$, peaks in the lower energy region of the ATI spectra start to become suppressed [11]. In this regime, the laser field can no longer be treated as perturbation and LOPT applied to extensions of the multiphoton picture become redundant. At intensities $\geq 10^{14}$ W/cm^2, a plateau structure was observed in ATI spectra [11]. LOPT predicts a strong exponential decrease in the ionization cross section with increasing ATI order, which fails to explain the existence of the plateau structure. The first non−perturbative treatment of the interaction between the laser field and the bound electrons of an atom/molecule was first introduced by Keldysh in 1965 [13]. Keldysh realised that if the incident field is strong enough and the frequency low, then an alternative ionization mechanism can occur other than multiphoton processes. This semi-classical treatment of the laser field lead to a distortion of the potential barrier of the Coulomb potential which enables the electron to tunnel ionise into the continuum.

Strong field processes

Equation 1.3 loses its strict validity when the applied laser field strength exceeds that of the characteristic atomic field strength, E_{at}. E_{at} is the electric field strength at a point in space and is the force per unit charge As an example, we can calculate E_{at} for the hydrogen atom using equation 1.8 below:

$$E_{at} = \frac{e}{4\pi\epsilon_0 a_0^2} \tag{1.8}$$

where $-e$ is the charge of the electron, ϵ_0 is the permittivity of free space and a_0 is the Bohr radius of the hydrogen atom which is calculated to be 5.3×10^{-11} m from equation 1.9 below:

$$a_0 = \frac{4\pi\epsilon_0\hbar^2}{me^2} \tag{1.9}$$

The laser intensity associated with the peak field strength, E_{at} can be calculated from equation 1.10 below:

$$I_{at} = \frac{1}{2}\epsilon_0 c E_{at}^2 = 3.5 \times 10^{16}\ W/cm^2 \tag{1.10}$$

In other words, the laser intensity we imply here is comparable to or exceeding the laser intensity associated with the peak electric field strength of 3.5×10^{16} W/cm^2. Above this intensity, relativistic effects can take place as a consequence of the magnetic field component of the field no longer being negligible.

1.2 Ionization processes

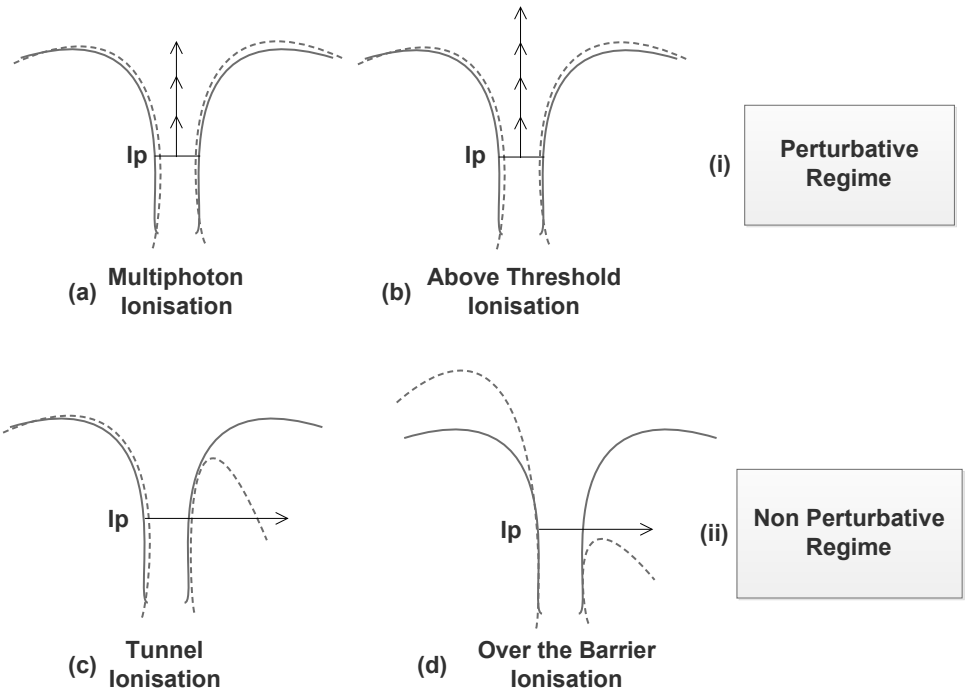
The non-linear effects mentioned in the last section are based upon the assumption that the laser field is weak ($\approx 10^{13}$ W/cm^2) in comparison to the static atomic Coulomb field of the media in question. This defines the perturbative regime and allows for the expansion of the polarization in a power series of the electric field.
As the intensity of the laser field increases, the electric field strength becomes comparable to the binding Coulomb field of an atom. In this situation perturbation theory breaks down and we enter the non-perturbative regime and the field of strong field physics because the size of the Nth order correction to the LOPT is no longer small with respect to the $(N-1)$th order. The mathematical approach for explaining the phenomena that occur in the presence of intense laser fields needs to be modified to a non$-$perturbative regime.

There are two situations wherein we can analyse the ionization of a target in the perturbative regime - Multiphoton Ionization (MPI) and Above Threshold Ionization (ATI). Typically we are in the $10^{12} - 10^{14}$ W/cm^2 range however this magnitude

is target dependent. It is probably more efficient to specify the required intensities in terms of the saturation intensity, I_{sat}. The saturation intensity invokes that the majority of the atoms/molecules are ionised before the peak intensity. For example, in Xenon $I_{sat} = 8.2 \times 10^{13}$ W/cm^2. If we assign I_0 as the laser intensity then we can specify the ionization regimes relative to the Over The Barrier Ionization (OTBI) value. OTBI implies a severe lowering of the potential barrier and is another term for the saturation intensity, as will be described later on.

- If $I_0 << I_{OTBI}$ then we are in the perturbative regime where MPI and ATI occur
- If $I_0 < I_{OTBI}$ we have entered the non-perturbative regime and tunnel ionization (TI) is the dominant process and HHG occurs
- If $I_0 \approx I_{OTBI}$ we are in the regime where OTBI dominates and there is little HHG
- If $I_0 >> I_{OTBI}$ the system is saturated and depletion occurs, thus there is no HHG and the onset of relativistic effects approaches

If the laser field matches or exceeds the Coulomb field retaining the outer-most electron of the target then the interaction can no longer be treated as a weak perturbation and we enter the non-perturbative regime where the ionization is dominated by 2 processes - Tunnel Ionization (TI) which is valid for applied intensities of $10^{14} - 10^{15}$ W/cm^2 and Over The Barrier Ionization (OTBI) which occurs for field strengths exceeding 10^{15} W/cm^2. A schematic of the different ionization processes is given in Figure 1.3.



;

Figure 1.3: Ionisation mechanisms that occur in (i) the perturbative regime: (a) Multiphoton Ionisation (b) Above Threshold Ionisation and the (ii) non perturbative regime: (c) Tunnel Ionisation and (d) Over The Barrier Ionisation

1.2.1 Multiphoton ionisation

In the multi-photon regime the electron gains enough energy to be ionised from its parent atom/molecule by successive absorption of single photons through transitions via virtual states. Thus the photon flux must be dense enough such that every photon can be absorbed on a timescale less than the lifetime of the virtual state which is determined by the uncertainty principle.

The ionisation rate is dependent upon the number of photons needed to reach the ionisation potential and the flux of photons in the interaction region and is given by [14]:

$$R_N = \sigma_N I^N \tag{1.11}$$

where N is the minimum number of photons necessary to ionise the atom, I is the

laser peak intensity and σ_N is the generalised cross section for the Nth order process that depends on the amplitude of the electric field and its wavelength. As illustrated in Figure 1.3 (a), MPI results in an electron absorbing many photons to gain enough energy to reach the ionisation potential.

1.2.2 Above threshold ionisation

Above threshold ionisation was first observed by Agostini *et al.* [15] and is distinguished from multiphoton ionisation due to the fact that once the N photons are observed, an additional S number of photons are also absorbed by the electron in the continuum after it is ionised. This is also a perturbative effect and typically occurs for intensities in the $10^{12} - 10^{14}$ W/cm^2 range. By increasing the intensity the ionisation manifests from MPI to ATI. The electron acquires kinetic energy in discrete units equal to the photon energy. The ionisation rate describing this process is given by:

$$R_{N+S} = \sigma_{N+S} I^{N+S} \tag{1.12}$$

1.2.3 Tunnel ionisation

Tunnel ionisation is the mechanism of main interest to the planned molecular High Harmonic Generation (HHG) experiments in this report. As shown in Figure 1.3(c) it can be deduced that this is a quantum mechanical effect whereby an electron tunnels through the potential barrier. Since the process occurs for intensities in the $10^{14} - 10^{15}$ W/cm^2 range this is a strong field effect. At these intensities the electric field disturbing the binding potential lowers the height of the barrier that the electron sees - a lower barrier presents the opportunity for the electron to tunnel ionise. Due to the fact that the electric field of the laser is suppressing the barrier the tunnelling time for the electron must be less than half an optical cycle because the field reverses direction and therefore the barrier is raised again - think of it as the ionisation potential binding the electron oscillating with the laser field in a periodic fashion.

The tunnelling rate is exponentially sensitive to the area under the barrier which is

determined by the bound state energy and the laser field strength [16].

$$\Gamma \approx exp[-\frac{2(2I_p)}{3E(t)}]^{\frac{2}{3}} \tag{1.13}$$

where I_p is the ionization potential (eV) and $E(t)$ is time varying electric field strength (V/m). The exponential dependence of the tunneling rate ensures that (a) the highest energy electronic states are field ionized first and that (b) the ionisation is confined in time to $\approx \pm 200$ attoseconds (or 1/10 th of an optical cycle) around the cycle peak [17].
The potential that the electron sees is a combination of the atomic potentials and the potential generated by the laser field.

$$V(x,t) = \frac{-Ze^2}{4\pi\epsilon_0 x} - exE_0 cos(\omega t) \tag{1.14}$$

where Z is the charge state of the target (note that $Z = 1$ when a atom is ionised once), x is the distance from the centre of the atom, ω is the angular frequency of the laser and t is the time in the laser pulse.

1.2.4 Over the barrier ionisation

As the intensity is increased to above 10^{15} W/cm^2 the atomic potential is severely distorted such that the barrier is lowered below the ionisation potential and the bound electron is free. The potential seen by the electron is a combination of the atoms potential and the maximal electric field of the laser light:

$$V(x,t) = \frac{-Ze^2}{4\pi\epsilon_0 x} - exE(t) \tag{1.15}$$

where e is the electronic charge, ϵ_0 is the permittivity of free space, x is the distance from the centre of the atom and $E(t)$ is the time varying electric field produced by the laser light. This relation can be used in a very straightforward manner to calculate the peak intensity at which OTBI occurs [2].
The following relationship can be used to determine the intensity required to observe OTBI in different systems depending upon the ionization potential of the target:

$$I_{OTBI} = \frac{c\epsilon_0}{2} {E_0}^2 = {I_p}^4 \frac{\pi^2 c \epsilon_0^3}{2Z^2 e^6} \tag{1.16}$$

This expression can also be simplified to the following, more commonly used format:

$$I_{OTBI}[W/cm^2] = {I_p}^4 \frac{\pi^2 c \epsilon_0^3}{2Z^2 e^6} = 4 \times 10^9 \frac{(I_p[eV])^4}{Z^2} \tag{1.17}$$

within which Z is the final charge state of the ion and I_p is the ionization potential. Taking an example, for Ne $\rightarrow$ Ne^+ by OTBI, we have $I_p = 21.56$ eV and $Z = 1$. A value for the critical intensity can be calculated to be: 8.7×10^{14} W/cm^2. In a similar fashion to tunnel ionisation, OTBI is different in atoms and molecules. This is due to the multicentre potential inherent to molecules. In OTBI, the oscillating electric field distorts and suppresses the potential barrier below the ground state energy of a molecule thus allowing electrons to escape into the continuum.

1.3 Ponderomotive energy

The ionisation mechanisms described in the previous sections permit an electron to be ionised and liberated from its parent atom/molecule. Once free, the electron position and velocity oscillate in the laser field. The electrons are accelerated in the continuum by the oscillating electro-magnetic field of the laser and start to wiggle along the polarization vector of the electric field component. The motion of the oscillating electron is associated with an energy termed the ponderomotive energy, U_p, which is the cycle-averaged kinetic energy of the electron as it moves under the action of the oscillating force:

$$U_p = \left\langle \frac{e^2 {E_0}^2}{2m_e\omega^2} cos^2(\omega\tau_{cycle}) \right\rangle \tag{1.18}$$

$$U_p = \frac{e^2 |E_0|^2}{4m_e\omega^2} \tag{1.19}$$

where ω is the laser frequency and E_0 is the electric field amplitude. Knowing the following equation for laser intensity we can derive another, more convenient format of the equation for the ponderomotive energy:

$$I = c\epsilon_0 \frac{{E_0}^2}{2} \tag{1.20}$$

$$U_p = \frac{e^2 I}{2m_e \epsilon_0 c\omega^2} \propto I\lambda^2 \tag{1.21}$$

To put this quantity into perspective the example of a wavelength of 1μm at an intensity of 10^{14} W/cm^2 gives a ponderomtive energy of ≈ 10 eV. This quantity scales linearly with the laser intensity. It is evident from this equation that the ponderomotive energy of an electron can be quadrupled just by doubling the wavelength (e.g. the ponderomotive energy can be increased from 10 eV to 40 eV just by doubling the wavelength from 1μm to 2μm at a fixed intensity of 10^{14} W/cm^2.

1.4 The Keldysh parameter

The Keldysh parameter [13] is used to distinguish the different ionisation mechanisms detailed above (ATI, MPI, TI and OTBI) as a function of the atomic species, laser wavelength and intensity. In essence, it is the ratio of laser frequency ω_0 to the tunnelling frequency, ω_t. There is no sudden change at some given intensity where the ionisation process flips from multiphoton to strong field regimes, but as intensity is increased the probability of the ionisation occurring by strong field processes increases whilst that of the multiphoton mechanisms diminishes.
Hence we can arrive at the following equation for the tunnelling frequency:

$$\omega_t = \frac{2\pi e E_0}{I_p}\sqrt{\frac{2I_p}{m}} \approx \frac{eE_0}{\sqrt{2I_p m}} \tag{1.22}$$

where m is the mass of the electron.

Equation 1.22 above suggests that the tunnelling process is only dependent upon the laser intensity but once $\omega_t << \omega_0$, the electron does not have enough time to tunnel through the barrier during one laser cycle. In this case the ionisation should become laser frequency dependent. This motivates using the ratio between the laser and the tunnelling frequencies as an indicator of the frequency dependent (hence, multiphoton) and frequency independent (tunnel) ionisation processes.

$$\gamma = \frac{\omega_0}{\omega_t} = \frac{\omega_0\sqrt{2I_p m}}{eE_0} \tag{1.23}$$

such that for $\gamma << 1$ ionisation is taking place in the tunnelling regime and for $\gamma >> 1$ the ionisation is taking place via the multiphoton process. Hence we can say that we are in the pure strong field regime for cases where $\gamma << 1$. For the case where $\gamma \approx 1$, there is a mixture of ATI and tunnelling. OTBI is evidently not referred to here due to the fact that the barrier is suppressed below the ground state energy of the electron and thus there is no barrier for it to traverse before it reaches the continuum. Even though it is not inherent in the expression for the Keldysh parameter, strong field ionisation implicitly requires short laser pulses. This is due to the fact that for a fixed pulse energy the highest intensity is reached for the shortest pulse duration. For a longer pulse the ionisation would saturate before peak intensities required for strong field effects are reached.

It is often more convenient to use the following format of the Keldysh parameter expression as it directly incorporates the ponderomotive energy:

$$\gamma = \frac{T_{tunnel}}{T_{laser}} = \sqrt{\frac{I_p}{2U_p}} \tag{1.24}$$

where in this format γ is the ratio of the time it takes to tunnel through the barrier, T_{tunnel} to the oscillation period of the laser field T_{laser}.

1.5 High harmonic generation

This section will detail the physics behind the HHG process before going on to extend this theory to molecules which are the targets relevant to this dissertation. A summary of the work already performed on large organic molecules with HHG will also be presented. Chapter 3 will discuss what we propose to achieve by extending HHG spectroscopy to benzene and substituted benzene molecules.

The 3 step model of HHG [18] [19] is generally accepted as the most appropriate explanation of the process. This semi-classical description breaks HHG into three distinct events; ionization, continuum propagation and recombination. Figure 1.4 below illustrates the 3 step model of HHG.

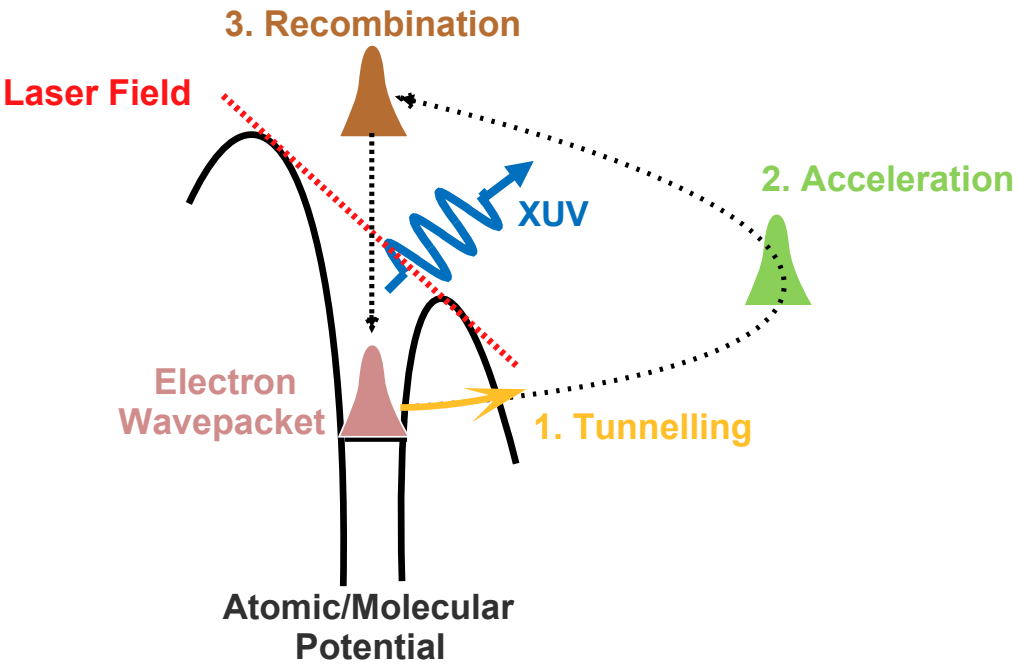


Figure 1.4: Diagram of the 3−step model. The first step involves a portion of the bound electron wavepacket tunnelling through the potential barrier. The liberated electron wavepacket is then accelerated along the laser field polarization in the second step. In the third step, once the electric field reverses direction the accelerated wavepacket is brought back towards the parent ion where it can recombine to the ground state resulting in the emission of a harmonic XUV photon.

1.5.1 Step 1: Ionisation

In the first step a laser field of sufficient intensity is applied to an atomic or molecular target, typically in the range $10^{13} - 10^{15}$ W/cm^2. The strong electric field of the laser distorts the binding potential to such an extent that a portion of the bound electron wavepacket can tunnel ionise through the barrier and make a transition to the continuum. In the strong field limit ($\gamma < 1$) this picture of the tunnelling mechanism leads to accurate predictions of the ionisation process. As the barrier is lowered, its width decreases which makes tunnel ionisation more probable. Tunnel ionisation occurs with high probability near the peak of the sinusoidally varying electric field amplitude due to the exponential dependence of the tunnelling rate on the factor derived by Ammosov, Delone and Krainov (ADK) rate [16]:

$$\Gamma = e^{-\frac{2(2I_p)^2}{3E_0}} \tag{1.25}$$

This ADK rate is valid for static fields such that at any instant in time the potential barrier does not change much while the electron is tunnelling. We can quantify the meaning of how "much" the barrier changes via the adiabaticity parameter - the Keldysh parameter [13]. In the case where $\gamma << 1$ the barrier can be considered as quasi-static and E_0 in equation 1.25 can be replaced by an oscillating field $E(t)$; this implies that the exponential in the ADK rate equation 1.25 leads to extremely short bursts of electrons around the peak of the laser electric field. However it is worth noting that in a HHG experiment, the Keldysh parameter is in a grey area with respect to being much greater or much less than 1. For example, using equation 1.26 below we can calculate γ for the experimental conditions of $I_p = 9.2$ eV, $I = 5 \times 10^{13}$ W/cm^2, and an 1800 nm drive laser field. In atomic units these values are as follows: $I_p = 0.34$, $\omega_0 = 0.0253$ for the laser frequency and we get a value of $E_0 = 0.038$ from using the laser intensity to calculate the field strength. We arrive at equation 1.26 from equation 1.23 using atomic units since $\hbar = m_e = e = 4\pi\epsilon_0 = 1$.

$$\gamma = \omega_0 \frac{\sqrt{2I_p}}{E_0} \tag{1.26}$$

For the values above we get $\gamma \approx 0.55$. In these circumstances, the tunnelling can become non-adiabatic such that the barrier moves during the tunnelling [20]. The non-adiabatic tunnelling rate has been derived; it remains a non-linear function of the field modulus, just less sharply peaked than the ADK rate [4].

Traditionally tunnelling rates for strong field ionization in both the multiphoton and tunneling regimes are averaged over the laser cycle. Sub cycle dynamics are of key importance to processes such as ATI and HHG. The advent of sub two cycle laser pulses [21] has presented a new tool for probing electron and nuclear dynamics in molecules which involves the measurement of the absolute carrier envelope phase (CEP) of the electric field oscillation under the field envelope. In a few cycle laser pulse the intensity changes from one cycle to the next which makes the cycle averaging inherent to traditional formulations meaningless. The instantaneous laser phase varies significantly from both the multiphoton and quasistatic regimes.

Yudin and Ivanov [20] have developed a model for calculating the time dependent ionization rates independent of the value of γ. The model does not depend upon the quasistatic approximation and is referred to as non-adiabatic tunnelling. Figure 1.5 shows the dependence of the ionization rate, $\Gamma(\theta)$ on the instantaneous phase of the laser field.
The tunnelling rate for molecules has to take into account the fact that there are multiple nuclei in a molecule; this breaks the spherical symmetry of the field free system which implies that we now need to modify how we describe the molecular wavefunctions. The MO-ADK [22] also needs to account for the the orientation of the molecule with respect to the laser polarization. In the case of atoms, the valence electronic state has well defined spherical harmonics in the region where the wavefunction behaves asymptotically. In the asymptotic region the potential is negligible and the total wavefunction can be considered as a superposition of plane waves all with the same absolute value of momentum, $\hbar k$. To extend this representation to molecules the approach is to express the molecular wavefunctions as a summation of spherical harmonics in a one-centre expansion. The asymptotic wavefunction of a valence electron in a diatomic molecule at large distances from the core can be expressed in atomic units as:

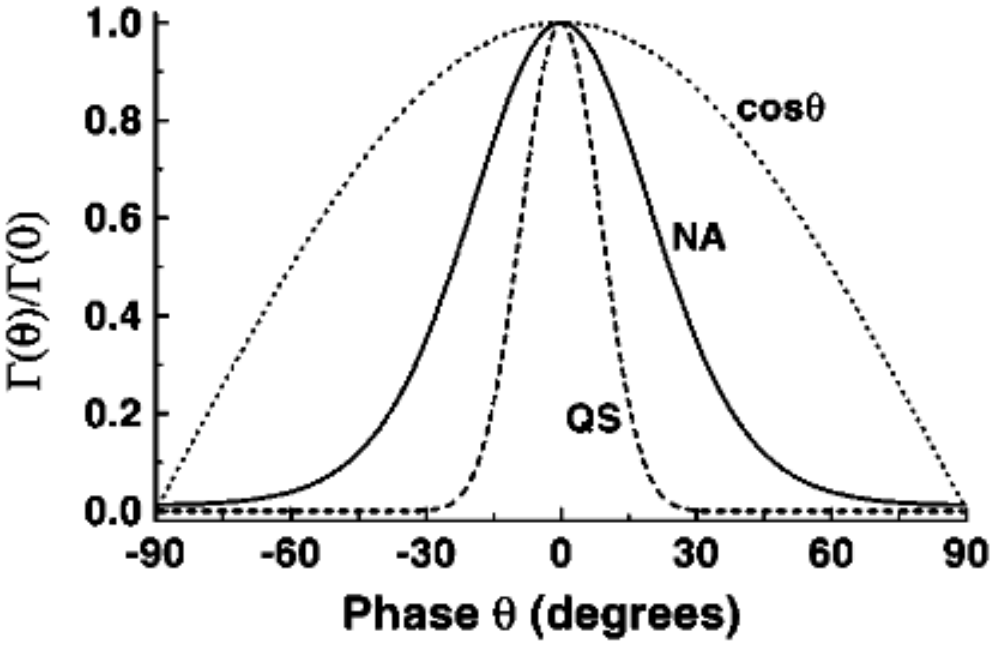


Figure 1.5: Dependence of instantaneous ionization rate, $\Gamma(\theta)$ on phase of the laser field, θ. Data is normalised to $\Gamma(0)$. QS stands for quasistatic and NA stands for non-adiabatic. The dotted $\cos(\theta)$ represents a single laser cycle. Calculations were performed in He for a 780 nm laser field with an intensity of $I = 5 \times 10^{13}$ W/cm^2 [20]

$$\Psi^m(\mathbf{r}) = \sum_{l,m} C_{lm} F_l(r) Y_{lm}(\hat{\boldsymbol{r}}) \tag{1.27}$$

where m is the magnetic quantum number, Y_{lm} are the spherical harmonics and C_l is a normalisation coefficient such that we can express the wavefunction in the asymptotic region as:

$$F_l(r \to \infty) \approx r^{\frac{Z_c}{\kappa}-1} e^{-\kappa r} \tag{1.28}$$

where Z_c is the charge of the residual ion and $\kappa = \sqrt{2I_p}$. In this expression we assume that the molecular axis is aligned along the electric field polarization so the electron will be ionised at $\theta \approx 0$. This gives a static tunnelling rate for a molecule of:

$$\omega_{stat}(E_0, \mathbf{R}) = \sum_{m'} \frac{B^2(m')}{2^{|m'|} \mid m \mid !} \frac{1}{\kappa^{\frac{2Z_c}{\kappa-1}}} (\frac{2\kappa^3}{E_0})^{\frac{2Z_c}{\kappa-|m'|-1}} e^{-\frac{2\kappa^3}{3E_0}} \tag{1.29}$$

where E_0 is the peak field strength. The term $B(m')$ accounts for the orientation of the molecule relative to the electric field polarization. If the molecule is at an arbitrary angle $\mathbf{R}$ with respect to the laser electric field direction then $B(m')$ can be expressed as:

$$B(m') = \sum_{l,m} C_{lm} D^l_{m',m}(\phi, \theta, \chi) Q(l, m') \tag{1.30}$$

where $D^l_{m',m}(\phi, \theta, \chi)$ is the rotation matrix. The summation over l,m accounts for the breaking of the spherical symmetry by the molecular system. $Q(l, m')$ depends on the angular momentum of the molecule; m=0 corresponds to a σ orbital and m=1 corresponds to a π orbital.

The ionization rate is not only dependent upon the orbital symmetry, ionization potential and molecular orientation with respect to the laser electric field polarization, but also upon the lasers average electric field strength in the focus and the beams spatial and temporal profiles. The electric field is taken to be that of a Gaussian beam and has the form:

$$E(t, r, z) = \frac{E_0 \omega_0}{\omega(z)} e^{-\frac{2ln2r^2}{\omega^2(z)}} e^{-\frac{2ln2t^2}{\tau^2}} \tag{1.31}$$

where $\omega(z) = \omega_0 \sqrt{1 + \frac{z^2}{z_R^2}}$, where ω_0 is the size of the focal spot, $z_R = \frac{\pi \omega_0^2}{\lambda}$ is the Rayleigh range and λ is the laser wavelength, E_0 is the peak electric field strength of the laser and τ is the pulse length at full width half maximum (FWHM). For a molecule that is aligned along $\mathbf{R}$, which defines the Euler angles between the molecular axis and the laser field direction, the ionization probability can be expressed as:

$$P(E, \mathbf{R}) = 1 - e^{[-\int \omega(E, \mathbf{R}) dt]} \tag{1.32}$$

In order to be able to compare this to what can be measured experimentally we need to calculate the ionization signal which can be expressed as:

$$S_0(\mathbf{R}) \propto \int P(E, \mathbf{R}) 2\pi r dr dz \tag{1.33}$$

for molecules that are aligned in a direction defined by the Euler angles $\mathbf{R}$. The integration can be performed on an equi-intensity surface - this will reduce the two-dimensional integration to a one-dimensional integration.

If the molecules are randomly oriented then the ionization signal can be calculated as:

$$S_1 \propto \int S_0(\mathbf{R}) d\mathbf{R} \tag{1.34}$$

Tong *et al.* [22] have applied this theory for calculating the ionization rates for homonuclear diatomic molecules such as D_2, H_2, O_2 and N_2 compared to atoms of a similar ionization potential such as xenon for O_2. Calculations have been compared to experimental data and good agreement is made for the cases where the molecule exhibits ionization suppression (i.e. D_2 and O_2) and for the cases without supression (i.e. N_2). Stapelfeldt *et al.* [23] have also applied MO-ADK to nonlinear polyatomic molecules of different point group symmetries such as benzene and fluorobenzene. This work is also in good agreement with what we expect.

Murray *et al.* [24] have investigated the reliability of this MO-ADK method and how it relates the tunnel ionization rate to the ionising orbitals electronic density profile. Intuitively it is expected that that tunnelling rate will peak along the most spatially extended component of the HOMO. Indeed, this is what the MO-ADK theory predicts. In CO_2, the tunnelling rate is expected to peak at an angle of 30° between the laser field and the molecular axis. In the experiment it has been observed that this sharp peak in ionization actually occurs at an angle of 45°. The modified tunnelling rate theory developed by Murray *et.al* [24] infers that this a general trend in polyatomic molecules. The tunnelling rate can be written as:

$$\Gamma = \Gamma_{A,s} R(\theta_L) = \left[\frac{\pi}{\tau_T} C_\kappa^2 e^{-\frac{2\kappa^3}{3E_0}} \left(\frac{2\kappa^3}{E_0} \right)^{\frac{2Q}{\kappa}} \right] R(\theta_L) \tag{1.35}$$

where $\tau_T = \kappa/E_0$ The first term, $\Gamma_{A,s}$ is simply the standard tunnelling rate for an atomic s orbital with no angular structure. The second term, $R(\theta_L)$ takes into account all aspects of the orbital structure including the interference of tunnelling currents which arise from different lobes of the orbital. In order for the theory to be extended to molecules in a more complete manner it has to take into account the contributions from lower lying orbitals and to a lesser extent the effect of the linear Stark effect on the ionization potential due to the orbital dipole [25]. The linear Stark effect increases or decreases the ionization potential when the laser field polarization is parallel or antiparallel, respectively, to the orbital dipole. It is important to stress that in general absolute tunnelling rates are not necessary for interpret a HHG spectrum from a molecule but are critical in cases where the orientational dependence of the molecule is fundamental.

1.5.2 Step 2: Continuum propagation

In the second step of the HHG process the electron wavepacket that has tunnelled through the suppressed barrier is born into the continuum and moves in response to the laser field, first it is accelerated away from the parent ion before returning after the laser field reverses direction; typically after a quarter of an optical cycle. The propagation of the electron in the continuum can be very well described classically as the motion of a charge in an oscillating electric field. The motion is dictated by the phase of the field when the electron is ionised, the laser field frequency and the laser field amplitude. The equation of motion is given by:

$$\frac{d^2x}{dt^2} = \frac{e}{m_e} E_0 cos(\omega t + \phi) \tag{1.36}$$

We set the initial conditions such that a portion of the electron wavepacket is liberated from the parent molecule at time t_0 with zero initial kinetic energy; $v(t_0)$. It is also a necessary boundary condition that the electron wavepacket must return to its parent

ion in order for recombination to occur.

$$\left.\frac{dx}{dt}\right|_{t=t_0} = 0 \tag{1.37}$$

$$x(t_0) = 0 \tag{1.38}$$

The solutions for $x(t)$ and $v(t)$ are as follows:

$$v(t) = \frac{dx}{dt} = \frac{eE_0}{m_e\omega}\left[sin(\omega t) - sin(\omega t_0)\right] \tag{1.39}$$

$$x(t) = -\frac{eE_0}{m_e\omega^2}\left[cos(\omega t) - cos(\omega t_0) - \omega(t-t_0)sin(\omega t_0))\right] \tag{1.40}$$

The kinetic energy can be very easily calculated from the expression $E_{kin}(t) = \frac{1}{2}m_e v^2(t)$:

$$E_{kin}(t) = 2U_p\left[sin(\omega t) - sin(\omega t_0)\right]^2 \tag{1.41}$$

where $U_p = \frac{e|E_0|^2}{4m_e\omega^2}$ is the ponderomotive energy that was discussed in section 1.3. The ponderomotive energy is the energy acquired in the continuum as it is accelerated in an oscillating laser electric field. We can write the ponderomotive energy over one laser cycle as:

$$U_p[eV] \approx 9 \times 10^{14} I\lambda^2 \tag{1.42}$$

where I is the laser intensity in units of W/cm^2 and λ is the laser wavelength in μm. The spectrum of radiation emitted upon recombination of the electron with the parent ion is given by $E_{XUV} = 3.17U_p + I_p$. The $3.17U_p$term arises from equation 1.41 where $sin(\omega t_0) = 17^\circ$ is the phase of ionization and $sin(\omega t) = 255^\circ$ is the phase of recombination. Thus if we want to maximise the spectrum we observe, we need to

increase U_p as we have no control over the target ionization potential for a given atom or molecule. The ponderomotive energy scales linearly with intensity and quadratically with wavelength. Increasing the intensity has many limitations; presently we are confining this discussion to single molecule HHG but the role of intensity will become important when we discuss the macroscopic response in section 1.6. In the case of working with the organic molecules, using a high intensity can easily induce ionization saturation and molecular fragmentation which are detrimental for performing HHG spectroscopy on these molecules. It is also useful noting that a very high ($\geq 10^{16}$ W/cm^2 intensity can imply the $\vec{\mathbf{B}}$ field component of the electromagnetic field is no longer negligible which can start to play a role and interfere with the HHG process.

Alternatively, the drive wavelength can be increased [26] [27]. The technology to do this will be elaborated upon in Chapter 2. The λ^2 scaling of the cutoff frequency is offset by an unfavourable conversion efficiency from the laser energy into XUV energy of $\lambda^{-(5-6)}$. This scaling can be attributed to the spatio−temporal spreading of the electron wavepacket in the continuum [28]. Due to the fact that the molecules we are interested in performing HHG spectroscopy on have quite low ionization potential values (< 10 eV) it is preferable to keep the drive intensity low to prevent ionization saturation. It is also more practical to increase the drive wavelength as these molecules are carbon heavy (contain carbon−carbon bonds) and their nuclear dynamics are expected to be on the few femtosecond timescale so we need to ensure that the cut-off frequency is as high as attainable so we can get a thorough snapshot of the dynamics in these molecules from our HHG spectra.
The time at which the electron wavepacket is born into the continuum is important as it dictates if the liberated wavepacket will follow a short or a long trajectory.
Figure 1.6 is the calculated electron trajectories for an 800 nm field with an intensity of 1×10^{14} W/cm^2. Electrons that are born into the continuum between the peak of the field and 1/20th of a cycle follow "long trajectories". Analogously, electrons that are launched into the continuum between 1/20th of a cycle and the zero crossing of the electric field follow "short trajectories". Electrons that follow short trajectories follow the shortest path and return with relatively low energy as they have not spent a long time being accelerated by the electric field. Long trajectories have the opposite dependence, the electrons spend longer in the field and return with smaller energy. For electrons that are born at 1/20th of a cycle after the field peak, the short and

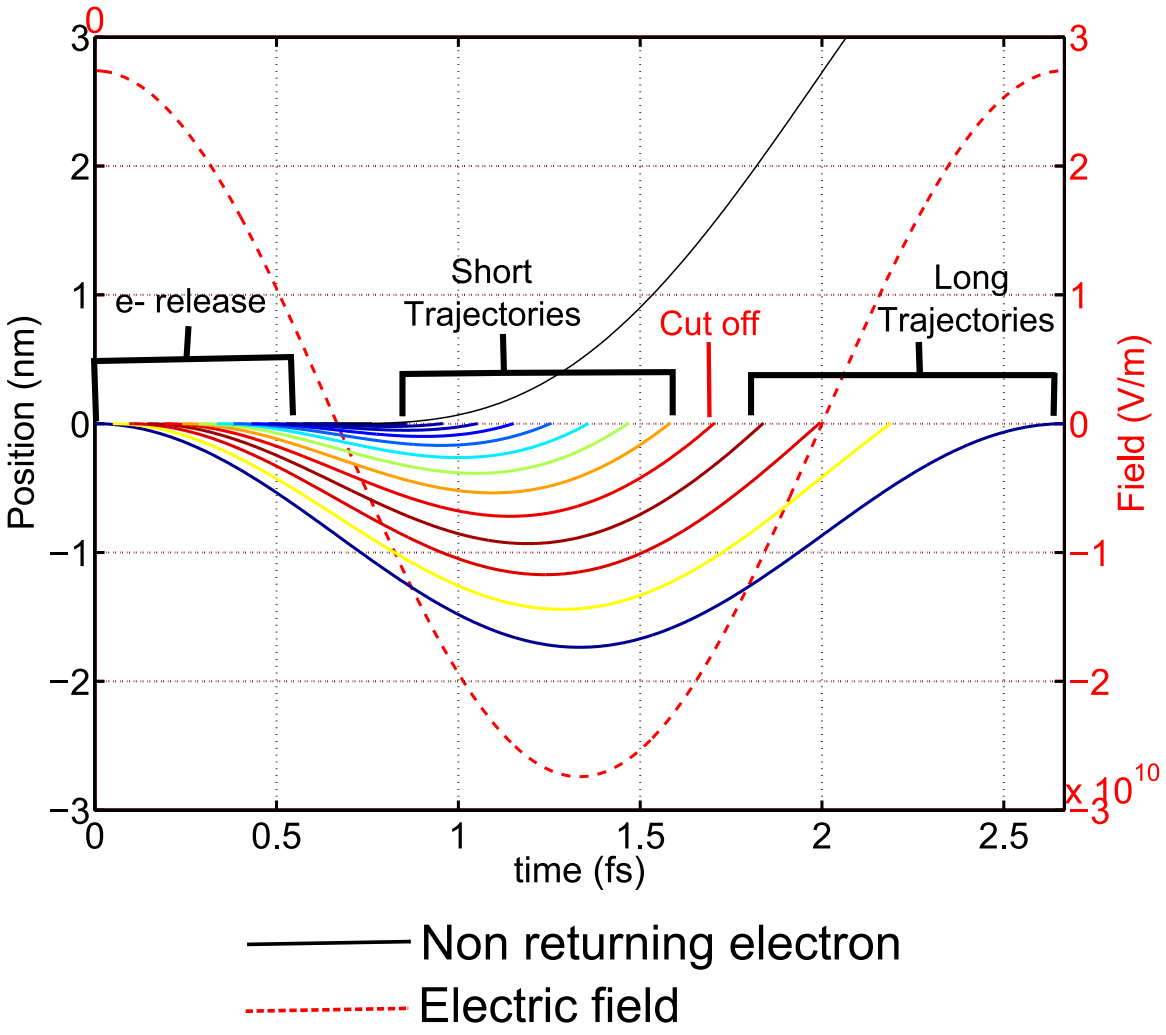


Figure 1.6: Classical calculation of the short and long trajectories from an 800 nm field with a peak intensity of 1×10^{14} W/cm^2. The black solid line represent a non−returning electron which is ionised at t= 0.1 fs.

long trajectories converge and have the highest energy upon return which gives rise to the cut-off. We will return to the discussion of trajectories when we introduce the macroscopic effects.

1.5.3 Step 3: Recombination

In the final step of the 3 step model, the electron that has been accelerated in the continuum and has been gaining energy is brought back in the vicinity of the parent ion to which it recombines and results in the emission of a high energy photon. This process happens with the same properties every cycle of the laser field for a multi-cycle driving laser pulse. The process is repeated with inversion symmetry every half cycle of the field meaning that the recollision direction of the electron wavepacket in the continuum changes sign. In a spectrometer the contributions of the individual XUV bursts interfere, and because the process is repeated every cycle with the same properties, the spectrum consists of harmonics of the driving laser field. Due to the inversion symmetry of the process the HHG spectrum only contains harmonics that are odd multiples of the driving laser field [4] - provided that the driving field is single colour. The inversion symmetry can be broken by using a two colour driving field such that the spectrum will contain both odd and even harmonics of the driving laser field [29]. A schematic of a typical HHG spectrum is shown in Figure 1.7.

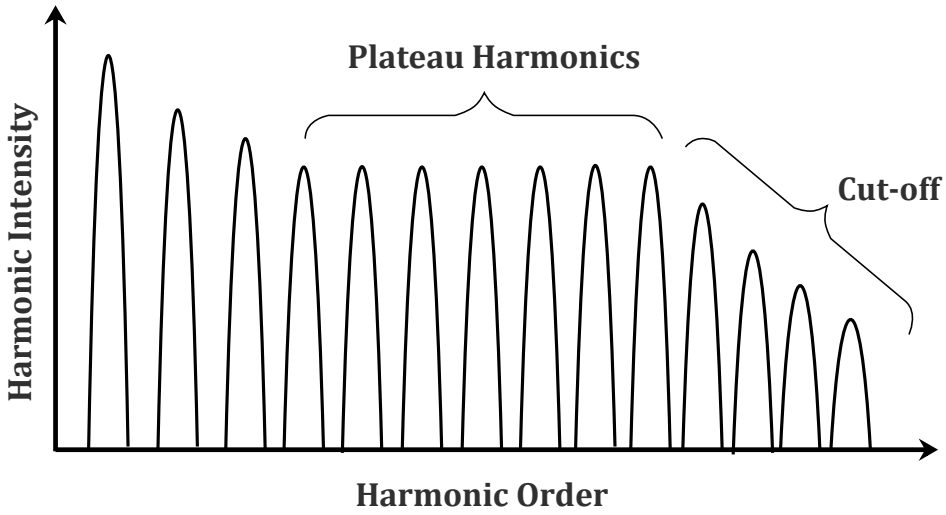


Figure 1.7: Diagram of the characteristic shape of a typical HHG spectrum

Since it was first demonstrated [3], HHG has been performed in a diverse range of media consisting of atoms, molecules and clusters and with many targets such as solid targets,continuous gas jets, gas cells and gas filled hollow waveguides. As seen

in Figure 1.7, there is a rapid drop in signal in the first few orders, followed by an extended plateau of harmonics and finally a cut-off at the highest orders.

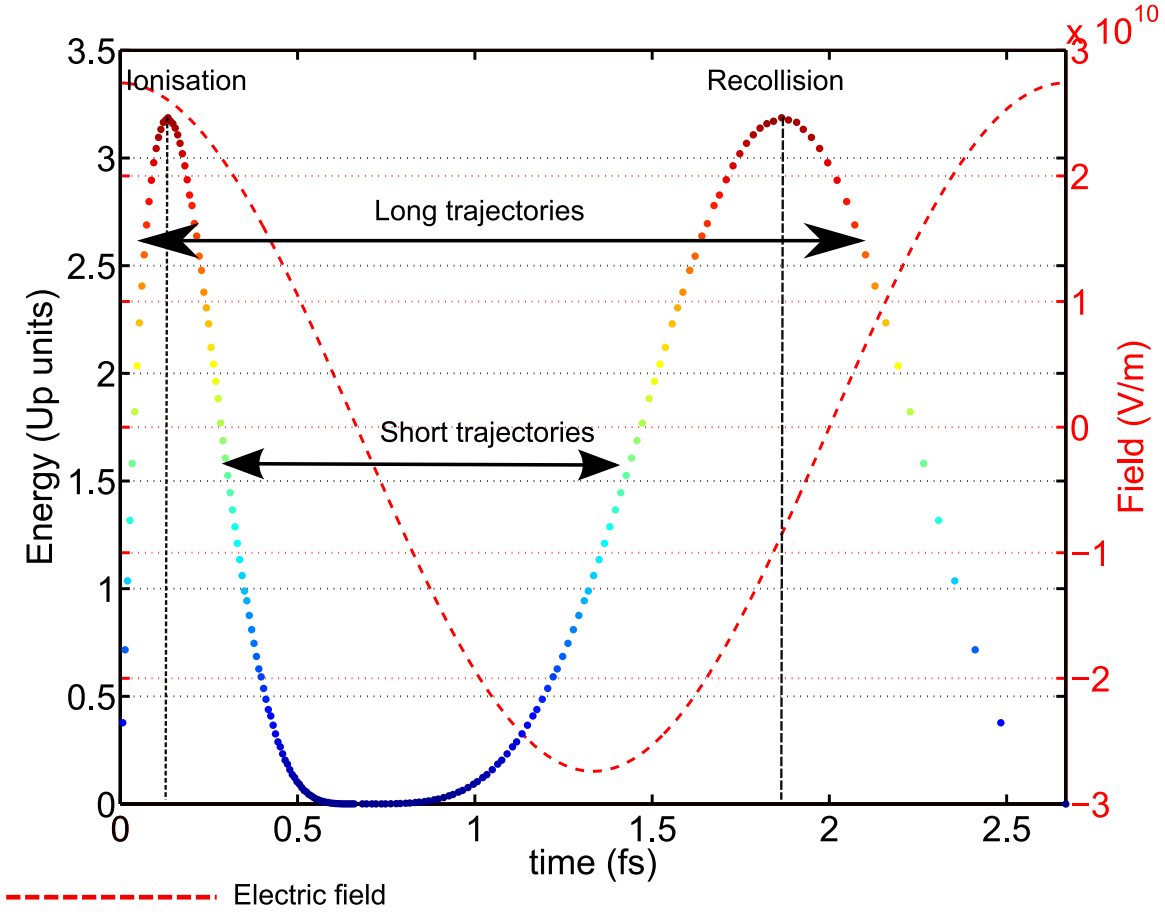


Figure 1.8: Ionization and recombination times for short and long trajectories from an 800 nm laser field with an intensity of 1×10^{14} W/cm^2. The left vertical axis represents the electron kinetic energy in terms of ponderomotive energy/ The right vertical axis shows the laser electric field amplitude

As shown in Figure 1.8, ionization can occur at a range of times around the peak of the electric field. Components of the electron wavepacket born at different times follow different trajectories, and gain varying amounts of energy from the field. Therefore each harmonic has a different emission time which implies that the electron wavepacket that has been accelerated in the continuum is chirped [30] [31]. Naturally this chirp needs to be compensated for in experiments where measurements are to made using the attosecond duration XUV pulses such that they will have the minimum possible duration [32] [33]. The chirp of this wavepacket can be thought of as

a clock per se. Taking just the case where the short trajectories are present we can see that for each short trajectory the electron returns to the parent ion at a different time delay and each is associated with a different electron kinetic energy at the point of recollision. Higher order harmonics are generated at successively longer time delays. This inherent characteristic of HHG provides a one-to-one mapping between temporal delay and photon frequency otherwise known as time-frequency mapping. The application of time-frequency mapping to HHG Spectroscopy will be discussed in chapter 3.

As shown in Figure 1.9, there is a clear relationship between the harmonic orders and the arrival time of the returning electron. The time window over which we can clock ultra-fast processes is limited by the maximum excursion time of the electron in the continuum - the cut-off. Plotted in Figures 1.9 and 1.10 are the time−frequency mapping plots as a function of drive wavelength and intensity respectively. Expressions for the electron wavepacket excursion times in these plots for both the short and long trajectories as a function of harmonic order were derived by Zaïr *et.al* [34]. As shown in Figure 1.9, if using the 800 nm laser field, the plateau harmonics from short trajectories give a time window of 0.9−1.6 fs and for the long trajectories this window can be extended to 2.4 fs. Increasing the wavelength to 1300 nm gives a maximum possible time window of 4 fs. The linear relationship between the time window size and the drive wavelength is evident; even just using the short trajectory emission from the 1800 nm laser field extends the time window to 4 fs, or in excess of 6 fs is using the long trajectory emission. Since we are working with molecules that are predicted to have femtosecond timescale dynamics it is necessary for us to work in the mid-IR at the idler wavelengths.

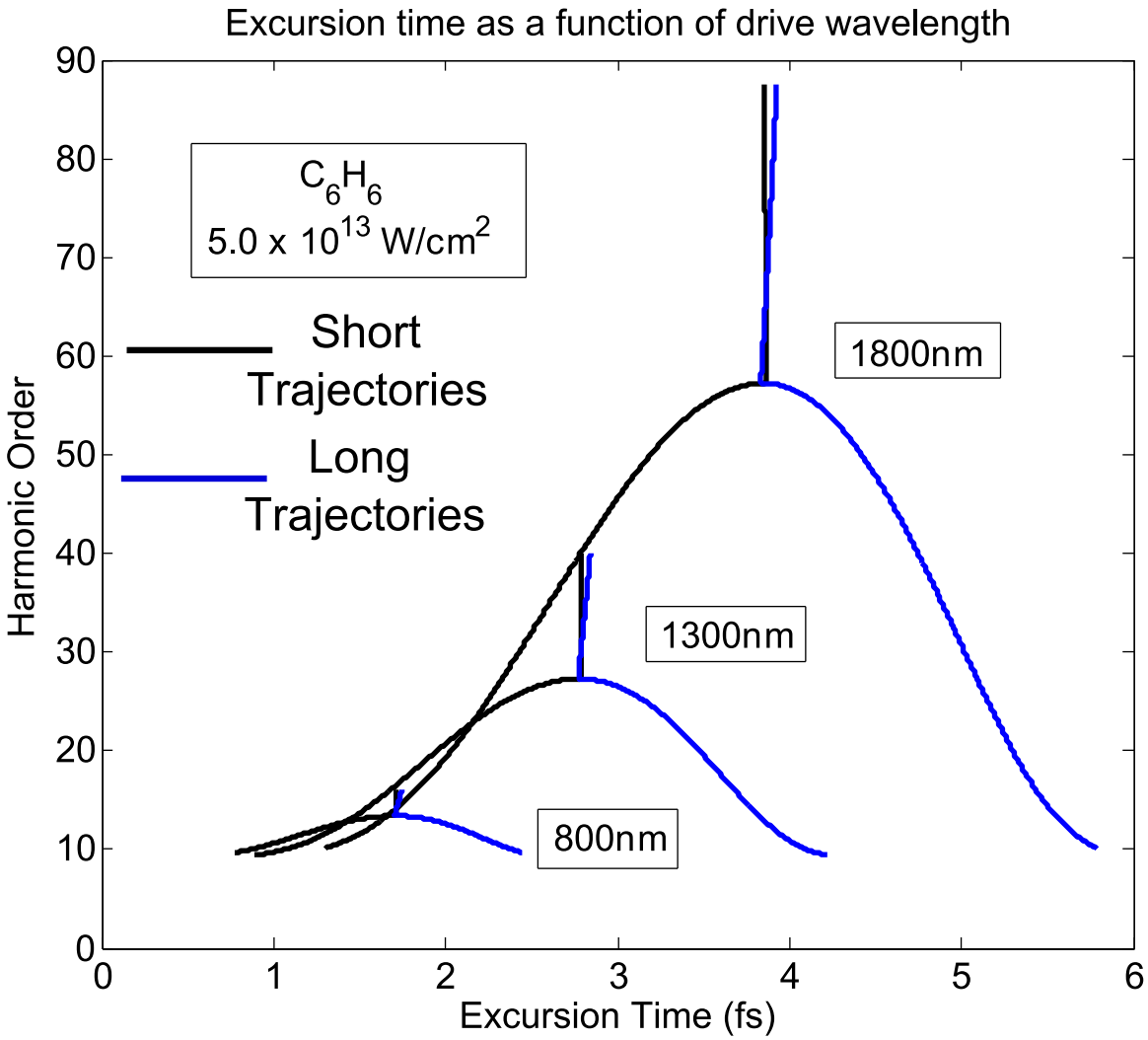


Figure 1.9: Excursion time of an electron in the continuum as a function of drive wavelength. The black lines represent the short trajectories and the blue lines represent the long trajectories which converge to the cut−off trajectory. The tails for each of the plots is not physical and emerges as an artefact of the calculation. This calculation was performed on benzene I_p= 9.2 eV. Calculations done by F. McGrath.

Plotting the time-frequency mapping as a function of varying laser intensity is shown in Figure 1.10. It is clear from this plot that increasing the laser intensity does not modify the time window but it does affect the temporal resolution.

For a given laser wavelength, the cut-off energy will always correspond to the same excursion but as we see increasing the intensity implies that there are more harmonics in the time window at higher intensity values. Note that for this plot it is a single colour generating field so it is only odd order harmonics that are present in the time

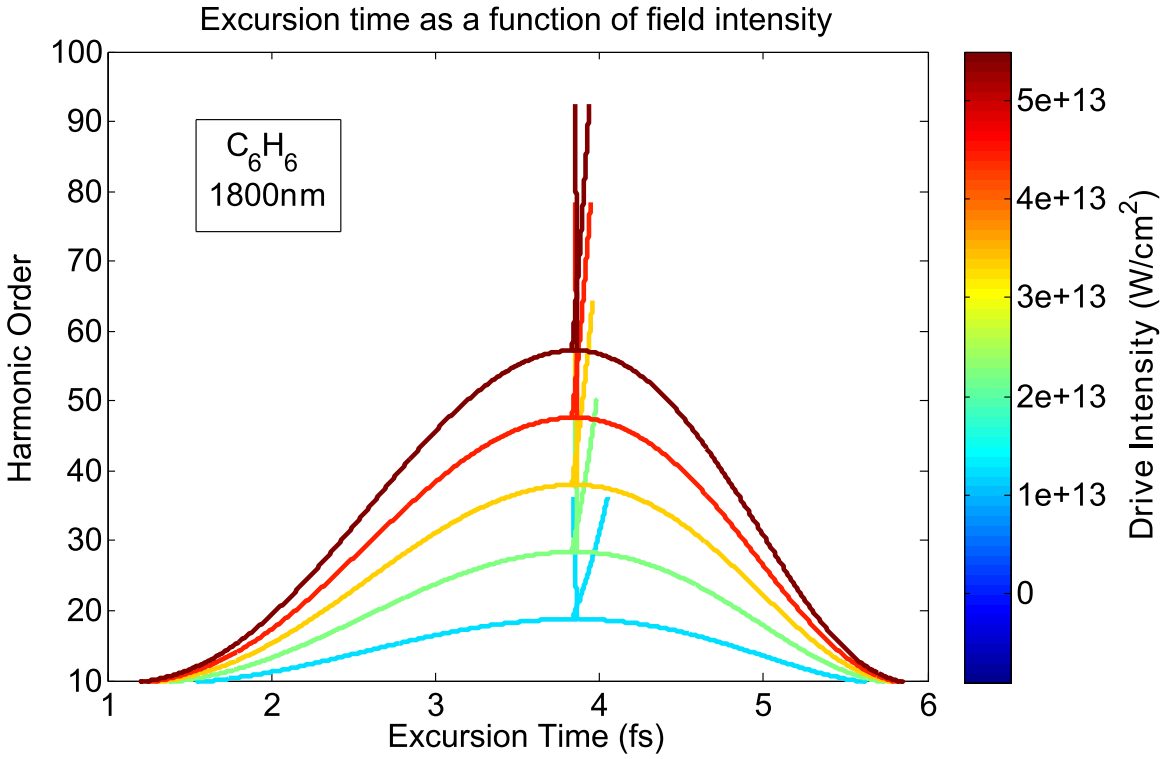


Figure 1.10: Time−frequency mapping as a function of field intensity for the benzene molecule and a drive wavelength of 1800 nm.

window. Increasing the intensity is analogous to having more frames in a movie sequence; this means we will have more points at which we can measure dynamics in the large organic molecules.

1.6 Phasematching in HHG

So far only the single atom response has been considered in the discussion of HHG. In reality the overall XUV that is generated arises from the coherent sum of many atoms involved in the process. In order to permit constructive interference it is important that the HHG field is in phase with the driving laser field over the interaction length. Take the example of having two emitters − each will individually emit radiation with a fixed phase from the fundamental beam. The phase difference between these emitters determines if the signal adds up constructively or destructively. The process of ensuring that all emitters emit radiation at the same phase is termed phase matching. This allows for signal to build up over a number of emitters which leads to the efficient generation of radiation [35] [36] [37]. The phase mismatch can be written as follows:

$$\Delta k = qk_0 - k_q \tag{1.43}$$

where Δk is denoted the wave vector mismatch between the fundamental fields wave vector, k_0 and the q^{th} harmonic's one, k_q. For the case where $\Delta k = 0$ the harmonic signal adds up coherently, essentially this is the ideal situation where there is no mismatch, until the fundamental beam is depleted. On the other hand for the $\Delta k \neq 0$ the harmonics are propagating at different speeds in the medium such that harmonics will interfere constructively and destructively as the field propagates through the medium. The distance over which the signal adds up constructively or destructively is known as the coherence length, $L_{coh} = \frac{\pi}{\Delta k}$ [35]. Δk has contributions from a number of sources primarily dispersion, geometric and intrinsic phases. With this in mind the total phase mismatch equation becomes:

$$\Delta k_q^{total} = \Delta k_q^d + \Delta k_q^g + \Delta k_q^i \tag{1.44}$$

1.6.1 Material Dispersion

Δk_q^d is the mismatch associated with material dispersion. In the presence of a sufficient intensity and a high gas density the fundamental beam can ionise the medium leading to a free electron population that induces a phase shift of both the laser and harmonics as the refractive index changes. There are two contributions to this term − dispersion from neutral atoms/molecules and dispersion from charged particles.
It is often more convenient for the experimentalist to express the mismatch from the neutral atoms/molecules in terms of atomic polarizability, α and the atomic gas density N_{at}:

$$\Delta k_q^n = \frac{q\omega_0 N_{at}(\alpha_q^{at} - \alpha_1^{at})}{2c} \tag{1.45}$$

This expression is intuitive as it illustrates a direct relation between the phase mismatch and the atomic density, the latter is partially governed by the pressure of the gas jet.
The second component of the mismatch from dispersion is due to charged particles such as free electrons. Ionization of the gas medium by the fundamental beam produces a free electron population that induces a phase shift of both the laser beam and the harmonic beam as the refractive index changes. Hence the total contribution to material dispersion can be written as the sum of the neutral particle dispersion and that of the charged particles [35]:

$$\Delta k_q = \Delta k_q^{e-} + \Delta k_q^n = \frac{(q^2-1)\omega_p^2 N_{at}}{2cq\omega_0} + \frac{q\omega_0 N_{at}(\alpha_q^{at} - \alpha_1^{at})}{2c} \tag{1.46}$$

1.6.2 Geometric Phase

The geometrical phase arises from the focusing of the laser beam, $\vec{k}_{geo}(r,z)$ [38]. As the beam is focused in the focal volume there is a phase shift induced by the curvature of the wavefronts. Evidently this term becomes important when tight focusing geometry is implemented. We first analyse the $\vec{k}_{geo}(r,z)$ term which denotes the geometrical phase accumulated by the beam going through the focus, also known as the Gouy phase [35]. Along the propagation axis the Gouy phase is given by the expression below.

$$\phi_{gouy}(z) = -arctan(\frac{z}{z_R}) \tag{1.47}$$

This phase is dependent upon the ratio of the distance from the focus to the interaction zone, z, to the Rayleigh range, z_R. The Rayleigh range is defined as the distance from the focus where the area of the beam has doubled as compared to its thinnest waist, ω_0. The confocal parameter, b, is defined as twice the Rayleigh range. Plotted in Figure 1.11 is the Gouy phase shift through the focus for two values of z_R which shows that a smaller Rayleigh range (implying tighter focusing of the beam) leads to steeper phase gradients so the signal is harder to phase match under these conditions. The Gouy phase is the phase flip that the laser beams wavefronts undergo as they propagate through the focus. For $r = 0$ along the propagation axis the Gouy phase flips from $\frac{\pi}{2}$ to $-\frac{\pi}{2}$; a total phase of π is accumulated when going through the focus. Hence the wavefronts that pass through the focus will advance faster than those that do not [35]. In the absence of dispersion the fundamental wave vector, k_1 is related to the q^{th} harmonics wave-vector k_q by $k_q = qk_1$. Thus, the total geometrical wave-vector, k_{geo} is the sum of the spatial differential of the Gouy phase in addition with the fundamental wave-vector:

$$k_{geo} = k_0 + \nabla\phi_{gouy} \tag{1.48}$$

Since tight focusing is the factor permitting the manifestation of this mismatch ($\frac{b}{L_{coh}} << 1$) as loose a focusing geometry as possible is recommended to minimise the contribution of this term to the phase mismatch .

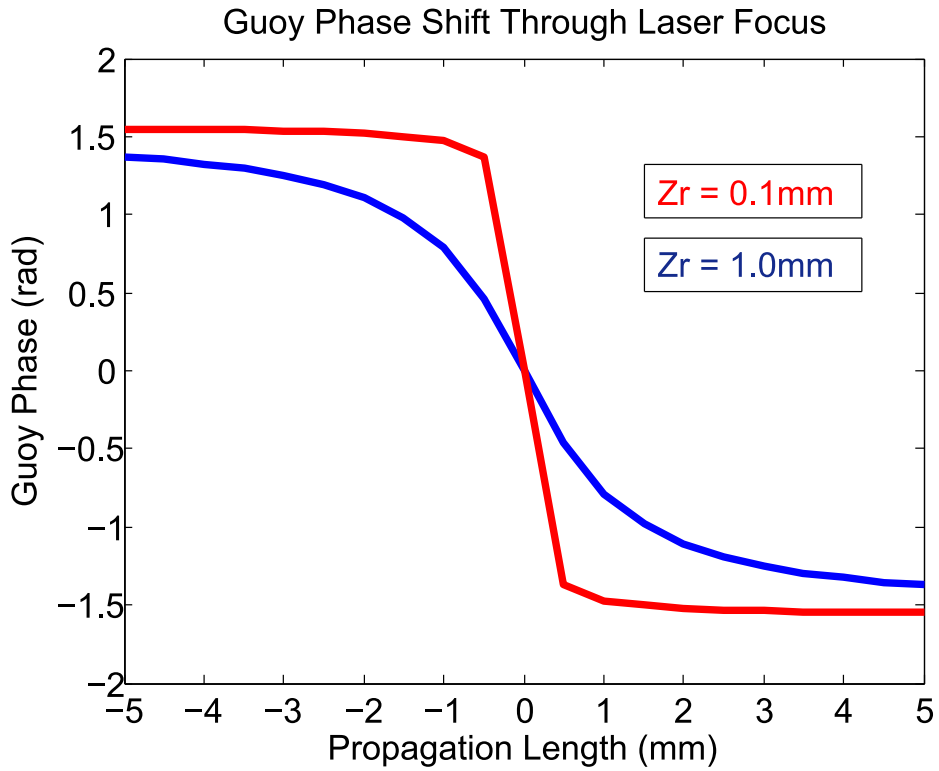


Figure 1.11: Plot of the Gouy phase shift through the focus for two values of z_R: the red curve is for $z_R = 0.1$ mm and the blue curve is for $z_R = 1$ mm. This plot illustrates that the tighter the focusing conditions are, the steeper the phase gradients will be.

1.6.3 Atomic Dipole Phase

Another contribution to the phase mismatch we consider is that of the phase of the dipole moment accumulated as the electron is accelerated in the continuum [39] [40]. The electron accumulates phase from the moment it enters the continuum until it recombines. Here we can introduce the following notation for the phase term $\phi^j_{at,q}$: q, as before is the harmonic order, α is a coefficient associated with the trajectory, at denotes atomic for the phase term, and j is the trajectory type; $j = 1$ being the short trajectory electrons and $j = 2$ being the long trajectory electrons [41]. For a single emitter the atomic dipole phase is:

$$\phi^j_{at,q}(r, z, t) \approx -\alpha^j_q I(r, z, t) \tag{1.49}$$

The atomic phase has the following wave vector, $\mathbf{K}$:

$$\mathbf{K_{at}} = \nabla\phi^i_{at,q}(r,z) \tag{1.50}$$

$$\approx -\alpha^i_q \nabla I(r,z) \tag{1.51}$$

The difference in α coefficient between the long and short trajectories results in different spatial properties, long trajectories being much more affected by the spatial gradients of the generating field. The phase for a given harmonic is intensity dependent because of the dependence of the excursion time of the electron responsible for the emission of that particular harmonic order upon the intensity. An increased intensity corresponds to a shortening of the excursion time for the emission of a given harmonic order for short trajectory electrons whereas a longer excursion time is inherent for the long trajectory case. This mismatch becomes significant in tight focusing regimes and with the application of higher intensities since the intensity dependence is inherent in the HHG process.

Phasematching also influences the prevalence of short or long trajectories in the HHG spectrum. Calculations performed by Chipperfield *et.al* [42] incorporating pulse broadening during propagation, geometrical phase and atomic dipole phase are shown in Figure 1.12 below. These phasematching maps illustrate the best regions for phasematching for short or long trajectories. Inspection of the maps shows that phasematching is optimal on−axis and downstream from the focus with a low divergence for the short trajectories. On the other hand the long trajectories are best phase matched off axis before the focus of the laser and are more divergent.

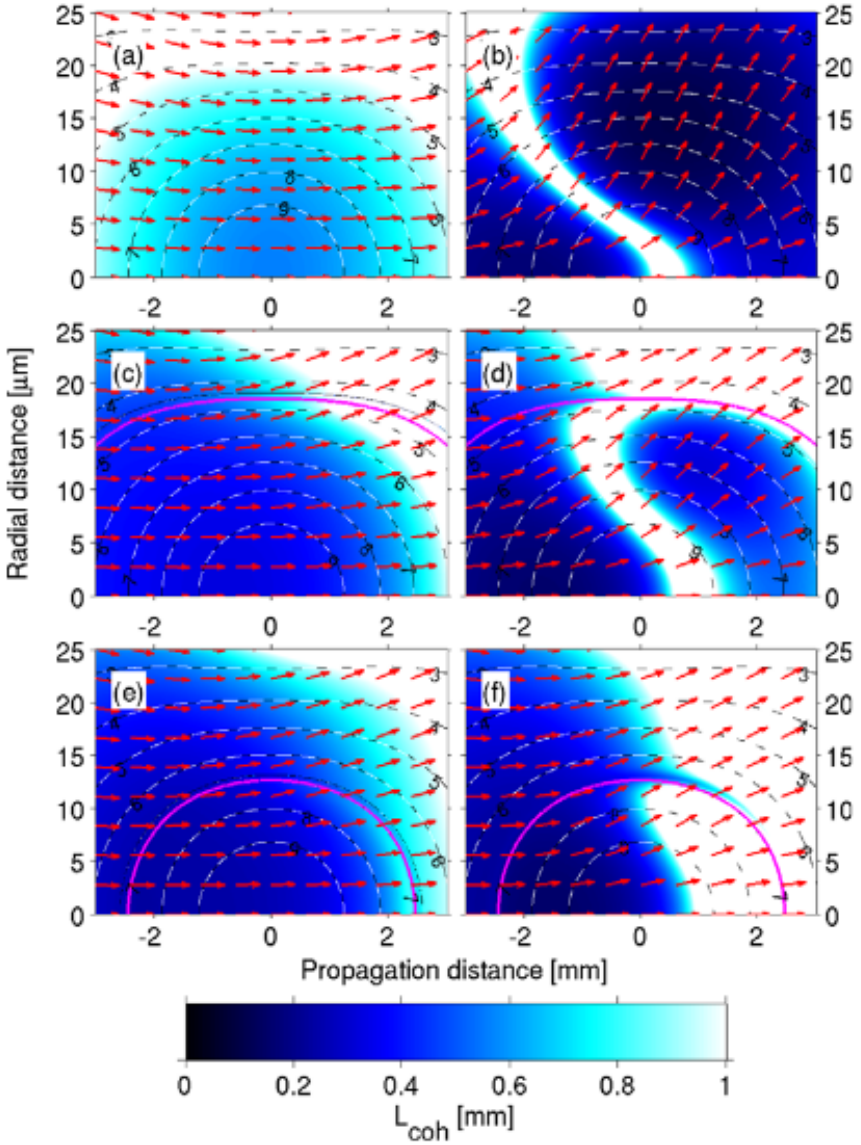


Figure 1.12: Phase matching maps for short(left) and long(right) trajectories of the 21st (a,b), 35th (c,d) and 45th (e,f) harmonics in neon driven by a 750 nm laser field at an intensity of 4×10^{14} W/cm^2. The red arrows represent the direction of the best phase-matching. [42]

It is evident that HHG is a process that is very sensitive to the phasematching. Circumventing the dispersion induced by free electrons can be achieved by using an intensity that is below that of the saturation intensity of the medium and using low sample densities. Keeping the medium length of the target shorter than the confocal parameter is also essential for minimising propagation effects and distortions to the

pulse that is inducing the HHG process. From an experimental perspective, the influence of the various target configurations on the phasematching will be discussed further in the next chapter.

1.7 Basic molecular physics

All the experiments that will be presented in this dissertation have focused on revealing molecular structure and dynamics in organic molecules such as benzene and halogenated benzenes. Molecules present very interesting environments for ultrafast experiments; their additional degrees of freedom lead to both the nuclear and electronic dynamics influencing them. The 'Holy Grail' of attosecond science is to ultimately be able to track the motion of electrons in complex molecules and to be able to control and drive electron motion in these molecules. Many fundamental questions can also be addressed such as the validity and breakdown of the Born-Oppenheimer approximation. The Born−Oppenheimer approximation exploits the fact that the masses of the nuclei are much greater than that of the electron. We can thus expect that the nuclei will move much more slowly than the electron. This leads to the assumption that the electronic motion and the nuclear motion in molecules can be separated which is the basis for the Born−Oppenheimer approximation. [43] [44].

1.7.1 The electronic wavefunction

In atoms, bound electrons are contained within an atomic potential and the nucleus is considered to be a point like ion. The motion of each electron is represented by a wavefunction of the form $\psi(x, y, z)$. The probability of finding an electron in a volume element $dv = dx.dy.dz$ is expressed by the square of the wavefunction $|\psi(x, y, z)|^2 dv$ and is known as the atomic orbital (AO) [45].
When the two atomic orbitals are bought together their electronic wavefunctions overlap resulting in the formation of a new electronic state. This new electron wavefunction is known as a molecular orbital and can be envisaged by applying the Linear Combination of Atomic Orbitals (LCAO). This can be quantified as follows:

$$\Psi_{mol}(x, y, z) = C_A \Psi_A(x, y, z) \pm C_B \Psi_B(x, y, z) \tag{1.52}$$

In H_2^+ there are two possible outcomes. Ψ_A and Ψ_B are the wavefunctions of atoms A and B. C_A and C_B are normalisation coefficients, the square of these coefficients represents the relative proportions of the atomic orbitals contributing to the resultant molecular orbital. In the trivial example of a homonuclear diatomic molecule, an electron can be found in either orbital A or orbital B thus the squares of these coefficients must be equal which implies that $C_B = \pm C_A$. As equation 1.52 infers, the molecular electronic wavefunction can exhibit a bonding $\Psi_{mol} = C_A\Psi_A + C_B\Psi_B$ or an antibonding $\Psi_{mol} = C_A\Psi_A - C_B\Psi_B$ orbital. [45].

The symmetric sum leads to a bonding orbital where the electrons are localised in between the nuclei, the repulsion between the nuclei is minimised and the electron-nucleus attraction is increased. The resultant molecule has a stable, low energy configuration. The form of this orbital is shown in Figure 1.13. This illustration is also accompanied by that of the bonding molecular wavefunction along the internuclear axis. This orbital is known as a σ orbital because it resembles an s orbital when viewed along the axis. Taking the H_2^+ ion, there is a single 1σ electron so the ground state configuration can be described as $1\sigma^1$.

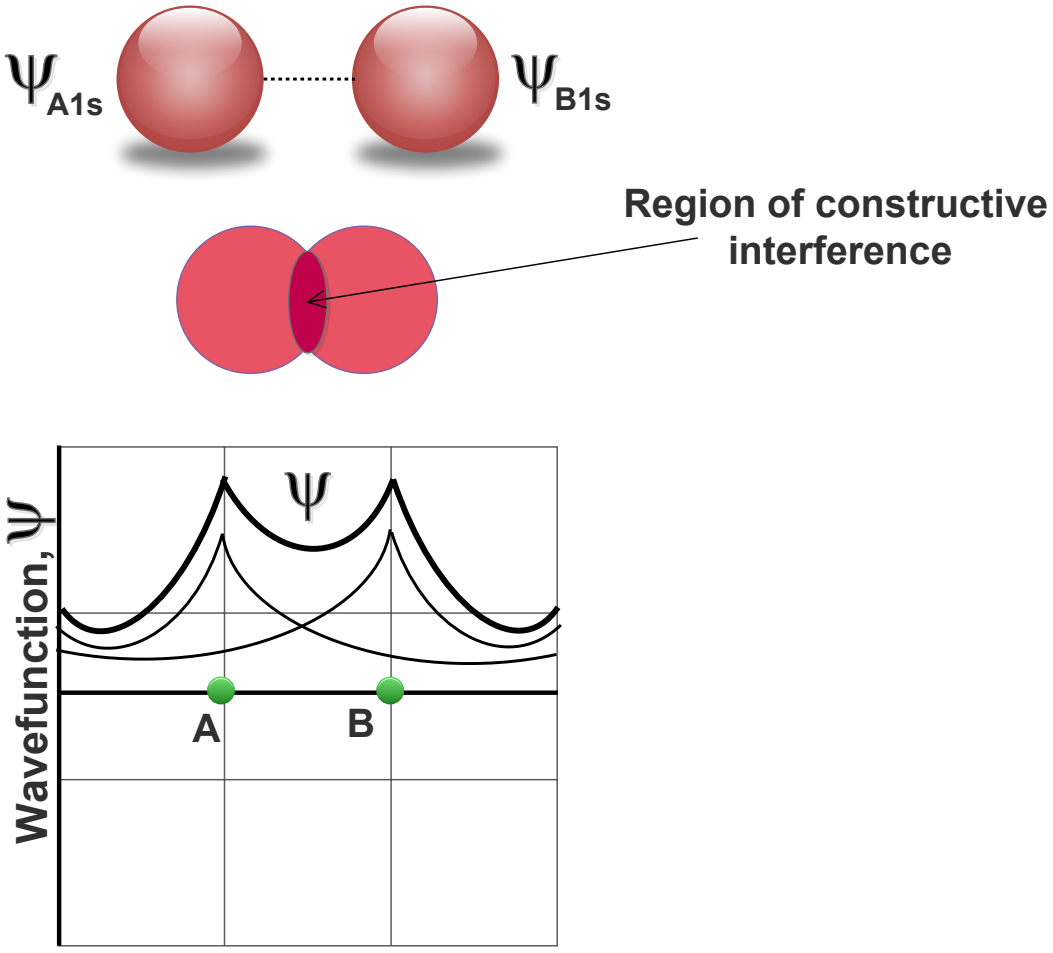


Figure 1.13: Top: The formation of a bonding molecular orbital (a) Two H 1s orbitals come together (b) The orbitals overlap, interfere constructively and yield an enhanced amplitude in the internuclear region. The resultant orbital has cylindrical symmetry about the internuclear axis. Bottom: The bonding molecular wavefunction along the internuclear axis. The enhanced amplitude between the two nuclei indicates there is an increased probability of finding the bonding electrons in that region [45]

The anti-symmetric sum results in an antibonding orbital wherein the electrons are localised in a region outside the two nuclei and hence a repulsion results between the two nuclei. Due to the fact that the positive charges are not shielded from each other like in the bonding case, the minimum energy configuration can only be reached at infinite separation. As in the case of the bonding orbital because this configuration is also cylindrically symmetric around the internuclear axis it is also a sigma orbital

but denoted as $1\sigma^*$. This orbital has not only higher energy than the corresponding σ orbital but also is of higher energy than either of the two atomic orbitals. The origin of this high energy trait can be attributed to the existence of a nodal plane – a plane on which the wavefunction passes through zero. This plane lies halfway between the nuclei and cuts through the internuclear axis. The two atomic orbitals cancel on this plane due to their destructive interference because they have opposite signs. The antibonding molecular orbital is shown in Figure 1.14.

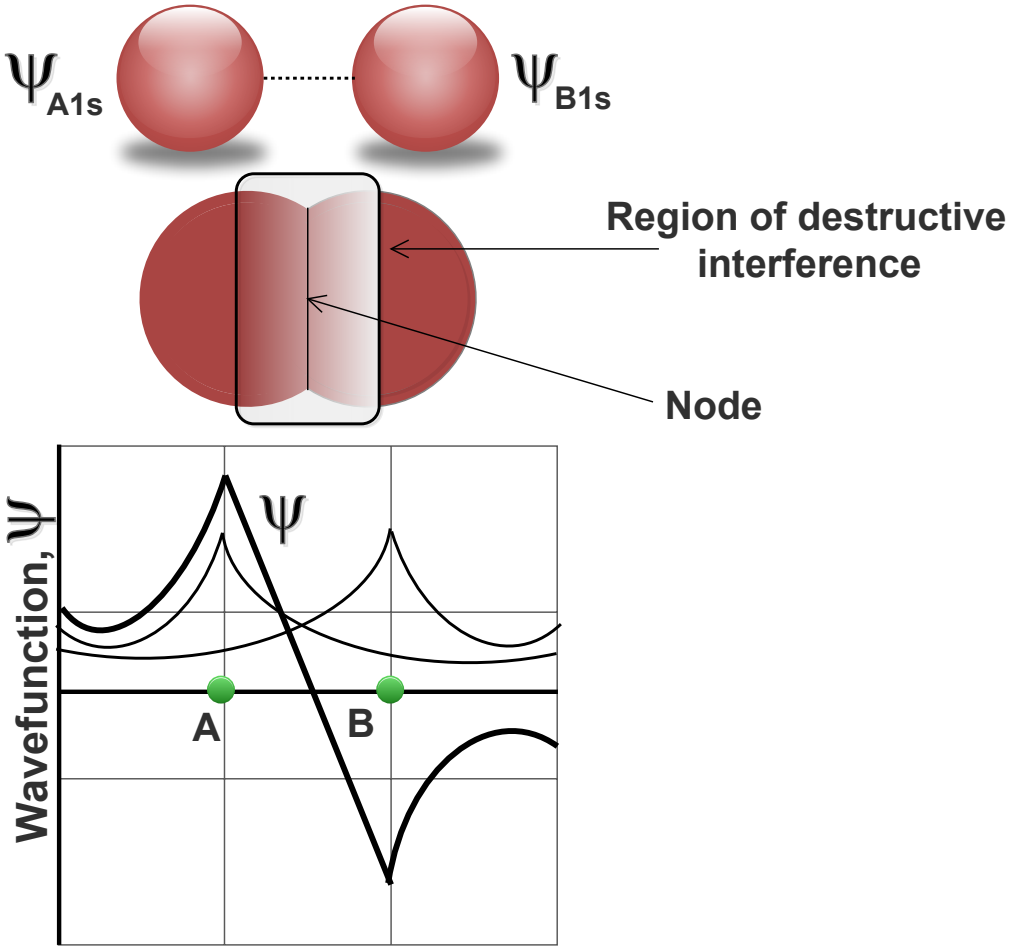


Figure 1.14: Antibonding molecular wavefunction along the internuclear axis. The decreased amplitude between the nuclei infers that there is a low probability of finding an electron in that region [45]

It has been noted that a molecular wavefunction which is cylindrically symmetric - the molecular orbitals are unchanged by any rotation about the axis -is denoted as a σ orbital. A molecular orbital which vanishes on the plane through the nuclei is known as a π molecular orbital. In a similar fashion to denoting that an antibonding σ orbital is represented as σ^* we can apply the same nomenclature to an antibonding π orbital as π^*. It is also necessary to characterize molecular orbitals according to their symmetry about the centre of the molecule. As illustrated in Figure 1.15 below, consider any point of the said sigma bonding orbital and project it through the centre of the molecule and out an equal distance the other side, arriving in an identical value of the wavefunction - this is known as g symmetry (even) such that we have σ_g. In the same manner for a wavefunction that is projected through the centre of a molecule and arrives at a wavefunction of equal magnitude but opposite sign we have u symmetry (odd).

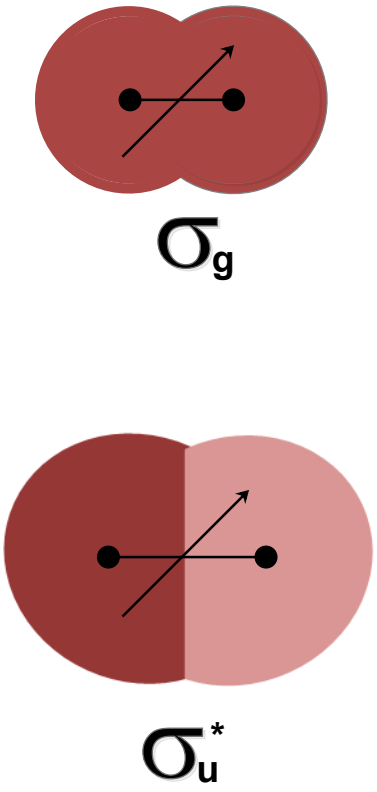


Figure 1.15: The gerade (g) and ungerade (u) character of σ bonding and antibonding orbitals [45]

1.7.2 Energy spectrum

Molecular energy levels are qualitatively comparable to those in atoms, however the addition degrees of freedom due to rotation and vibration need to be accounted for. Calculations are simplified by invoking the Born-Oppenheimer approximation [43] [44]. In essence this approximation separates the electronic from the nuclear parts of the wavefunction. Due to the nuclei being much heavier than the electrons we can regard them as stationary while the electrons move around them. In a molecule, to each electronic state, E_e there are many bound vibrational states of energy E_v, and to each vibrational state there are many bound rotational states of energy E_r [46].

For a given electronic configuration there is a potential energy curve whose minimum is at an equilibrium separation of R_0. Near R_0 this curve can be approximated as a parabola such that small oscillations can be considered simple harmonic. The energy of such oscillations can be quantised to satisfy the relation:

$$E_v = (v + \frac{1}{2})hv_0 \tag{1.53}$$

where v is the vibrational quantum number $v = 0, 1, 2, 3, \ldots$, and the classical vibration frequency is $v_0 = \frac{1}{2\pi}\sqrt{\frac{C}{\mu}}$, where C is the force constant and μ is the reduced mass of the system. The separation, hv_0 is 0.04 eV in NaCl and because the dissociation energy is 1 eV, there are approximately 20 vibrational levels in a potential well. As the energy rises the potential energy curve becomes anharmonic such that the levels are not equally separated but begin to get closer together. The rotational levels are also spaced closer together, there being 40 rotational levels for NaCl in between each pair of vibrational levels [46]. The rotational motion of a diatomic molecule can be envisaged as the rotation of a rigid body about its centre of mass as illustrated below in Figure 1.16.

The angular momentum of the system about the axis of rotation is quantized such that the rotational energies are given by:

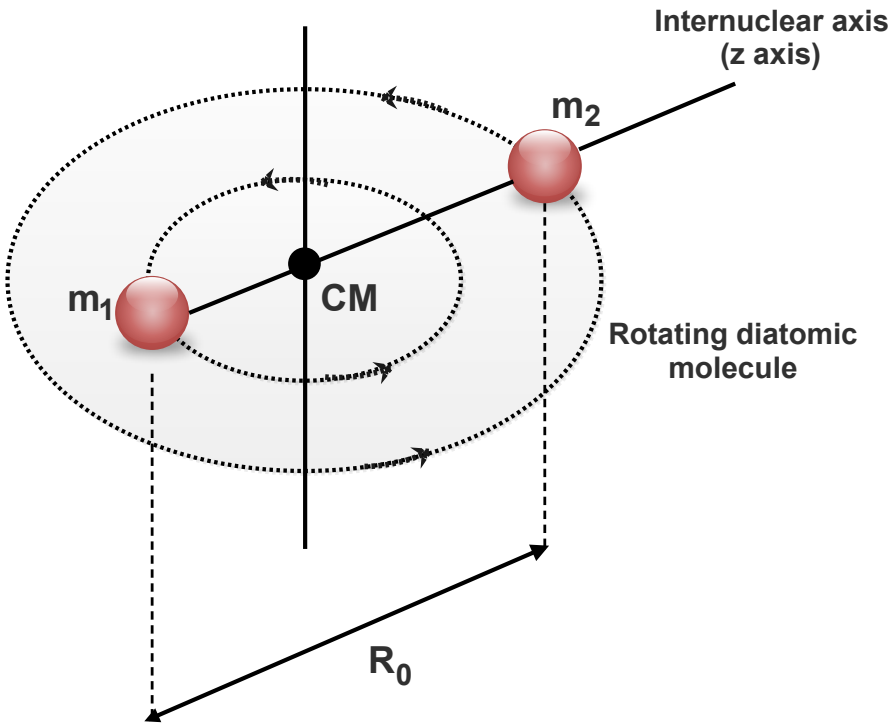


Figure 1.16: Simplified schematic of a diatomic molecule consisting of two masses m_1 and m_2 rotating about their common centre of mass (CM) with separation R_0 [46]

$$E_r = \frac{\hbar^2}{2I} J(J+1) \tag{1.54}$$

where J is the rotational quantum number, $J = 0, 1, 2, 3\ldots$ and I is the rotational inertia. Successive rotational levels are separated in energy by:

$$\Delta E_r = E_J - E_{J-1} = \frac{\hbar^2}{2I} \left[J(J+1) - J(J-1) \right] = \frac{\hbar^2}{I} J \tag{1.55}$$

Rotational energy level distribution of molecules is dependent upon the geometry of the constituent atoms. There are four main classes of geometry known as linear, symmetric top, spherical top and asymmetric top molecules. These structures will be revealed to be of high importance when discussed in the context of molecular alignment.

1.7.3 Molecular orbital theory: quantum mechanics of multiple electrons

The energy and other properties of a molecular system may be obtained by solving the Schrödinger equation. The nuclei and electrons of a molecule can be fully described by properties such as their mass and their charge. The Schrödinger equation is written as:

$$\underbrace{\left\{\frac{-h^2}{8\pi^2 m}\nabla^2 + \mathbf{V}\right\}}_{\mathbf{H}}\Psi(\mathbf{r},t) = \frac{ih}{2\pi}\frac{\partial\Psi(\mathbf{r},t)}{\partial t} \tag{1.56}$$

In this equation, Ψ is the wavefunction, m is the mass of the particle, h is Plancks constant and $\mathbf{V}$ is the potential field in which the particle is moving. The wavefunction is a function of the coordinates of the positions of the electrons and nuclei of the molecule as well as t. We can designate $\mathbf{r}$ and $\mathbf{R}$ as the coordinates for electrons and nuclei respectively. Subscripts on each of these vectors corresponds to a particular electron or nucleus: $\mathbf{r}_i$ and $\mathbf{R}_I$. The Hamiltonian operator,$\mathbf{H}$, describes how the system evolves over time. The molecular Hamiltonian contains a kinetic energy and a potential energy term such that $\mathbf{H} = \mathbf{T} + \mathbf{V}$. The kinetic energy term can be written as a summation of ∇^2 over all the particles in the molecule [47]:

$$\mathbf{T} = -\frac{h^2}{8\pi^2}\sum_k \frac{1}{m_k}\left(\frac{\partial^2}{\partial x_k^2} + \frac{\partial^2}{\partial y_k^2} + \frac{\partial^2}{\partial z_k^2}\right) \tag{1.57}$$

The potential energy term is the Coulomb repulsion between each pair of charged particles in the molecule where we treat each atomic nucleus as a single charged mass:

$$\mathbf{V} = \frac{1}{4\pi\epsilon_0}\sum_j\sum_{k<j}\frac{e_j e_k}{\Delta r_{jk}} \tag{1.58}$$

where Δr_{jk} is the distance between two entities, e_j and e_k are the charges on particles j and k respectively. The charge on an electron is -e while for a nucleus the charge is

Ze, where Z is the atomic number for the particular atom. We can expand equation 1.58 to be [47]:

$$\mathbf{V} = \frac{1}{4\pi\epsilon_0}\left(-\sum_{i}^{electrons}\sum_{I}^{nuclei}\left(\frac{Z_I e^2}{\Delta r_{iI}}\right) + \overbrace{\sum_{i}\sum_{j<I}}^{electrons}\left(\frac{e^2}{\Delta r_{ij}}\right) + \overbrace{\sum_{I}\sum_{J<I}}^{nuclei}\left(\frac{Z_I Z_J e^2}{\Delta R_{IJ}}\right)\right) \quad (1.59)$$

The first term describes the electron-nuclear attraction, the second term corresponds to the electron-electron repulsion and the final term represents the nuclear-nuclear repulsion. The Schrödinger equation for molecules can be further simplified by invoking the Born−Oppenheimer approximation. In essence, this approximation separates the nuclear and electronic motions in a molecule. It is a reasonable approximation since the mass of a typical nucleus is greater than two orders or magnitude heavier than that of an electron. The nuclei move slowly relative to the electrons so one can imagine that the electrons respond instantaneously to changes in nuclear position. Essentially the nuclei appear fixed to the electrons and the electronic motion can be described as occurring amongst fixed nuclei [44]. The Born−Oppenheimer approximation allows one to construct an electronic Hamiltonian which excludes the kinetic energy term for the nuclei. This Hamiltonian can be used in the Schrödinger equation to describe the motion of the electrons in a field of fixed nuclei:

$$\mathbf{H}^{elec}\psi^{elec}(\vec{\mathbf{r}}, \vec{\mathbf{R}}) = E^{eff}\psi^{elec}(\vec{\mathbf{r}}, \vec{\mathbf{R}}) \quad (1.60)$$

Solving equation 1.60 for the electronic wavefunction gives the effective nuclear potential function, E^{eff}. E^{eff} depends on the nuclear coordinates and describes the potential energy surface (PES) of the system. Furthermore, it is also used as the effective potential for the nuclear Hamiltonian which can be written as [47]:

$$\mathbf{H}^{nucl} = T^{nucl}(\vec{\mathbf{R}}) + E^{eff}(\vec{\mathbf{R}}) \quad (1.61)$$

This Hamiltonian describes the vibrational, rotational and translational states of the system when it is solved using the Schrödinger equation for nuclear motion. Invoking the Born−Oppenheimer approximation means we are now focusing entirely on

solving the electronic Schrödinger equation. A further approximation can be applied to further simply the problem at hand, by applying Hartree−Fock (HF) theory [47]. At its very basic, HF theory assumes that the potential energy of each electron in a given molecule is an average over the motions of the other electrons. Molecular orbital theory decomposes the wavefunction into a combination of molecular orbitals which are a normalized, orthogonal set of orbitals. This is realised by forming the Hartree product which is given by:

$$\psi(\vec{\mathbf{r}}) = \phi_1(\vec{\mathbf{r}_1})\phi_2(\vec{\mathbf{r}_2})\dots\phi_n(\vec{\mathbf{r}_n}) \tag{1.62}$$

Equation 1.62 is an inadequate representation of the wavefunction as it is not antisymmetric. This problem can be mitigated by multiplying a molecular orbital wavefunction by an α or β function which includes the electron spin in the overall electronic wavefunction [47] [44]. A Slater determinant is a determinant of spin orbitals for an N electron system. There are $\frac{N}{2}$ molecular orbitals and electrons are assigned to these orbitals in pairs of opposite spin for a closed shell wavefunction. Interchanging two electrons implies swapping two rows of the determinant which does result in a sign change to the wavefunction. Molecular orbitals can be expressed as linear combinations of a set of one−electron functions known as basis functions. A molecular orbital can be expressed as:

$$\phi_i = \sum_{\mu=1}^{N} c_{\mu i}\chi_\mu \tag{1.63}$$

where $c_{\mu i}$ are the molecular orbital expansion coefficients and χ_μ refers to an arbitrary basis function. Gaussian-type atomic functions are commonly used as basis functions in electronic structure calculations. Gaussian functions can be represented by the general expression:

$$g(\alpha, \vec{\mathbf{r}}) = cx^a y^b z^c e^{-\alpha r^2} \tag{1.64}$$

where c is a normalisation constant, a,b,c control the angular momentum such that l = a+b+c, $\mathbf{r}$ is composed of the x, y, z coordinates of the electron, α governs the radial

extent of the orbital; for instance a small value for α gives a diffuse function meaning that the electron is held at a considerable distance from the nucleus. Examples of Gaussian functions for s and d_{xy} type orbitals are given by equations 1.65 and 1.66 below, respectively [47]:

$$g_s(\alpha, \vec{\mathbf{r}}) = \left(\frac{2\alpha}{\pi}\right)^{\frac{3}{4}} e^{-\alpha r^2} \tag{1.65}$$

$$g_{d_{xx}}(\alpha, \vec{\mathbf{r}}) = \left(\frac{2048\alpha^7}{9\pi^3}\right)^{\frac{1}{4}} x^2 e^{-\alpha r^2} \tag{1.66}$$

Linear combinations of these primitive Gaussian functions are used to construct the basis functions and are able to approximate the nodal properties of atomic orbitals. These basis functions are known as contracted Gaussians and take the form:

$$\chi_\mu = \sum_p d_{\mu p} g_p \tag{1.67}$$

where the $d_{\mu p}$ terms are fixed constants within a given basis set. Following these constructions we arrive at the following expansion for molecular orbitals:

$$\phi_i = \sum_\mu c_{\mu i} \chi_\mu = \sum_\mu c_{\mu i} \left(\sum_p d_{\mu p} g_p\right) \tag{1.68}$$

This expression is valid for closed shell systems. Once the electronic wavefunctions and corresponding energies have been calculated for a closed−shell molecule using the Hartree−Fock method (also known as the Self−Consistent Field (SCF) method), the ionization of the molecule can be approximated. This is done by invoking Koopmans theorem [44]. Koopmans theorem states that ionization, which consists of the removal of an electron from a closed−shell molecule, can be represented as the removal of an electron from a given self−consistent field orbital, leaving the remaining electrons unaffected, or in other words, that the ionization energy is equal to that of the orbital from which the electron came from. Koopmans theorem neglects effects such as the

difference that arises between the correlation energies of the neutral and the ion since Hartree−Fock neglects correlations between electrons of opposite spin. It also fails to account for the reorganisation of the energy of the electrons in the ion; essentially the charge distribution of the electrons in the neutral gives rise to an effective potential for each particular electron and the removal of an electron will naturally alter this effective potential. Koopmans theorem is assuming that this change in effective potential is negligible.

Hartree−Fock theory can also be extended to open shell systems − unrestricted Hartree−Fock − by introducing two separate expansion coefficients, one treating the α electrons and one to treat the β electrons [47]. The α and β spin functions can be defined as follows:

$$\alpha(\uparrow) = 1 \quad \alpha(\downarrow) = 0$$
$$\beta(\uparrow) = 0 \quad \beta(\downarrow) = 1$$

This is a basic introduction to how the problem of solving the electronic Schrödinger equation can be approached in the case of molecules. Whilst there are a number of fundamental flaws with a methods such as Hartree−Fock such as the inability to correlate the motion of electrons of opposite spin, it remains a good starting point for introducing more elaborate electronic structure methods. These will be briefly discussed when the Strong Field Approximation (SFA) [48] calculations are introduced in section 1.8.

1.7.4 Molecular orbital theory applied to benzene

The benzene molecule is built from hydrogen atoms ($1s^1$) and carbon atoms ($1s^2 2s^2 2p_x^1 2p_y^1$). Since each carbon atom has to bond with three atoms (one hydrogen and two carbons) and it has not enough electrons to form the necessary bonds, it must promote one of the $2s^2$ pair into the empty $2p_z$ orbital in order to minimize the energy of the system for stability. Each carbon is only joining up with three other atoms so it only hybridises three of the four of its orbitals; the 2s, $2p_x$ and $2p_y$ atomic orbitals to form sp^2 hybrids. Each carbon atom uses the sp^2 hybrids to form sigma bonds with its two carbon and one hydrogen neighbours. The remaining $2p_z$ orbital is at right angles to the hybrid orbitals. The p electron on each carbon atom overlaps with the p orbital either side of it; this overlap forms a system of pi bonds which are spread over the carbon ring [44]. Since the electrons are no longer shared between

two carbon atoms but are spread over the whole ring the electrons are said to be de-localised as shown in Figure 1.17.

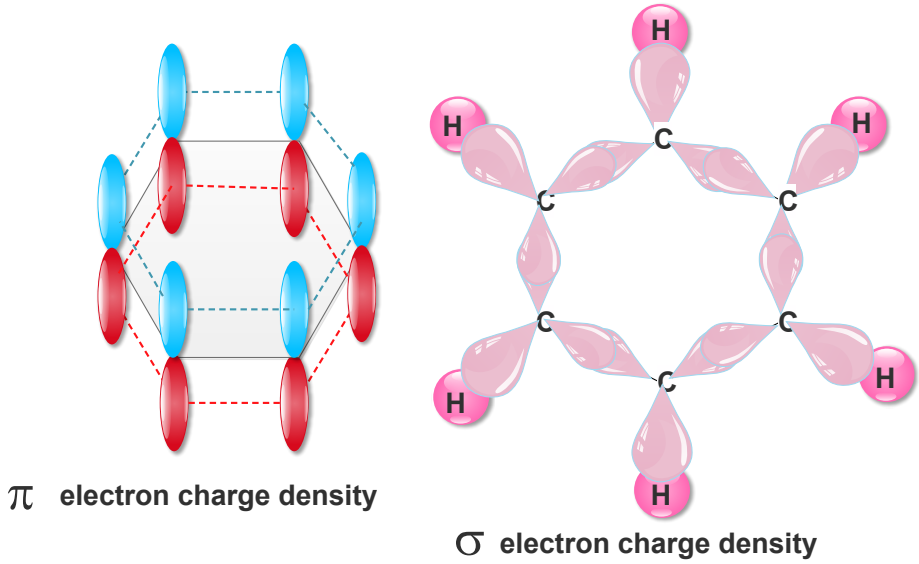
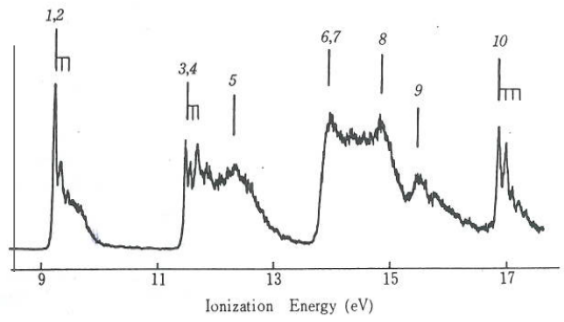


Figure 1.17: Schematic of the π and σ electron charge density on the benzene ring

The molecular orbitals of benzene are shown in Figure 1.18. The orbitals displayed are ranked in terms of increasing ionization potential. The Highest Occupied Molecular Orbital (HOMO) of benzene is of π character and has an ionization potential of 9.2 eV; this orbital is also degenerate. The next lowest lying orbital is that of the HOMO-1 (11.53 eV) which is also degenerate but is of σ character.



	Exptl. I_v (eV)	SCF MO [4-31 G] MO	Character	
1	9.25	$1e_{1g}$ (21)	π_3	HOMO
2		$1e_{1g}$ (20)	π_2	
3	11.53	$3e_{2g}$ (19)	σ	HOMO-1
4		$3e_{2g}$ (18)	σ	
5	12.38	$1a_{2u}$ (17)	π_1	HOMO-2
6	13.98	$3e_{1u}$ (16)	σ	
7		$3e_{1u}$ (15)	σ	
8	14.86	$1b_{2u}$ (14)	σ	HOMO-n
9	15.46	$2b_{1u}$ (13)	σ	
10	16.84	$3a_{1g}$ (12)	σ	

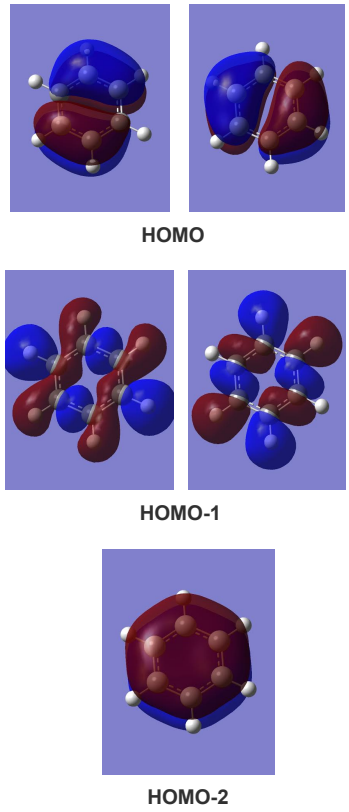


Figure 1.18: Left: Photoelectron spectrum from benzene with a table showing the corresponding energies of the peaks. The final column of the table lists the orbital symmetries [49]. Right: Orbitals of benzene for the HOMO, HOMO-1 and HOMO-2 plotted using the GAUSSIAN electronic structure program

Benzene is a very interesting molecule in the context of performing experiments to extract electronic and nuclear sub−femtosecond dynamics. Benzene is a highly symmetric molecule belonging to the D_{6h} point group [50] [44]. Group theory can be used to determine the structure of a molecule. Symmetry is classified by the ability to carry out rotation or reflection operations to rearrange some or all of the atoms in a molecule to result in a structure that is indistinguishable from the initial arrangement. As point group theory is a very broad and extensive area, this thesis will only describe the primary operations and the relevant point groups.

The main/principal axis, denoted as C_n is an $n-$fold rotation axis with n operations through multiples of $(\frac{360}{n})^\circ$ each of which leaves the resulting molecule indistinguishable from the original arrangement. As there are six carbons in benzene, it can be rotated six times at 60° rotations per operation implying that its principal axis is described as C_6. Lower order n axes also exist as shown in Figure 1.19. The C_6 axes can also be represented as a C_3 or C_2 axes which is easy to see. There are also $C_2^{'}$ and $C_2^{"}$ rotation axes which bisect the atoms and the bonds respectively. There are also three classes of reflection planes:

- a horizontal mirror plane, σ_h, is one which is perpendicular to the main rotation axis.
- a vertical mirror plane, σ_v, is a mirror plane which contains the main rotation axis.
- a dihedral mirror plane, σ_d, is a vertical mirror plane which bisects the bonds of the molecule.

These rotation and reflection operations are represented in Figure 1.19. There is also an inversion operation which entails moving every point (x,y,z) to the corresponding position (x',y',z'). Molecules with an inversion centre can also be described as being centrosymmetric [50].

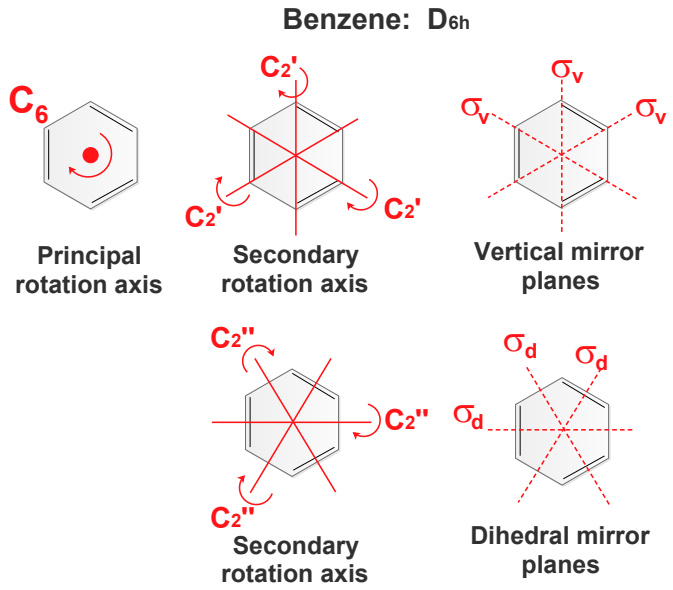


Figure 1.19: Rotation and reflection symmetry operations for the D_{6h} benzene molecule

There are also identity, E, and improper rotation, S_n operations. Identity implies performing a 360° rotation about the principal axis and is the equivalent of doing nothing to the molecule. Improper rotation consists of performing a rotation about a C_n axis followed by a reflection in a mirror plane that is perpendicular to this axis. A point group is defined as a collection of the symmetry operations that are required to describe the structure. There are numerous point groups that can be assigned based on the presence or absence of these operations. A flow chart such as the one shown below in Figure 1.20 are very useful for determining which point group a molecule belongs to based on its structure.

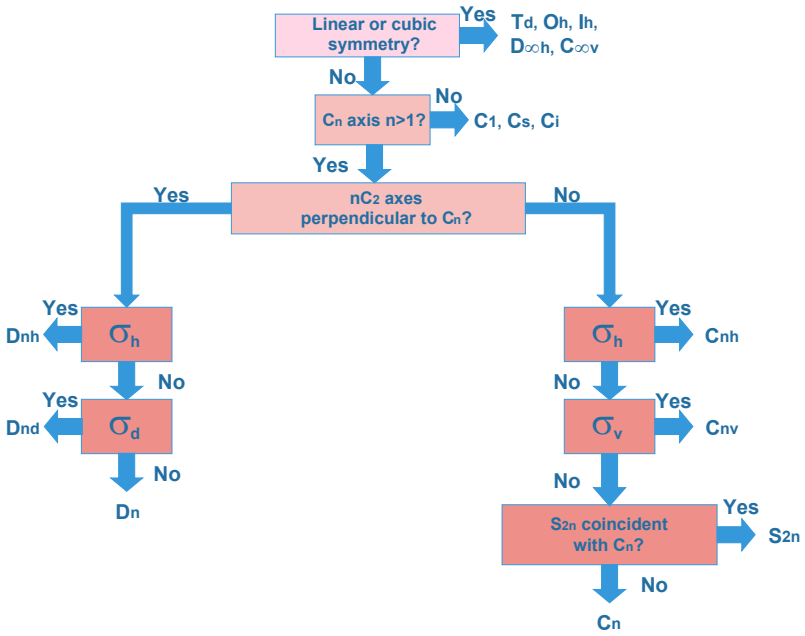


Figure 1.20: Flow chart representing the different point groups a molecule can belong to based on decisions concerning its symmetry properties [50]

1.7.5 Substituted benzene molecules

Benzene can react with halogens such as bromine or chlorine to form halogenated benzene molecules i.e. chlorobenzene, bromobenzene, iodobenzene, fluorobenzene. These monosubstituted benzene molecules belong to the C_{2v} point group as they possess a C_2 axis and lack any rotation axes perpendicular to the C_2 axis. They also lack a σ_h plane but have two σ_v mirror planes. The reaction mechanism that results in the formation of these molecules is known as electrophilic aromatic substitution [51]. Other common monosubstituted benzenes include toluene, aniline and phenol. Di-substitutions can also be performed on the benzene ring. As shown in Figure 1.21, for the example of xylene, there are three options for where the second substituent can be placed on the ring once the first one has occupied the ipso position. From the flow diagram one can deduce that para-xylene belongs to the D_{2h} point group due to its higher degree of symmetry than ortho- and meta xylene which both belong to the C_{2v} point group.

If the two substituents are the same, then the structures formed can be classed as

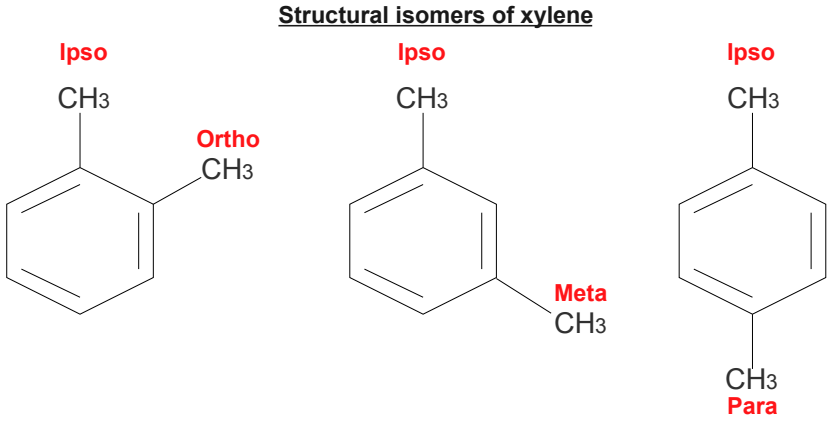


Figure 1.21: Structural isomers of xylene (C_8H_{10}) molecule

being structural isomers. Isomers are a group of two or more molecules that have the same empirical formula but differ in their structural arrangement [51]. Benzene is regarded as a fundamental building block of many proteins and biomolecules. As a known carcinogen along with many of its substituted counterparts, it is also a very topical molecule for biochemists and pharmacologists to understand.

Benzene as a molecule is an ideal prototype for performing ultrafast spectroscopy experiments on. Its highly symmetric (or achiral [52]) framework and availability of substituted derivatives make it a very rich environment for studying its electronic and nuclear dynamics as well as the effects of various mono and di−substitutions on the ring.

1.8 Modelling HHG in Molecules

The Strong Field Approximation (SFA) [48] is a fundamental starting point for the modelling of HHG in molecules. Other methods do exist for calculating HHG from atoms and molecules such as solving the one electron TDSE. However, this is quite computationally intensive and does not provide a logical interpretation of the HHG process. The SFA is based upon three approximations for a Single Active Electron (SAE) in a linearly polarised laser field:

- 1. In the continuum, the electron is treated as a free particle moving in the

electric field with no effect on the ionic potential.

- 2. Depletion of the ground state can be neglected.
- 3. Bound states are unperturbed by the laser field such that only the ground state is contributing to the evolution of the system. Only the outermost electron, from the HOMO, is participating in the process of HHG.

These assumptions are justifiable in the context of HHG. Assumption 1 is feasible during the propagation step of HHG as the electron is born into the continuum rapidly and moves along the laser field such that when the trajectory is reversed that it is far enough away from the ionic potential not to be under the influence of it. Assumption 2 is valid when the intensity of the laser driving the HHG process is kept below the saturation intensity of the medium. Assumption 3 is accommodated by the fact that the HHG process is instigated by tunnel ionization such that it is the outermost electron from the HOMO that is released into the continuum. It is further justified by the requirement that the electron must return to its parent ion in the recombination step for the emission of an XUV photon to be allowed. The full quantum−mechanical treatment by Lewenstein *et.al* provides a more accurate description and intuitive understanding of the HHG process [48]. The time dependent wavefunction can be expressed as:

$$|\psi(t)\rangle = e^{i} I_p t \left(|\psi_0\rangle + \int \frac{d^3\mathbf{k}}{(2\pi^3)} a(\mathbf{k}, t) \, |\mathbf{k}\rangle \right) \tag{1.69}$$

The electron is in a superposition of states, predominantly in its bound state $|\psi_0\rangle$ which has energy, $-I_p$. The term $a(\mathbf{k}, t)$ are the amplitudes of the continuum states which are denoted as $|\mathbf{k}\rangle$. We can use this expression to calculate the dipole matrix elements for a bound−continuum transitions. The time dependent expectation value, $\mathbf{d}(t) = \left\langle \psi(t) \left| \widehat{\mathbf{d}} \right| \psi(t) \right\rangle$ is given by:

$$\mathbf{d}(t) = -i \int_0^t dt_i \int d^3\mathbf{p} \mathbf{d}_{rec} \left[\mathbf{p} + \mathbf{A}(t) \right] exp \left[iS(\mathbf{p}, t_i, t) \right] \times d^L_{ion} \left[\mathbf{p} + \mathbf{A}(t), t_i \right] + c.c. \tag{1.70}$$

where $\mathbf{d}_{rec}$ represents the recombination dipole matrix elements, S is the semi-classical action which describes the motion of the electron in the continuum, d_{ion}^{L} is the ionization amplitude in length gauge since the operator here is not selected by our choice of $\hat{\mathbf{d}}$ but comes from the length−gauge interaction Hamiltonian $\mathbf{r}.\mathbf{E}(t)$ in the TDSE, $[\mathbf{p} = \mathbf{k} - \mathbf{A}(t)]$ is the canonical momentum of the continuum electron which is a conserved quantity during continuum propagation because the ionic potential is neglected. $\mathbf{A}(t) = -\int_{-\infty}^{t} \mathbf{E}(t')dt'$ is the vector potential of the laser field. We can retrieve the three steps of the HHG process from the integrand as follows [4]:

- (i) At a time, t_i, a portion of the electron wavefunction makes a transition to the continuum state. The ionization rate can be calculated using the approach discussed in section 1.5.1: ionization by using the ADK rate or the MO−ADK rate depending on the level of accuracy necessitated. The part of the wavefunction that is born into the continuum has momentum given by $\mathbf{k} = \mathbf{p} - \mathbf{A}(t_i)$

- (ii) In the continuum, the electron propagates under the influence of the laser field and acquires a phase relative to the ground state which is known as the semi−classical action:

$$S(\mathbf{p}, t_i, t) = -\int_{t_i}^{t} dt" \left[\frac{[\mathbf{p} + \mathbf{A}(t")]^2}{2} + I_p\right] \tag{1.71}$$

- (iii) At a time, t, the electron has a momentum of $\mathbf{k} = \mathbf{p} + \mathbf{A}(t)$ and recombines with the core. The recombination amplitude is given by the Dipole Matrix Element (DME):

$$\mathbf{d}_{rec}(\mathbf{k}) = \left\langle \psi_0 \left| \hat{\mathbf{d}} \right| \mathbf{k} \right\rangle \tag{1.72}$$

The XUV spectrum is proportional to the Fourier transform of the radiating dipole which is given by [4] [48]:

$$\begin{aligned}\epsilon(\omega) \propto \int \mathbf{d}(t) e^{i\omega t} dt = -i \int dt \int_0^t dt_i \int d^3\mathbf{p} \mathbf{d}_{rec} \left[\mathbf{p} + \mathbf{A}(t)\right] \\ \times exp\left[i\omega t + iS(\mathbf{p}, t_i, t)\right] d_{ion}^{L} \left[\mathbf{p} + \mathbf{A}(t), t_i\right]\end{aligned}$$

In this expression the integration between 0 and t runs over the duration of the driving laser pulse. The wavefunction for the HOMO can be calculated from a superposition

of Gaussian functions. Computational packages such as GAUSSIAN can calculate molecular wavefunctions if they are given a molecular geometry as an input. The Hartree−Fock method described in section 1.7 is commonly used to compute the molecular wavefunctions.

So far, the SFA has only been considering ionization from the HOMO. In molecules, the energies of the valence orbitals are much closer than in atoms so the contribution of lower lying orbitals such as the HOMO−1 and HOMO−2 etc. can become significant [4]. It is also noteworthy that ionization from the HOMO can be strongly suppressed when the laser field is polarised parallel to a nodal plane. The different channels for ionization take the molecule from the same initial state to the same final state via different states of the ion. In the total amplitude for the HHG process the individual channel amplitudes interfere. The recombination dipole matrix elements can be written as a sum over the participating channels; $c = X, A, B, ...$ where X is the ground state, A is the first excited state, B is the second excited state and so on:

$$\mathbf{d}_{rec}(t) = \left\langle \sum_c b_c \psi_c^D \right| \hat{\mathbf{d}}_f \left| \mathbf{k} \right\rangle \tag{1.73}$$

where b_c represent the relative weight of the participating channels which is determined by the tunnelling process and can also have a time dependence if the channels are coupled by the laser. If the laser induced coupling of the channels can be ignored then the b_c terms are constant and the hole−wavepacket dynamics are determined by the free evolution of the coherent superposition of eigenstates. $\hat{\mathbf{d}}_f$ is the f electron dipole operator. Equation 1.73 is a recombination DME between a continuum electron which is in state $|\mathbf{k}\rangle$ and a bound ionic wavepacket which is formed by the channel specific Dyson orbitals, $|\psi_{hole}\rangle = \left|\sum_c b_c \psi_c^D\right\rangle$ which corresponds to a time dependent hole in the ion. The Dyson orbital implies projecting out the difference between the neutral and the ionic core which can be interpreted as a hole in the ion [4]. Cross-channel HHG is a very prolific area of research in HHG spectroscopy with many milestone publications being made in the last 10 years [53] [54] [55] [56] [57] [58] [59] [60] [61] [62] [63]. SFA can also be employed to calculate impulsive alignment distributions in molecules [64]. This is done by keeping the electric field fixed in one direction and introducing different orientations of the molecule by applying the Euler operator, $\widetilde{\mathbf{R}}_{\phi\theta\chi}$, on the

spatial co−ordinates of the orbitals.

There are, however, a number of drawbacks to the SFA. It is not gauge invariant [65] [23] [64] − the SFA depends on the choice of gauge because the choice of the initial ansatz, $|\psi(t)\rangle$, is gauge dependent. For example, molecular SFA in the velocity gauge has previously failed to explain orientational effects in the ionization of the nitrogen molecule [66]. However the SFA in length gauge to describe the field−molecule interaction has produced results in good agreement with experimental findings. Neglecting the effect of the Coulomb potential is also leads to several problems with the theory. It is incorrect to neglect the influence of the molecular core as the electron must tunnel through the barrier to be liberated into the continuum, the shape of the barrier is influenced by the molecular core. This implies that the ionization amplitude will be different if the effect of the Coulomb tail is incorporated into the electron action [67]. The propagation in the continuum is also different as electron not only oscillates in the electric field but also can scatter of the molecular core. This has been included additionally in the SFA2 formalism which has been derived by Lewenstein [68]. Despite these drawbacks the SFA is still a powerful theoretical tool for modelling the HHG from molecules and can reproduce alignment distributions [69], multi−orbital contributions [61], orbital tomography [70] and ellipticity dependences [71].

Improvements to the SFA include incorporating electron-electron correlations which accounts for the interactions between multiple electrons during the ionization process. The tunnelling rate is strictly only valid if the state that the resultant ion is in is frozen during the tunnelling process. If the state is allowed to evolve then the ionization dynamics change to reflect the interaction between the ejected electron and the ionic core [72]. The use of eikonal-Volkov states to represent the continuum electron includes the laser field, the interaction between the continuum electron and the ionic core and the coupling between them [73]. Ionization can be improved by including the influence of sub-cycle dynamics, the core potential and the shape of the initial state on the ionization rate. The propagation step of HHG is further improved by including nodal planes in the bound states of molecules as they leave fingerprints on the electron wavepacket after ionization and the shape of the recolliding wavepacket will affect the recombination.

Chapter 2

Laser requirements for High Harmonic Generation

This chapter will discuss the requirements of the laser source required for high harmonic generation, with a particular focus on those for optimal HHG in organic molecules. I will then introduce the laser system used for the experiments presented in the next chapter. This discussion will include chirped pulse amplification (CPA), optical parametric amplifiers (OP-CPA systems), hollow core fibre pulse compression and ultrashort pulse characterisation.

2.1 Laser parameters

In order to perform HHG, there are a few pre−requisites required from the driving laser. These will each be introduced along with a discussion on their influence on the HHG process.

2.1.1 Drive wavelength

As discussed previously, the highest frequency produced for a given ionization stage is given by $\Omega_{max} = I_p + 3.17U_p$. The ponderomotive energy, U_p, scales as $I\lambda^2$, where I is the laser peak intensity and λ is the laser wavelength. One approach to extending the cut−off of the spectrum is to increase the laser intensity. There is a drawback to doing this as there is a practical limit beyond which the laser intensity can no longer be increased. This occurs when the state is fully ionized and is reached quite quickly

in low I_p molecules such as the organic molecules of interest to this thesis (< 10 eV). We can calculate the saturation ionization intensity as follows: the potential that the electron sees is a combination of the atomic/molecular potentials and the potential generated by the laser field.

$$V(x,t) = \frac{-Ze^2}{4\pi\epsilon_0 x} - exE_0 \tag{2.1}$$

where Z is the charge state of the target (note that $Z = 1$ when an atom is ionised once), x is the distance from the centre of the atom, ω is the angular frequency of the laser and t is the time in the laser pulse. The force applied on the electron is given by the derivative of this equation. When the derivative is set to zero it indicates that the laser electric field removes the atomic/molecular potential therefore releasing the electron.

$$\frac{\partial V(x_{max})}{\partial x} = \frac{Ze^2}{4\pi\epsilon_0 x^2} - eE_0 \tag{2.2}$$

From this equation, x_{max} can be found which is the distance from the centre of the atom/molecule at which the force on the electron is zero:

$$x_{max} = \sqrt{\frac{Ze}{4\pi\epsilon_0 E_0}} \tag{2.3}$$

Substituting this expression for x_{max} into equation 2.1 gives the height of the barrier potential seen by the electron.

$$V(x_{max}) = -\sqrt{\frac{Ze^3E_0}{\pi\epsilon_0}} < -I_p \tag{2.4}$$

where $V(x_{max})$ is the potential seen by the electron is a combination of the atoms potential and the maximal electric field of the laser light, Z is the charge state of the resultant ion (i.e. $Z = 1$ for $C_6H_6^+$), e is the charge of an electron, ϵ_0 is the permittivity of free space, E_0 is the electric field strength. For example, knowing that $I_p = 9.2$ eV for benzene we get $E_0 = 1.5 \times 10^{10}$ V/m. We can calculate I_{sat} from the

following expression:

$$2740\sqrt{I_{sat}} = E_0 \tag{2.5}$$

where E_0 is in units of V/m and the resultant value for I_{sat} is in units of W/cm^2. For benzene, where $Z = 1$ we get a value of the saturation intensity of $I_{sat} = 2.9 \times 10^{13}$ W/cm^2. For the molecules of interest to this thesis that have $I_p \approx 10$ eV we get $I_{sat} \approx 4 \times 10^{13}$ W/cm^2.

The alternative approach is to use longer wavelength sources. The λ^2 scaling is offset by an unfavourable scaling of the conversion efficiency from laser energy into XUV energy. The conversion efficiency scales as $\eta(\lambda) \propto \lambda^{-(5-6)}$ due to the spreading of the continuum electron wavepacket in both space and time. This wavelength scaling dependence was investigated by Shiner *et.al* [28].

The investigation of using longer drive wavelengths to extend the cut−off of the HHG spectrum has been a fruitful area of research in the attosecond community [26] [27]. Sheehy *et.al* [26] observed harmonics extending to the 19th order of the fundamental (3.2 μm) in alkali metal vapours such as potassium and rubidium. Also in the early 2000's, Shan *et.al* [27] observed a cut−off extension from 64 to 160 eV in argon using a 1.51 μm field as opposed to a 0.8 μm drive laser wavelength. Further advances into the application of longer drive wavelength sources is reviewed by DiChiara *et.al* [74] which details how the harmonic cut−off, yield and spectral phase change with driving laser wavelength. Another notable publication is that by Schmidt *et.al* which investigated HHG with long wavelength, few cycle laser pulses [75]. In this study, 1.8 cycle duration pulses at 1.8 μm were used to enable the cut−off extension in xenon to reach 160 eV which has facilitated the observation of a giant resonance in xenon at ≈ 95 eV.

The wavelength of the drive laser also have an influence upon the fragmentation of the molecules of interest to this thesis. In order to perform ultrafast measurements on benzene and substituted benzenes it is of utmost importance that the laser parameters for HHG in these molecules are selected to ensure HHG is performed on intact molecules and not fragments. In the multiphoton picture, the number of photons, N,

required to reach the second ionization threshold of 26.4 eV for benzene to produce dications is $N = 9$ for a drive wavelength of 395 nm which is about half of the corresponding number of photons, $N = 17$, when the wavelength is 790 nm. Thus, a larger yield of dications is expected for $\lambda \approx 395$ nm than that for $\lambda \approx 790$ nm for the same photon flux which is achieved when the laser intensity for the 395 nm beam is twice that of the 790 nm beam. However, as observed by Itakura *et. al* [76], even when the laser intensity is doubled, fragmentation is still the dominant process over dication formation.

A strong dipole allowed resonance coupling between the $\widetilde{C}$ and $\widetilde{X}$ states of the benzene cation suppresses the formation of dications and induces the dissociation of the cations into $C_4H_i^+$ and $C_3H_j^+$ fragments. In the case of the 790 nm wavelength multiple ionization was found to dominate the dynamics of the benzene cations and the neutral benzene molecules which implies that the resonance coupling observed at 395 nm is not induced on the neutral, singly or doubly charged states by the 790 nm wavelength beam.

Itakura [76] and other authors [77] [78] have studied the degree of fragmentation from benzene as a function of drive wavelength in Time of Flight (TOF) experiments. In the study by Itakura, using the same pulse duration and intensity, there is a higher degree of fragmentation when the 395 nm field is used compared to the 790 nm field as shown in Figure 2.1. This dissociation can be attributed to resonances in the cation. This process is only possible if the relaxation time preceding excitation is of shorter duration than the laser pulse duration. Some cation resonances can directly lead to dissociative states. This result plays in our favour for HHG experiments as a consequence of the $U_p \propto I\lambda^2$ relation wherein increasing the intensity of the drive beam can be detrimental to phase matching and still accelerates fragmentation in the molecule. The above arguments are a sound basis for using longer drive wavelengths for HHG in organic molecules.

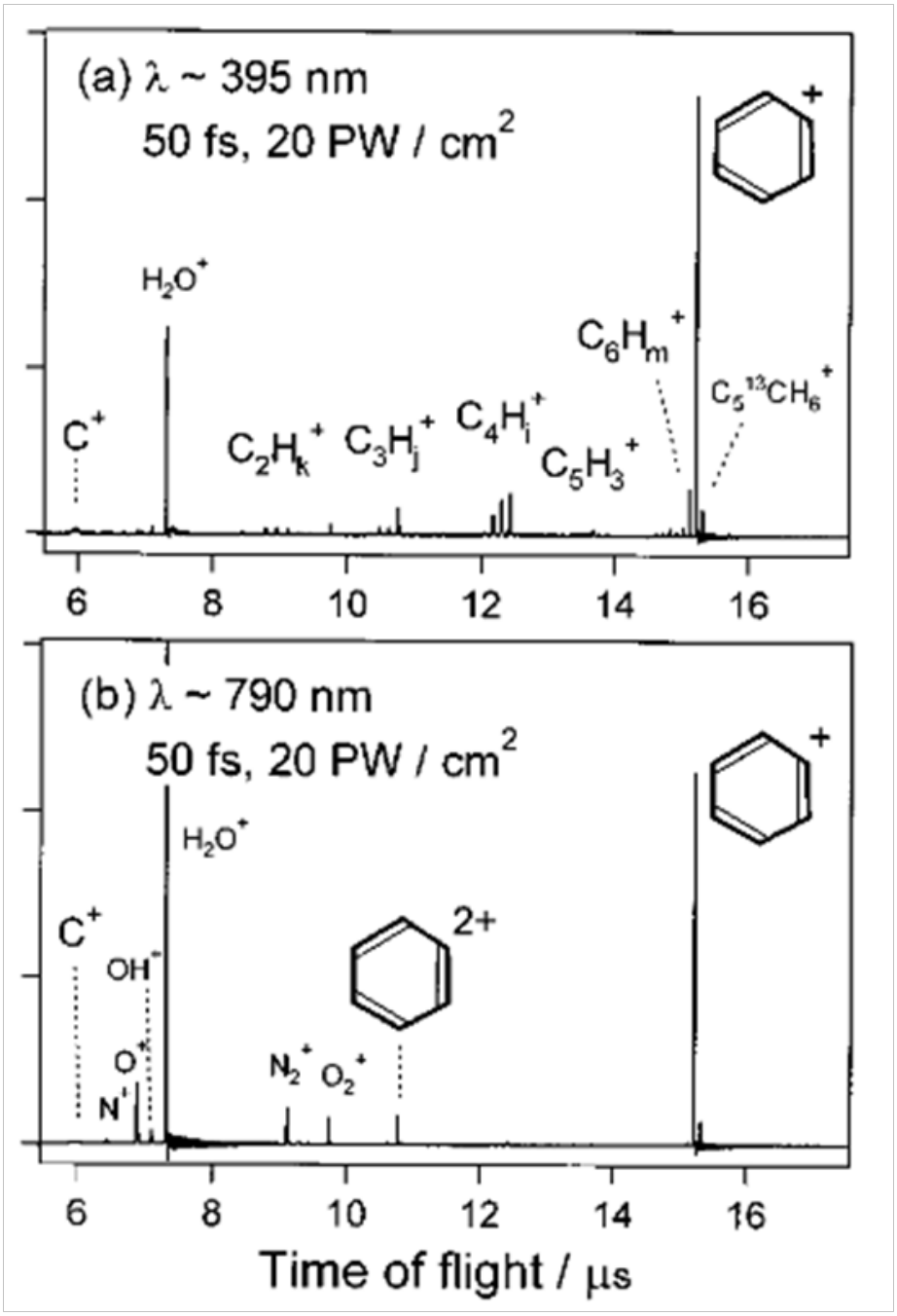


Figure 2.1: The TOF-MS when benzene was irradiated with a wavelength of 395 nm (top) and 790 nm (bottom). The intensity was 2×10^{16} W/cm^2 in both cases [76]

2.1.2 Pulse duration

Femtosecond laser pulses are more suited to experiments with organic molecules [79] under the presence of a strong laser field intrinsically because of the evidence for parent ion retention in comparison to longer pulses. This is primarily due to the fast up−pumping of the parent ion states which defeats dissociative states [76]. Shorter pulses in HHG are highly advantageous as there will be no temporal averaging as in the case for employing a longer pulse. Shorter pulses also increase the time resolution which will be pivotal to experiments mapping nuclear dynamics. It is necessary here to define what I mean by "short" in terms of what we desire for our experiments:

- Ideal case: A half-cycle or even single cycle laser pulse as this would mitigate temporal averaging in the data.
- Acceptable case: Multiple half-cycles which all contribute similarly.
- Worst case: A few cycle pulse because there are larger changes at each half cycle which will contribute to temporal averaging and movement of the cut-off of the spectrum.

Hay *et.al* studied the dependence of the pulse duration on the HHG spectra [79] as shown in Figure 2.2. There is a marked discrepancy between HHG in the atom xenon and the organics benzene and cyclohexane. Whilst it can be argued that an initial steep rise followed by saturation, characteristic of HHG from atoms, which is mimicked in the molecules for intensities below 5×10^{14} W/cm^2 using the 240 fs pulse, the features above this intensity can be attributed to ionization and dissociation occurring during the laser pulse. In the case of employing the 70 fs pulse, the spectra in the organics resemble that of the atom in intensity dependence. It is proposed that using the 240 fs pulse leads to significant fragmentation of the parent molecule occurring at higher intensities. In the case of employing the 70 fs pulse the structure is absent in the intensity dependent curves which infers that there is insufficient time for the parent to break apart concurring that HHG is by and large from intact parent molecules and not fragments.

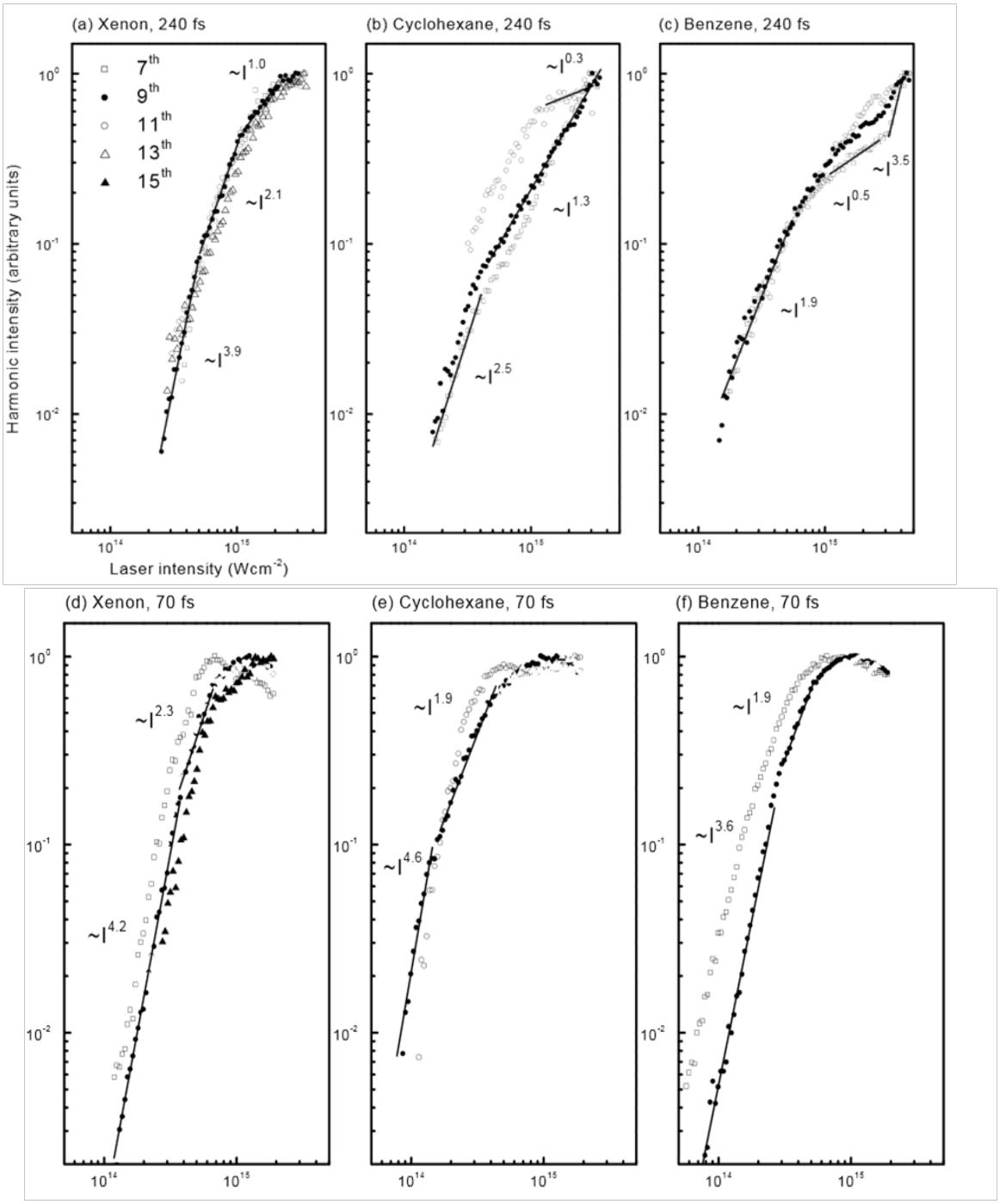


Figure 2.2: Harmonic intensity as a function of laser intensity for xenon, cyclohexane and benzene with a 240 fs pulse (top panel) and using a 70 fs pulse (bottom panel) [79]

Moving to much shorter − approaching single cycle duration − pulses also presents advantages for the HHG process, particularly for low ionization potential targets [80]. In Figure 2.3, typical HHG spectra in neon with a backing pressure of 250 torr, $\lambda_0 = 0.8\mu$m, and a peak intensity of $\approx 3 \times 10^{14}$ W/cm^2 are plotted for a 30 fs and a 7 fs pulse [81].

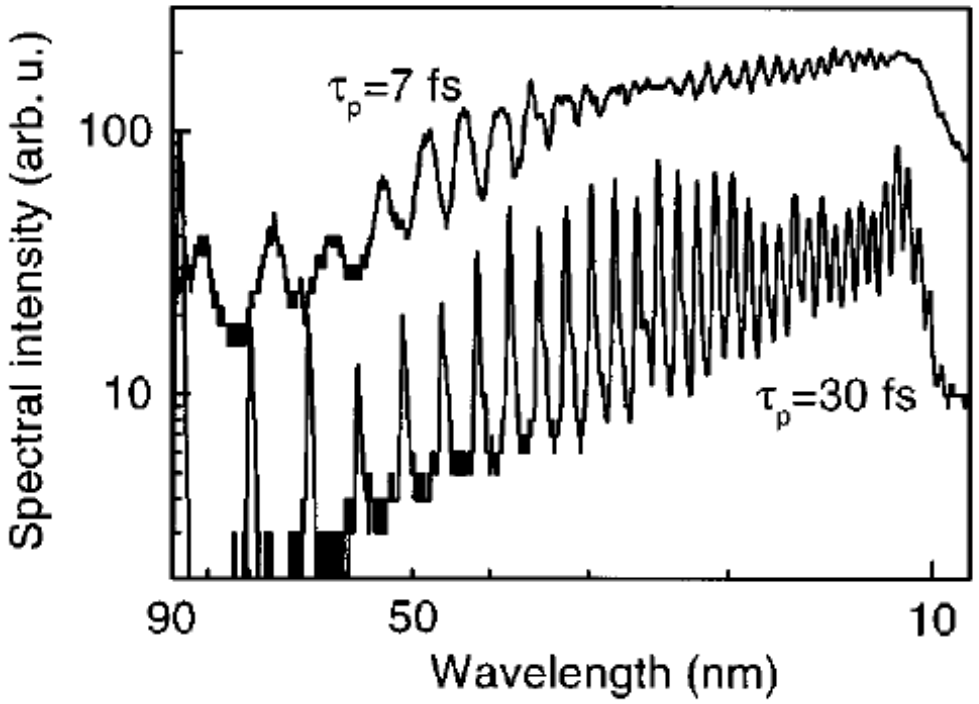


Figure 2.3: Harmonic spectra in neon at 250 torr backing pressure for 30 fs and 7 fs pulse durations and an 0.8 μm drive wavelength. The peak intensity for both pulses is $\approx 3 \times 10^{14}$ W/cm^2. For the 30 fs duration pulse, this implies roughly 10% of the neon atoms are ionizes whereas only $\approx 1\%$ are ionized for the 7 fs pulse [81]

It is clear that for the 30 fs duration pulse that the spectrum consists of discrete, well resolved harmonics. For the 7 fs pulse duration, this discrete structure is much less pronounced and even disappears in the cut−off region. This is because for few cycle pulses the highest order harmonics are generated by a single−electron trajectory close to the pulse peak such that the periodicity of the HHG process is completely suppressed. Since the pulses in Figure 2.3 have the same peak intensity, the harmonic spectra are cut−off at the same frequency, which is easily realised from the equation for the harmonic photon energy at which the cut−off occurs: $E_{cut-off} = I_p + 3.17U_p$.

In a regime where the probability of stripping an electron from the parent atom or molecule approaches one, well before the target constituents are exposed to the pulse peak, the harmonic cut−off is no longer determined by the peak laser field intensity but by the intensity at which the ground state is depleted at the front edge of the pulse [81].
For shorter pulses, the ground state depletion is shifted to higher intensities and hence, the cut−off is shifted to higher harmonic orders. Increasing the intensity of the 7 fs drive pulses has enabled the cut−off to be extended below 4.37 nm into the water window in neon. This could not be previously achieved using the 30 fs pump pulses due to early depletion of the ground state.

2.1.3 Laser intensity

In light of the discussions above with respect to target fragmentation and ground state depletion, a number of trivial arguments for the laser intensity arise. Naturally, for the organic molecules of sub 10 eV ionization potential which are considered to be "soft" targets, keeping the laser intensity low ($\leq 10^{15}$ W/cm^2) is necessary to mitigate any fragmentation of the target. Time of Flight (TOF) studies have been employed to study the fragmentation in the organics such as benzene as a function of drive wavelength, pulse duration and a strong emphasis on the effects of laser intensity [82] [83] [77] [84] [78].

For the organic molecules, it is important to stay below the saturation intensity of the species. Experiments by Hay *et.al* determined the saturation intensity for benzene to be ($\approx 6 \times 10^{14}$ W/cm^2) using a 70 fs duration pulse at 800 nm [79]. Referring back to our calculated value for the saturation intensity of benzene we get $\approx 3 \times 10^{13}$ W/cm^2 which is over an order of magnitude smaller than the value measured by Hay. This highlights the difficulties in making measurements of the saturation intensity which shall be discussed further in the Results chapter. Relativistic effects can also be induced at intensities 10^{16} W/cm^2 where the $\vec{B}$ component of the electromagnetic field no longer has negligible amplitude. It is also of no concern to this thesis as it typically at intensities ≥ 100 times that of the atom or molecules saturation intensity.

2.1.4 Repetition rate

Most of the previous studies on organic molecules performed in our laboratory have been done with a 10 Hz laser system [85] [79] [86]. Higher repetition rates are desired to obtain a higher flux in the XUV, enabling faster measurements at a higher signal−to−noise ratio. Previously, due to limitations in average power, high energy pulses suitable for HHG experiments were obtained at a cost to the lasers repetition rate. A higher repetition rate laser system would enable better statistics on the acquired data. The commercial CPA laser system that will be introduced in the following section has a repetition rate of 1 kHz which is a marked improvement on that of the previous 10 Hz laser system. It is noteworthy to mention that other research groups have also reported on HHG a repetition rates in the range of 50 kHz − 25 MHz [87] [88] [89]. The ideal case for the work of concern in this thesis would be to have higher repetition rates and longer wavelengths which would allow us to obtain better statistics on our data with a sufficiently large time window in which to observe dynamics from larger organic molecules.

2.2 Fundamentals of laser physics for ultrashort pulses

This section will introduce the physics that is necessary for understanding the complexity of generating ultrashort optical pulses. Non-linear optics is fundamental to the advancement of the field as many optical non-linearities have been exploited to facilitate with modelocking, pulse picking, chirped pulse amplification and difference frequency generation to name but a few. The characterisation of ultrashort optical pulses will also be introduced with reference to the technologies employed in our laboratory. The quality of the laser pulses used for HHG spectroscopy is of utmost importance as instabilities arising from fluctuations in the laser, inhomogeneities in the mode quality and contributions from higher order spectral phase terms which have not been correctly compensated for can all be detrimental to the data acquisition.

2.2.1 Description of optical pulses

A laser pulse can be defined by its electric field, $\xi(t)$. The electric field also has a complimentary description in the spectral domain where the pulse can be described by an amplitude function and spectral phase. $\xi(t)$ is a real function and its Fourier transform is given by $\widetilde{\xi}(\omega) = 1/2(\widetilde{E}(\omega)+\widetilde{E^*}(-\omega))$, where $\widetilde{E}(\omega)$ is the complex electric field which has non zero values only for positive values of frequency, ω. $\widetilde{E}(\omega)$ is a complex function which contains all of the information about the pulse, and from which $\xi(t)$ can be obtained. The inverse Fourier transform of $\widetilde{E}(\omega)$ results in a complex field in the temporal domain, $E(t)$ whose real part is given by $\mathrm{Re}[E(t)] = \xi(t)$:

$$\xi(t) = \int_{-\infty}^{+\infty} \widetilde{\xi}(\omega) exp(-i\omega t)\frac{d\omega}{2\pi} \tag{2.6}$$

The shape of an ultrashort pulse can be defined by its electric field, $\xi(t)$, by its complex electric field in the time domain, $E(t)$, or in the spectral domain as $\widetilde{E}(\omega)$. $\widetilde{E}(\omega)$ is a very practical and widely used definition of an ultrashort pulse and is given by [90]:

$$\widetilde{E}(\omega) = A(\omega)e^{i\varphi(\omega)} \tag{2.7}$$

where $A(\omega)$ is the spectral amplitude and the spectral phase is $\varphi(\omega)$ which both contribute to the shape of the pulse. For a given spectral amplitude, the spectral phase completely dictates the pulse shape and duration. For a flat phase profile over the bandwidth of the spectrum, the pulse is at its shortest duration and is said to be *Fourier limited*. A Fourier limited pulse has a duration which is inversely proportional to its spectral width. Time−bandwidth product (TBP) provides an estimation of how far a pulse is from being transform limited. The TBP is the product of the time duration and the spectral width of a given pulse:

$$TBP = \Delta t \cdot \Delta\omega \tag{2.8}$$

where Δt and $\Delta\omega$ are the full width at half maximum (FWHM) in intensity of the

pulses temporal and spectral profiles respectively. For a Gaussian pulse, the TBP is given by:

$$TBP = \frac{4ln(2)}{\pi} = 0.441 \tag{2.9}$$

The spectral phase is fundamental to determining the shape of an ultrashort pulse. In order to gain a more intuitive insight into the role of the spectral phase, we can expand it in terms of a Taylor series if the spectral phase varies slowly with frequency [91]:

$$\varphi(\omega) = \varphi(\omega_0) + \left.\frac{\partial\varphi}{\partial\omega}\right|_{\omega_0}(\omega - \omega_0) + \frac{1}{2}\left.\frac{\partial^2\varphi}{\partial\omega^2}\right|_{\omega_0}(\omega - \omega_0)^2 + \ldots$$

- $\varphi(\omega_0) \equiv \varphi^{(0)}$ is the absolute phase that is accumulated at ω_0 which is a reference usually taken to be the central frequency of the spectrum. This term is known as the carrier envelope phase (CEP) which corresponds to the phase between the envelope of the electric field and the carrier. The carrier envelope phase is given by: $\varphi_{CEO} = \varphi^{(0)} - \omega_0\varphi^{(1)}$. This quantity becomes important for pulses comprising a few optical cycles as the cut-off position is very sensitive to the CEP value for each half cycle in a few cycle pulse. Many cycle pulses are less sensitive to the CEP as there are more half cycles which contribute to temporal averaging of each half-cycle cut-off position.

- $\left.\frac{\partial\varphi}{\partial\omega}\right|_{\omega_0} \equiv \varphi^{(1)}$. This term corresponds to a delay between the pulse and an arbitrary origin in time and is known as the group delay. For propagation through a medium of length L, $\varphi^{(1)} = \frac{L}{v_g}$ where v_g is the group velocity. The group delay is the time taken for the envelope of the pulse to propagate between the two planes of the medium.

- $\left.\frac{\partial^2\varphi}{\partial\omega^2}\right|_{\omega_0} \equiv \varphi^{(2)}$. This term is known as the group delay dispersion (GDD), quadratic phase, or more commonly as the chirp. Chirp induces an increase in the pulse duration and is generally expressed in units of fs^2. $\varphi^{(2)}$ causes the transit time to increase linearly with frequency. For positive values of the GDD, positive dispersion, longer wavelengths arrive before shorter wavelengths

which is generally known as positive frequency chirp. The opposite case in which long wavelengths lag shorter wavelengths is termed negative frequency chirp or anomalous dispersion. Dispersion through a medium usually results in a positive chirp which can be compensated by using a device or material that imposes negative dispersion on the pulse to counteract this and enable a transform limited pulse to be obtained.

- $\varphi^{(3)}$ corresponds to the cubic phase which leads to pre and post pulses forming in the temporal domain. When aiming for few cycle pulses it is essential that the cubic phase and higher order phase terms be compensated.

Origins of the discussed spectral phase terms and methods for compensating them shall be discussed in the context of ultrashort pulse generation in section 2.5.

2.2.2 Nonlinear optics for ultrashort pulse generation

Reverting back to the expression defined in section 1.1.3, the induced dipole per unit volume − the polarization −can be expressed as a Taylor expansion of the incoming electric field strength:

$$P(t) = \epsilon_0[\chi^{(1)}E(t) + \chi^{(2)}E^2(t) + \chi^{(3)}E^3(t) + \ldots] \tag{2.10}$$

Non linear optical effects that are accessible with modern day laser technology and this section shall discuss the $\chi^{(2)}$ and $\chi^{(3)}$ processes such as optical parametric amplification and self phase modulation.

Optical Kerr effect and the Pockels effect

The Pockels effect is a fundamental second order, χ^2, nonlinear optical process which has become key to the advancement of ultrafast laser technology [10]. The Pockels effect relates to the change of the refractive index of a non−centrosymmetric medium when a DC electric field is applied. Examples of such non−centrosymmetric media include potassium diphosphate (KDP) and lithium niobate which are suitable for visible and near−IR wavelengths. If we include a DC term, E_0, in the expression for the laser electric field we get:

$$E = E_0 + E_1 \cos\{\omega t - k_1 z\} \tag{2.11}$$

where k_1 is the angular wavenumber of the fundamental beam ($k_1 = n_1\omega/c$) and the field is propagating in the z direction. Substituting this expression into eq 2.5, we get a new non−linear term which has the same space−time dependence as linear polarization [10].

$$P = \epsilon_0(\chi^{(1)} + 2\chi^{(2)}E_0)E_1 \cos\{\omega t - k_1 z\} + \ldots \tag{2.12}$$

The electric displacement is written as: $D = \epsilon_0 E + P = \epsilon_0(1 + \chi^{(1)})E = \epsilon_0\epsilon E$ where $\epsilon = 1 + \chi^{(1)}$ is the relative dielectric constant. In comparison to the original expression, $P = \epsilon_0(1 + \chi^{(1)})E = \epsilon_0\epsilon E$ for the electric displacement, where ϵ is the square of the refractive index such that $n = \sqrt{1 + \chi^{(1)}}$, we can now see that the refractive index is now represented as $n = \sqrt{1 + \chi^{(1)} + 2\chi^{(2)}E_0}$. The Pockels effect is used in ultrafast laser science as it creates an optical switch which allows the polarization properties of light to be controlled electrically in combination with a polarizing beamsplitter. The change in refractive index of the material which varies linearly with applied electric field strength can be used to modify the polarization properties of the incident laser pulses. The Pockels effect is named after the German physicist, Friedrich Pockels who studied it extensively in 1893 [92] [91]. The first practical Pockels cell was not developed until the 1940s when suitable crystals were finally developed. The role of the Pockels effect will be discussed when the anatomy of the laser system in our laboratory is introduced.

Optical parametric amplification

Optical parametric processes involve the mixing of two or more primary beams of different frequencies in nonlinear dielectric media that have a non−zero $\chi^{(2)}$ [8]. This can be understood intuitively by substituting a wave of the form:

$$E = E_{01}\sin(\omega_1 t) + E_{02}\sin(\omega_2 t) \tag{2.13}$$

into the simplest expression for P which is given by eq 2.7.
The second order contribution is then:

$$P(t) = \epsilon_0 \chi^{(2)}(E_{01}^2 \sin^2(\omega_1 t) + E_{02}^2 \sin^2(\omega_2 t) + 2E_{01}E_{02}\sin(\omega_1 t)\sin(\omega_2 t)) \tag{2.14}$$

The first two terms in this expression can be expressed as functions of $2\omega_1$ and $2\omega_2$ respectively, while the last term of the equation gives rise to sum and difference terms, $\omega_1 + \omega_2$ and $\omega_1 - \omega_2$. Satisfying the phase matching conditions for either process determines whether it will be the sum or the difference frequency generation. The photon of frequency $\omega_1 + \omega_2$ corresponds to a coalescing of the two original photons into a new photon as it does in the case of second harmonic generation in which both quanta have the same frequency. The energy and momentum of the annihilated photons are carried off by the created sum photon. A schematic of the optical parametric process is shown in Figure 2.4.

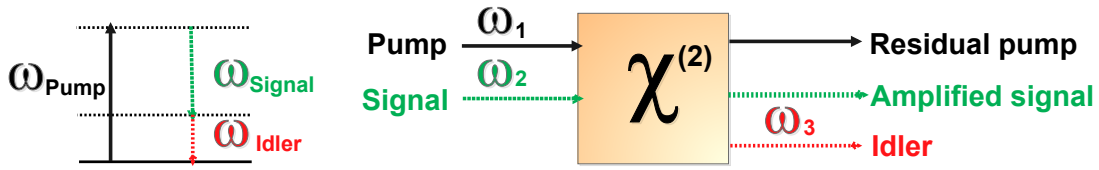


Figure 2.4: Difference frequency generation (DFG): (left) energy level schematic of the process (right) geometry of the interaction that occurs in the OPA at Imperial College.

In the case of $\omega_1 - \omega_2$, the conservation of energy and momentum necessitates that, upon interacting with an ω_2 photon, only the higher frequency ω_1 vanishes therefore resulting in the creation of two new quanta, one being an ω_2 photon and the other being a difference photon. An application of this is optical parametric amplification. If a strong wave of frequency ω_p, called *pump light*, and a weak *signal wave* of frequency ω_s are mixed within a non linear crystal, then the pump light is converted into both signal light and a difference wave, which is known as *idler light*, which has a frequency of $\omega_i = \omega_p - \omega_s$. If the idler is made to beat with the pump light then

the latter is converted into equal amounts of idler and signal light such that both the signal and idler are amplified. The first optical parametric oscillator (OPO) was operated in 1965, and optical parametric amplification is now a cornerstone phenomenon for strong field physics as will be elaborated upon when the OPA used to create the near−IR light used for the experiments in this thesis is introduced in section 2.7.

The Kerr effect

The Kerr effect is the first electro−optic effect and is named after Scottish physicist John Kerr who discovered it in 1875. In a similar manner to the Pockels effect, the Kerr effect also induces a change in refractive index of a material but this change is proportional to the square of the applied electric field strength in this instance. The Kerr effect can also be used to create electro−optical switches. I will now introduce special cases of the optical (AC) Kerr effect in which an intense laser beam in a medium can itself produce the modulating electric field without the need for an external field to be applied, as is the case for making an electro−optics Kerr switch. At high enough intensities, non-linear effects are induced in a media with a non−zero $\chi^{(3)}$ [9]. The Kerr effect is responsible for the intensity dependent refractive index:

$$n(\mathbf{r},t) = n_0 + n_2 I(\mathbf{r},t) \tag{2.15}$$

The non-linear refractive index, n_2, is related to the third order non-linear susceptibilty of the medium. For the Kerr effect, the third order non-linear polarization, $\tilde{P}^{(3)}(t) = \epsilon_0 \chi^{(3)} \tilde{E}(t)^3$, can be expressed as follows [8]:

$$\tilde{P}^{(3)}(t) = \frac{1}{4}\epsilon_0 \chi^{(3)} E^3 cos(3\omega t) + \frac{3}{4}\epsilon_0 \chi^{(3)} E^3 cos(\omega t) \tag{2.16}$$

where the following substitutions were made to the previous expression: $\tilde{E}(t) = Ecos(\omega t)$ and the identity $cos^3(\omega t) = \frac{1}{4}cos(3\omega t) + \frac{3}{4}cos(\omega t)$ was used. Since the first term of the above equation is a source of third harmonic radiation at a frequency 3ω , it is the second term which gives rise to the Kerr effect. The incident laser pulse intensity, $I(\mathbf{r},t)$ is a function of the spatial and temporal properties of the beam. The spatial dependence results in *self focussing* of the laser beam whilst the temporal

dependence leads to the generation of new frequency components in the pulse in a process called *self phase modulation (SPM)*. Self focussing can create inhomogeneities in the beam such as hot spots which can damage optical components. SPM can modify the temporal properties of the laser pulse. Both effects are significant in ultrafast laser science provided that they are adequately controlled and/or compensated for.

Self focussing

Self−focussing occurs when a beam of light that has a non−uniform transverse intensity distribution propagates through a material that has a positive n_2 [8]. For the typical case of a Gaussian beam, this effect leads to a higher refractive index in the middle of the pulse and a lower index at the flanks of the pulse. Similar to a lens, this means that the optical path length is now longer at the centre of the pulse which results in a focussed beam. This process is illustrated in Figure 2.5. The material acts as a positive lens which causes the rays to curve towards each other. The intensity at the focal spot of the self−focussed beam is sufficiently large and can lead to optical damage of the material. Optical damage can occur when the beam power exceeds the critical power which is given by [10]:

$$P_{crit} = \frac{0.148\lambda^2}{nn_2} \tag{2.17}$$

where n is the refractive index of the material, n_2 is the nonlinear index expressed in units of m^2/W and λ is the beam wavelength in nanometers.

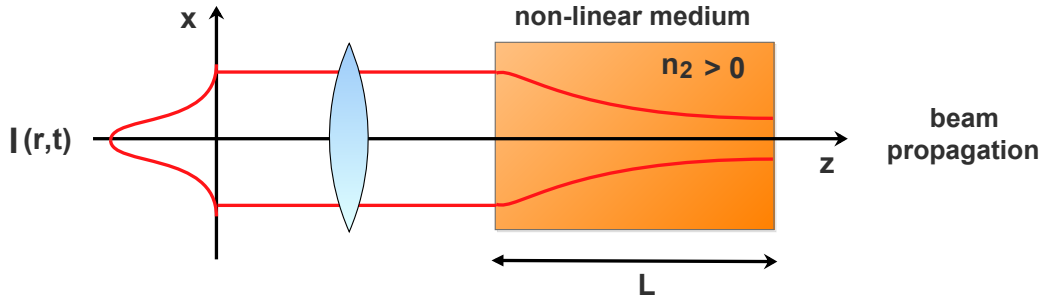


Figure 2.5: Self focusing of light in a non−linear medium as described in the text.

Thermal lensing, in which the heating of the gain medium results in temperature gradients, can also result in self−focussing occurring. Self−focussing has a very important application in Kerr−Lens modelocking which will be introduced in the next section of this chapter.

Self phase modulation

Self−phase modulation is the change in the phase of an optical pulse resulting from the non−linearity of the refractive index of the material medium [10] [91]. Assuming that the medium can respond instantaneously to the pulse intensity and that the length of the non−linear medium is short enough such that no reshaping of the pulse can occur, then the only effect of the medium is to change the phase of the transmitted light by:

$$\phi_{NL}(t) = -n_2 I(t)\omega_0 L/c \tag{2.18}$$

This time varying phase causes the spectrum of the transmitted pulse to be modified and will be typically broader than that of the incident pulse. The spectral content of the transmitted pulse can be understood more intuitively by introducing the concept of *instantaneous frequency*, $\omega(t)$, which is given by:

$$\omega(t) = \omega_0 - \frac{2\pi}{\lambda_0} n_2 L \frac{\partial I}{\partial t} \tag{2.19}$$

The leading edge of the pulse will have $\frac{\partial I}{\partial t} > 0$ and SPM will result in a decrease in frequency − red shift − for that materials with $n_2 > 0$. The trailing edge of the pulse will be blue shifted and as a result, the pulse will develop a positive chirp. This results in the spectrum being broadened in both directions as shown in Figure 2.6.

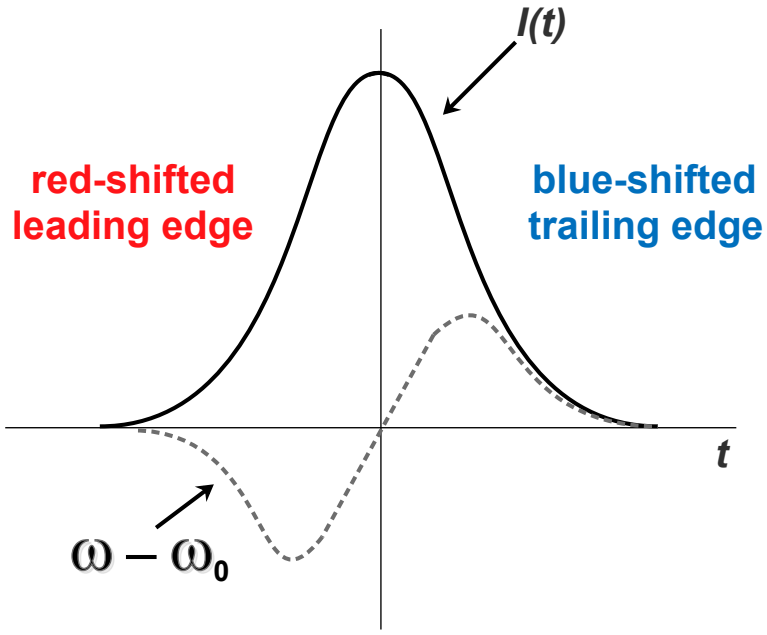


Figure 2.6: Origin of the frequency chirp of a pulse with an initial carrier frequency, ω as a result of self phase modulation (SPM): the solid line represents the temporal profile of the pulse. The dashed line is the frequency shift that arises from the SPM process.

Again, if we look at the expression for the total phase accumulated for a pulse propagating a distance, L, with a wavelength of λ_0 and a constant intensity I [91]:

$$\phi = \frac{2\pi}{\lambda_0}\int_0^L nI(z)dz = \frac{2\pi}{\lambda_0}\int_0^L n_0 dz + \frac{2\pi}{\lambda_0}\int_0^L n_2 I(z)dz$$

we see that the second term on the right hand side of this expression gives the intensity dependent part of the phase, ϕ_I. This quantity is better known as the *B-integral* [91]. The intensity of the beam will vary with transverse position such that the beam is more intense near the axis of propagation than at its wings. In this situation, the centre of beam will accumulate a greater phase than the wings of the pulse such that it will act like a positive lens and leads to self−focussing. The value of n_2 for sapphire is $\approx 2.5 \times 10^{-16}\text{cm}^2\text{W}^{-1}$. The importance of the B−integral will be stressed when chirped pulse amplification (CPA) is introduced in section 2.5.1. The B−integral provides an estimate of when the onset of self−focussing occurs.

2.3 Ultrashort pulse production

Pulsed lasers offer numerous advantages over continuous wave (CW) sources. For the same average power, the temporal confinement of a pulsed laser leads to higher peak intensities. The short interaction time of the pulse with the target medium also decreases the probability of inducing damage to the medium as a consequence of the high peak powers it is exposed to. Ultrafast pulse duration also enables fast temporal resolution. A modelocked laser can effectively "freeze" the motion of fast moving objects such as molecules or their constituent electrons which enables the measurement of ultrafast processes such as chemical reaction dynamics, relaxation processes of carriers in semiconductors or electro−optical sampling of high speed electronics, to name but a few [93]. The 1999 Nobel prize in chemistry was awarded to A.H. Zewail for measuring the dissociation dynamics of molecules [94].

Six years after Maiman demonstrated the first laser [1], De Maria produced the first ultrashort pulses [95] which were estimated to be picoseconds in duration and were generated from a passively modelocked Nd:glass laser. As shown in Figure 2.7, ultrashort pulse generation was dominated by dye lasers until the end of the 1980s with state of the art specifications of 27 fs duration, $\approx$ 10 mW average power at a central wavelength of 630 nm being published. External pulse compression resulted in pulses as short as 6 fs which was achieved by C.V. Shank [96] and remained an unsurpassed milestone for almost a decade.

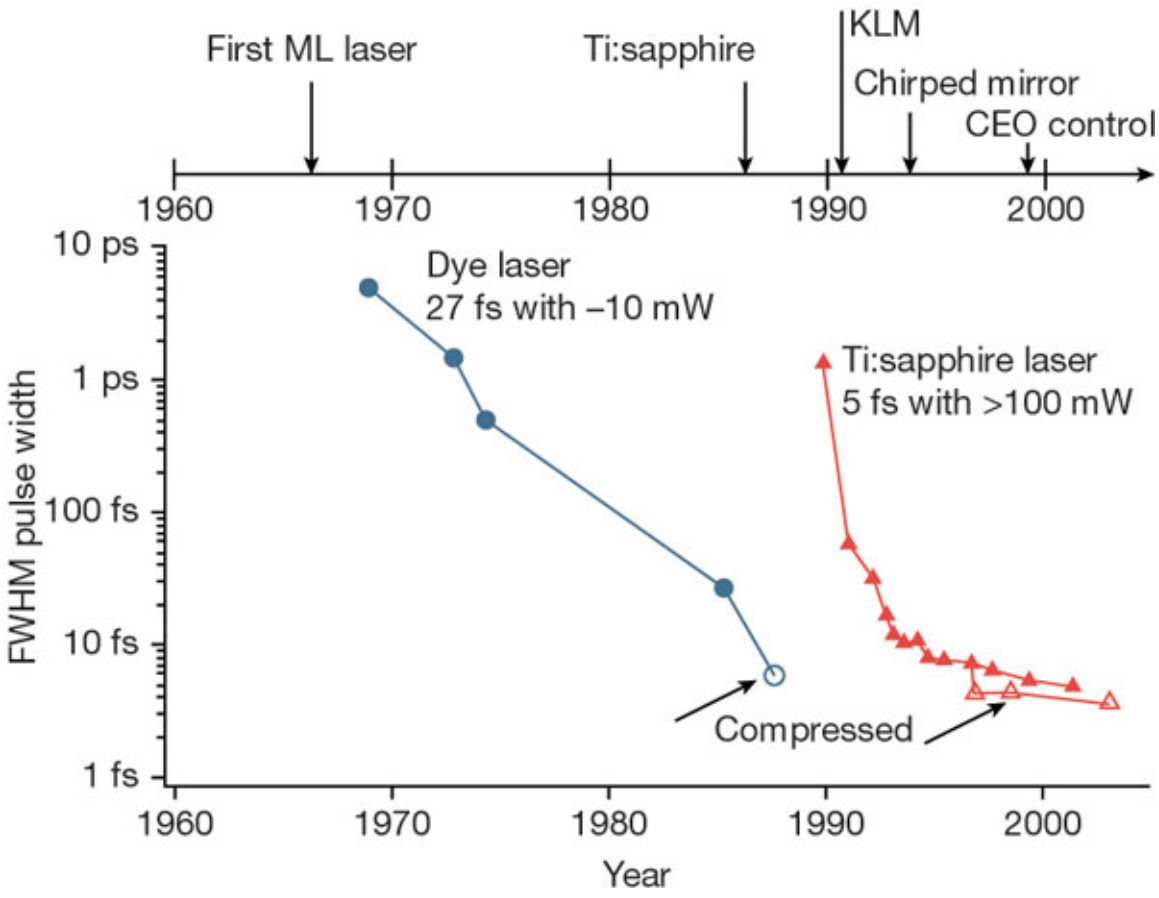


Figure 2.7: Roadmap of the advancements in ultrashort pulse generation since the laser was first demonstrated by Maiman in 1960. [93]

2.4 Modelocking

Modelocking is achieved by forcing the longitudinal modes in the laser cavity to maintain a fixed phase relationship [97]. This is accomplished by modulating the loss in the laser cavity at a frequency that is equal to the intermode frequency separation of:

$$\Delta\upsilon = \frac{c}{2L} \Leftrightarrow \Delta\omega = \frac{\pi c}{L} \tag{2.20}$$

This can be better understood by visualising a loss modulation provided by a shutter that is placed near one of the mirrors in the laser cavity. For the majority of the time

the shutter remains closed which leads to very high losses and is opened every $2L/c$ seconds which corresponds to the round trip time of the wavepacket in the cavity [97]. If the wavepacket is exactly as long in time as the period of time the shutter stays open and provided it arrives exactly when the shutter is open then it will be unaffected by the presence of the shutter. However, any parts of the wavepacket that arrive before the shutter opens or after it closes will be eliminated. Thus, the phase relationships of the oscillating modes are continuously restored by the periodic operation of the shutter. A variety of devices or materials can be used to perform the function of the shutter.

Electro−optic or acousto−optics modulators are used in *active modelocking* laser systems [98]. For active modelocking, an external signal is applied to an optical loss modulator. An electronically driven loss modulation produces a sinusoidal loss modulation that has a period given by the cavity round−trip time. The saturated gain at steady state will only support net gain around the minimum of the loss modulation and will therefore only support pulses that are significantly shorter than the cavity round trip time.

Passive modelocking employs a saturable absorber, such as a laser dye, to obtain self−amplitude modulation of the light in the laser cavity [97]. This absorber produces a loss in the cavity which can be relatively large for low intensities but may be significantly smaller for a short pulse with a high intensity. A short pulse induces a loss modulation due to the fact that the high intensity at the peak of the pulse saturates the absorber faster than the lower intensity wings of the pulse. Passive modelocking is initiated by normal noise fluctuations in the laser. Initially, the laser emits spontaneous radiation which gives rise to fluctuations in the energy density. Short duration fluctuations can be amplified in the medium and grow in irradiance to such an extent that the peak part of the fluctuation is transmitted through the saturable absorber with little attenuation. The nonlinear nature of the absorber, such as a dye, causes the shortest and most intense fluctuations to grow at the expense of the weaker ones. An initial fluctuation may grow into a narrow pulse bouncing back and forth in the laser cavity producing a periodic train of modelocked pulses [93]. The recovery time of the absorber can be very fast so the loss modulation is fast such that pulses produced by this method opposed to active modelocking are of much

shorter duration because there is no need for electrical switching. Saturable absorbers provide a very intuitive method to modelock a high power laser such as Nd:glass and ruby − the dye solution 9740 and cryptocyanaine are commonly used as saturable absorbers in Nd:glass lasers [97]. Using a saturable absorber to modelock a laser also simultaneously makes it *Q−switched*.

This effect was first demonstrated by De Maria and differs from modelocking in the sense that it produces an amplitude modulated pulse train unlike a regular pulse train attained by modelocking. The process can be initiated by introducing a time dependent loss to the laser cavity such as blocking one of the cavity mirrors briefly. As the mirror is blocked, the pumping of the gain medium builds up the population inversion. Due to the elevated losses in the cavity in this configuration, the population inversion can build up to levels greater than that of the threshold inversion for lasing in the cavity without any lasing occurring as one cavity mirror is temporarily blocked. Once the population inversion has grown significantly the blocked cavity mirror is then unblocked which switches the quality factor, "Q", of the cavity from low to high [97]. Stimulated emission then causes the upper laser level to depopulate below the threshold value as a high density of photons is emitted in the cavity. Once the gain has fallen below the threshold value the lasing stops. The output from the laser under these conditions is then essentially a single giant pulse of radiation. Q−switching is most effective in media with a lifetime of the upper laser level on a typically mircosecond timescale such as ruby. This enables the population inversion to build up slowly without a large fraction of the atoms in the upper level decaying back down to the ground state by spontaneous emission. Pumping in Q−switched lasers may be initiated by continuous wave (CW) or pulsed lasers, the obvious difference being that there will be a higher peak output power from the pulsed laser system.

Reverting back to passively modelocked lasers, the success of this technique in the 70's and 80's with laser dyes was largely at the expense of solid state media used in the same manner. Taking the example of the result by De Maria in 1966 [95] that presented a passively modelocked train of pulses of picosecond duration from Nd:glass, they measured an amplitude modulated pulse train. In this regime, known as *Q-switched modelocking* the modelocked picosecond pulses are modulated by a much longer Q−switched envelope which occurs at a lower repetition rate. This problem

compromised the performance of passively modelocked solid state lasers for over 20 years.

A breakthrough in 1992 has dramatically advanced the average powers, pulse energies and pulse durations of ultrafast solid state lasers. Self−starting passive modelocking was demonstrated in diode pumped sold state lasers with an integrated semiconductor saturable absorber (SESAM). A SESAM is usually integrated into one of the cavity mirrors and is designed such that its reflectivity increases as the incident optical intensity increases. Adjusting the properties of the SESAM material such as response time and saturation fluence, can also eliminate the conditions of the cavity which are favourable for Q−switched modelocking. The mirrors can be manufactured using semiconductor materials such as AlAs/AlGaAs, dielectrics or metal coatings [91]. In 1990, Ishida *et.al* [99] published a passively modelocked Ti:Sapphire laser with an intracavity saturable absorber producing stable 190 fs duration pulses.

In 1990, Sibbert [100] also demonstrated a self−modelocked Titanium−doped sapphire laser of 60 fs duration but, in contrast to Ishidas result, no saturable absorber was present. Titanium sapphire has extremely desirable properties for a solid state laser material. These include a gain bandwidth spanning the wavelength range from 700 to 1100 nm, a very high thermal conductivity and has an energy storage density approaching 1 J/cm^2 [101]. The high energy storage density was initially thought to inhibit Ti:sapphire as a gain medium for femtosecond modelocked lasers. This is because the pre−existing passively modelocked dye lasers relied on the low energy storage density of the laser dye to facilitate the modelocking process.
Sibberts result was puzzling as no saturable absorber was present but Ishidas publication was equally enthralling. This is because dye saturable absorbers with nanosecond recovery times cannot support ultrashort pulses with a Ti:sapphire laser as they can with dye lasers. Ti:sapphire relies on a different mechanism to facilitate short pulse generation − the Kerr nonlinearity of the laser crystal which was introduced in section 2.2.2. In Kerr lens modelocking (KLM), the Kerr nonlinearity can be employed as an effective saturable absorber [10]. The Kerr effect produces a non−linear lens that focuses the high intensity part of the incident beam more strongly than the low intensity wings [102]. In combination with an intracavity aperture, the Kerr lens enables less loss for higher intensities . As a non−resonant saturable absorber it is

inherently broadband, and is broader than other saturable absorbers available. With the application of Kerr lens modelocking, 5 fs pulses with > 100 mW average power at a central wavelength of 800 nm can be generated. As show in Figure 2.8, external compression can also further reduce this to pulses with a sub 4 fs duration. KLM is not self−starting and usually requires one of the cavity optics to be perturbed to increase the laser noise.

2.5 Ultrashort pulse generation in a modelocked laser

The generation of ultrashort pulses is performed in an oscillator. A schematic of a typical oscillator cavity configuration is shown in Figure 2.8 [101]. Ti:sapphire is by far the most commonly used laser medium for ultrashort pulse generation and will be the focus of the discussion here. Argon−ion or frequency doubled Nd:YAG lasers can be used for the energy source to pump the gain medium. The CW light is focused co−linearly into the Ti:sapphire crystal with the laser cavity mode. An end mirror and an output coupler complete the cavity configuration together with a prism pair that compensates for dispersion of the gain medium. The Kerr lens effect is used to instigate modelocking.

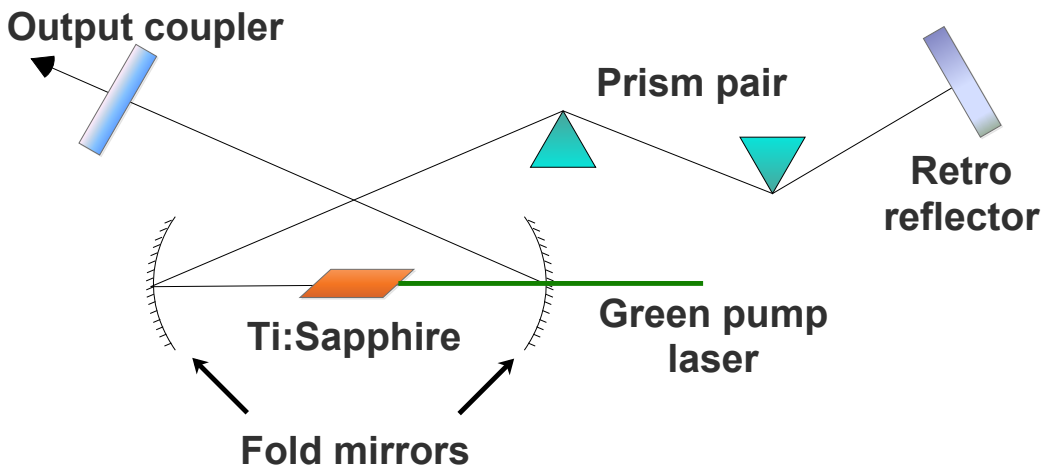


Figure 2.8: Schematic of a typical self−modelocked Ti:sapphire oscillator. Adapted from [101]

The cavity is first aligned for optimum efficiency before one of the fold mirrors is displaced a small distance $\approx 5-10$ mm away from the optimal CW configuration which introduces a loss into the cavity as the Kerr lens comes into effect. Kerr lensing thus couples the oscillators spatial and temporal modes of operation (CW and pulsed) so the laser can actually be aligned to be stable in either mode [101].

The most significant improvement made to the Ti:sapphire laser since it was first demonstrated is the dramatic reduction in the pulse duration achievable. This is accomplished by using shorter Ti:sapphire crystals and dispersion compensating prisms and mirrors. Commercially available Ti:sapphire lasers can now produce pulses of 10 fs duration, with a central wavelength of 800 nm at an 80 MHz repetition rate with typical pulse energies in the $\approx 5-10$ nJ range with excellent stability. These oscillators are ideally suited for high power, chirped pulse amplification (CPA) laser systems which is the fundamental tool for performing HHG.
The design of the Ti:S oscillator used in the CPA laser system at Imperial College is shown in Figure 2.8. The oscillator is pumped by 5.2 W of 532 nm light from a diode pumped Nd:YAG CW laser (Verdi, Coherent). Pulsed operation is achieved through Kerr-lens modelocking. Two fused silica prisms are used to control dispersion during a cavity round trip. When the oscillator is optimised for modelocking it typically delivers 300 - 400 mW. Movement of one of the prisms initiates modelocking with an

increase in output power up to 450 - 550 mW. The larger the discrimination between the CW (continuous wave) and ML (modelocked) powers, the better the stability of the modelocked operation of the oscillator. The cavity length is 1.7 m corresponding to a cavity round trip time of 11 ns and a repetition rate of 89 MHz. For a ML output power of 450 - 550 mW this implies a pulse energy of 5 -6 nJ. Ideally the oscillator will deliver $\approx$ 20 fs pulses centred at 790 nm with a spectral bandwidth of 50 - 70 nm. Optimisation of the oscillator involves striking a balance between bandwidth, power and stability. The central wavelength also has to match the gain profile of the laser amplifier and thus needs to be 790 - 800 nm.

2.5.1 Chirped Pulse Amplification

Since the typical pulse energies available from this most modern of laser oscillators is on the nJ level, a means of amplifying the pulse is necessary to achieve the high peak powers necessary for HHG and other ultrafast experiments – chriped pulse amplification (CPA) [103]. Before the oscillator output is fed into a secondary Ti:sapphire amplification stage, the femtosecond duration pulse needs to be stretched in time by introducing a frequency chirp. The extent of the chirp to be imposed on the pulse is determined by the necessity to stay below the optical damage threshold of the amplification stages components. Typically, an oscillator output in the 10 fs – 1 ps range is stretched by a factor of $\approx 10^4$ to a duration of the order of $\approx$ 100 ps.

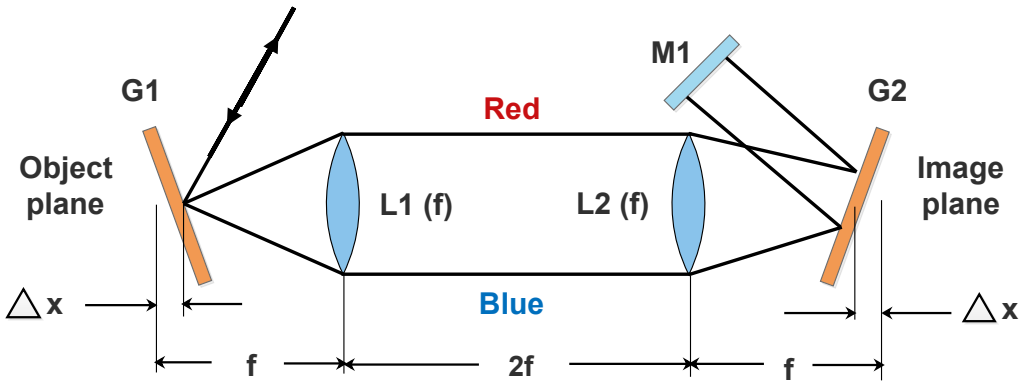


Figure 2.9: Schematic of a pulse stretcher employed in a CPA laser system

A grating pair is commonly uses to introduce the necessary frequency chirp to the oscillator seed beam. As shown in Figure 2.9, a telescope is placed between the stretcher

grating pair to enable the dispersion to be controlled by the effective distance between the second grating and the image of the first one. A unity magnification telescope is placed between two gratings in an antiparallel rather than parallel geometry. This reverses the sign of the dispersion of the grating pair which are separated by $2f$, with the pair of gratings each at a distance, s_1 from the nearest lens. The distance $s_1 - f$ is the effective grating separation where s_1 is the distance from the lens to the grating. If $s_1 = f$, the focus is right on G_2, there is no dispersion in the output beam. If $s_1 \neq f$, the focus will be either $2(s_1 - f)$ before or after G_2, which is proportional to the stretching factor that is defined as the stretcher pulse length divided by the oscillator pulse length. If $s_1 < f$, the pulses will be positively chirped. The optical path length for the red wavelengths is shorter than for the blue. Pulses leaving the stretcher will have positive slope of frequency versus time, i.e. a positive chirp. The mirror M1, directs the beam through a second pass of the stretcher to avoid walk off of the beam. For a small beam size, this mirror may be aligned slightly angularly deviated from retroreflection without introducing an undesirable amount of spatial chirp [101].

After pulse amplification, the chirp that was introduced by the stretcher must be compensated for to recover a transform limited pulse. This is done by using a compressor. In the same fashion as the stretcher module, the compressor consists of two gratings as shown in Figure 2.10. The gratings must be of high optical flatness ($\lambda/4 - \lambda/10$) to ensure a good output beam quality. Usually one of the gratings is fixed and the other is mounted on a translation stage as the chirp introduced by the stretcher needs to be correctly compensated and the parallelism of the gratings faces must be preserved to avoid spatial chirp on the output beam. In the compressor, a pair of mirrors is used in a roof geometry to direct the output beam above and parallel to the input beam.

2.5.2 CPA laser system at Imperial College

After the oscillator, the beam first passes through a Faraday isolator to prevent potential back reflections from the amplifier to travel back into the oscillator which can compromise the stability of the oscillator. The beam is then directed into an Offner configuration stretcher that consists of a single grating and a folding mirror which ensures the beam hits the grating four times with a throughput efficiency of

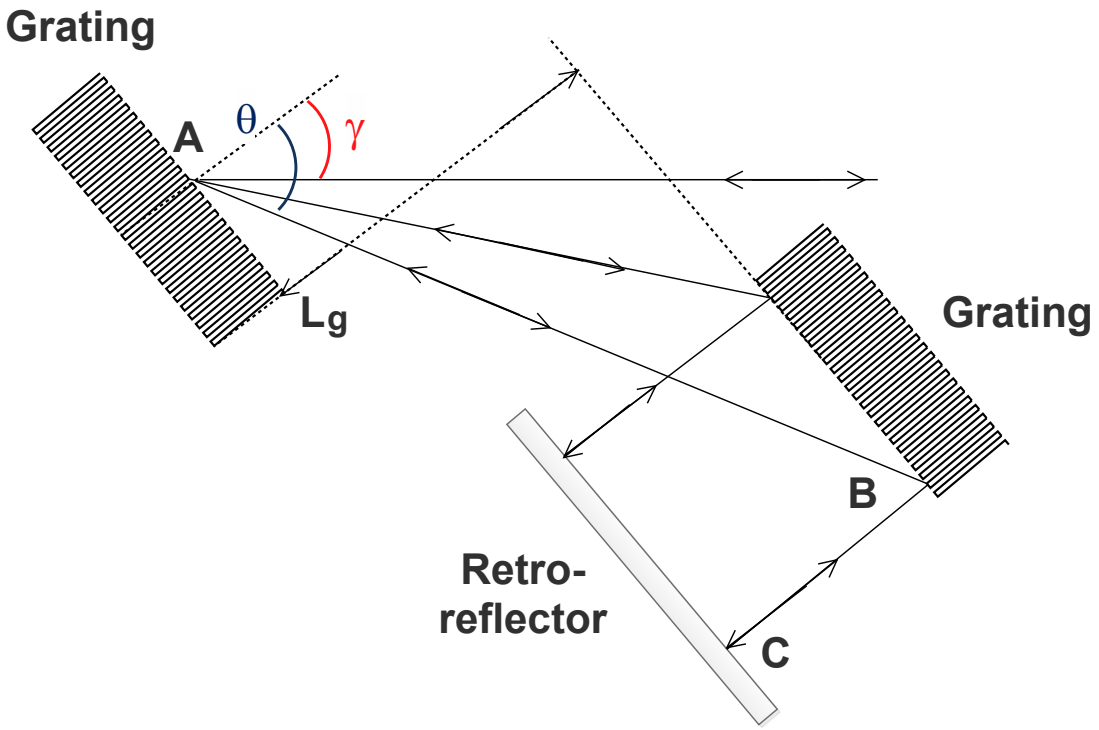


Figure 2.10: Schematic of a pulse compressor employed in a CPA laser system which is complimentary to the stretcher stage. Adapted from [101]

$\approx 50\%$. Pulses are stretchers to $\approx 150 - 200$ ps to ensure a sufficiently low intensity during amplification to prevent damage to the optical elements in the amplifier. The spectral bandwidth of the seed pulses from the oscillator must be ≥ 45 nm to ensure the pulse is stretched sufficiently.

Before the pulses are sent for further amplification the 89 MHz pulse train is selected down to 1 kHz as it passes through a Pockels cell and polariser configuration. The Pockels effect was described in section 2.2.2. When no voltage is applied the pulses remain horizontally polarised and are blocked by the polariser. When voltage is applied to the Pockels cell, it acts as a half−wave plate and vertically polarises the light allowing it to enter the first amplification stage as only vertically polarised pulses will pass the subsequent polariser. The Pockels cell is triggered at 1 kHz which tunes down the pulse train frequency [98] [10].

Amplification is achieved via a 13 pass multi-pass amplifier which boosts the pulse energy from the 5 nJ at the oscillator output to 2.5 mJ. The amplifying medium is a Titanium:Sapphire crystal which is cryogenically cooled by liquid helium and kept under a vacuum of 10^{-7} mbar − this is to avoid thermal lensing effects and to prevent condensation on the crystal surfaces. Liquid helium is used to maintain a crystal temperature of $\approx$ 75K during pumping. This ensures a high damage threshold and thermal stability.

In the same manner that the oscillator uses, a pump laser is used to create the population inversion required for amplification in the Ti:sapphire crystal of the amplifier. The laser used in this case is the DM30 which is a Q-switched Nd:YAG laser (frequency doubled to operate at 532 nm) which performs with 30 W of power, 1 kHz repetition rate and a 15 ns FWHM. The timing between the pump pulse and the seed pulse is optimised such that the gain is maximised and any amplification of spontaneous emission (ASE) is minimised. The last of the 13 passes through the amplifier is picked off by a mirror and is steered towards the pulse cleaning stage. There is a second Pockels cell/polariser pair located at the output of the first amplifier which serves to "clean up" the pulse train, in other words to reject any small pulses which may have seeped through the first Pockels cell/polariser pair and were subsequently amplified. It is important to have this stage in the system to remove any pre or post pulses as they can be further amplified by the second amplifier.

To further increase the energy the pulse train is sent to a second amplification stage which serves to bump up the energy from 2.5 mJ to 14 mJ. Again for this stage two pump lasers are used − one is identical to that used in the first amplification stage and the other is the same model but a 40 W output power. Due to the fact that the pulses are now of higher energy than those entering the first stage and the fact that the energy gain is exponential, it only takes two passes to extract all the pump energy from the crystal. In the last stage the pulses are directed towards a compressor as illustrated below in Figure 2.10. After two bounces off the gratings the pulse is compressed down to 25 fs. The angle of the compressor grating angle with respect to the input beam has to approximately match that of the stretcher grating to correct for third order dispersion effects which inhibit attaining a transform limited pulse. The distance between the two gratings is used to correct for second order dispersion

effects. Parallelism of the gratings mitigates spatial chirp in the output beam. The throughput efficiency of the grating compressor is $\approx 65\%$ which results in an output energy of ≈ 8 mJ.

At the end of the CPA module the end product is a short, intense pulse. The resultant pulse train has a repetition rate of 1 kHz, centred at 800 nm with a bandwidth of ≈ 45 nm and a typical pulse duration of 25 fs and powers in excess of 8 W can be achieved.

A full schematic of the laser system used in this PhD is shown in Figure 2.11 on the next page.

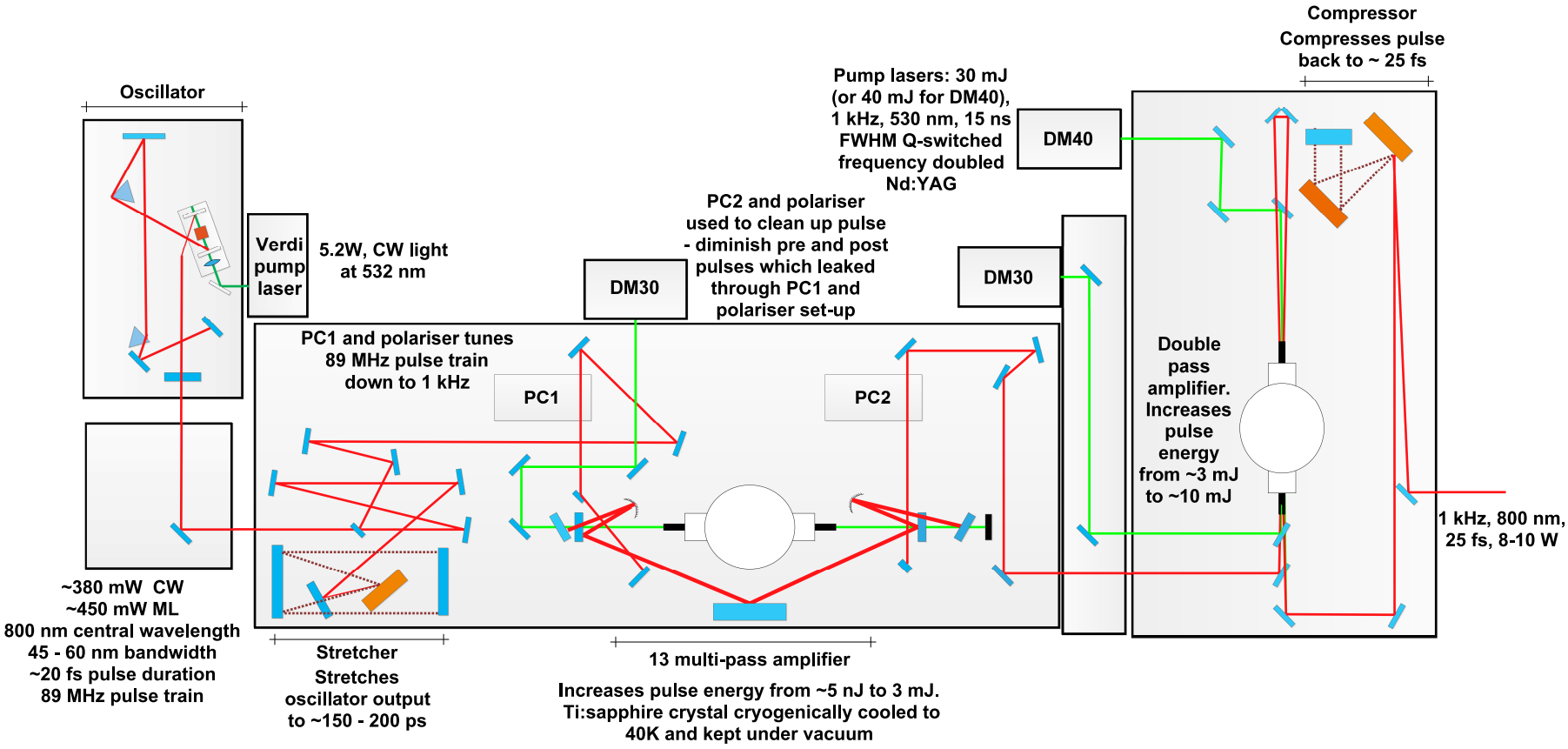


Figure 2.11: The complete layout of the CPA laser system - KM Labs Red Dragon - used in this thesis. CW stands for continuous wave, ML is modelocked, PC is Pockels cell.

2.6 Pulse characterisation

Whilst it is all well and good to boast the achievement of a 25 fs pulse, this needs to be diagnosed and measured in the laboratory. The method of choice that has been used for the KM Labs Red Dragon in this project insofar is that of Spectral Phase Interferometry for Direct Electric Field Reconstruction (SPIDER) [104] [105] .
Figure 2.12 is an outline of a typical SPIDER apparatus. SPIDER is a spectral shearing interferometry technique in which all measurements are made in the frequency domain. In essence what happens is that the beam is split in two by a beamsplitter − one part is passed through a 2 grating stretcher which introduces a negative chirp that stretches the pulse, the other is further split in two by another beamsplitter upstream to create the two time delayed replicas, delayed by τ, via an etalon. To put some numbers to this technique take a 150μm thick etalon; by the relation $\tau = \frac{2L}{c}$ the delay is 1.5 ps [106].

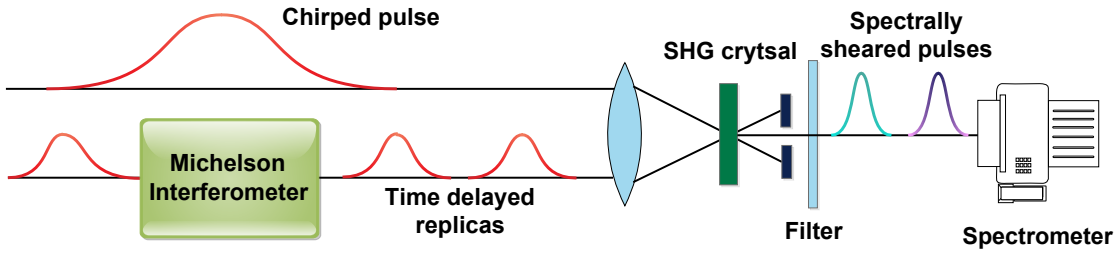


Figure 2.12: Schematic of a general SPIDER for pulse characterisation

The amount of chirp introduced by the grating stretcher is -2×10^5 fs^2 which stretches the pulse to 20 ps. The stretched pulse is recombined with the replicas by focusing them into an SHG crystal with a lense; using a beamsplitter is impractical as it causes a loss of signal from the replicas therefore reducing the SPIDER signal. The pair of time delayed pulses are then upconverted along with the chirped pulse in a non−linear crystal, e.g. BBO. The purpose of this step is to interfere each of the pulse replicas with a different temporal, hence spectral portion of the stretched pulse which results in the generation of a pair of pulses that are sheared by an amount Ω. The amount of shear is dependent upon the chirp and the time delay selected: $\Omega = \frac{\tau}{\phi^{(2)}}$ [106]. The spectrally sheared pulses interfere to generate a spectral interferogram which encodes the phase information of the original pulse. The up conversion of the two 800 nm replica pulses with the chirped pulse generates two pulses at 400 nm which

are separated by a delay τ and are sheared in frequency by $\Omega = \frac{\tau}{\phi^{(2)}}$. The beams are then focused onto a slit into a spectrometer. The SPIDER trace, $S(\omega)$ is Fourier transformed to the time domain to produce:

$$S(t) = FT\left\{S(\omega)\right\} = S(t) = A_{DC}(t) + A_{AC}(t-\tau) + A_{AC}(t+\tau)^{*} \tag{2.21}$$

The Fourier transform of the interferogram produces three peaks, the first term in the above equation contains information about the spectral intensity of the initial pulse, the second and third terms are the AC terms which are born out of the interferences and contain the phase information. Filtering around $t = +\tau$ and applying an inverse Fourier transform reconstructs the total phase: $\delta\phi(\omega) + \omega\tau$. It is also necessary to remove the linear spectral phase term $\omega\tau$ since it introduces a shift in the time domain. The value of $\omega\tau$ is measured by recording the interference pattern from the two pulse replicas since the only phase contribution is from $\omega\tau$. The contribution from the third term of the above equation is also filtered out since it contains the same information as the second term being a time reversed replica of it. The resultant phase difference is given by:

$$\delta\phi(\omega) = \frac{1}{\Omega(\phi(\omega+\Omega+\omega_0) - \phi(\omega+\omega_0)} \tag{2.22}$$

The spectral phase is retrieved from the phase difference by the concatenation technique wherein the phase is sampled at intervals of the spectral shear. Setting $\phi(\omega_0) = 0$ the phase at each frequency ω_n can be reconstructed:

$$\phi(\omega_n) = \sum_{j=0}^{n-1} \frac{1}{\Omega}\delta\phi(\omega_j) \tag{2.23}$$

The summation of these phase differences in conjunction with the spectral phase measurements can be used to reconstruct the pulse in the spectral and temporal domains. Figure below is a measured SPIDER trace from the KM Labs Red Dragon CPA laser system. The trace of the intensity of the second harmonic signal versus the amount of optical delay is known as the autocorrelation function (ACF) trace.

By assuming the shape of the pulse, its duration can be determined by multiplying the width of the ACF by a form factor. For example for a Gaussian pulse it is $\frac{1}{\sqrt{2}}$, which, when multiplied by the ACF FWHM of 39 fs as in Figure 2.13 gives a retrieved duration of 29 fs.

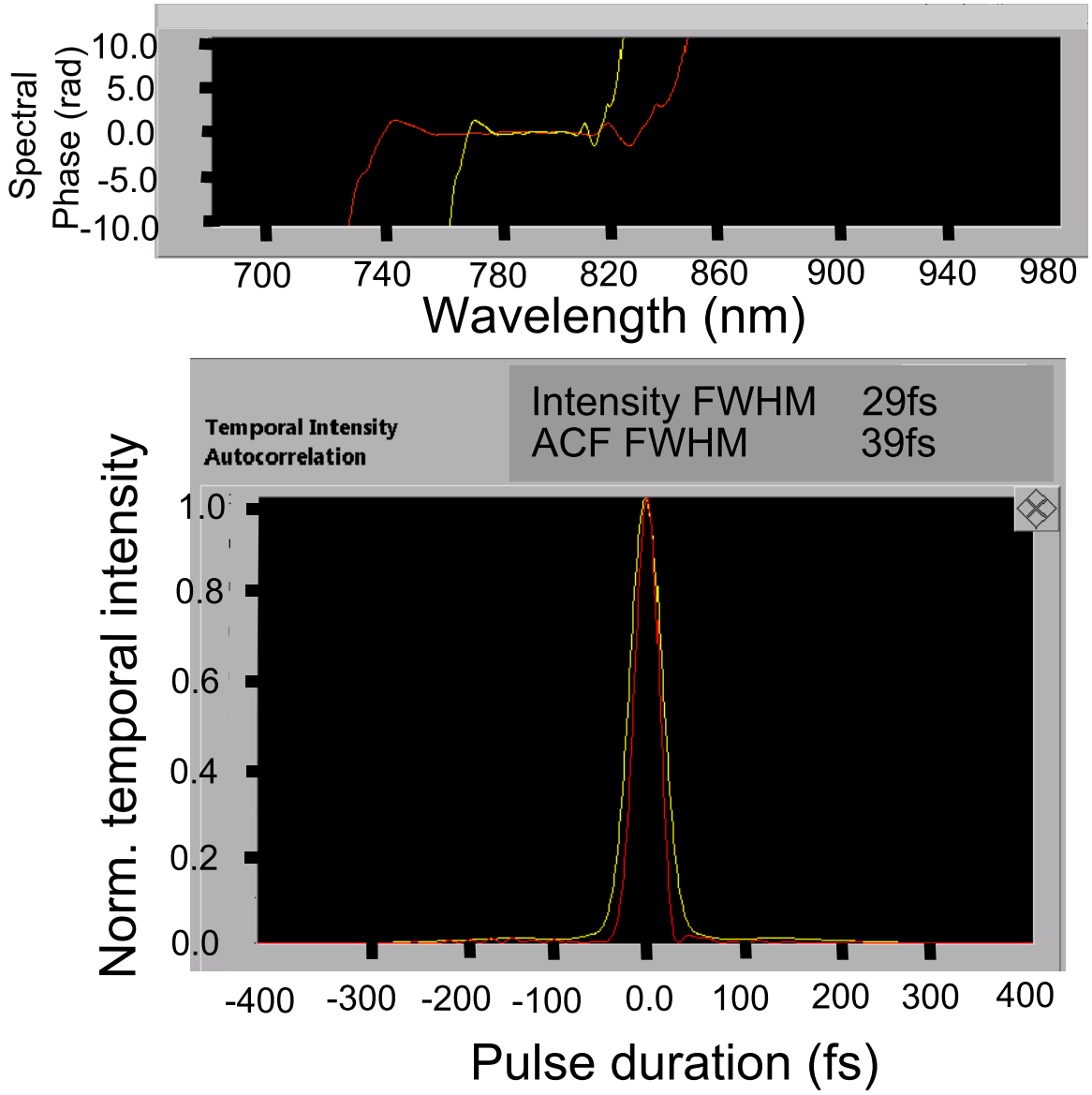


Figure 2.13: Typical SPIDER trace measured in the laboratory. The top panel shows the spectral phase which is flat for the wavelength range of pulse being measured indicating that the pulse is compressed optimally. The bottom panel shows the pulse duration measured. The red trace is that of the retrieved pulse we measure and the yellow trace is the autocorrelation function trace.

2.7 Generation and characterisation of the idler

In order to realize our goals of extending the cut-off of the HHG spectra to access dynamics on a longer timescale and to eliminate temporal averaging in the HHG process a long wavelength, short pulse source needs to be developed. Following the work by Schmidt *et.al* [21] where a 1.6 cycle pulse at 1800 nm was generated and characterized we intend to employ the idler from the TOPAS OP−CPA system [107] in conjunction with propagation through a hollow core fibre to clean up the spatial mode of the beam but also has a primary function in further pulse compression through self phase modulation in a gas filled hollow core fibre. This section will detail the intended procedure for ultrashort mid−IR pulse production, characterization and considerations to be noted when working with this beam.

2.7.1 Near-IR wavelength generation

The commercial TOPAS OP-CPA (from Light Conversion) laser can be tuned to operate at wavelengths in the range 1100-2000 nm, typically outputting ≈2 mJ at 1300 nm. The TOPAS does not operate independently and must be pumped by ≈8 mJ from the 1 kHz KM Labs Red Dragon laser which generates ≈ 30 fs pulses at 800 nm. This is one downfall of working with the TOPAS in the sense that it inherits any instabilities or mode profiles from the pump laser which can be detrimental to the TOPAS operation. The principal components of the TOPAS are outlined in Figure 2.14

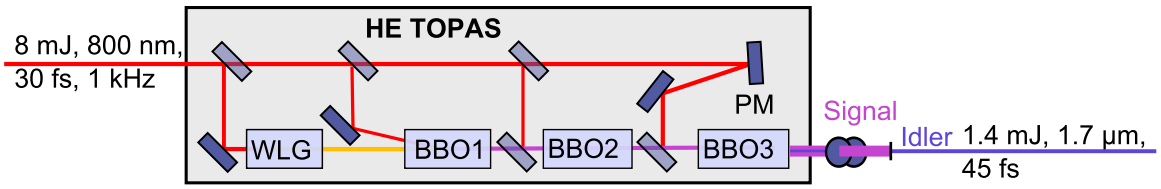


Figure 2.14: Layout of the main components and stages of the HE−TOPAS OP−CPA NIR wavelength generation system. The WLG (white light generation stage) produces the white light continuum. From [107]

The HE-TOPAS is the source of radiation from 1100 − 1700 nm in the lab. The apparatus is seeded with 8 mJ of 800 nm radiation. A fraction of the 800 nm input

beam ($\approx 1-3\mu$J) is focused into a sapphire plate to generate a white light continuum (WLC). The WLC beam and another split off of the 800 nm beam ($\approx 30-50\mu$J) are focused into the pre−amplifier crystal non−collinearly. The non−collinear geometry enables the amplified signal beam to be separated easier from the idler and the residual pump beam. The angle of the crystal can be tuned by the software module to select the amplified signal wavelength. The delay of the pump beam can also be adjusted in a similar manner to maximise the amplification efficiency.

The residual pump and idler are blocked by a beam block after the crystal and the signal beam is collimated by a lens telescope before it is sent to the second amplification stage. $0.3-0.6$ mJ of the 800 nm pump beam energy is used to pump the second amplification stage. The pump and signal beams are overlapped collinearly in the second non−linear crystal. The signal and idler generated from this stage are further used to seed the high power amplification stage along with the $7.0-7.5$ mJ of the input 800 nm beam. These beams are collinearly overlapped in a third crystal.

Parametric amplification in this crystal will amplify the signal (idler) and produces an idler (signal). Both the signal and idler beams are collinear after this crystal. A dichroic mirror is used to reflect the 800 nm pump beam into a beam block. The amplified NIR output is then composed of an S−polarised signal ($1200-1600$ nm) and a P−polarised idler beam ($1600-2000$ nm).
The signal and idler are separated with an appropriate wavelength separator (dichroic optic). It is from this HE−TOPAS system that we obtain the 40 fs pulses at 1.7 μm with a power of $\approx$ 1.5 W at 1 kHz. It is intuitive to see that propagation of the Fourier−limited 800 nm input beam is altered by the transmissive optics in the TOPAS. Detuning the 800 nm lasers compressor to compensate for the chirp introduced by the TOPAS will ensure the system is optimised to achieve the maximum output power and the shortest attainable duration pulse. The operation of the TOPAS is almost totally dependent upon the quality of the beam from the 800 nm pump laser (of course it can not be totally attributed to the pump laser as the quality and alignment of the OP−CPA optics may also compromise the operation of the laser). The pump intensity needs to be high enough to drive the final amplification stage into saturation. OPA's instantaneously adapt the gain to the amplified signal power level, since they do not store energy in the gain medium in the same

way that, say, Ti:sapphire crystals or laser dyes do. Too low a pump intensity will give a low conversion efficiency and may impede the consecutive amplification stages from operating correctly [8].

2.7.2 Spectral broadening

Spectral broadening in a gas filled hollow core fibre [108] is the method in which further temporal compression is achieved. Spectral broadening can be achieved by using an argon filled hollow core fibre. Typical fibre specifications are a 1 m heavy wall capillary with a 400 μm inner diameter. The fibre is fitted with anti-reflection CaF_2 entrance and exit windows to minimize dispersion. A 1 m focal length mirror is used to focus into the fibre and a similar optic is located at the end of the fibre to collimate the beam. Non linear processes in the fibre such as self-phase modulation (SPM) can occur which results in the trailing edge of the pulse becoming steeper than the leading one − this results in an asymmetry in the spectral phase. This can be compensated by inserting ≈ 3 mm fused silica window in the beam path. The amount of spectral broadening a pulse of temporal FWHM, τ_0 , undergoes as it propagates through the hollow core fibre is given by equation 2.24:

$$\Delta\omega = \frac{0.86}{\tau_0} \int_0^L \gamma(z) P(z) dz \tag{2.24}$$

where the power, $P(z) = P_0\ \xi \exp(-\alpha z)$ wherein α describes the attenuation coefficient for the intensity losses in the walls of the fibre, P_0 is the power incident on the fibre, ξ is the coupling efficiency and z is the propagation distance. $\gamma(z)$ takes into account the non-linear refractive index of the gas, pressure variation along the fibre, central frequency of the pulse and the area of the first Bessel mode. L is the fibre length. A schematic of the laser set-up used to instigate spectral broadening is shown in Figure 2.15.

The idler generated from the HE-TOPAS which is typically centred at 1750 nm with 1 mJ pulse energy and a 40 fs duration. This beam is focused into a hollow core fibre that is 400 μm in diameter and 1 m long. The fibre can be evacuated or filled with argon or neon up to a maximum pressure of 2 bar. As seen in section 2.2.2 where self-phase modulation is described, broadening is a linear function of n_2 and I. Argon

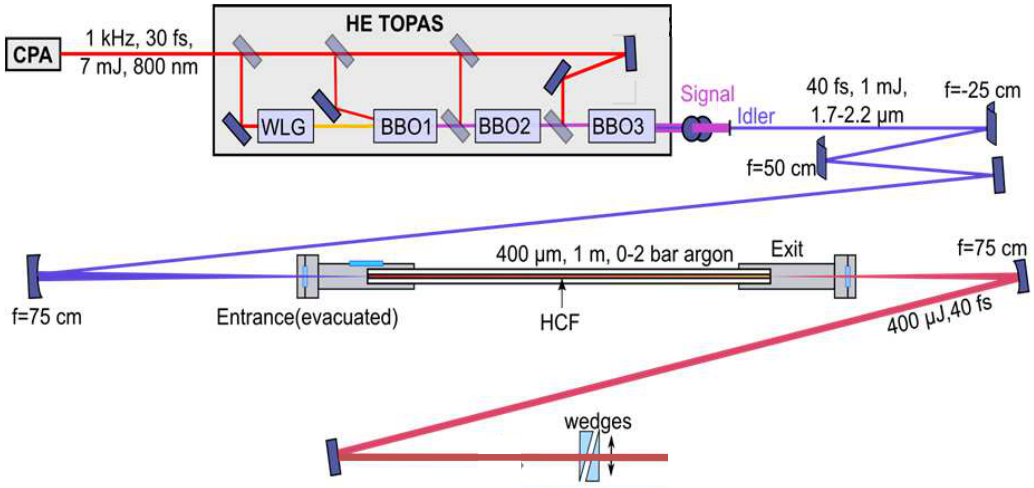


Figure 2.15: Layout of the spectral broadening beam line including the main components and stages of the HE−TOPAS OP−CPA NIR wavelength generation system and the hollow core fibre. The WLG (white light generation stage) produces the white light continuum. From [107]. HCF is the hollow core fibre.

is used by those who have a low intensity available as it has a high n_2 value and a low ionisation potential of 15.6 eV. Neon is better used when the incident beam of a high intensity as it has a smaller value of n_2 which is compensated by a higher ionisation potential of 21.6 eV.

There is a limit to the maximum intensity that can be used in the spectral broadening process. If the intensity exceeds that of the ionisation saturation intensity of the medium this will cause significant free electron dispersion. This will distort the pulse such that the chirp will not be linear and thus very difficult to compensate for at the output of the hollow core fibre.

The fibre can either be statically filled or differentially pumped. There are entrance and exit tubes on the fibre where a dry scroll pump can be used to evacuate the fibre or to fill the fibre with gas. For a statically filled fibre both the pump is isolated and both the entrance and exit tubes are filled with gas. If a fibre is statically filled

with gas, a plasma can form at the entrance of the fibre if the focusing is quite tight and this can cause defocusing, which reduces the coupling efficiency, and can cause potential damage to the fibre.

The fibre can also be differentially pumped - as is the case for the fibre used in this PhD. The entrance tube is evacuated to $\approx 10^{-1}$ mbar whilst the exit tube is filled with gas, up to 2 bar. Figure 2.16 below shows the spectrum of the idler, centred at 1700 nm, starting at 0 bar before the fibre is filled with argon at increments of 0.2 bar. The spectral broadening is evident, the shape of the broadened spectrum presents modulations which are characteristic of the self phase modulation process.

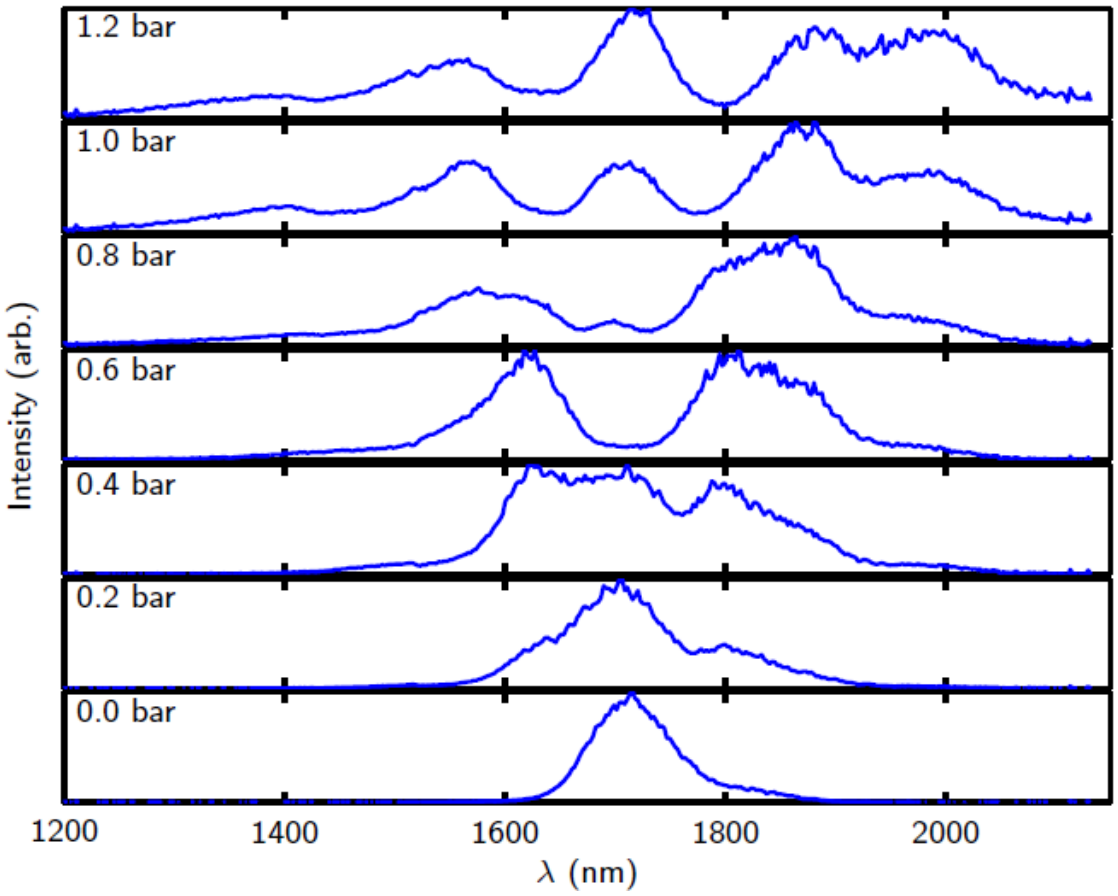


Figure 2.16: Broadened spectra as a function of pressure of argon in the hollow core fibre.

At the fibre exit the beam is collimated using a concave mirror and is directed towards chirp compensation optics. Chirped mirrors are commonly used for chirp compensated for an 800 nm broadened spectrum. In the case of the idler wavelengths of

interest to this thesis, the pulses are compressed in time by exploiting the anomalous dispersion provided by fused silica wedges. Bulk material like fused silica provides negative group velocity dispersion (GVD) in the idler spectral range of 1600 - 2200 nm. In this scheme, sub-two cycle pulses at 1800 nm have been achieved.

The hollow core fibre was not used for generating intense, few cycle, IR laser pulses in this thesis. In this thesis, the evacuated hollow core fibre was used for the purpose of mode cleaning. The beam profile of the idler tends to exhibit distortions in its intensity and phase profile which are often caused by scattering from optical defects or particles in the air. The beam is focused into the fibre by the $f = 75$ cm mirror into the 400 μm diameter fibre and is recollimated by a second concave mirror at the fibre output as shown in Figure. As a result of the beam propagating through the spatial filter, higher order transverse electromagnetic (TEM) modes are suppressed and the emergent beam has a higher beam quality represented by an M^2 value closer to unity. In essence, the spatial filter involves focusing the beam, thus producing an image of the input beam, with all of the imperfections in the beam profile defocused in an annulus about the axis. The fibre diameter acts as a pinhole to block the majority of the high spatial frequency intensity components of the beam which, if propagated could cause damage to the optics in the beamline to the chamber and can compromise the resolution in the HHG data which needs to be very clean for the experiments discussed in this thesis.

2.7.3 NIR pulse characterisation methods

SEA−SPIDER (Spatially Encoded Arrangement- Spectral Phase Interferometry for Direct Electric field Reconstruction) [109] was implemented for the pulse characterization for the first two years of this PhD and will be briefly described here before the currently implemented technology, frequency resolved optical gating (FROG) is discussed. This technique poses a number of advantages over conventional SPIDER [110]. There is no phase distortion introduced to the pulse to be measured prior to up conversion. Instead of the conventional SPIDER technique of mixing two time delayed replica with an ancillary chirped pulse, the pulse to be measured is sent directly into the crystal with two delayed ancillas to end up with the two sheared and delayed replica. A schematic of the SEA−SPIDER as implemented in the laboratory is shown in Figure 2.17.

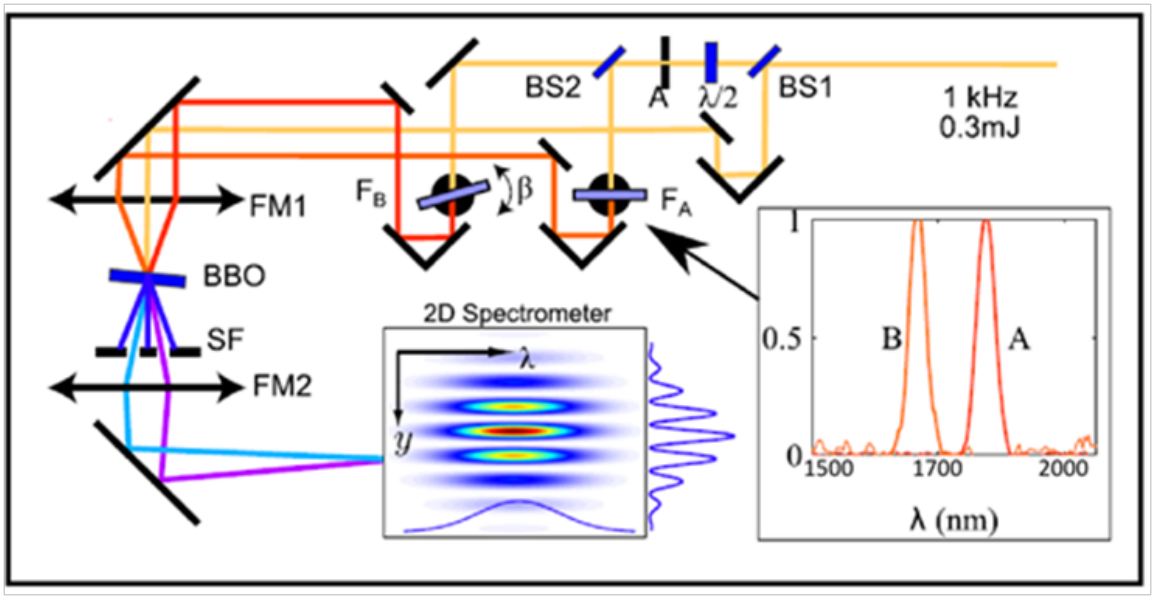


Figure 2.17: Concept of the mid-IR SPIDER apparatus. Adopted from [111]

Within the SEA−SPIDER pulse reconstruction lies another advantage of the design in the sense that the spectral phase and amplitude are reconstructed for every position y along the vertical axis. This means that complex distortions such as pulse front tilt and spatial chirp can be measured [90]. The SEA-SPIDER trace (as described by

equation 2.25) is also very easy to interpret as shown in Figure 2.18, a tilt of the fringes corresponds to a $\varphi_0^{(2)}$ phase term, which can be interpreted as chirp from the Taylor expansion, this corresponding increase in pulse duration can usually be corrected by adjusting the translation of one of the compressor gratings in the CPA laser system whilst monitoring the phase on the interferogram until it is flat. Curvature of the spatial fringes is introduced by the $\varphi_0^{(3)}$ term and can be understood as cubic phase which manifests itself as pre or post pulses in the temporal domain. The tilt of the compressor gratings can usually be corrected for this distortion. For a pulse with a field defined by $E(y,t) = \int_{-\infty}^{+\infty} A(y,\omega)\exp[i\phi(y,\omega) - i\omega t]dt$ where $A(y,\omega)$ and $\phi(y,\omega)$ are the spectral and amplitude of the pulse respectively and y is the vertical spatial co-ordinate, the SEA-SPIDER trace is given by:

$$\begin{aligned} S(y,\omega) = \quad & |E(y,\omega)|^2 + |E(y,\omega-\Omega)|^2 + 2|E(y,\omega)|\,|E(y,\omega-\Omega)| \\ & \times \cos\left[\phi(y,\omega) - \phi(y,\omega-\Omega) + \Delta k y\right] \end{aligned} \tag{2.25}$$

where Ω is the spectral shear, Δk is the difference of the two wavevectors arising from the angle between the two signal beams. The complete temporal field $E(y,t)$ can be reconstructed from $S(y,\omega)$ for every spatial position y_i leading to a spatially resolved single shot characterization of the pulse.

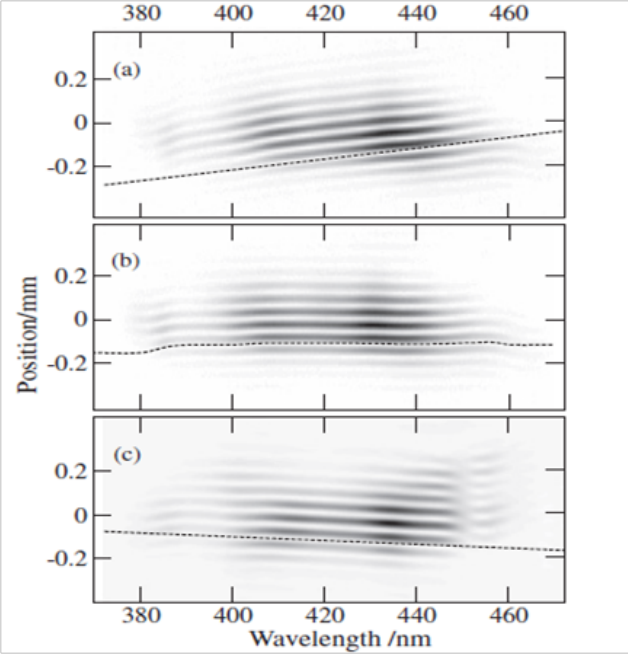


Figure 2.18: SEA-SPIDER traces from a femtolasers oscillator (a) for a positive $\varphi_0^{(2)}$, (b) for a recompressed pulse and (c) for a negative chirp. The small wiggles in (b) are indicative of residual higher order phase terms. Taken from [90]

Figure 2.19 is an example of a SEA-SPIDER trace recorded in the laboratory for the 1.7 μm wavelength idler pulse that was used for the preliminary experiments in this thesis. The pulse to be measured is the idler output of the TOPAS which has $\approx$ 40 fs duration, 1.4 mJ energy per pulse and is centred at 1700 nm.

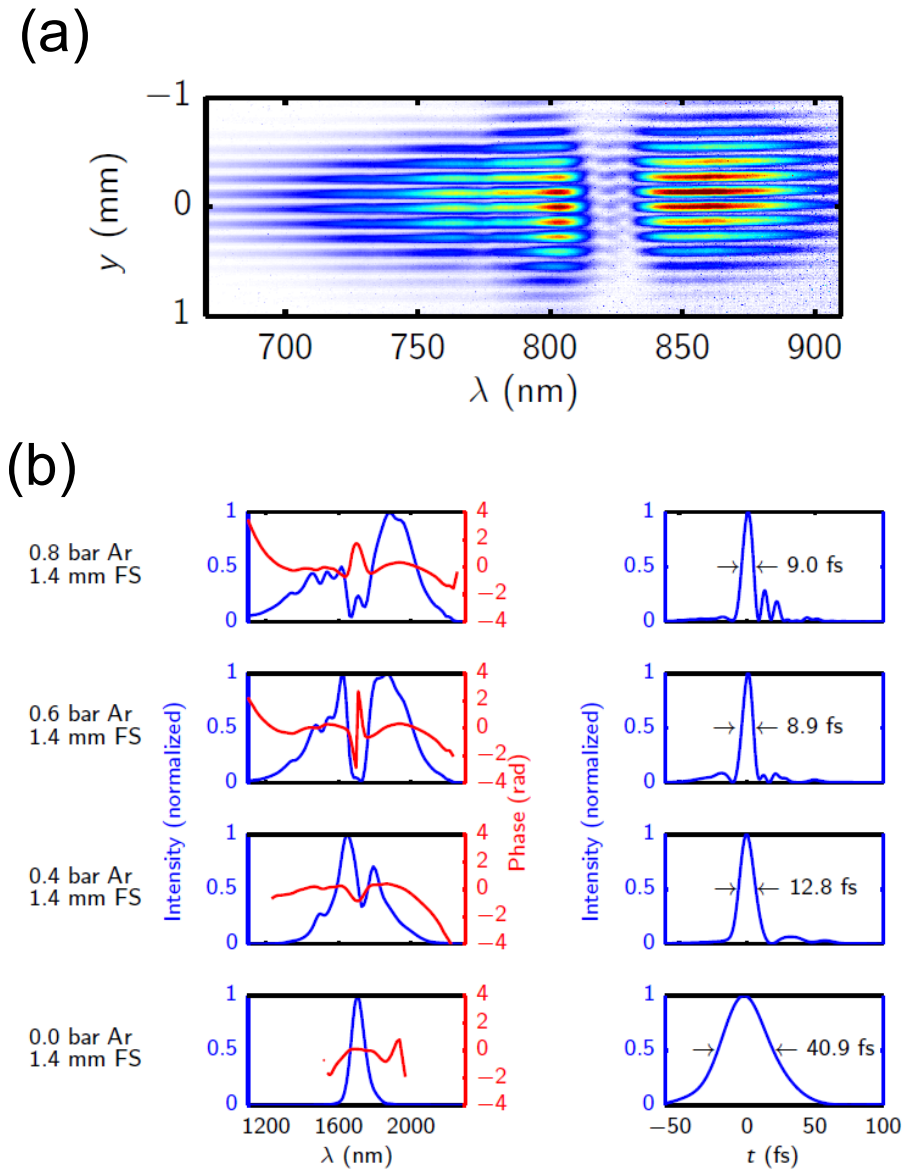


Figure 2.19: (a) SEA-SPIDER fringes across a 1D slice of the pulse (spectrometer slit) generated from the upconversion of the test pulse with two spatially chirped pulses (ancillas). (b) Temporal profiles of pulses characterized by the SEA-SPIDER. Traces are shown as a function of argon pressure in a hollow core fibre to illustrate the generating of shorter pulses by self phase modulation in the fibre. 1.4 mm of fused silica is used for the temporal compression of the pulse. Images courtesy of Dr. Dane Austin.

2.7.4 Frequency Resolved Optical Gating

Although the SEA−SPIDER is a very intuitive pulse characterisation device, it was found to be very time consuming to operate. In 2014, Dr. Dane Austin constructed a single shot SHG FROG [112] which has been implemented to characterise the majority of the NIR pulses that were used in the experiments whose results are presented in chapter 6.

Autocorrelation is a very widely used incomplete characterisation method. It provides an estimate of the pulse duration but a limited insight into the structure of the pulse to measured [90]. In a simple SHG autocorrelator the pulse to be measured is split into two identical replicas in a Michelson interferometer with a relative delay, τ. Both replicas are focused into an SHG crystal at an angle, θ, where they are spatially and temporally overlapped. The angle of incidence of the pulses determines the scaling of the mapping between time and space:

$$x = \frac{c\tau}{2sin(\theta/2)} \tag{2.26}$$

where c is the speed of light, τ is the delay between the two replicas and θ is the angle between the two replicas. The intensity of the SHG signal is then recorded as a function of delay − better overlap results in a higher SHG signal. The SHG in the crystal contains three contributions:

- The upconversion of the first replica with itself, *E(t)*
- The upconversion of the second replica, *E(t-τ)*, with itself
- A cross−term between both replicas

Each of the contributing terms exits the crystal at a different angle with the cross−term being on axis. A spatial filter is used to select this component onto a slow photodiode. The electric field on the photodiode is given by:

$$E_2(t,\tau) \propto E(t)E(t-\tau) \tag{2.27}$$

The response of the photodiode is assumed to be much slower than the pulse duration such that the electric signal is proportional to the integrated intensity of $E_2(t,\tau)$:

$$S(\tau) \propto \int |E_2(t,\tau)|^2 \, dt \propto \int I(t)I(t-\tau)dt \tag{2.28}$$

This can be described as an *intensimetric autocorrelator* [90] which allows one to make a measurement of the intensity envelope of the test pulse. It is also background free in the sense that the signal goes back to zero when the two replicas are not overlapping. To make an estimate of the pulse duration however requires an assumption to be made on the pulse profile. This is included by a deconvolution factor relating the spatial width of the signal, Δx to the pulse duration Δt such that $\Delta t = \Delta x/k$ where, for example, k is 1.41 for a Gaussian shaped pulse.

An *interferometric autocorrelator* [90] can give some insight to the pulse spectrum. This differs from the intensimetric autocorrelator as the pulse replicas are focused collinearly in the second harmonic crystal. The second harmonic signal is now given by:

$$S(\tau) \propto \int |E(t) + E(t-\tau)|^4 \, dt \tag{2.29}$$

which is recorded as a function of delay and produces a signal that has a width related to the pulse duration and is modulated with a period of $2\pi/\omega_0$. This is because the interferometric signal exhibits fast oscillations which correspond to the beating between different terms of the SHG process. For a transform limited pulse these modulations are strong with a characteristic shape which is washed out when a pulse is strongly chirped.

Due to the fact that autocorrelators are insensitive to pulse intensity and phase structure in a pulse they are not reliable for the accurate measurement of ultrashrot pulses. A full self−referenced characterisation based on autocorrelation can be performed by frequency resolved optical gating (FROG). FROG involves measuring a spectrally resolved autocorrelation which provides a spectrogram of the pulse. A phase retrieval algorithm can be implemented to recover the pulse intensity and phase of the subject.

There are many variations of FROG but here the discussion shall be limited to the familiar technology of the SHG FROG.

SHG FROG

The idea of FROG is to temporally slice (gate) the pulse, $E(t)$, and to measure the spectrum of this gated pulse as a function of delay between the gate, $G(t)$ and the test pulse as shown in Figure 2.20.

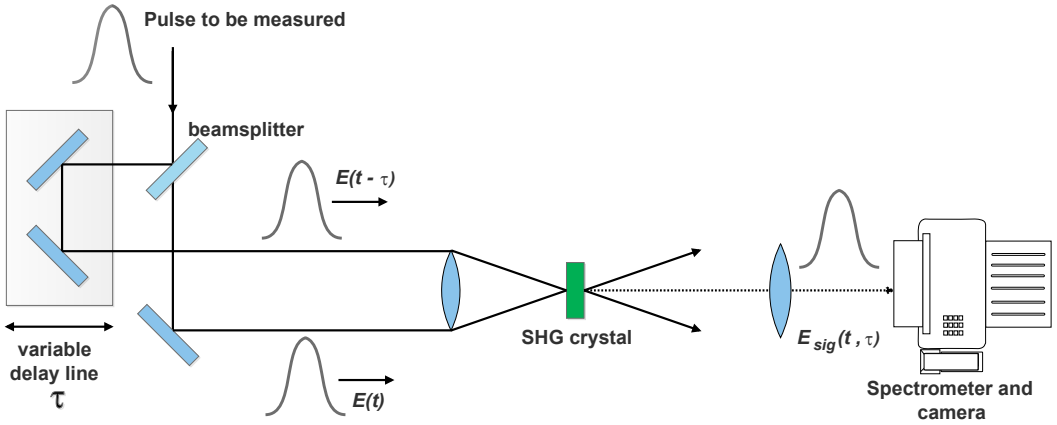


Figure 2.20: Typical layout of a second harmonic generation FROG (SHG FROG). Adapted from [105]

The 2D FROG signal is given by:

$$S(\tau,\omega) \propto \left| \int E(t)G(t-\tau)e^{i\omega t}dt \right|^2 \tag{2.30}$$

where $E(t)$ is the electric field of the pulse and $G(t-\tau)$ is the intensity dependent gate which, in the case of SHG FROG is given by $G(t-\tau) = E(t-\tau)$ such that gate is just a time delayed replica of the test pulse. The SHG signal field is proportional to the product of the electric field of the pulse and that of the delayed pulse. The spectrum of the SHG field is measured for each delay position, τ which generates the FROG spectrogram which is the optical intensity as a function of frequency, ω and delay, τ. As shown in Figure 2.20, the SHG FROG is extremely easy to implement and is akin to a intensimetric autocorrelator with the photodiode replaced by a spectrometer. An iterative algorithm, which shall not be discussed in detail, is

implemented to retrieve the spectral phase and amplitude of the subject pulse. The algorithm basically reconstructs the original pulse by minimising the error between the measured FROG trace and the trace generated by the reconstructed pulse. An example of a FROG trace taken in the laboratory is shown in Figure 2.21.

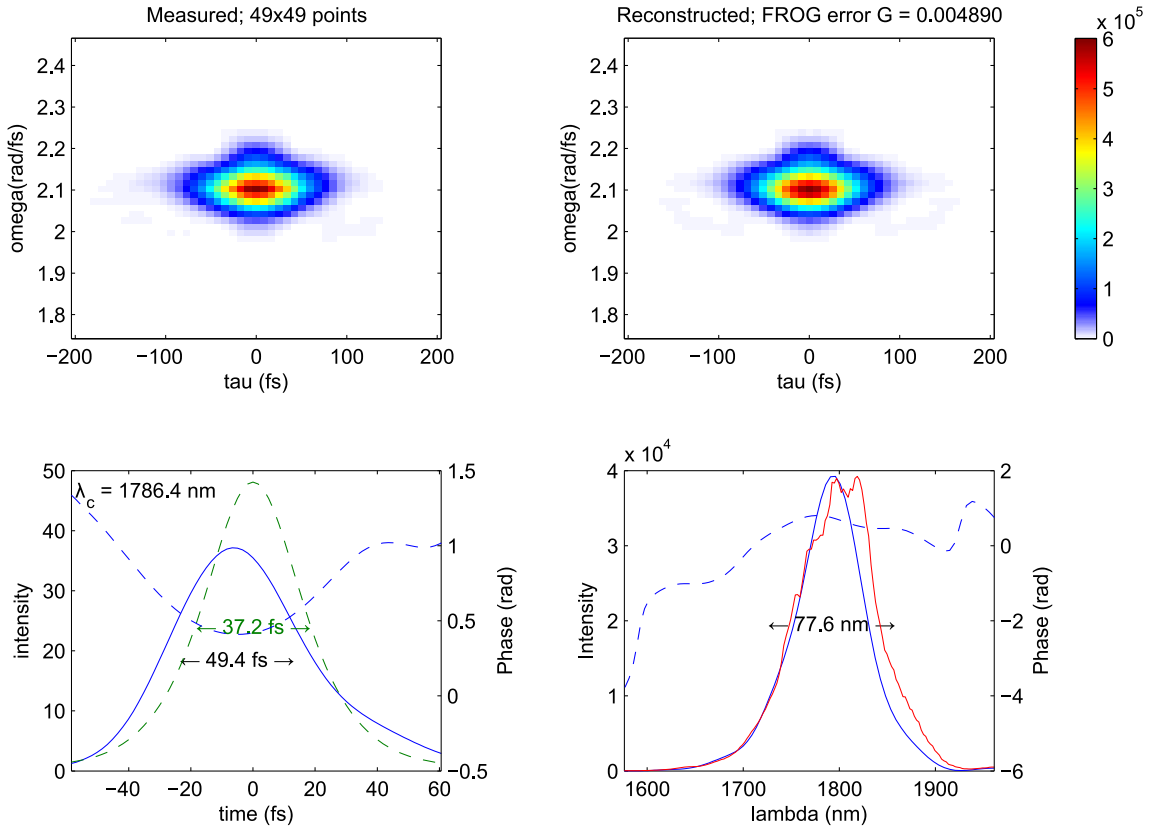


Figure 2.21: Measured and reconstructed FROG traces acquired using the SHG FROG constructed in our laboratory. Measured FROG trace (*top left*), reconstructed FROG trace (*top right*), retrieved pulse shape (green dashed line) and phase (dashed blue line) (*bottom left*), retrieved power spectrum (blue solid line), and phase (dashed blue line) and independently measured spectrum (red line) (*bottom right*). Courtesy of Dr. Dane Austin

Chapter 3

HHG Spectroscopy

HHG Spectroscopy is a rapidly advancing field for probing the ultrafast electronic and nuclear dynamics in molecules with exquisite temporal resolution on an attosecond timescale and Angstrom spatial resolution. HHG Spectroscopy has already been applied to an abundance of hydrocarbons [113] [114] [115]. Studies have also recently been performed on molecular isomers [116]. In this chapter I shall discuss the capabilities of HHG spectroscopy in terms of the nature of the dynamics and structural information that can be gained about a molecule. I will finish each subsection with a comment on what information we propose we can gain from HHG spectroscopy on benzene and substituted benzene molecules.

3.1 Molecular alignment

The previous sections of this thesis have instilled an appreciation for the complexity of molecular structure in the reader. Hence it is of great importance to have the ability to control the molecular axis with respect to the electric field of the laser.
As was discussed previously, the rigid rotor treatment can be applied to molecules to determine its rotational energy. In this case we can envision the molecular bonds as rigid rods and the molecule as a rigid rotor. It has already been shown that the quantised rotational energy is given by: $E_r = \frac{\hbar^2}{2I}J(J+1)$. It is more common to employ the rotational constant B (units of cm^{-1}) in this expression such that $E_r = BhcJ(J+1)$ where $B = \frac{h}{8\pi^2 cI}$. The rotational period of the molecule is an important parameter in molecular alignment. The evolution of the rotational part of the rotors wavefunction is given by $\Psi \propto e^{i\frac{E}{\hbar}t}$ and hence the period of evolution is $T_{rot} = \frac{h}{I}$. For the first

rotationally excited state we have J = 1 so we can deduce that the rotational energy is $E_{R,J=1} = 2Bhc$ which results in a rotational period of $T_{rot} = \frac{1}{2Bc}$. Rotational revivals are only a feature of impulsive alignment which will be discussed as this section progresses.

The degree of alignment is quoted in terms of $\langle cos^2(\theta)\rangle$, where θ is the angle between the electric field of the laser and the molecular axis. Perfect alignment along the direction of the laser field would yield $\langle cos^2(\theta)\rangle = 1$ whilst anti-alignment wherein the molecules are perfectly aligned in the plane perpendicular to the laser electric field is described by $\langle cos^2(\theta)\rangle = 0$. An isotropic distribution of angles is given by $\langle cos^2(\theta)\rangle = \frac{1}{3}$.

The expression for the quantised rotational energy of a molecule holds for any coordinate transformation and is true in general. This treatment is also applicable to polyatomic linear molecules as well as symmetric top species. Symmetric top molecules have equal moments of inertia in two axes and can be prolate (the equal moments are larger than that of the third moment) as is the case for allene, or oblate (the moments are smaller than that of the third moment) as for benzene. Symmetric top molecules have an additonal rotational quantum number K which measures the component of $\hat{J}$ along the top (molecular symmetry) axis. Thus, the rotational angular momentum vector $\hat{J}$ has components $\hbar$K along the top axis and $\hbar \mathrm{M}_J$ along the laboratory z axis. This treatment is not applicable to asymmetric top molecules since they have three different moments of inertia. There is no general energy level formula available for an asymmetric top molecule.

3.1.1 Static electric field alignment

One of the first methods to achieve molecular alignment was to apply a static electric field to polar molecules. In this regime, the molecule feels a torque, τ, due to the interaction of the applied D.C field of magnitude E with the dipole moment of the molecule, μ. The magnitude of the torque is given by [117]:

$$\tau = \mu E sin(\theta) \tag{3.1}$$

In the presence of the applied electric field the molecule experiences a torque which leads to the alignment of the molecular axis along the electric field direction. The main disadvantages of this technique are the fact that alignment of the molecules is only realised in the presence of the field, this can be detrimental to some applications especially when effects such as distorting the molecular potential and affecting the continuum electron trajectories are undesirable. Whilst this method of alignment works efficiently for rotationally cool molecules in strong electric fields it is limited in the sense that the strength of the applied field is restricted by the electrical breakdown of the medium.

3.1.2 Laser induced alignment in the adiabatic limit

As mentioned above the restriction of only being able to align polar molecules is a potential problem for those wishing to work with more sophisticated molecules. This can be overcome by applying laser light whose electric field oscillation strength is sufficient to induce a dipole in non-polar molecules. The induced dipole then aligns itself along the direction of the applied electric field vector. If this is achieved in a regime where the laser pulse duration (ns-ps duration), τ_{laser} is longer than the rotational period of the molecule T_{rot} then this is referred to as adiabatic alignment [118].

The interaction potential between the electric field and the dipole induced in the linear molecule is given by [119]:

$$V_{\alpha}(\theta) = -\frac{1}{2}E^2(t)(\alpha_{||}cos^2(\theta) + \alpha_{\perp}sin^2(\theta)) \tag{3.2}$$

In this equation, $E(t)$ is the magnitude of the time varying electric field and θ is the angle between the internuclear axis and the electric field. $\alpha_{||}$ and $\alpha_{\perp}$ are the parallel and perpendicular polarisabilities of the molecule which are define relative to the internuclear axis and θ. Knowing that we can rewrite $E(t)$ as $E(t) = Ecos(\omega t)$ and make the following substitution $sin^2(\theta) = 1 - cos^2(\theta)$ formats the equation for the potential to:

$$V_\alpha(\theta) = -\frac{1}{4}E^2(\alpha_{||} - \alpha_\perp)cos^2(\theta) = -\frac{1}{4}E^2\Delta\alpha cos^2(\theta) \tag{3.3}$$

In this expression, $\Delta\alpha = \alpha_{||} - \alpha_\perp$. For effective alignment it is necessary that a molecule has a large polarisability along one axis and a small polarisability along the perpendicular axis. Since the laser pulse is taken to be longer than that of the rotational period of the molecule this implies that the intensity of the pulse must be kept low enough ($< 10^{13}$ W/cm^2) to prevent ionization of the medium. As was a problem with static field alignment discussed above, the presence of the aligning field can distort other experimental interactions such as distorting the molecular potential and continuum electron trajectories. It has also been experimentally observed that the strength of the applied field and the weight of the molecule determine the timescale for the alignment to occur. For example, applying a 100 fs laser pulse with a peak intensity of 10^{14} W/cm^2 results in hydrogen molecules being fully aligned in that timescale, whilst CO_2 is hardly affected in that time window.

3.1.3 Impulsive alignment

In this regime the laser pulse is of much shorter duration than the rotational period of the molecules. During this short interaction the molecules in the interaction region receive a "kick" from the laser electric field that causes the molecules to rotate. For linear and symmetric top molecules, which have a regular energy level structure, the molecules will align along the direction of the laser field at regular intervals when left to evolve as free rotors. These intervals are known as revival times and correspond to the fundamental period of rotation of the molecule. Alignment which occurs just after the laser pulse is called post-pulse alignment whereas the revivals are seen to occur at fractions of the rotational period of the molecule.

At the time of revival the peak of alignment, which is along the direction of the electric field, is followed by an anti-alignment peak. During this anti-alignment peak all the molecules lie in a plane perpendicular to the electric field - oblate alignment. At half the rotational period, a half revival is evident except it differs from the full revival in the sense that the ordering of the alignment and anti-alignment peaks is reversed. In some cases, quarter and eighth revivals of lesser magnitude are visible. Figure 3.1

shows a half revival obtained in benzene during this PhD. We have achieved molecular alignment of benzene using an 800nm-800nm alignment-generation configuration. The beams were focused using a 30cm focal length mirror onto a thin 100μm gas-jet. The backing pressure for benzene was 1 bar and the nozzle was moved 10 nozzle diameters below the interaction region in order to obtain sufficient cooling for the alignment. The alignment beam was 0.1 mJ and the generation beam was 0.65 mJ after the iris before the chamber entrance which was used to control phase matching in the medium. The harmonic yield is measured at the alignment peak (t = 44.41 ps) and the anti-alignment peak (t = 43.63 ps) of the half revival. As shown in Figure 1.17, the HOMO of benzene can be treated as a p orbital on each carbon nucleus perpendicular to the plane of the hexagon. The molecular axis is defined as being perpendicular to the plane of the hexagon, in other words in the same direction as the maximum electron density of the π_g HOMO orbital. The harmonic yield is expected to be highest when the molecular axis is aligned along the harmonic probe laser field polarisation direction (alignment peak) and the yield is expected to decrease to a minimum when the molecular axis is perpendicular to the laser field polarisation (anti-alignment) peak.

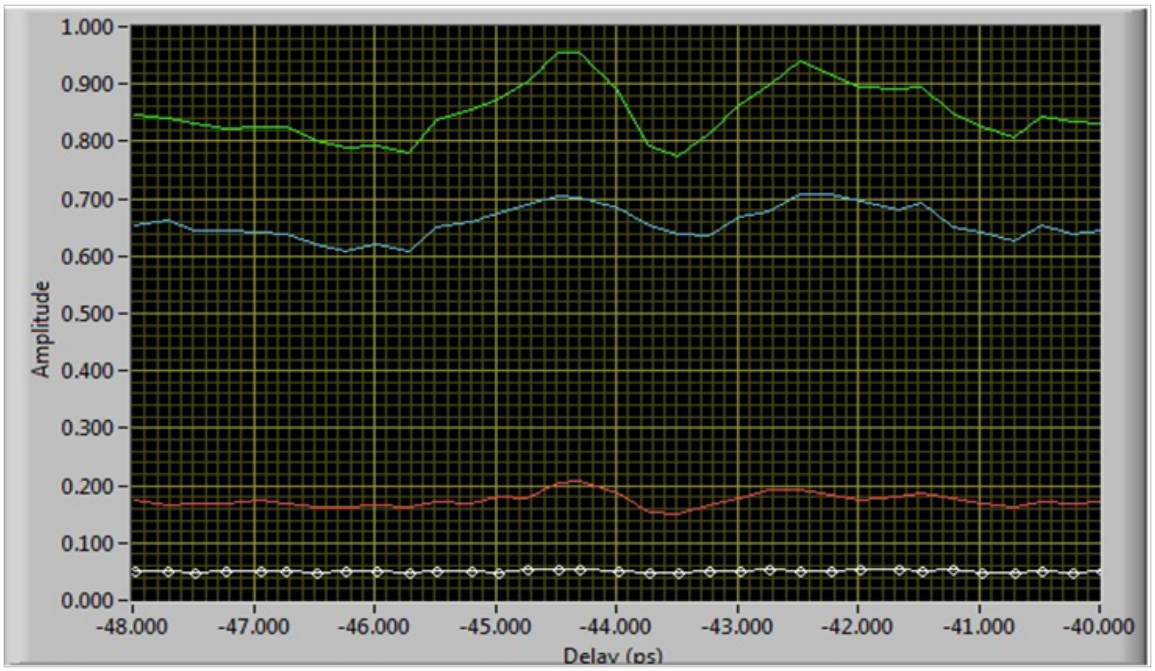


Figure 3.1: Half revival obtained in benzene using an 800 nm-800 nm alignment-generation collinear interferometer. The gas jet was placed ten nozzle diameters (of 100 μm) below the interaction region. The green curve is the 17th harmonic of the 800nm generating field, the blue is the 19th harmonic and the red and white curves are the integration over the 21st and 23rd harmonics respectively.

Impulsive alignment can only be explained by quantum mechanics with respect to the population of the J levels. The laser pulse kicks the molecules and places them in a superposition of rotational states through Raman like transitions [118]. The interaction can be described by the following equation [119]:

$$|\psi_{J_0 M_0}(\theta, \phi, t)\rangle = \sum_{J \geq |M_0|} F_{J_0,J}(t) Y_J^{M_0}(\theta, \phi) e^{(-i\frac{B}{\hbar}J(J+1)t)} \tag{3.4}$$

In this equation, $\psi_{J_0 M_0}$ denotes the original states, $F_{J_0,J}(t)$ is the complex coefficient associated with the transition from each rotational state, J is the angular quantum number, M is the projection of J on the z axis and the subscript 0 denotes the state before the laser-molecule interaction has taken place. The above relationship can be concluded from the following analysis. Assuming that the laser is far from resonance with any electronic transition in a molecule, the molecule can be rotationally excited

via the absorption of two photons (Raman Excitation) [118].

Reverting back to equation 3.4 it can be deciphered as follows: The $Y_J^{M_0}(\theta,\phi)$ terms are the eigenfunctions of $\vec{J}^2$ and J_z and are known as spherical harmonics. These entities represent the probability of finding an electron at angles (θ,ϕ) in the solid angle $d\Omega$:

$$\left|Y_J^{M_0}(\theta,\phi)\right|^2 d\Omega \approx |P_J^{M_0} cos(\theta)|^2 d\Omega \tag{3.5}$$

The $F_{J_0,J}(t)e^{(-i\frac{B}{\hbar}J(J+1)t)}$ term is the hybridization factor which contains the transition matrix element from the initial ground state to the rotationally Raman excited states $J \pm 2n$ where n is an integer. The short interaction time leaves the molecule in a superposition of rotational states that, once the laser pulse has passed, evolve as dictated by the unperturbed Hamiltonian. The moduli of the components of the wavepacket remain constant whilst the phases keep evolving as they would in a field free rotor, that is

$$\phi_J(t) = \phi_J(0) - \frac{E_J t}{\hbar} \tag{3.6}$$

E_J are the eigenvalues of the field free rotor which are given by $E_J = B_0 J(J+1)$ for a rigid rotor. This infers that each element of the wavepacket rotates with a period defined by J causing a periodic dephasing and rephasing at times multiple of the fundamental rotational period. This leads to revivals of the aligned field generated in the interaction with the laser pulse. Note that if the interaction is so strong that the higher J levels are populated then the deformation caused by the centrifugal force in the fast spinning molecules means that the eigenvalues of the field free rotor must be written as [119]:

$$E_J = B_0 J(J+1) - D_0 J^2 (J+1)^2 \tag{3.7}$$

where D_0 is the centrifugal distortion parameter. The onset of this effect serves to break the coherence within the wavepacket which prevents a perfect reconstruction

of the wavepacket. It skews the revivals lowering the degree of alignment until all traces of a revival are diminished after a number of cycles. This effect is only crucial for cases where $\gamma = \frac{kT}{B_0} \geq 300$ [119]. Taking the example of N_2 which has a rotational constant in the ground state level, B_0 of 1.989 cm^{-1}. If we assume $\gamma = 300$ the temperature can be calculated to be $\approx$ 800K which is well outside the catchment of temperatures we deal with for the experiments concerned here.

The two main factors governing the degree of alignment are the strength of the aligning field and the number of rotational states populated at the interaction time. The strength of the field, the intensity, is limited by the ionization threshold of the sample - the fact that it is unfavourable to generate harmonics with the aligning field as this skews the signal generated. The population of the states can be kept to a minimum by using cold molecules. This can be achieved via rotational cooling, which will be discussed in the next section.

3.1.4 Rotational cooling

Rotational cooling is produced by the supersonic expansion of a gas from a high pressure region to a low pressure region. The key concept behind rotational cooling is that the molecules transfer some of their rotational energy to translational energy through collisions with other molecules. The regime of interest for this PhD is the application of nozzle expansions wherein the nozzle diameter is much larger than the mean free path of the gas molecules. In this regime there will be many collisions amongst the molecules in the vicinity of the jet orifice.
As the gas propagates supersonically the collisions the molecules have with the background gas molecules establish a shock wave around the flow. This shock wave protects the beam from intrusions by warm, background gas molecules. The boundaries of this shock wave are referred to as barrel shock which extends outwards from the jet orifice to the Mach disk which is the disc shaped area perpendicular to the flow direction. The gas expansion occurs at a velocity higher than the sound velocity in the medium in the zone of silence region. This zone of silence can extend in length according to the equation:

$$x_M = 0.67D\sqrt{\frac{p_0}{p_b}} \tag{3.8}$$

where x_M is the location of the Mach disc, D is the nozzle diameter and p_0 and p_b are the source and background pressures respectively. In this region the further the molecules travel from the nozzle the lower the temperature will be, however this desirable trait is met with a lower particle density - both a low rotational temperature and a high particle density are required for HHG experiments incorporating molecular alignment [120].

Achieving low temperatures requires large values of the pressure diameter product which implies a large gas jet diameter and a large backing pressure value. Note that the mass throughput from the nozzle is given by p_0D^2 so ultimately it will be the pumping capacity of the vacuum chamber system that sets the upper limit on this. If you back the gas jet with too high a pressure then you risk causing damage to the spectrometer elements as will be discussed in Chapter 4. It also puts undue strain on the pumping system which results in overheating and an increased risk of system failure. Implementing a pulsed gas jet will inevitably allow a higher amount of gas to be dumped into the chamber since it is only open for a certain period as opposed to the continuous flow designs which constantly dump gas into the chamber. It is important to note that in order for a supersonic expansion to develop the pulsed valve must be open for a time of [120]:

$$\Delta t \geq \frac{4D}{a_0} \tag{3.9}$$

where a_0 is the speed of the sound in the reservoir given by $a_0(T) = \sqrt{\frac{\zeta RT}{m}}$ where R is the gas constant and ζ is the ratio $\zeta = \frac{C_p}{C_v}$. In this regime, an ideal gas is assumed. For rare gases such as helium expanding through a 1 mm orifice this inequality implies that the nozzle needs to be open for 4 μs in order for a supersonic expansion to develop.

3.2 Charge coupled nuclear dynamics

The unique properties of HHG enable direct time domain measurements to be made on the electronic structure in molecules which is expected to occur on a timescale in the sub femtosecond to attosecond range. The goal of this work is to develop the theoretical and experimental tools required to understand the mechanisms of charge migration in prototypical molecules such as benzene which is a common building block in a variety of biomolecules. The ability to manipulate the electronic degrees of freedom in a molecule on an attosecond timescale will inevitably pave the way for the advent of attosecond chemistry in which novel methods for controlling chemical processes and dynamics may be developed [121].

The advent of attosecond chemistry also addresses the breakdown of the Born−Oppenheimer approximation [43]. Traditionally, following ionization, the ground and lower lying electronic states of a molecule rely on this approximation to describe the interaction between the electrons and nuclei in the system. Since the nuclei have much larger masses ($> 10^4 m_e$), where m_e is the mass of an electron, the molecules electronic configuration is assumed to adapt instantaneously to the changes in nuclear motion. Potential energy surfaces (PES) describe how the electronic energy depends upon the nuclear configuration which determines the extent of the forces exerted on the nuclei. The Born−Oppenheimer approximation is valid provided that the energy gap between the electronic states is quite large − when the energy gap is of a comparable magnitude to the energy within the nuclear degrees of freedom this approximation loses its validity. Under these conditions, a minor perturbation of the nuclear co-ordinates instigates large alterations to the electronic properties which leads to the nuclear and electronic motion becoming strongly coupled. Light atoms such as hydrogen will move considerably on a femtosecond to sub−femtosecond timescale. Nuclear motion involving light atoms can thus lead to cases where the attosecond electron dynamics are influenced by non Born−Oppenheimer ramifications [121].

Ionization of a molecule by a laser field of sufficient intensity forms a coherent superposition of electronic states which is followed by the migration of charge around the molecule which may last up to a few femtoseconds before nuclear dynamics commence. The *sudden ionization* of an electron populates a series of ionic eigenstates

and creates a hole-like wavepacket that will evolve in time. However, the sudden approximation is generally valid for 90-100 eV XUV ionization from outer/inner valence states with attosecond pulses. For core ionization, the sudden approximation requires keV photons. The Keldysh parameter for the sudden ionization of an outer valence electron can be estimated if we take the an electric field of $E_{max} = 0.01$ a.u. for an XUV laser field and a target $I_p \simeq 11$ eV (0.4 hartrees) using $\gamma = \sqrt{\frac{I_p}{2U_p}}$. For this calculation we get $\gamma \approx 20 - 30$. If we recall than the Keldysh parameter for tunnel ionization is $\gamma << 1$ then we can deduce that within the sudden approximation tunnel ionization can be neglected. This is not an ideal circumstance to be in when trying to compare theoretical calculations with experimental data from HHG but is a fundamental approximation for theoretical chemists to base calculations on.

Following ionization, which initiates the superposition of electronic states evolving in time, the nuclear geometry will also become distorted from its equilibrium configuration such that it must also evolve in time. *Charge migration* occurs when the electronic motion is not coupled to the nuclear motion. Charge migration typically takes place after the ionization of an inner valence shell electron. The positive charge, or hole, created can migrate through the molecule driven by multiple electron effects. Since the electronic motion typically occurs on a femtosecond to sub-femtosecond timescale, the charge migration can be calculated by neglecting nuclear dynamics. This is valid if the time window for the calculations is on a few femtosecond (typically < 5 fs) timescale but nuclear motion must be included to deduce what occurs on longer timescales in the system. Tracking charge migration necessitates the calculation of the *hole density* which is defined as:

$$Q(\vec{r},t) = \left\langle \Psi_0 \left| \hat{\rho}(\vec{r},t) \right| \Psi_0 \right\rangle - \left\langle \Phi_i \left| \hat{\rho}(\vec{r},t) \right| \Phi_i \right\rangle$$

which can be expressed simply as Q($\vec{r}$,t) = ρ_0 ($\vec{r}$,t) - ρ_i ($\vec{r}$,t) where $\hat{\rho}$ is the density operator, $|\Psi_0\rangle$ is the wavefunction for the ground state of the neutral and $|\Phi_i\rangle$ is the wavefunction for the cationic state prepared upon sudden ionization. The electron densities in the ground and cationic states are given by $\rho_0(\mathbf{r})$ and $\rho_i(\mathbf{r},t)$ respectively. Calculations have previously been performed on charge migration in complex biomolecules such as the Tryptophan-terminated tetrapeptide Trp-Leu-Leu-

Leu where Trp and Leu are the amino acids Tryptophon and Leucine respectively. These results predict that a hole generated by the sudden ionization of the HOMO localised on the Trp end of the molecule will migrate to the opposite end of the molecule in ≈ 750 as [122]. The spin density allows one to track the location of the unpaired electron post ionization. Cederbaum *et.al* have also performed calculations on large biomolecules such as PENNA [123].

If the displacement of charge in the molecule is due to changes in the nuclear geometry we term this *charge transfer*. Obviously if the nuclei in a molecule remain fixed such that only the temporal evolution of the wavepacket is permitted then oscillatory charge migration will occur between the two participating states. The coupling of nuclear motion to the electronic motion results in a damping of the electronic motion in the system. Here we shall discuss the rationale behind choosing benzene and the methylated benzenes for the calculations along with the calculation methodology and the predicted dynamics.

Benzene, being a Jahn-Teller molecule [124] [44] will be used as a reference molecule for calculations on electron and nuclear dynamics. The Jahn-Teller theorem states that any molecule in a degenerate electronic state will be subject to an instability due to coupling between nuclear and electronic motion. The benzene cation is a famous example of a system that exhibits this distortion. The benzene cation has a $^2E_{1g}$ ground electronic state configuration in the D_{6h} point group with 3 electrons in the doubly degenerate orbital. The degeneracy is removed by Jahn-Teller distortion of the molecular framework to a lower symmetry.

In essence what happens is the benzene cation loses its degeneracy upon distortion along one of two vibrational co-ordinates in the branching space. X_1 is the *gradient difference* co-ordinate and connects the quinoid/anti-quinoid forms of the molecule. As shown in Figure 3.2, the moat of the conical intersection contains the minimum (Min) which is also known as the quinoid structure. Similarly, the transition state (TS) labelled structures are also known as anti-quioinds. X_2 is the *interstate coupling* vector which moves one quinoid (or anti-quinoid) structure to an anti-quinoid (or quinoid) structure which is rotated 60° relative to the previous structure. This behaviour is depicted in Figure 3.2. The neutral geometry D_{6h} is reduced to a lower

symmetry point group, either D_{2h} or C_{2h} depending on which vibrational co-ordinate is chosen. There will be three pairs of quinoid and anti-quinoid structures, one pair for each of the $C_2^{"}$ axes of the molecule. The adiabatic potential energy surface (APES) of the two states becomes a surface of revolution (the "Mexican hat") when plotted versus the two coordinates that lift the degeneracy present at the D_{6h} geometry. The quinoid structures are termed minima on the APES whereas the anti-quinoids are labelled as "transition states". The degeneracy point becomes a conical intersection.

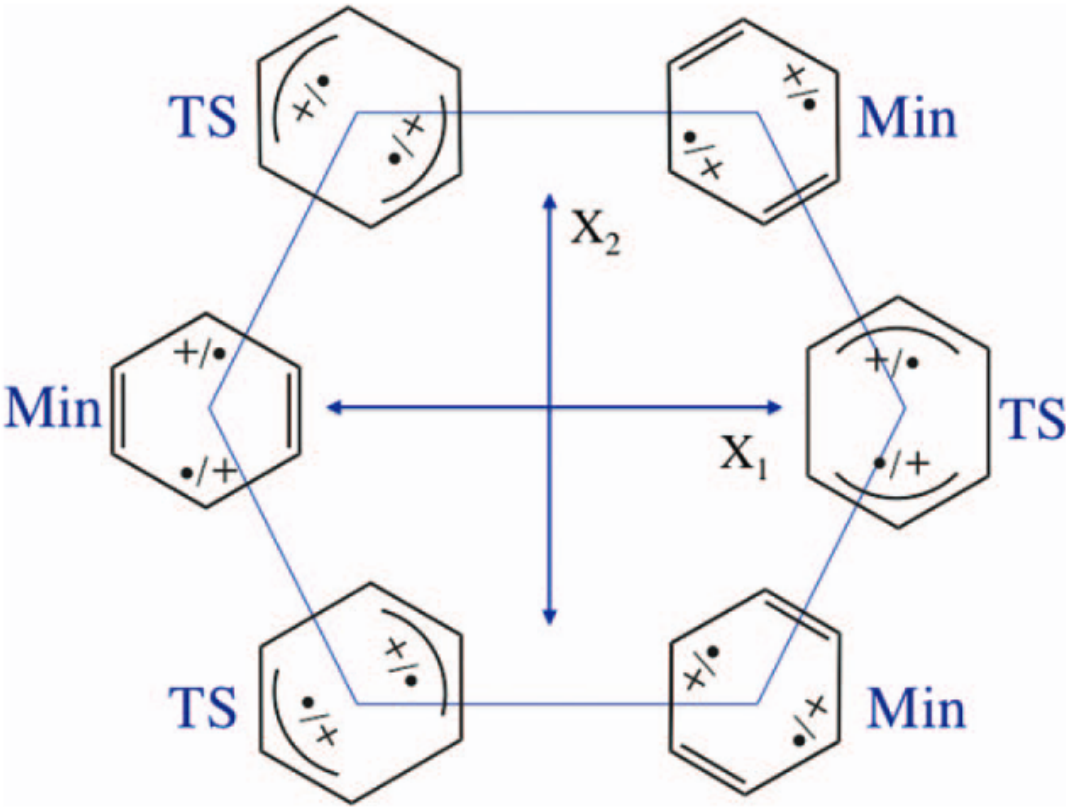


Figure 3.2: Resonance structures of the benzene radical cation. The directions X_1 and X_2 are the gradient difference and the gradient of the inter-state coupling vector respectively. [125]

The calculations performed by Vacher *et.al* [125] are based on the Ehrenfest-CASSCF approach. In the Ehrenfest approach, nuclear motion is described by classical mechanics following a trajectory. Electronic motion is described quantum mechanically by a time dependent wavefunction which satisfies the time-dependent Schrödinger

equation:

$$i\frac{\partial\Psi(t)}{\partial t} = \hat{H}\Psi(t) \tag{3.10}$$

As discussed in section 1.7.3 the real wavefunction of a system is often too complex to be directly found, so it is necessary to approximate it by a simpler wavefunction which means it is possible to then solve the Schrödinger equation numerically. The self-consistent field method (SCF) is an iterative method which involves firstly making an initial guess of the initial molecular orbital coefficients $\phi(r)$ using either Slater type orbitals (STOs) or Gaussian type orbitals (GTOs). This is then used to approximate the Hamiltonian and thus solve the linear Schrödinger equation to obtain a more accurate set of orbitals, $\phi_{improved}(r)$. These steps are repeated by resetting $\phi(r) = \phi_{improved}(r)$ after each calculation until the results converge and a self consistent wavefunction is obtained [47].
The electronic wavefunction is expanded in terms of a set of eigenstates of the electronic Hamiltonian with energies at fixed nuclear geometries. Once the initial wavefunction at time t_0 is defined, the time-dependent wavefunction at time t_n can be expressed as:

$$\Psi(t, q; Q(t)) = \exp\left[\frac{-i}{\hbar}Ht\right]\Psi(t_0, q, Q(t)) \tag{3.11}$$

where q denotes the electronic co-ordinates and $Q(t)$ are the nuclear co-ordinates. The electronic Hamiltonian is parametrized by Q(t) and varies slowly on the timescale $\tau = t - t_0$. After each electronic timestep, the nuclear positions are updated following Newtons equations of motion. The corresponding potential energy function for the classical nuclear degrees of freedom is defined as the expectation value of the electronic Hamiltonian.

An example of the dynamics that can be extracted from C_6H_6 which we propose to detect experimentally is the charge migration and charge transfer whilst the nuclei are moving. The spin density oscillates between the quinoid and anti-quinoid resonance structures around the moat successively as shown in Figures 3.3 and 3.4 for stationary and moving nuclei respectively. It is evident in the simulation that after 2 fs the effect of nuclear motion cannot be neglected.

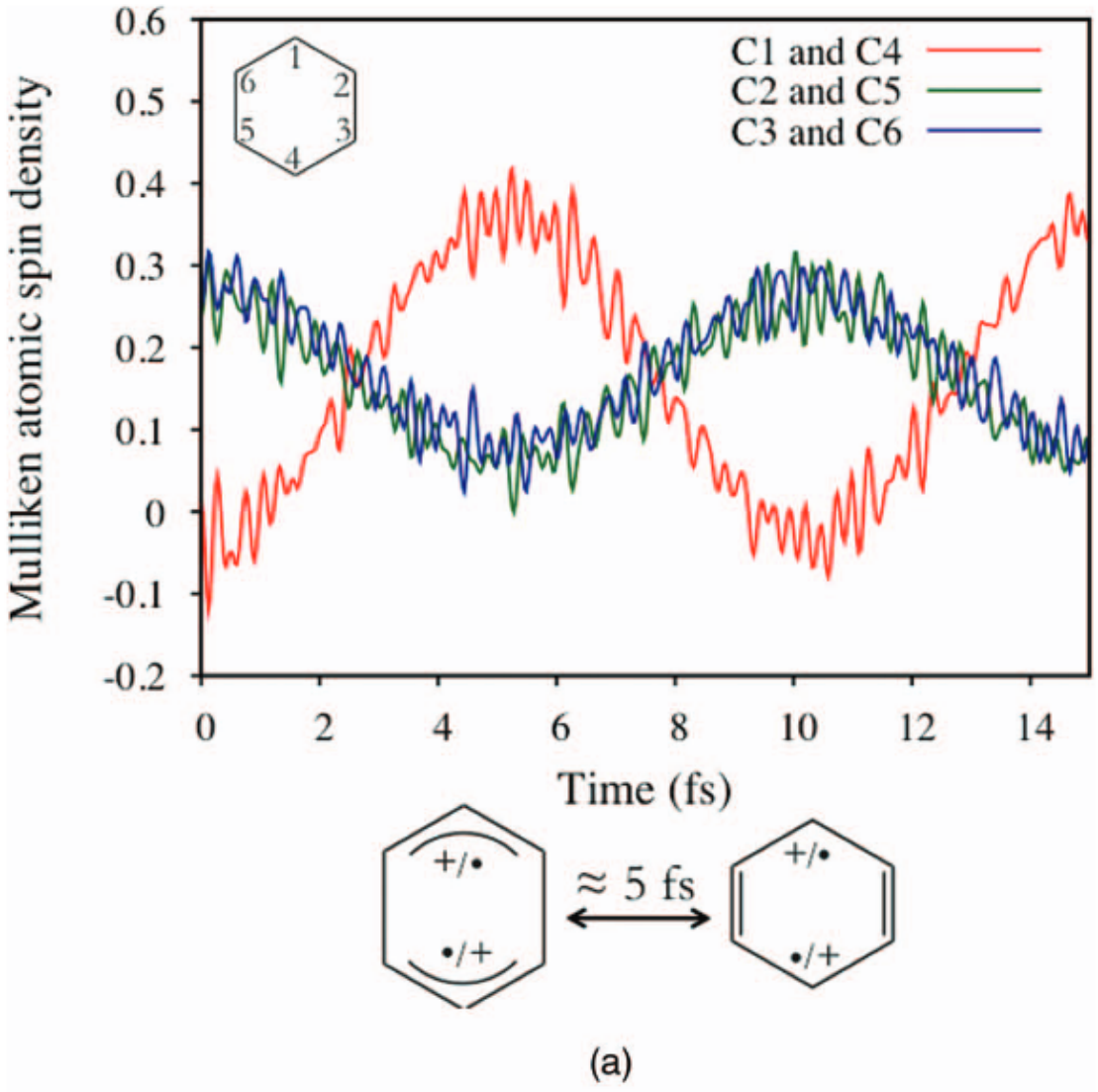


Figure 3.3: Simulation of the charge migration and charge transfer for the benzene radical cation with fixed nuclei [125]

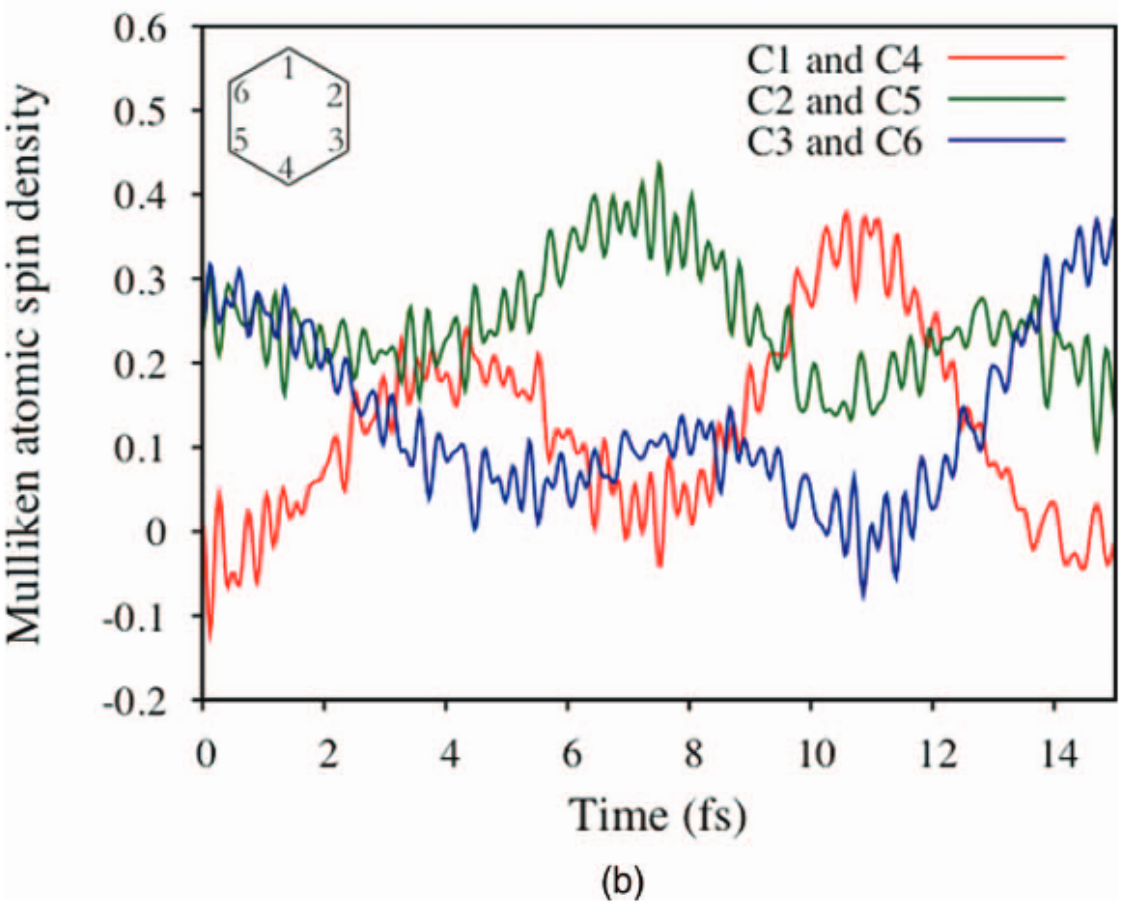


Figure 3.4: Simulation of the charge migration and charge transfer for the benzene radical cation when nuclear motion is allowed. [125]

Adding methyl substitutions to the benzene ring lifts the Jahn-Teller degeneracy of the HOMO and HOMO-1 without significantly perturbing the electronic structure. Further calculations by Vacher *et.al* performed as part of the collaboration with the Theoretical Chemistry group at Imperial College have been done on toluene and para-xylene using the Ehrenfest-CASSCF method described above [126]. These molecules are expected to exhibit considerably faster oscillations due to the larger energy gaps between the first two eigenstates of the cation. In Figure 3.5, for the case of benzene with fixed nuclei there are no oscillations produced. This is due to the degeneracy of the molecule - because the eigenstates are degenerate the electronic superposition is propagated in time but no phase factors are included due the degeneracy of the participating states. Since the energy gap is 0 eV, this indicates that the oscillation

period is infinite.

On the right panel of Figure 3.5, the same calculation as in the left panel is shown but with the nuclei moving. There is no significant change in the first 15 fs after ionization which is similar to the case where the nuclei are fixed. However, on a longer timescale it is expected that charge transfer will manifest as a consequence of the Born-Oppenheimer approximation.

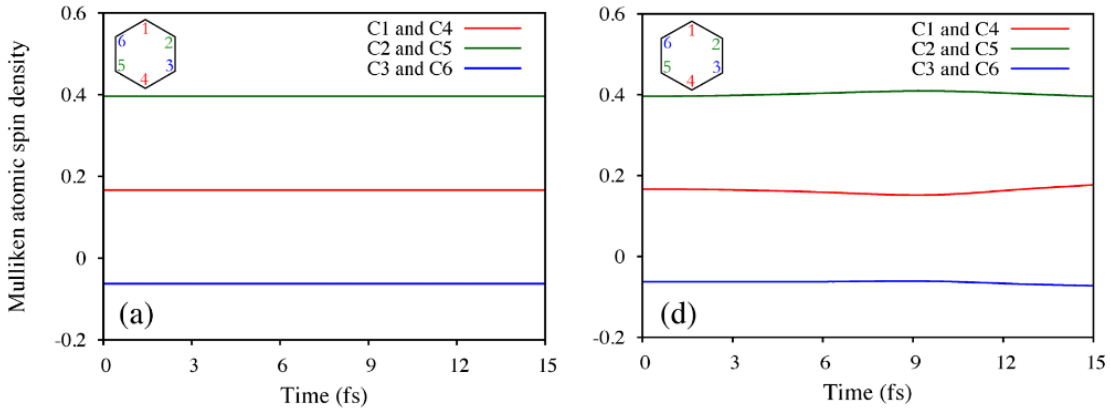


Figure 3.5: Spin densities partitioned on carbon atoms as a function of time after ionization. Calculation has been performed for benzene with fixed nuclei (left) and moving nuclei (right) [126]

In Figure 3.6 the calculations for toluene with fixed nuclei are shown and then with nuclear motion included. For the case with fixed nuclei oscillations of the spin densities partitioned on opposite carbons oscillate with a period of ≈ 20 fs. This is directly related to the energy gap between the eigenstates at this geometry. The calculations used an energy gap of 0.21 eV between the ground and first excited states of the cation at equilibrium geometry of the neutral. Unlike benzene, the addition of the methyl group has broken the symmetry of the molecule such that the spin densities on opposite carbon atoms is no longer the same. When nuclear motion is coupled, as shown on the right panel of Figure 3.6, the evolution of the spin densities is identical to that of the case with fixed nuclei for the first 2-3 fs post ionization. The spin density does exhibit an oscillatory behaviour but this is not perfectly sinusoidal.

As discussed in the case of non Born-Oppenheimer dynamics, a difference in the spin density oscillations between the fixed and moving nuclei scenarios is an indication of

the strong interaction between the electronic and nuclear degrees of freedom. This can be explained further in terms of the nuclear motion evolution. As the nuclear trajectory moves away from the conical intersection it gains a component along the X_2 gradient of the interstate coupling, such that it moves towards geometries where the energy gap between the ground and first excited states gets larger. This speeds up the the period of spin density oscillations between opposite carbon atoms.

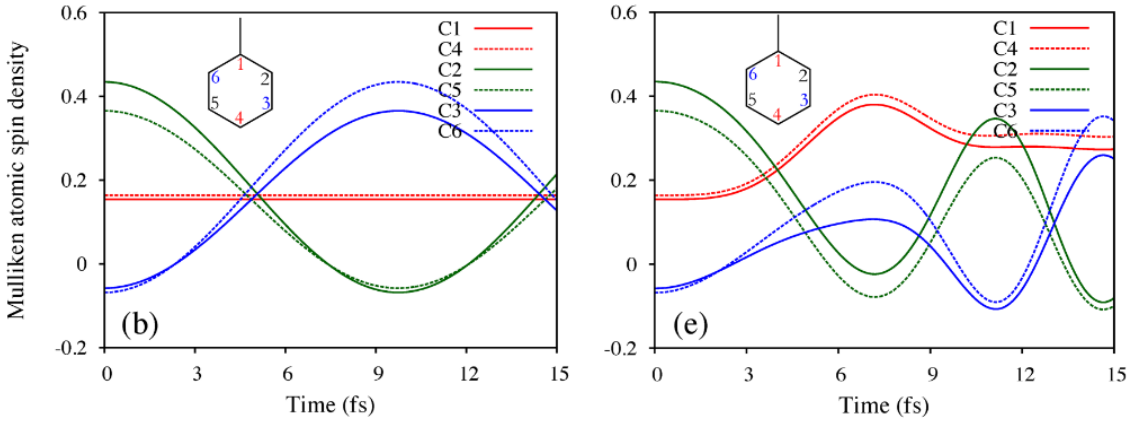


Figure 3.6: Spin densities partitioned on carbon atoms in toluene as a function of time after ionization. Calculation has been performed for toluene with fixed nuclei (left) and moving nuclei (right) [126]

In Figure 3.7 the calculation results for p-xylene with fixed and moving nuclei are shown. For the case with fixed nuclei, since the energy gap used for these calculations is 0.39 eV, the $\approx$ 11 fs period of oscillations is easily predicted. The addition of a methyl group at the para position in toluene restores the symmetry of the molecule such that the amplitude of the spin densities on opposite carbons is equal as it was in benzene. The faster oscillations due to the larger energy gap between the participating eigenstates shows that we can exploit chemical substitution to gain a control over the timescale of electron dynamics. When nuclear motion is coupled the oscillation amplitudes are similar to the case with the fixed nuclei up to $\approx$ 3 fs after ionization. After this, similar trends are observed to what was seen in the toluene cation but the electron dynamics are less pronounced in p-xylene than in toluene. This can be understood in the context of the time evolution of the nuclear and electronic gradients. Since the electronic character changes faster in p-xylene than in toluene the nuclear gradient also reverses faster which leads to less nuclear motion.

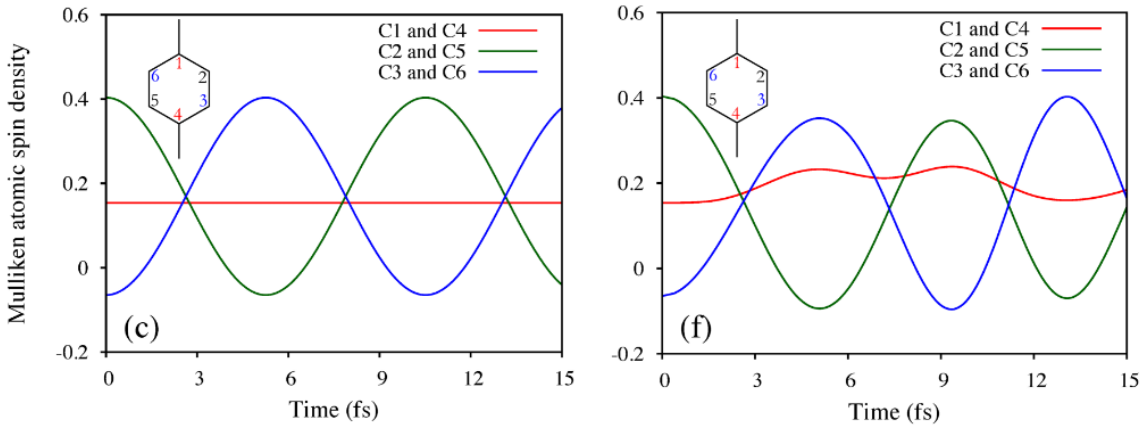


Figure 3.7: Spin densities partitioned on carbon atoms in p-xylene as a function of time after ionization. Calculation has been performed for p-xylene with fixed nuclei (left) and moving nuclei (right) [126]

The intentions for continuing this campaign will be focused on recording multiple sets of data from the methylated benzenes. Calculations presented by Vacher *et.al* are flawed in the application of the sudden approximation for the removal of an electron from the molecule. The sudden approximation necessitates very short laser pulses (a few hundred attoseconds) and high energy photons and is not representative of the tunnelling ionization picture in HHG. They are, however, a starting point for modelling such complex dynamics in large organic molecules.

3.3 PACER on large organic molecules

High harmonic generation can also be used to observe nuclear dynamics in molecules on a sub-femtosecond timescale using the PACER (Probing Attosecond Chirp Encoded Recollision) technique [7]. The harmonic signal is dependent upon changes in the nuclear part of the wavefunction $\chi(R,t)$ hence, it is possible to exploit the chirp of the re-colliding electron wavepacket to probe the nuclear motion during the electron excursion time, τ. The entire HHG spectrum is determined by the square modulus of the nuclear correlation function (NCF) which is defined as the overlap between the initial and final parts of the molecular wavefunction as given by [127]:

$$c(t) = \int \chi(R,0)\chi(R,t)dR \tag{3.12}$$

In our laboratory, Baker *et.al* [128] have previously implemented this method by observing the ratio of harmonic spectra generated in the isotope pairs for example H_2 and D_2 or CH_4 and CD_4. Due to the similarity in electronic states between isotopes, the variation in HHG spectra can only be attributed to differing nuclear dynamics which is retrieved by taking the ratio between harmonic peak intensities.

The time-frequency mapping inherent to HHG can be used to gain an insight into ultrafast nuclear dynamics instigated by the rearrangement of the protons post-ionization of the molecule. In this sense we can think of HHG as a *pump-probe* technique wherein ionization is the pump step and recollision followed by the emission of an XUV photon is the probe step. The chirped nature of the recolliding wavepacket in the third step of the HHG process allows us to study these nuclear dynamics with attosecond temporal resolution since the emission of successive harmonic orders is typically separated by ≈100 as. The strength of the harmonic signal at different frequencies can help us probe the displacement of the nuclei in a molecule at a range of time delays specified by the ionization-recollision times. For example, the HHG signal gets weaker the more nuclei have moved in a system. Phasematching can be exploited to filter out the contributions from long trajectories such that we obtain a one to one mapping between the ionization-recombination time delays and the emitted XUV photon energy.

A previous technique that has also been used to measure ultrafast dynamics in molecules using a pump probe scheme was developed by Niikura *et.al* [129] which also used ionization as a pump step. In contrast to HHG, this method uses recollision induced ionization as the probe signal as the duration of the electron-ion recollision determines the duration of the attosecond photon pulse produced. H_2^+ was used a molecular clock for the pioneering experiments as its potential energy surface gradient is steep such that the vibrational wavepacket is moving on this surface very fast and since the states of this cation directly dissociate. The probe step for this technique requires the laser wavelength to be tuned over a large range in order to obtain the required pump-probe delays. The PACER technique is advantageous over this method as the pump-probe steps are inherent to HHG in the molecule which is less stringent on both data reproducibility as consequence of laser fluctuations from tuning the drive wavelength.

PACER requires the comparison of HHG spectra, acquired under ideally identical conditions, from deuterated and protonated species. The use of isotopes allows us to measure dynamics which are a consequence of nuclear motion in a molecule as the electronic structure of both species is very similar. It is also important that the pump pulse has a duration shorter than the rotational period of the molecule to prevent any significant alignment effects occurring which can result in two centre interference manifesting. A schematic of the PACER technique and results from a comparison of H_2 and D_2 is shown in Figure 3.8.

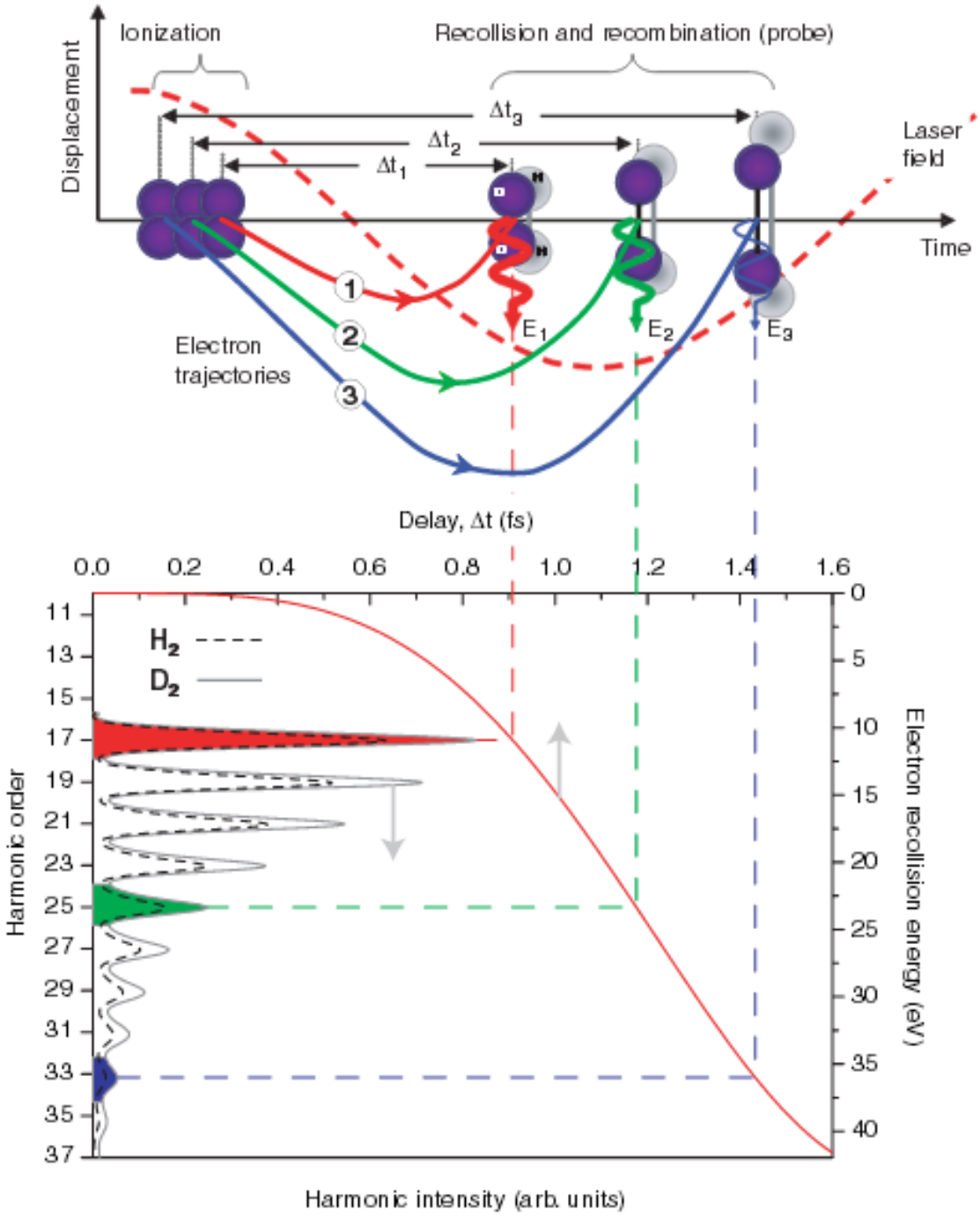


Figure 3.8: Encoding of nuclear dynamics in HHG from exploiting the chirped nature of the wavepacket (top). Electron recollision energy as a function of delay which is colour coded to correspond to the picture in the top panel (bottom) [7]

In Figure 3.9 the results of the PACER technique applied to H_2 and D_2 at equal gas density. The top panel shows the experimental results obtained using an 8 fs pump pulse centred at 775 nm and focused to an intensity of 2.4×10^{14} W/cm^2. Using the 775 nm drive wavelength yields a time window of 0.9 - 1.6 fs over which dynamics can be tracked with a temporal resolution of $\approx$ 100 as. An increase in the ratio of harmonic signal is observed as the harmonic order increases. Since the ionization potential of both molecules are very similar the effects of phasematching on the spectrum are negligible.

The bottom panel of Figure 3.9 shows the nuclear dynamics that have been retrieved from the data using a genetic algorithm [127] [7]. The genetic algorithm retrieves the internuclear separation versus time information for both species. The algorithm generates the optimum Born-Oppenheimer potential by calculating the wavepacket motion. The initial wavepackets for both molecules are taken to be identical to the vibrational ground state wavefunction of both molecules. The algorithm calculates the wavepacket motion to minimise the sum of squared deviations between the autocorrelation ratio and the ratio of the harmonic signals. At the time of ionization the equilibrium separation in hydrogen is 0.75 Å (1.41 Bohrs). The molecule is then promoted onto the H_2^+ potential surface and on this surface the wavepacket begins to move towards the H_2^+ equilibrium separation of 1 Å (1.89 Bohrs). This demonstrates the sensitivity of PACER to changes in the bond length along the internuclear axis in a simple diatomic system.

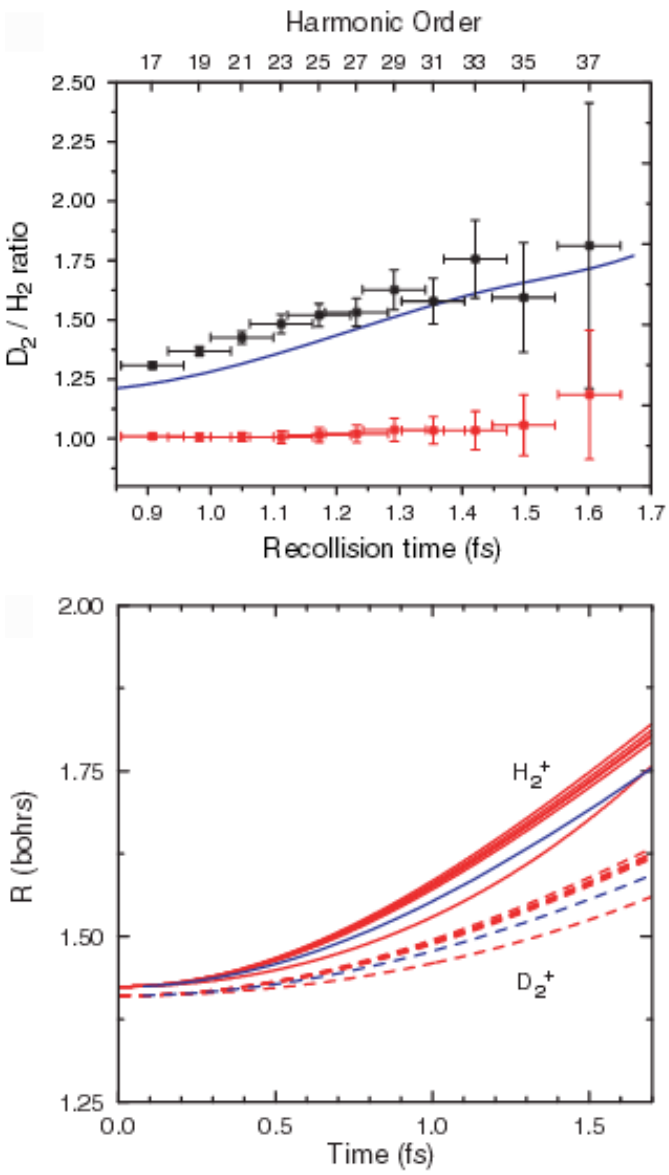


Figure 3.9: Ratio of harmonic peak intensities for D_2 to H_2 (black curve). The red line is a control ration of two separate benzene spectra to check the reproducibility of the data. The blue curve is the results of the NCF calculation - the method is described in [7]. Nuclear motion due to bond length changes in H_2 and D_2. Red curves are modelling results and the blue curves represent the data. Solid lines are for H_2 data and dashed lines are for that of D_2 (bottom). Taken from [7]

The PACER technique has also been applied to CH_4 and CD_4 also using the 8 fs probe pulse. A similar effect to what was observed in the D_2/H_2 comparison - the harmonic signal is stronger in the deuterated isotope since the heavier nuclei are expected to move more slowly. The results are shown in Figure 3.10.

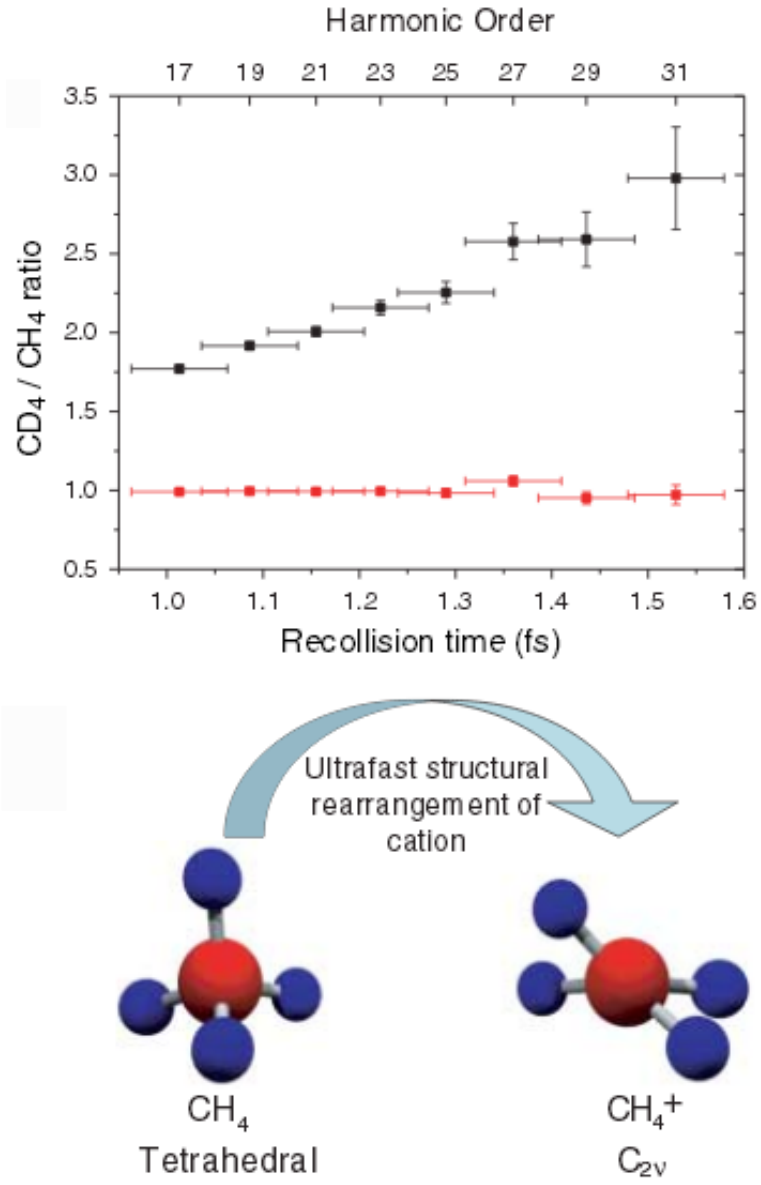


Figure 3.10: Ratio of the harmonic signals from both molecules. The control ratio is marked in red (top). The geometrical structures of both methane and the cation (bottom) [7]

The methane molecule belongs to the tetrahedral T_d point group and has bond angles of 109.5°. the CH_4^+ cation adopts a C_{2v} geometry with bond angles diminishing to <

60° as illustrated in Figure 3.10. The rapid rise of the signal ratios (> 2 in a time of 1.2 fs after ionization) can be attributed to the ultrafast re-arrangements of protons in the cation since the technique is sensitive to bond angle changes as well as along the internuclear axis.

In terms of performing calculations to model to nuclear dynamics in methane, it is complicated by the intrinsic property of the molecule being a triply degenerate Jahn-Teller system which is characteristic of the T_d point group. Patchkovskii [130] has previously derived a simple analytical theory of short time autocorrelation functions and has applied it to a range of small molecules as shown in Figure 3.11.

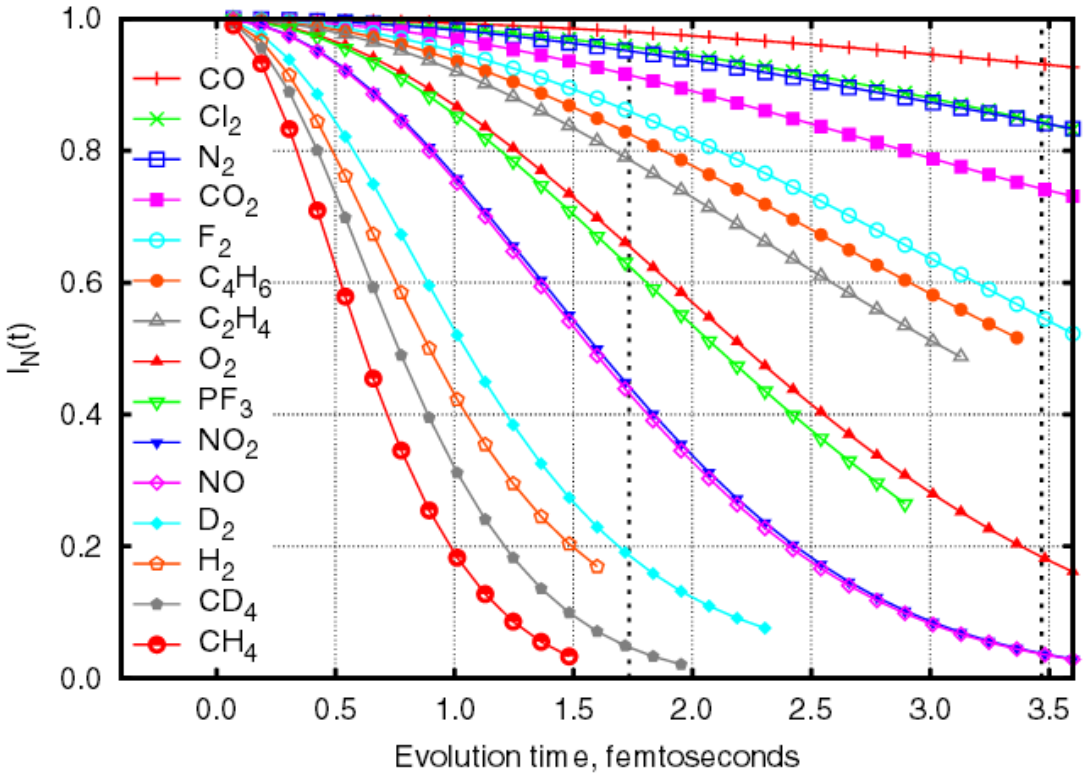


Figure 3.11: Nuclear vibrational factors calculated for a range of polyatomic molecules [130]

Nuclear vibrational factors were calculated and, as shown below, the fastest dynamics occur in H_2, D_2 and CH_4, CD_4. The autocorrelation contribution to the isotope effect was also shown to be in good agreement to the data recorded from the PACER experiments of Baker *et.al* [7] [131] as shown in Figure 3.12. It was observed that the gradient and curvature of the potential energy surface was quite large in the methane cation. This is a characteristic inherent to Jahn-Teller molecules and we thus expect to see a similar trend from calculations done on the benzene molecule.

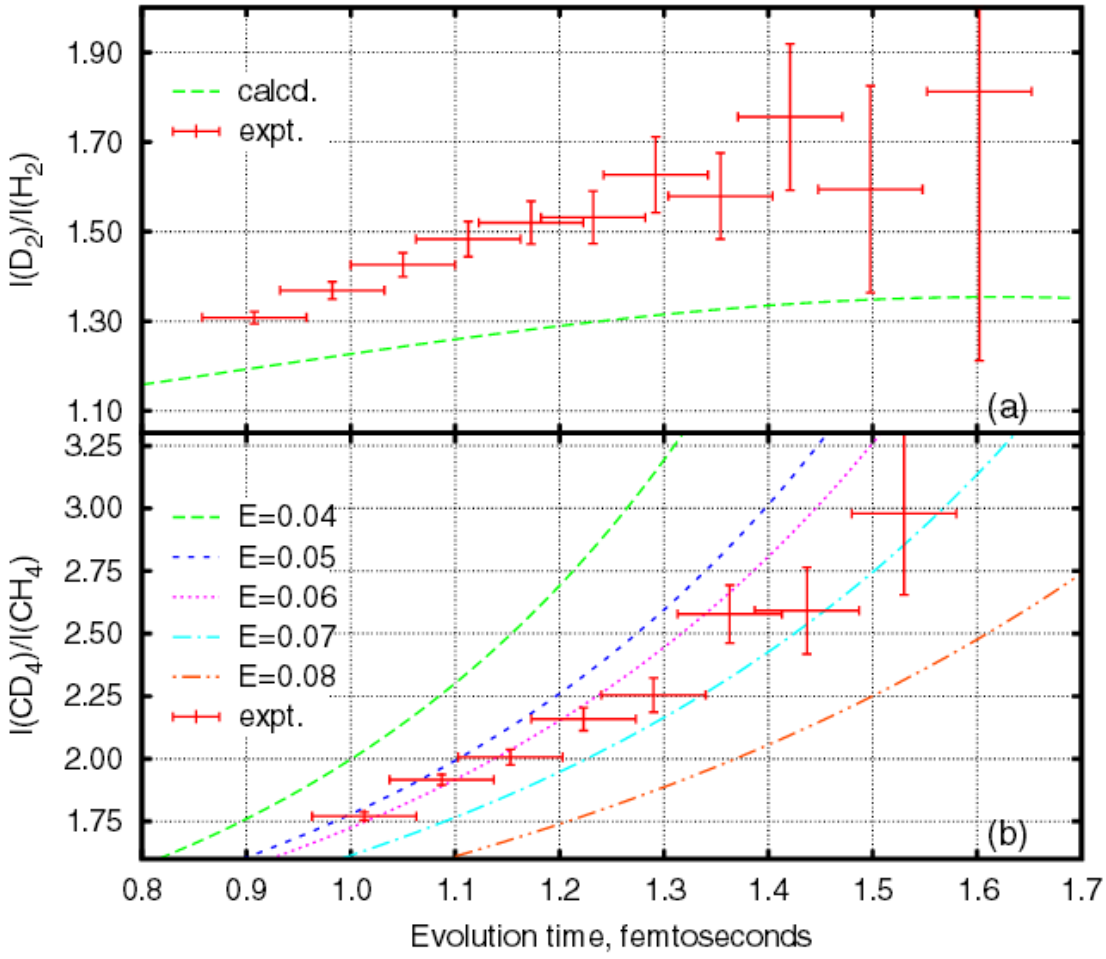


Figure 3.12: Autocorrelation function calculations for the ratio of D_2 to H_2 compared with experimental data from [7] (top). The same calculation performed for the ratio of CD_4 to CH_4 which is plotted for laser field strengths between 0.04 a.u. and 0.08 a.u and an 800 nm laser field. (corresponds to intensities in the range of $\approx 6 \times 10^{13} - 2 \times 10^{14}$ W/cm^2). Taken from [130]

One aim of this PhD project is to extend the PACER technique to larger molecules. PACER has been applied to H_2O and D_2O [132] to illustrate the contribution of a lower bound orbital to the isotope effect in water. Inherent to this goal is the requirement of a longer drive wavelength source - carbon rich molecules naturally will possess slower nuclear dynamics in comparison to those primarily containing hydrogen. The extension of the time window within which we can track the dynamics in larger molecules can be increased from 1.6 fs at 800nm to ≈5 fs at 1800 nm.

Another first for the application of the PACER technique will be to use it on a molecule that does exhibit an ambiguity as to which molecular electron is ionized. PACER will also be a method that will allow us to access a plethora of interesting dynamics from Jahn-Teller molecules as described in section 3.2.

The aim of a PACER experiment in the benzene systems will be to elucidate the origin of the electron when the molecule is ionized. Benzene will be the first molecular system trialled where the possibility of the origin of the electron could be from the pi system or the sigma system. There are two schools of thought on this dilemma −

- If the ionization occurs from the pi system then the C-C bond vibration period of ≈35 fs [133] will be too slow to detect in the evolution of the Nuclear Autocorrelation Function (NCF), equation 3.13, and thus the ratio will be 1 across the 5 fs time window we have access to. The harmonics are approximately proportional to the squared modulus of the NCF:

$$c(\tau) = \int \chi_0(R,0)\chi(R,\tau)f(k,R)dR \tag{3.13}$$

  where $\chi_0(R,0)$ and $\chi(R,\tau)$ are the initial and propagated vibrational wavepackets in the molecular ion, R is the internuclear distance and τ is the electron travel time. The term $f(k,R)$ takes into account two centre interference effects.

- If it is the sigma system that the ionization is instigated from then the C-H bonds are expected to stretch by 10 pm [133] and from the work of Patchkovskii [130] it is possible that this stretch could be detectable in the time window we have available, thus a change in the ratio would support this theory.

An abundance of Time of Flight (TOF) data infers that benzene parent ions are the abundant species post ionization [76] [77]. This would support the theory that the ionization takes places from the pi system. If it were the sigma system it is expected that the ring would possibly collapse upon scission of the C-H bond network and fragments of benzene would be dominant. The other postulate is that upon ionization one sixth of the positive charge is redistributed in the ring and concentrated on each carbon atom. ZEKE data [134] and the TOF data seem to confirm that the ionization occurs from the pi system but a PACER experiment would be a solid confirmation as it is reliant upon HHG which gives a much increased time resolution of the post ionization nuclear dynamics as opposed to the other two techniques which reach nanosecond resolution at best from the data studied using ZEKE and other methods.

3.4 The origin and interpretation of minima in molecular HHG spectra

To date, three classes of minima have been observed in molecular HHG spectra which are attributed to either structural or dynamical effects.

3.4.1 Cooper minima in organic molecules

Cooper minima result from the destructive interferences originating from the nodal structure of the ground state of the molecule. Cooper minima occur in photoionization and are representative of the ground state nodal structure of the atom in question. The photorecombination cross sections are what is measured during the HHG process and can be interpreted as the inverse of the photoionization cross sections, thus a signature of the Cooper minimum in atoms and indeed molecules will be present in HHG spectra. The absorption of photons by an atom/molecule induces

it to emit a bound electron and thereby become ionized. The recombination of the electron with the parent ion results in the emission of a photon, as in the HHG process.

Previous experiments on Cooper minima have been confined to PES data which have resolved the Cooper minima in a range of atoms [135] [136]. The most iconic example is that of the Cooper minimum in argon which is detected at 47 eV [137] . HHG spectroscopy using an 800 nm field is sufficient to locate this minimum in HHG spectra. However the Cooper minimum in krypton is believed to occur at 85 eV and necessitates a longer drive wavelength laser to resolve it. Increasing the intensity to extend the cut-off is not wise in this case as the influence of phase matching on the Cooper minimum has been shown to be crucial in HHG experiments. Spectral shifts and modulation depths in the Cooper minimum of argon have been shown to be strongly dependent upon gas jet position and harmonic divergence [138].

The first HHG Spectroscopy experiments to reveal the Cooper minima in organic molecules were published by Bhardwaj *et.al* in early 2013 [139]. The aim of these experiments was to show that molecules containing S and Cl atoms exhibit Cooper minima. The Cooper minima were monitored as a function of wavelength and drive intensity to isolate it from other interference effects such as two centre interference and multiple orbital interferences. It seems plausible to question why such experiments could not be pioneered in a more simplistic molecule such as CO_2. Atoms such as oxygen do not actually contain a Cooper minimum as its 2p subshell is nodeless, the same mantra applies to some of the Halogens and is a point to bear in mind when selecting molecules to study.

Table 3.1 details the ionization potentials and the Cooper minima positions for the three chloromethane molecules: CCl_4, CH_2Cl_2 and $trans-C_2H_2Cl_2$ taken with an 1800 nm field at an intensity of 9×10^{13} W/cm^2 using a finite gas cell of length 10 mm and 0.6 mm diameter.

Molecule	Ionization Potential (eV)	Cooper Minimum Position (eV)
CCl_4	11.47	40.4 ± 0.5
CH_2Cl_2	11.31	42.1 ± 0.4
$trans - C_2H_2Cl_2$	9.64	43.2 ± 0.5

Table 3.1: Ionization potentials and Cooper Minima positions for the chloromethane molecules [139]

The paper states that position of the minima in the spectra is independent of laser intensity and gas pressure. The argument here implies that this independence of laser parameters confirms that the minima do not arise as a consequence of dynamical interferences which are strongly laser dependent. One may also assume that since the samples are unaligned and the molecules are quite heavy that any structural interferences arising from multiorbital contributions can be assumed to be negligible.

These new results pave the way for identifying Cooper minima in benzene type molecules, which has not been demonstrated via HHG. The halobenzenes shown to possess Cooper minima are chloro and bromobenzene [140]. Flurobenzene will not exhibit this as flourine itself has a nodeless $2p$ orbital [141]. Iodobenzene has, through PES data, shown to be a red herring - whilst iodine itself theoretically should possess a Cooper minimum, it does not due to interchannel coupling between the $5p$ and $4d$ subshells [142]. Theoretical PES data for iodine has shown that atomic $5p$ Cooper minimum should occur at an electron kinetic energy of ≈ 80 ev. However, the threshold for the iodine $4d$ subshell is at a binding energy of ≈ 60 eV.

Once the probe photon energy exceeds 60 eV, the absorption can either result in the ejection of an electron from the $4d$ subshell or the $5p$ subshell. This interchannel coupling is so strong that the $5p$ Cooper minimum is not observed. We can thus infer that the same applies for iodobenzene and indeed no evidence of a distinguishable minimum has been seen in this molecule. The advantage of HHG in this circumstance is that we have the capacity to probe the molecule without encountering this interchannel coupling as our probe photon energy can never reach 60 eV. The extension of our spectra beyond 80 eV implies that we can access the Cooper minimum in iodobenzene, which would be the first ever experimental detection of this minimum.

Work done on the Cooper minimum in argon using a few cycle source (11 fs at 1800nm, achieved by hollow core fibre pulse compression) has identified a shortcoming of using such a broadband harmonic spectrum [143]. Second order diffraction was not an issue when the 800 nm source was employed as the spectrum falls off with increasing XUV photon energy. For the few cycle near-infrared source the continuum spectrum can be flat or even show a peak at higher energies which can appear in the second order at lower energies of the spectrum. The authors remedied this problem by replacing the Hitachi grating with a Shimadzu spherical grating which has a lower second order diffraction amplitude.

Proposed experiments for this PhD would be to identify the Cooper minima in bromobenzene and chlorobenzene. The advantage of our experimental set-up would be to minimize the effects of phase matching on the position and depth of the minimum by using a thin gas jet. The few cycle idler pulse at 1800 nm will also give us a higher energy cut off such that minima in species ≈ 80 eV can be resolved. I propose we first of all locate the minimum in argon as this is a well studied example and to optimize its visibility as a function of gas-jet position and phase matching conditions. Since we will have an extended cut-off it may also be practical to demonstrate our ability to access Cooper minima at higher photon energies as would be the case for Krypton where it is shown to occur at ≈ 85 eV. We are then in a position to acquire spectra in the halobenzenes. We have the added advantage over Bhardwaj of using the thin jet to minimize propagation effects which have been shown to influence the shape and position of the minimum. It may also be feasible to acquire spectra from iodobenzene to identify the interchannel coupling in HHG spectra as this has not been demonstrated before; a similar effect is known to occur in the xenon atom [143].

3.4.2 Structural minima in HHG spectra

Structural minima do not shift in position with variation of the laser wavelength and intensity and arise from destructive interferences between XUV emissions of a two-centre type molecule [144] [145]. However, these minima are sensitive to the molecular alignment angle with respect to the polarization of the driving laser field [53] [54].

It is well versed that HHG spectra from spatially aligned molecules can be analysed

to unravel the structures and symmetries of molecular orbitals [146] [57] [147] [148] [149] [56] [150] [55]. The de Broglie wavelength of the recolliding electron governs the spatial resolution of the HHG spectra. Hence, a HHG spectrum extending past 50 eV cut-off energy is required in order to observe structural features arising from systems with internuclear distances in the $1 - 2$Å range [148] [147]. Using a commercial 800 nm Ti:Sapphire system demands laser intensities in excess of 3×10^{14} W/cm^2 which is above the saturation intensity of most molecules we wish to study. This commercial system can be utilized for molecules with ionization potentials ≥ 13 eV such as N_2 or CO_2. Torres et.al [148] have studied the extension of HHG spectroscopy to longer wavelengths and have concluded that 1300 nm is a good compromise - there is a factor of 2.6 increase in the maximum photon energy obtained of the HHG spectra in comparison to the 800 nm field.

The advantage of this scheme in pushing the boundaries of HHG spectroscopy to previously unattainable territory can be appreciated by looking at the case of acetylene (C_2H_2) which has π_u HOMO symmetry and an ionization potential of 11.4 eV. When using the 800 nm field at the saturation intensity the cut-off only reaches ≈ 46 eV which falls short of the region wherein interference effects take place. On the other hand, using the 1300 nm field at a lower laser intensity of $\approx 10^{14}$ W/cm^2 extends the cut-off up to 60 eV.

In the experiments previously performed [147] [148] the delay between the driving and aligning pulses is set to correspond to the half revival (7.1 ps for acetylene) when the sample is maximally aligned. The harmonic intensity is then measured as a function of the angle between the aligning and driving fields, Θ. The most probable orientation of the molecules with respect to the driving field, θ can then be estimated. For this experiment, $\Theta = 0$ corresponded to a probable orientation angle of $\theta = 30°$. At $\Theta = 0$ a minimum in the HHG spectrum was observed for acetylene.

Interpretation of this result can be envisaged as follows: the HOMO is expected to have a characteristic two centre structure wherein the contributions to the recombination amplitude from each centre can interfere constructively or destructively if the recolliding electrons have a momentum $p = \frac{h}{\lambda_{deB}}$ where λ_{deB} satisfies the interference condition:

$$\frac{n}{2}\lambda_{deB} = Rcos(\theta) \tag{3.14}$$

n is an integer, R is the internuclear distance, (1.2Å for acetylene between the carbon atoms) and θ is the angle between the internuclear axis and the laser polarization vector. Since the HOMO of C_2H_2 is π_u which is a symmetric orbital then $n = 1$ is where the first destructive interference will occur since the two centres are separated by $\frac{1}{2}\lambda_{deB}$ in the direction of the driving field polarization [150].

3.4.3 Dynamical minima in HHG spectra

Dynamical minima are present when several molecular orbitals contribute to HHG. If a laser is of sufficient intensity to ionize two valence orbitals in a molecule, the amplitudes from these channels will interfere with a relative phase going through multiple points of constructive and destructive interference. The energy gap between the two participating ionic states, ΔE, is the primary determining factor for knowing the time dependent relative phase between the two channels which is given by:

$$\varphi \approx [\Delta E/\hbar]\, t \tag{3.15}$$

where t is the excursion time of the electron in the continuum during the propagation step of HHG [56]. Dynamical interference is expected to be destructive when the relative phase is an odd multiple of π which manifests itself as a minimum in the molecules HHG spectrum. Variation of the drive wavelength, intensity and the molecular alignment angle with respect to the polarization of the driving laser field can all shift the position of the dynamical minimum arising from the ionization of multiple orbitals [59] [55].

As an example of this, the results obtained by McFarland *et.al* [57] [146] for the observation of contributions from the HOMO and HOMO-1 in HHG from nitrogen as shown in Figure 3.13.

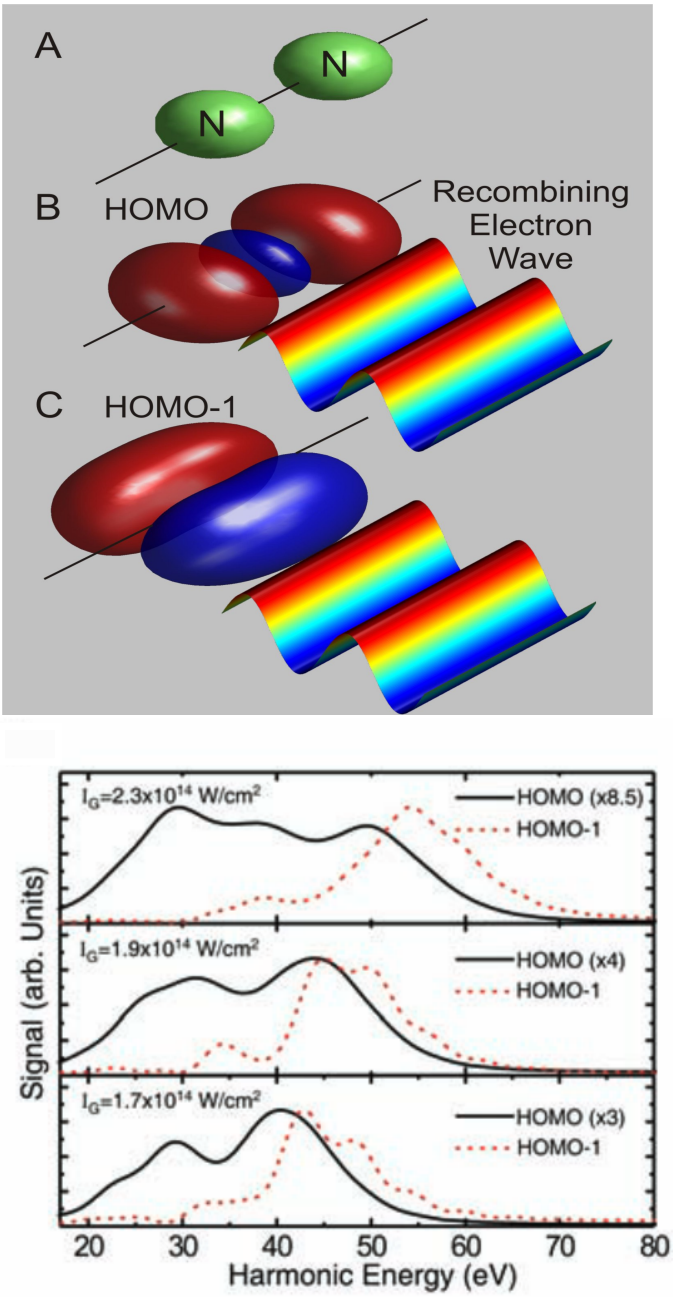


Figure 3.13: The shape of the HOMO and HOMO-1 orbitals in N_2 with respect to the internuclear axis. The recolliding electron is illustrated as a de Broglie wave (top). Results of a simulation of the modulation of the harmonic spectral envelope for different harmonic generation intensities. The solid black lines represent the contribution of the HOMO whilst the red dashed lines are that from the HOMO-1. Taken from [146]

The top panel shows the differing orbital symmetries of the HOMO and HOMO-1 in nitrogen. The HOMO which has σ_g symmetry ionizes more readily when the polarization of the generating laser field is aligned parallel to the internuclear axis. A clear contribution from the π_u HOMO-1 is evident in the experimental data and the calculations performed. The bottom panel presents the simulation of the spectral envelope for different generation field intensities. As the intensity is increased and the alignment angle changed the contribution from the HOMO-1 becomes increasingly evident. Tunnel ionization for the HOMO-1 is stronger than that of the HOMO when the polarization of the generating laser is aligned perpendicular to the molecular axis since it has a larger spatial extent along this direction. As is clear in the bottom panel of Figure 3.13, the spectra at different intensities are modulated by constructive and destructive interferences during recombination. The HOMO is the dominant contributor to the lower order harmonic whereas the HOMO-1 dominated the cut-off portion of the spectrum.

However, I must emphasise that the attribution of a minimum in a molecular HHG spectrum to a structural or dynamical effect is quite difficult. A famous example is the minimum observed in CO_2 which was initially thought to be a structural effect [53] [54]. Work by Smirnova *et.al* [59] contradicted this result as the observed minimum in their work changed spectral position as the drive laser intensity was adjusted. The variation in the harmonic spectral phase as a function of recollision angle was employed to elucidate which channel in CO_2 was the primary contributing orbital. Further work [55] [56] concluded that this minimum originates as an interplay between both structural and dynamical effects; this has also been observed in H_2 [128]. This scenario prompted developments of techniques to measure the harmonic spectral phase, such as Reconstruction of Attosecond Beating by Interference of Two-photon Transitions (RABBIT), which can be used to extract information on multi-orbital contributions in molecules [60]. Experiments performed independently by both Wong *et.al* [151] and Farrell *et.al* [152] in H_2O also report a contribution from the HOMO-1 to the harmonic spectral intensity. The energy gap between the HOMO and HOMO-1 in H_2O is ≈ 0.5 eV.

In a similar vein, the energy gaps between the HOMO and HOMO-1 (and indeed more tightly bound orbitals) in the substituted benzenes are quite small (see Appendix A

for ionization potentials in these molecules). For example, the energy gap between the HOMO and HOMO-1 in fluorobenzene is ≈ 0.6 eV, we would expect that a modulation of the harmonic spectral amplitudes in the substituted benzenes could be attributed to the influence of a lower lying orbital. We anticipate that the observation of a modulation in the harmonic intensities in the halogenated benzenes will prompt the implementation of more in depth experimental techniques to identify the phenomenon contributing to the suppression and indeed theoretical calculations to be performed on these molecular systems.

Chapter 4

Experimental methods and apparatus design and implementation

From an experimental perspective the following are fundamental requirements for HHG in organic molecules:

- Target dimension: As discussed in section 1.6 with regards to phasematching it was noted that keeping the target dimension short (< 1 mm) is important for minimising propagation effects and reabsorption of harmonics.
- Density: A high density of molecules in the interaction region is necessary in order to have enough emitters ($> 10^{17}$ molecules/cm^3) [86] coherently contributing to the HHG signal. The HHG signal is inversely quadratic with the density of the gas.
- Stability: A stable target is of absolute necessity. Any significant instabilities in the delivery of the gas/vapour/solid to the interaction region result in misleading, non-physical and unreproducible results being acquired.
- Vacuum base pressure: The chamber where the target is delivered to must be kept under a vacuum of base pressure $\approx 10^{-6}$ mbar for a number of reasons. Firstly, the generated XUV photons may be reabsorbed by the air thus inhibiting detection of the HHG. Secondly, the detector, a microchannel plate (MCP) requires $1 - 4$ kV to be applied across it; the detector must be operated under

vacuum to prevent arcing and damage to the detector. Thirdly, the vast majority of molecules of interest are carcinogenic, flammable and dangerous to ones health so they must be contained in a vacuum chamber.

- Target rotational temperature: Keeping the sample cool (a few tens of Kelvin) aids with performing impulsive alignment on the sample. This is because the hotter the molecules are, the greater the number of incoherent rotational states that are initially thermally populated.

The apparatus for High order Harmonic Generation (HHG) in our laboratory was primarily designed for working with inert gases. This chapter will begin by describing the function of each component of the existing arrangement and its integration into the apparatus. Upgrading and modifying this system to handle organic molecules required careful design with respect to every component. This chapter will proceed by detailing the modifications that have been made to the existing system and the advantages these upgrades bring in comparison to what has been previously presented in the literature.

4.1 Outline of existing HHG apparatus at the start of the project

Figure 4.1 illustrates the key components of the experimental apparatus in its original state used for the generation and detection of high harmonics. Prior to the experiments planned with the vapour phase organic molecules this system was designed to be used with gaseous, usually inert, and solid targets. The solid targets such as the DNA and RNA complementary bases, uracil and thymine, were vapourized using laser ablation. Organic molecules such as butane and butadiene [113], benzene, cyclohexane, napthalene and cyclopropane [85] [153] have been used previously in our laboratory but the requirements as detailed in the chapter introduction were not met adequately. The objective was to introduce a locally high density of gas, in some cases with a significant degree of rotational cooling, to the interaction region.

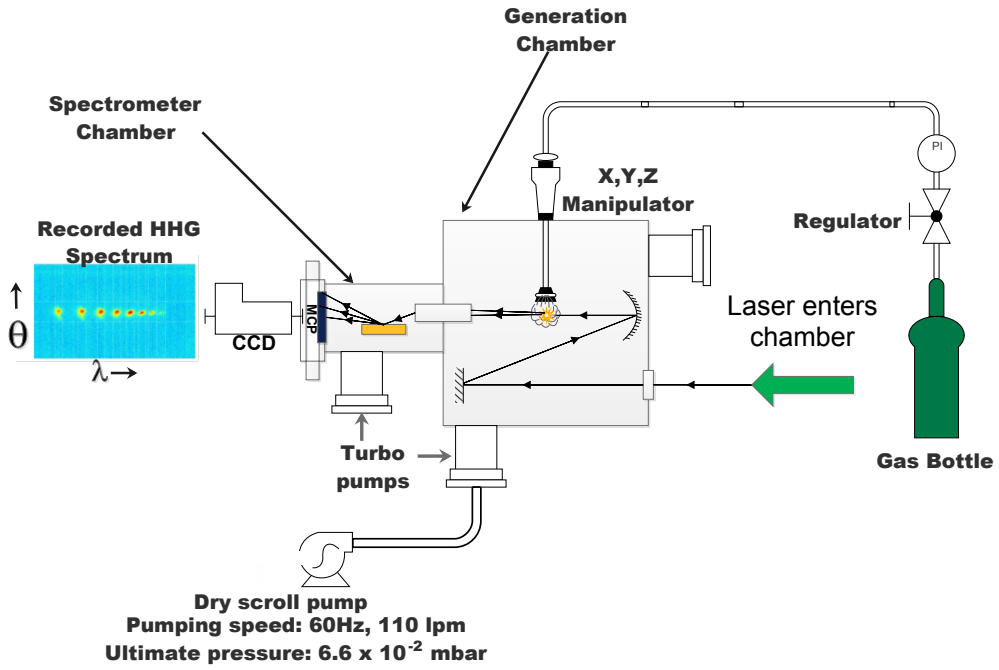


Figure 4.1: The original HHG chamber at Imperial College London

The vacuum system is separated into two chambers − the generation chamber and the spectrometer/detection chamber. A small tube with a 2 mm diameter hole divides the system in two by creating a pressure differential whereby the spectrometer chamber is kept at a pressure below 10^{-5} mbar which is necessary for safe operation of the detector which will be elaborated upon later in section 4.1 of this chapter. Two turbo pumps are used to evacuate the generation chamber, each of which is backed by a dry scroll pump and one turbo is used to keep the detection chamber at the required pressure.

The laser beam enters the chamber through a fused silica or calcium fluoride window depending on the wavelength of the beam being used. The windows are typically 1 mm in thickness to minimise distortions to the beam profile. An iris is located before the entrance window to the chamber and is used in conjunction with a second iris downstream to align the beam into the chamber. A CCD camera (Bosch LTC 0355) is mounted on a flange with a view-port perpendicular to the propagation path of the laser over the nozzle. This camera is interfaced to a CRT screen to image the gas−jet to ensure the laser is not ablating the nozzle and to give an indication of the shape

of the plasma plume at the interaction region. As the ionization potentials of the typical gases used for High Harmonic Generation (HHG) are in the $12 - 22$ eV range it is necessary to use beam intensities of the order of $10^{13} - 10^{15}$ W/cm^2. To reach these intensities the beam must be focused into the gaseous target. To achieve these values, the beam is focused using, typically, a spherical mirror in normal incidence as shown in Figure 4.1. Choice of focal length is dictated by either requiring a high number of emitters in the interaction volume, as would be desired in a molecular alignment experiment (loose focusing), or wanting to boost the maximum intensity, which is usually necessary when a target with a high ionization potential value is used (tight focusing). The focal spot is characterised by inserting a flip up mirror before the entrance to the chamber and constructing an identical beam path, including the entrance window to the chamber, to that inside the chamber and imaging the focus on a CCD camera. This diagnostic is useful for characterising the profile of the focus, getting a measure of the focal spot size for estimating the intensity at the interaction region and checking how certain optical elements introduce distortions to the beam profile.

The introduction of the target gas to the chamber can be done by a variety of methods, although this chamber has only ever operated with a solenoid valve or with a continuous flow gas jet. Solenoid, or pulsed gas jets are advantageous for experiments where a high gas density in the interaction region is desired because the jet can be configured to expel gas into the chamber only when a laser pulse is present below the gas jet. This configuration reduces the background pressure in the chamber thus enabling a higher backing pressure to be used without the compromising the conditions for keeping the detection system operating safely. These valves have typical opening times of 300 μs. The valves previously used in our laboratory operated at 10 Hz (as did the laser). High power laser systems for HHG that are now commercially available operate usually at 1 kHz which provides better statistics on data. Using a 10 Hz valve would be wasteful of laser shots in this case. Piezo−pulsed valves (i.e. Evan Lavie valve, which will be discussed more in section 4.2) or continuous flow valves are ideal for operation at 1 kHz, particularly in circumstances where a high degree of rotational cooling is needed. The continuous flow gas jet is much more commonly used due to its ease of implementation and operation. This jet is simply a blank stainless steel plug which has a 100 μm or 200 μm hole drilled in it. The pumping system installed

on the generation chamber and the differential pumping gradient permits gas to be continually expelled into the vacuum chamber whilst not compromising the vacuum of the detection chamber.

Figure 4.2 below illustrates a cross section of this home-made gas jet.

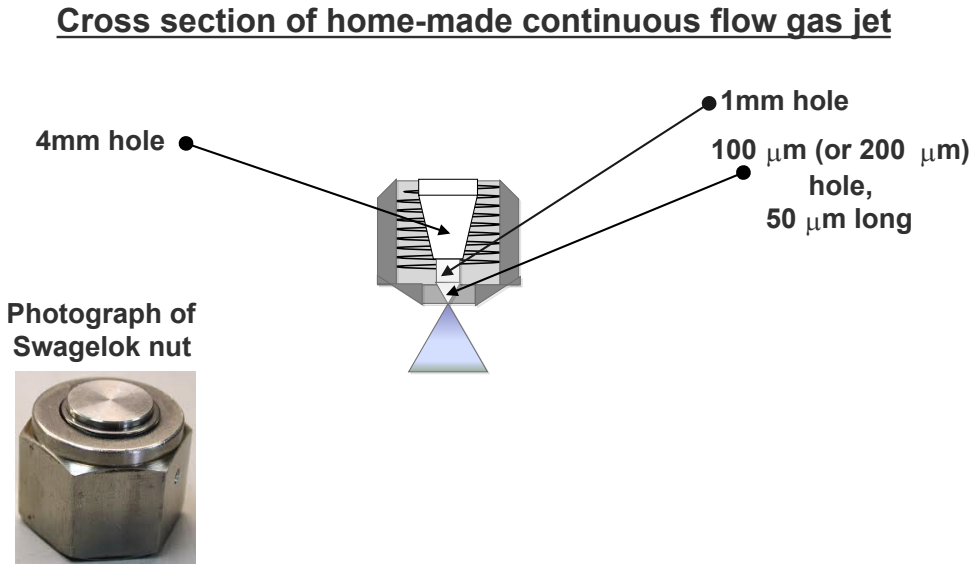


Figure 4.2: Schematic of the continuous flow gas jet used in the HHG chamber

The gas jet is mounted on a three axis manipulator as shown in Figure 4.1. The manipulator moves the gas jet in three directions; along the propagation axis (z) of the beam, vertically (y), and horizontally (x).

HHG detection

The harmonics propagate through the differential pumping tube into the spectrometer which consists of a grating and a microchannel plate (MCP) detector and phosphor screen which is coupled to a CCD optical camera. The spectrometer chamber is constructed from aluminium and is anodized and painted black to reduce light scattering. The harmonic beam passes to the spectrometer through a 100 μm aperture and is dispersed by a grating. The harmonic beam is typically tens of microns in diameter and has a typical divergence of $\approx$ 3 mrad. The distance from the focus to the flat field grating in our apparatus is $\approx$ 30 cm. There are two main designs of grating that

can be used − concave and flat field gratings, both of which can be designed to have uniform or varied line spacings. The first grazing incidence spectrometer design in our lab in the late 90's utilized a concave grating in which the dispersion and focusing of the spectral images are combined. A concave grating with uniform line spacing is not practical, as the optical layout needs to be in correspondence with the Rowland circle as shown in Figure 4.3 below. If the entrance slit is located at any position on a circle that has a diameter equal to the radius of curvature of the grating and contacts the centre of the grating, then the dispersed harmonics will be focused at other points on the same circle. The minimum and maximum diffracted wavelengths are λ_1 and λ_2 respectively [154]. The setbacks of this arrangement include the large amount of astigmatism inherent to this set-up and the difficulties in positioning the detector [155]. This arrangement is acceptable in a scanning spectrometer with an exit slit but will not suffice for the experiments presented in this thesis as an MCP, which is a plane detector array, is used for the HHG detection with necessitates that we use a flat field geometry for the spectrometer.

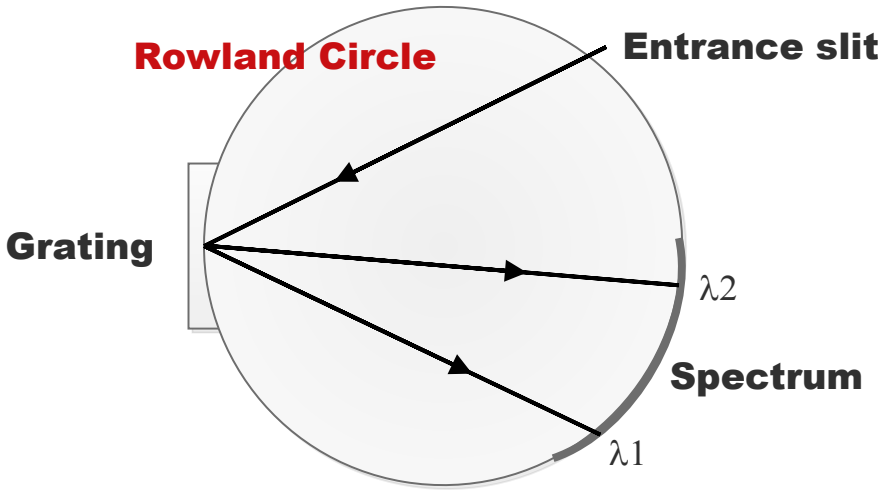


Figure 4.3: Illustration of the Rowland circle concept showing the diffracted wavelengths focused at different points on the circle. Adapted from [154]

Using a grating that focuses the dispersed harmonics onto a plane that is almost normal to the incident harmonics is clearly more advantageous for the mounting of the detector. The grating used in our spectrometer is a gold-coated grating that is curved in one dimension and has an average varied groove spacing of 1200 lines/mm [156]. This grating design is curved in one dimension with a line spacing variation such that is spectrally focuses the radiation 30 cm away. It is also flat in the other dimension to preserve the spatial information. This gives a spectrally resolved image that contains all the radial information of the intensity distribution of the harmonic beam. The harmonics on the detector are imaged on to a CCD camera by a compound lens. A schematic of the diffraction grating is shown in Figure 4.4. The harmonic beam hits the grating at an angle, α, of 3 degrees.

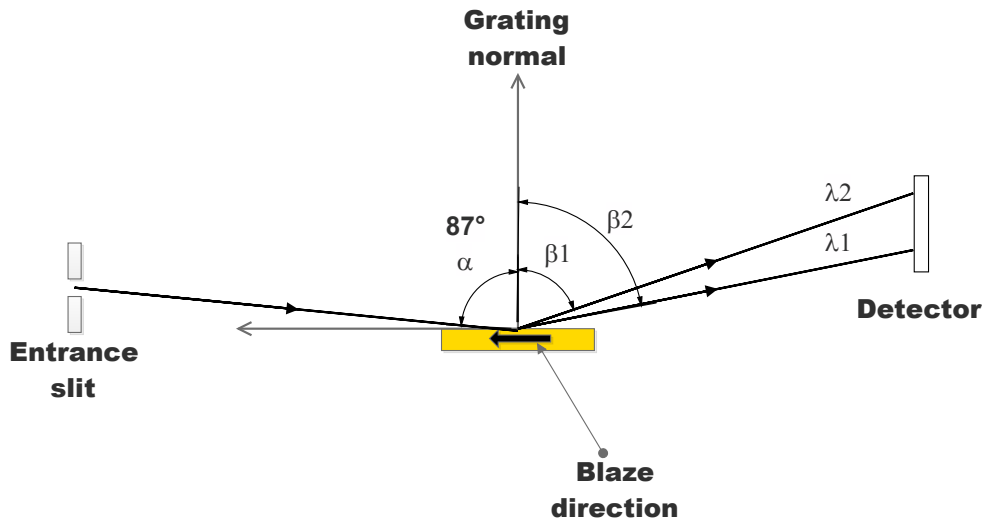


Figure 4.4: Alignment of the flat field XUV grating for HHG. Adapted from [157]

The harmonic beam which has been dispersed by the grating is then imaged onto a microchannel plate (MCP) detector. The assembly consists of two microchannel plates and a phosphor screen. An MCP is a lead glass array of 10^7 pores for a 40 mm diameter detector. Each channel is 10 μm in diameter and the length of a channel corresponds to the plate thickness [158]. Each of these channels acts as an electron multiplier. When an incident x-ray photon enters a channel it frees an electron from the channel wall via photoelectric emission. A potential difference of -1500V is applied across the length of the channel to accelerate the liberated electron which strikes the

adjacent wall of the capillary freeing more electrons. These electrons are accelerated along the channel until they strike the far surface giving rise to more electrons. A second plate is placed after the initial one to further amplify the electron current and subsequently resulting in a gain of the order of 10^8 electrons/photon. Figure 4.5 illustrates the avalanche amplification in a single channel of an MCP.

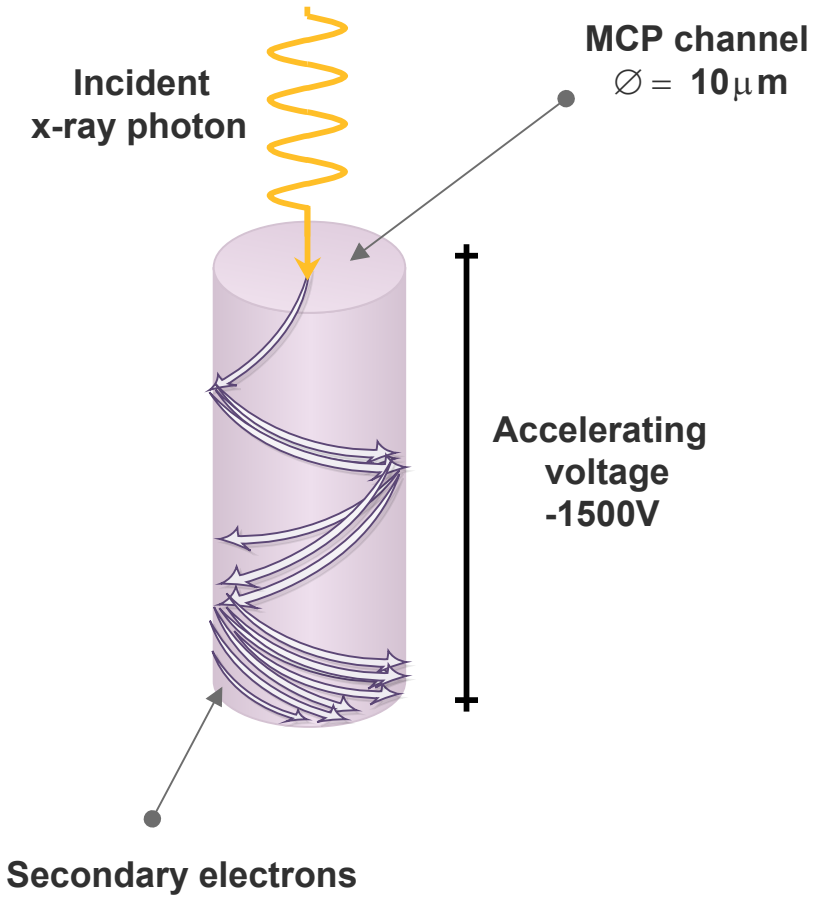


Figure 4.5: Avalanche amplification caused by secondary electrons in a microchannel plate pore

The channel bias angle is usually 8° from the normal to the plate surface, the purpose of this is to prevent incident particles from entering the channels and potentially getting lodged in there. Since the capillaries confine the propagating charge pulse inside them, the spatial pattern of the electron pulses at the rear of the plates preserves the spatial pattern of the incident x-rays. The resultant electrons are accelerated

towards a phosphor screen. A phosphorescent material is coated onto a glass plate and converts the incident electron avalanche into a visible image.

A P47 coating is commonly used - it has an 80 ns decay lifetime and its peak emission wavelength is 430 nm which results in a purplish blue emission. The phosphor screen is further coated with aluminium which acts to increase the efficiency of the signal generated. This increase can be as much as 100%, as light created at the phosphor is reflected back at the aluminium layer. It is necessary to apply a voltage of the order of 3 kV to the screen to enable the electrons to penetrate the aluminium layer. Indium Tin Oxide (ITO) is another common coating which also reduces the build up of charge from electrons and ions.

As has been stated earlier, it is necessary to keep the spectrometer chamber which houses the MCP assembly under vacuum. If the voltage is applied while the detector is at atmospheric pressure, ion feedback and electrical breakdown can occur which can cause both long term damage to the detector itself and potentially damage the optics also in the spectrometer chamber. Arcing tends to damage vacuum seals and other materials which can be melted, burnt or vaporized as a consequence of the large amount of heat that is released by a discharge. Materials that can be vaporized by discharges can be deposited on optical surfaces which in our case would be the flat field grating which is an expensive optic. The absorption of water can also cause the MCP to bow out of shape which can dramatically impede its efficiency and shorten its operating life significantly [159]. A compound lens (Schneider Fast C−Mount Lens, 17 mm FL, f/0.95) is used to image the harmonics from the MCP to the CCD camera. This lens is designed to provide excellent image quality under low light conditions in the visible region of the spectrum ($400 - 700$ nm) and this is ideal as the P47 coating on the MCP emits at ≈ 430 nm. A PCO Pixelfly 14 bit CCD camera is used to image the screen of the MCP in conjunction with the compound lens to enable recording of the HHG signal on a computer for data acquisition.

4.2 Vapour generation from organic molecules

The convenience of working with the gas phase targets was that their delivery to the vacuum chamber is as easy as adjusting a regulator on the associated gas bottle

for a stable flow of gas. Acetylene, benzene, iodine and carbon disulfide have been previously used in our laboratory and are reputed for being very corrosive. This is something to be very aware of when it comes to constructing a vapour delivery and vacuum system for working with these molecules. The organic molecules studied in this thesis are in the liquid phase at room temperature, are flammable and have the added complication of being genotoxic carcinogens. A genotoxic carcinogen can cause irreversible damage or mutations to an organism by binding to its DNA. This section will detail the design, construction and implementation of the apparatus to generate a stable vapour from numerous benzene substituted targets.

Previous experiments which have focused on studying organic molecules which are in liquid phase at room temperature have generated their vapour by two methods. The most common method is to just use the vapour pressure at room temperature and either inside a gas cell or through a pulsed gas valve to send the vapour to the interaction region [160] [151] [139] [161]. The other method, which so far has only been implemented at Imperial College London, is to heat the sample to generate the vapour [85] [79] [153].

4.2.1 Evaporation of liquid phase organics at room temperature

Three different high-order harmonic sources have been used in gaseous/vapour molecular HHG experiments to date − pulsed gas valves, continuous flow gas valves, semi-infinite gas cells (SIGC) and finite gas cells (FGC) [85] [139] [151] [162] [161] [115] [150] [56]. Each of these sources has its advantages and drawbacks, which will be briefly addressed here. Further elaboration of the high harmonic efficiency requirements are discussed in section 2.1. Bhardwaj *et.al* have compared these three sources using argon as a generating medium [163]. This study showed that using longer medium lengths and increasing the atomic density does not directly result in larger conversion efficiencies. Although the efficiency does have a quadratic dependence on the medium length and the atomic density, it is also dependent upon the negative exponential of their product which can be seen in the expression for the number of photons emitted on axis as detailed in [164]. This directly implies that the absorption of harmonics, and indeed the phase−matching, begins to become critical.

Whilst pulsed gas valves are commonly used, a physical limit is imposed upon how much backing pressure can be put behind them to avoid overpressuring the interaction chamber. This problem has been mitigated by the use of an Even−Lavie pulsed gas valve [165]. This design of valve has an opening time of 30 μs which facilitates efficient expansion conditions to provide a degree of rotational cooling. There are several designs of the valve which all share the following properties: can handle backing pressures up to 100 bar, operate at repetition rates up to 600 Hz and can achieve rotational cooling to $<$ 1K. Rotational cooling of 0.4 K has been achieved in aniline using this jet with no buffer gas [165]. If a very low vapour pressure is being delivered to the interaction region, a carrier gas of high ionization potential such as Helium can be used - this is particularly useful in molecular alignment experiments - where the atoms aid the rotational cooling by collisions with the target molecules.

Since most models operate at 10 Hz, they are also quite wasteful of laser shots since most commercial CPA laser systems used in these experiments operate at 1 kHz. One advantage they possess is an interaction length which is considerably shorter than that of a gas cell. Keeping the medium length shorter than the absorption length circumvents the absorption of the generated harmonics [164]. It is important to note that optimising the efficiency of the HHG process is not the principal aim of this work; efficiency in a continuous jet compared to a gas cell can be compensated by the laser power, better detection and using a higher repetition rate laser system. The key focus of this discussion on choice of target delivery is to ensure that the measured HHG spectrum from the organic molecules is as close as possible to the single molecule response.

Semi-infinite gas cells (SIGC) and finite gas cells (FGC) are used extensively in HHG experiments. A schematic of these cells is shown in Figure 4.6.
A finite gas cell commonly consists of a small inner cell which is encased in a larger outer cell. A teflon tube at the top of the cell delivers the gas to the inner cell - to the interaction region perpendicular to the laser beam propagation direction. The outer cell is typically pumped by a roughing pump (500 l/s) which is not shown in Figure 4.6. There are four inline pinholes in the beam path, two on each wall of the inner and outer cells. The cell is mounted on an XYZ manipulator to align it with

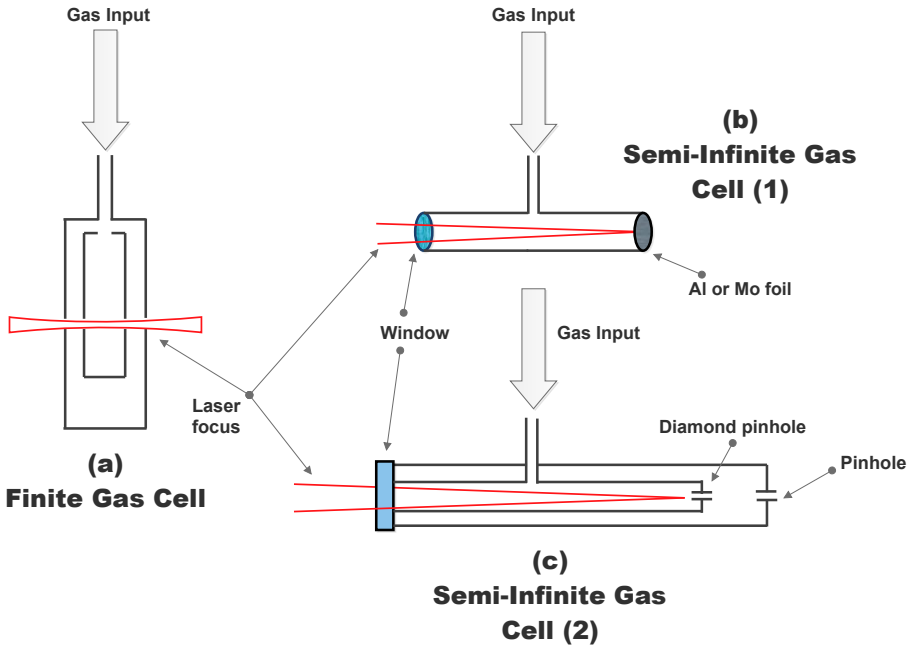


Figure 4.6: Schematic of the most common types of gas cells used in HHG experiments: (a) finite gas cell, (b) and (c) semi-infinite gas cells

the laser axis [163].

There are two common designs of semi-infinite gas cells as shown in Figure 4.6. In the cell labelled as (1) the incident beam passes through a window wherein the gas is injected through a teflon tube perpendicular to the beam path and is focused on a foil (Al or Mo) at the other end of the cell. The focused beam effectively drills a hole in the foil allowing the harmonics generated in the cell to be propagated on to the detection chamber [166]. In the design labelled as (2) there is an inner and an outer cell as in the case of the FGC. The gas is injected into the inner cell through a teflon tube, the end of which is fitted with a diamond pinhole. A diamond pinhole is used here as opposed to a standard metallic one as the focus of the laser can ablate the metal pinhole which can damage it. The outer cell is pumped by a roughing pump similar to the FGC and terminates in a pinhole to the source chamber [163].

Work currently being carried out in our laboratory by PhD student Allan Johnson is using a 3 mm finite gas cell to focus on maximising the HHG cut−off and getting high

efficiency. The purpose of this work is to extend to cut−off to reach the water window (4.37 nm) in helium. To reach these high energies, high gas pressures are required to achieve phasematching. A continuous flow gas jet is unable to provide the required backing pressures ($\approx$ 1.5 bar of helium) as these elevated backing pressures put an increased load on the backing pumps and will inevitably violate the base pressure level required to safely operate the MCP detector.

The design of the gas cells enables them to handle quite high backing pressures (can be 10's of bars in some designs) compared to gas jets (5 bar maximum for 100 μm nozzle in our laboratory). Cells essentially permit using higher atomic densities due to the increased number of emitters in the interaction region [167]. Longer medium lengths are also inherent to cells - typical medium lengths can be anything from a few millimetres to a few centimetres and more. As gas jets commonly have medium lengths much shorter than the absorption lengths, the absorption of generated harmonics by the medium can be negligible. It is also noteworthy that, in a gas cell, the incident laser pulse can undergo self-focusing and other non-linear distortions arising from the presence of free electrons in the medium. Over a long medium length these distortions can play a strong role in phase−matching which is another reason to opt for keeping the medium length as short as feasibly possible [168] [169].

Using data from the CRXO database for benzene at 100 K temperature, 20 torr backing pressure and two medium lengths of 500 μm and 1 mm we can see how the transmission of the XUV photons is affected by the medium length as shown in Figure 4.7. From this plot, it is evident that the transmission is a factor of two higher for the shorter medium length at 50 eV.
An Even−Lavie valve presents a number of advantages for our proposed work but was not chosen for a number of reasons. These valves are not a widely commercially available product and are also expensive. The heated version of the valve [170] can only operate up to 130° C which puts a strict limit on the molecules that can be used as any molecule with higher temperature requirements to prevent condensation cannot be used. It is also important to note that in a similar fashion to the jet designed by Hay in our laboratory, the sample cartridge is mounted on the same flange as the valve which implies that samples must be manually changed which requires stopping the experiment and spending several tens of minutes preparing and mounting a new

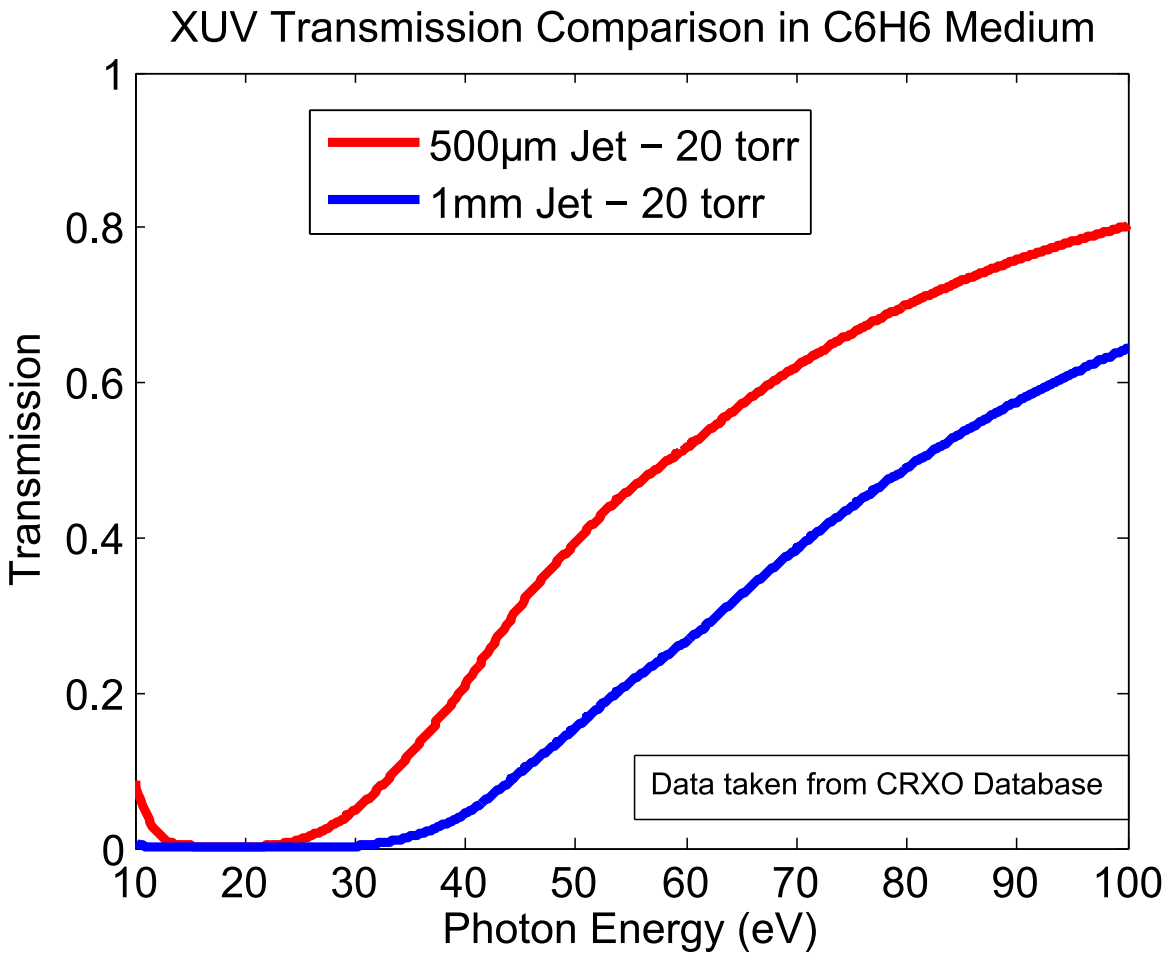


Figure 4.7: Plots of XUV transmission in benzene for 500 μm and 1 mm medium lengths. Data taken from CRXO website.

sample. Since the sample is heated at elevated temperatures, it is also important to note that the sample reservoir will need to cool down before another is inserted to prevent injury to the user. This adds on more time which impedes the ability for comparison experiments to be performed accurately and quickly between molecules. The re−heating of the sample reservoir when it has been swapped will also alter the thermal equilibrium of the mounting components which can affect the stability of the system. Another limitation of these valves is the moving parts inside the valve to control the opening and closing of the jet. The impact of corrosive molecules on the internal components of this valve have not been published or commented upon [170]. The use of corrosive molecules and elevated temperatures are not very valve friendly requirements for an experiment.

A continuous flow gas jet (200 μm orifice) is the best choice of source for the intended HHG experiments in this thesis. This has been chosen as it presents numerous advantages over the other previously used vapour sources. Evidently, this design is inexpensive in comparison to the other delivery methods available and can even be manufactured in−house. As opposed to a pulsed valve operating at 10 Hz, using a continuous flow jet allows each incident laser pulse to seed the medium and circumvents the need for having an apparatus to synchronise the laser shots with the opening time of the valve poppet. Using such a thin gas jet will also minimise the propagation effects which can complicate the phase−matching of the generated harmonics. A continuous flow jet can also be used in molecular alignment experiments provided that the jet construction fulfils the conditions for obtaining a supersonic expansion [120].

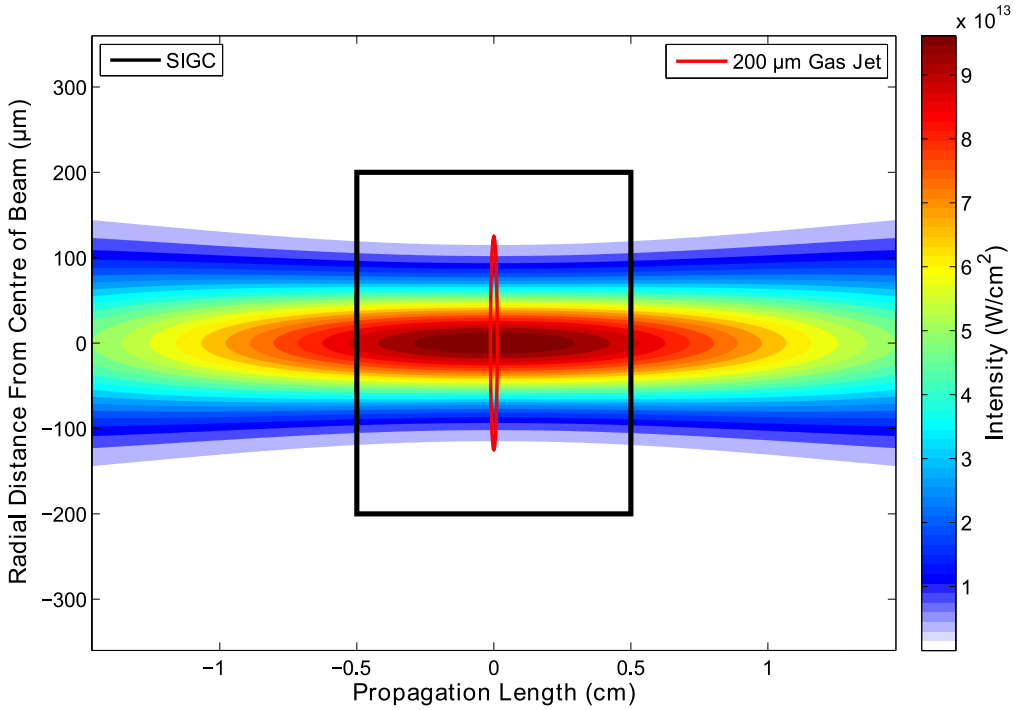


Figure 4.8: Simulation of a Gaussian pulse at 1735 nm with a 90 μm beam waist which propagates through a SIGC with 400 μm apertures, 1 cm long and a 200 μm orifice continuous flow gas jet

Whilst gas cells are a popular and functioning choice of source for some molecular

HHG experiments, they can be difficult to heat due to their shapes. Thus, in order to have the capability to work with an extensive range of molecules it is necessary to be able to heat the sample to generate sufficient vapour pressure to perform experiments, especially in the cases where some interesting molecules have extremely low vapour pressures at room temperature. The following sections will present the progress made towards the design and development of a heated gas jet source at Imperial College.

Figure 4.8 is a simulation of a Gaussian pulse traversing a SIGC and a gas jet. The purpose of this calculation is to illustrate the effects of the intensity gradients of the pulse over the medium length. The dimensions of the SIGC are 400 μm apertures and a length of 1 cm. The gas jet has a propagation length of 500 μm which has been calculated from assuming the laser focus is 2 nozzle diameters (200 μm) above the jet opening and that the angle of the supersonic expansion cone is 30°. This simulation takes the drive wavelength to be 1735 nm, as in the experiments performed in this thesis. We also assume a beam waist of 90 μm which is similar to that at the output of the hollow core fibre which is used to broaden the spectrum for further pulse compression. This will be elaborated upon in the laser technology chapter. The Rayleigh range is calculated from expression 4.1 below to be 14.66 mm:

$$z_r = \frac{\omega_0^2 \pi}{\lambda} \tag{4.1}$$

This plot assumes that the density of the medium is identical for both the cell and the gas jet. This illustrates that the phase−matching is simpler to understand and will have less of an effect upon the spectrum in the jet than in the cell. In the paper by Gaarde *et al* in 2006 [168] their calculations on how the ultrashort pulse and the non-linear medium interact illustrate how the intensity profile of a 7 fs pulse with a peak intensity of 9×10^{14} W/cm^2 is altered by propagating through a 3 mm neon medium. Figure 4.9 below shows the spatiotemporal intensity profile of the incident beam at the beginning and the end of the neon medium in which the XUV radiation is generated.

Since the ionization driven reshaping of the pulse profile occurs in the first half of the medium where the intensity is still high, the harmonics are generated by the

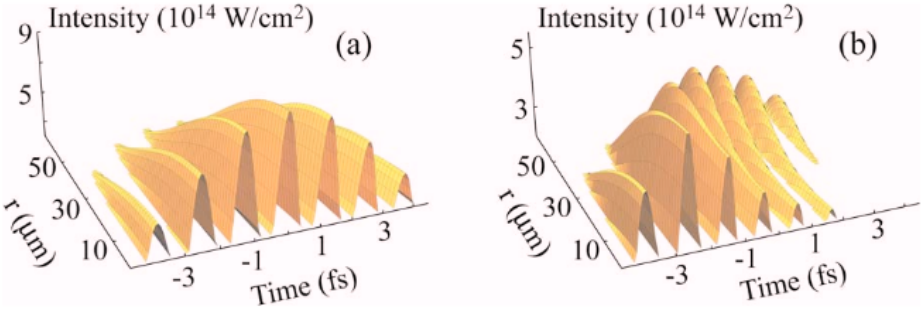


Figure 4.9: Intensity profile in space and time of a laser pulse at the (a) beginning and (b) end of a 3 mm long neon gas cell. The initial peak intensity of the 7 fs, 750 nm laser pulse is 9×10^{14} W/cm^2. The CEP is $\frac{\pi}{2}$ [168]

distorted pulse in the latter half of the medium. Free electrons will give rise to spatial and temporal variations in the refractive index of the medium which leads to self phase modulation and defocusing.

4.2.2 Earlier heated gas jet for vapour phase molecular HHG

The first heated gas jet system designed specifically for HHG in organic molecules was developed and implemented at Imperial College London in 2000. This apparatus consists of a commercial pulsed solenoid gas valve (General Valve Corporation - Series 9) which was incorporated into a heating system aimed at producing jets of organic molecules [153]. A schematic of this jet is shown in Figure 4.10.

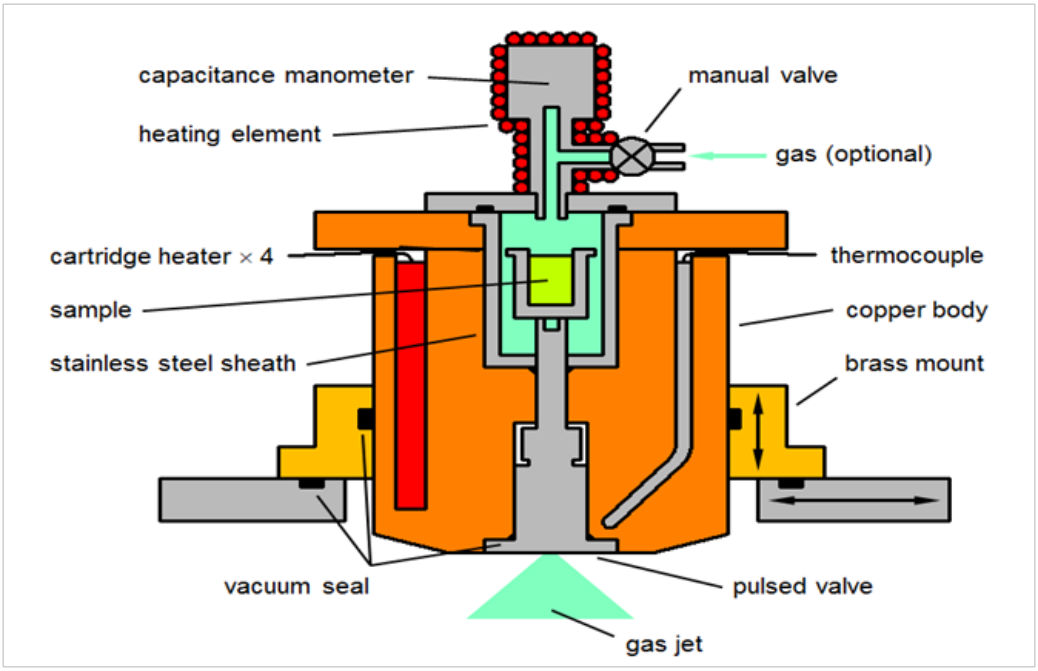


Figure 4.10: Temperature controlled pulsed valve that was first used at Imperial College for molecular HHG experiments on samples that are in the liquid phase at room temperature [153]

The commercial valve is encased in a cylindrical copper jacket that is mounted on top of the vacuum chamber. A stainless steel crucible is at the heart of the apparatus and can house ~ 5 mL of liquid phase sample. The crucible is held in a stainless steel sheath which is in contact with the outer copper jacket. There are four holes bored in the copper jacket each of which accommodates a 150 W cartridge heater. The temperature of the copper jacket is monitored by a K-type thermocouple, the tip of which is located close to the jet orifice. A feedthrough for gas is located on a T-piece at the top of the jet assembly for the purposes of flushing or purging the system. The sample vapour pressure is monitored by a capacitance manometer located on the top

branch of the T-piece. A Thermocoax heating element heats this section of the valve assembly and is kept at a higher temperature relative to that of the copper jacket to ensure no condensation occurs inside the capacitance manometer. The copper jacket can be heated to 200 °C. Since the manometer is only rated to operate at a maximum temperature of 150 °C, it must be removed for situations where the assembly temperature exceeds this value.

Whilst this valve worked very well for the system it was installed on [85] [171] [79] it does have some limitations in its design which render it unsuitable to be revived for the experiments planned in this thesis. As stated previously, the pulsed valve operates at 10 Hz whereas the current laser system is at 1 kHz which is wasteful of laser shots. Looking at the wavelength scaling relationship again, $\eta \propto \lambda^{-6}$ it is evident, for example, that moving from 800 nm to 1600 nm results in a factor of 1/64 less signal. This implies that we need a high repetition rate laser to compensate for this when we move to longer drive wavelengths. The laser system in our laboratory operates at 1 kHz, so a 1 kHz jet is a necessary upgrade but, as outlined with the Even−Lavie valve, the operating temperature tolerance of these 1 kHz jets is unknown.

A second limitation is the sample delivery. Since this design can only house 5 mL of any liquid sample at any one time it is impractical for experiments where a comparison between various samples is sought. The chamber would need to be let up to atmosphere in order to remove the crucible and to insert another one with a different sample making comparison experiments time consuming and difficult.

Since the experiments intended for this thesis involve using a wider range of molecules and where comparisons between samples is sought, a new gas delivery system is necessary. The rest of this chapter will present the developments which have been made towards an apparatus which will allow us to quickly switch between samples, non-invasive of the experiment. It is important that the apparatus is designed around using a continuous flow gas jet to keep the propagation length as short as possible to minimise phase−matching effects.

4.2.3 Design and development of an apparatus for multi-source HHG in vapours

The vapour generation procedure requires three different heating components: the initial vapour generation stage, the heating of the delivery lines to the vacuum chamber and the heating of the piping and gas jet internal of the vacuum chamber. Commercial heaters were used for both the vapour generation stage and the heating of the delivery lines external of the chamber.

Figure 4.11 illustrates the first apparatus designed for performing HHG in a benzene vapour. A commercial 7 L capacity waterbath (WNE 7, Memmert) was used to heat the stainless steel vessels containing the benzene liquid. The vessels containing the samples can be removed from the delivery lines via the quick connects allowing the samples to be switched efficiently without interfering with the vacuum chamber. Silicone rubber tape is used to heat the piping leading to the vacuum chamber to prevent the vapour from condensing. This design also incorporated a backing gas line. The intention of this was to use a higher ionization potential gas such as Helium ($I_p = 24$ eV) as a carrier gas. The carrier gas also assists in achieving greater rotational cooling of the benzene molecules for molecular alignment experiments. A gas bottle line was also included adjacent to the quick connect assembly for the cases where a comparison atom or molecules would be needed.

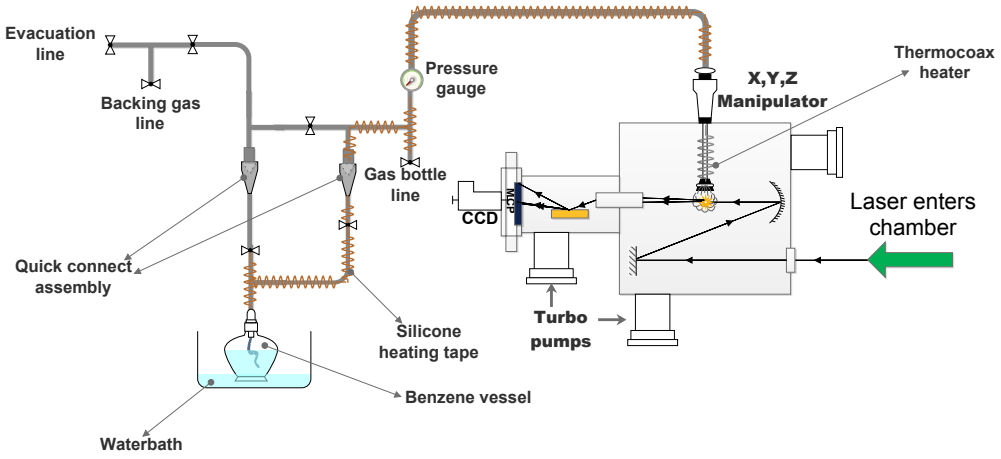


Figure 4.11: Layout of the mark I apparatus designed to perform molecular HHG experiments from a liquid phase target

A commercial heater (Thermocoax Ltd.) was used to heat the tubing and gas jet which are under vacuum. A schematic of the heater and how it was used to heat the tubing and gas jet under vacuum is shown in Figure 4.12. This tubular heating element consists of a nichrome (NiCr) core which is electrically insulated from an Inconel 600 alloy sheath by fused magnesium oxide (MgO) powder. This heater was selected as it was very easy to mould around the stainless steel piping and the gas jet. Inconel 600 is also corrosion resistant rendering it suitable to be exposed to the organic molecules.

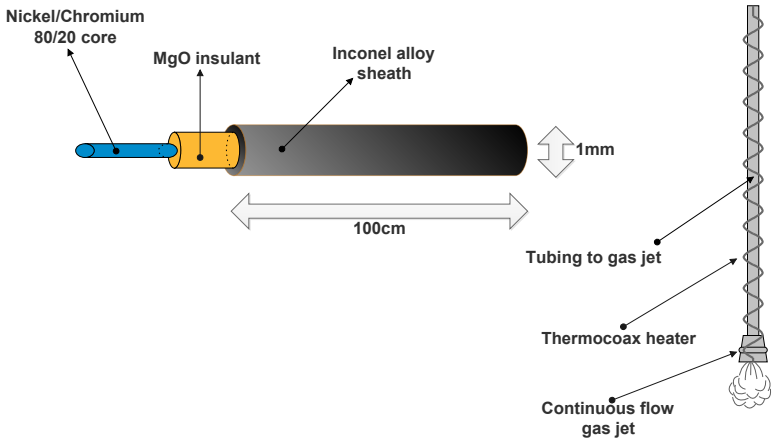


Figure 4.12: Layout of the Thermocoax heater used to heat the gas jet (left) and how it was fitted around the jet assembly (right)

Although this apparatus was sufficient to demonstrate the generation of harmonics from benzene using a continuous flow nozzle and the mid-IR radiation from the TOPAS, it did suffer from a number of complications as listed below:

- The coaxial cable used to resistively heat the tubing and the gas jet proved to be an unreliable and inefficient heater. The heater itself could only provide $\approx$ 40% coverage of the tubing due to its thin diameter and limited length of the hot ends. Since stainless steel is such a poor conductor of heat this lead to instabilities in the generation of a stable vapour.

- The poor coverage also led to problems in establishing contact between the thermocouple used to measure the temperature and the surface of the metal tubing.

- The thin diameter of the heating element also failed the application as it is not designed to be reshaped or remoulded after the initial installation. This is wholly impractical, as the gas jet needs to be changed periodically or removed and inspected for blockages. After no more than three of these checks the coaxial cable had fractured.

- The gas jet insertion geometry also proved to be impractical. Due to the gas jet manipulator being inserted from the top of the chamber and space constraints on the floor the vapour had to traverse a distance of $\approx$2.5 metres before reaching the gas jet. There was also an additional complication of the gas jet getting blocked due to the benzene vapour dissolving debris and residue in the tubing, which when dislodged, ended up falling and blocking the nozzle.

In light of these complications found in the first design, the vacuum heating system was completely redesigned. It was decided to insert the gas jet from below the laser beam as opposed to above in order to minimize problems with blockages of the jet occurring. This geometry was also favourable as it minimized the path length the vapour has to traverse before reaching the gas jet.

A mineral insulated band heater was chosen to heat the gas jet (Watlow Ltd.). Due to the small diameter of the jet in comparison to the heater, a copper jacket was constructed to establish contact between both elements. The jacket also incorporates a stable seat for the thermocouple for the gas jet. This design allows one to change the gas jet without compromising the installation of the tubing heater and its robust construction greatly diminishes the risk of damaging the heating element. The tubing leading to the jet is heated by a silicone rubber heater (Watlow Ltd) which provides >80% coverage of the tubing and has its own thermocouple installed in contact with the tubing. Both heating elements are controlled independently of one another by a 2 channel PID temperature controller. Figure 4.13 illustrates the construction of the new vacuum heating system and a block diagram explaining the operation of the heaters.

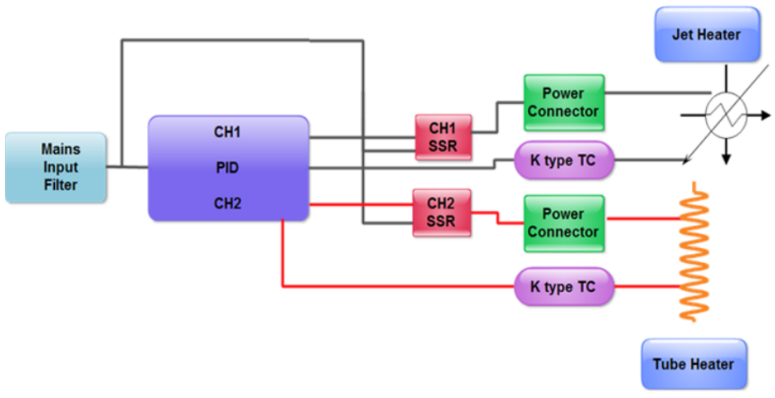


Figure 4.13: Block diagram of inhouse heating system mark II. SSR: solid state relay, CH1: channel 1, CH2: channel 2, TC: thermocouple, PID: proportional−integral−derivative controller

Two solid state relays (SSR) are used to switch power to the heaters. The type chosen are "zero switching" wherein the switching of the relay from a non-conducting to a conducting state occurs when the AC mains voltage reaches the zero-crossing point of the sine-wave. Figure 4.14 illustrates the operation of a zero-crossing solid state relay. At point (a) the control voltage is applied to the relay. The relay does not permit the load current to flow through to the output until the next crossing of the sine wave, which is at point (b). At point (c), the control voltage is removed from the SSR input which then stops conducting the load current at point (d).

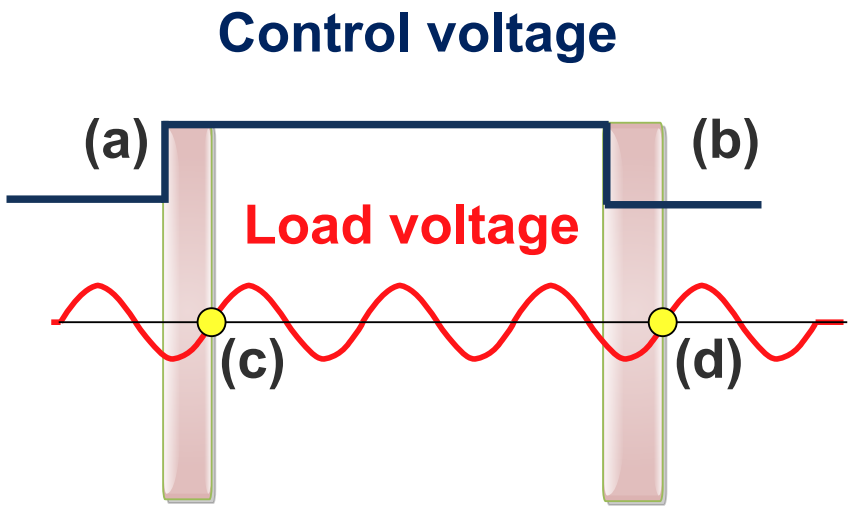


Figure 4.14: Stages of operation for a zero-crossing solid state relay

The brass jacket which forms a contact between the gas jet nut and the ring heater is held to the gas jet nut by four grub screws, each making contact with an exposed side of the gas jets hexagon shape. The gas jet thermocouple sits in a seat on the brass jacket. The gas jet and the thermocouple are not in direct contact; 2.0 mm of brass separates the two elements. This arrangement eliminates the problem with the previous design of having the thermocouple in direct contact with the gas jet nut which was prone to slipping as the gas jet was moved by the manipulator. Alignment of the gas jet could also present the possibility of ablating the thermocouple with the focused laser beam.

The length of pipe inside the chamber, which terminates with the gas jet nozzle, is

wrapped in Kapton tape before the tube heater is wrapped around it. The Kapton tape functions to electrically isolate the heater from the piping. This heater is pre-formed to fit a 6 mm diameter pipe and can be easily slid around the piping. The thermocouple accompanying this heater is inserted under the heating tape midway up the section of piping. There is nearly full coverage of the piping from its origin at the manipulator up to the union with the gas jet nut.

Naturally the piping which has to support the weight of the brass jacket assembly is prone to wobbling as the gas jet is moved by the manipulator. The first attempt at rectifying this problem was to install an anti vibration tube. This simply consisted of an outer tube around the tubular heater, a ring which could be moved up and down the tube and a spring which makes contact with the bottom of the brass jacket. The ring is wound around the tube such that the spring is tight under the brass jacket. Whilst this design did reduce the vibrations associated with translating the gas jet up and down, the lateral vibrations still remained. Figure 4.15 illustrates the heating system for the tubing and the gas jet as it is in the vacuum chamber.

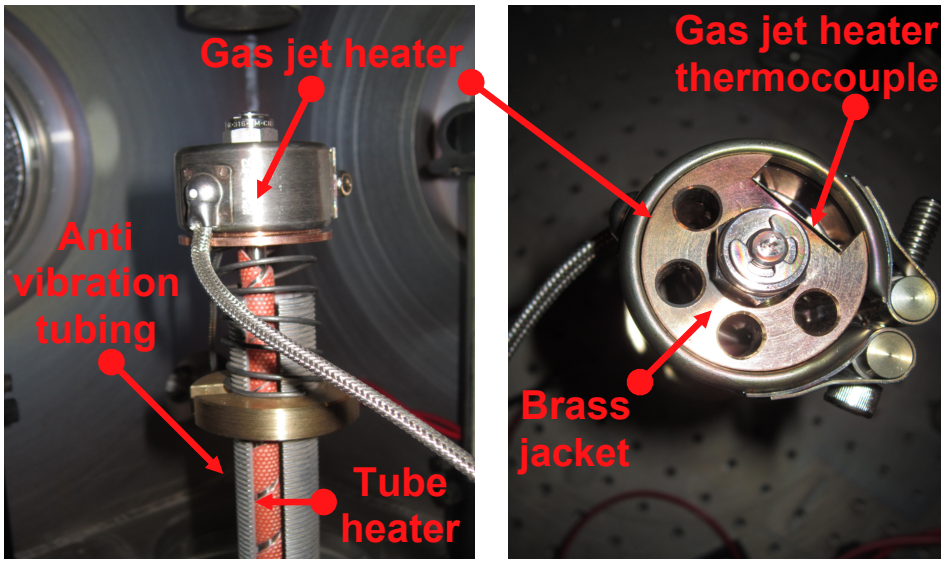


Figure 4.15: The in-house designed heaters for the gas jet and the tubing to the gas jet as it is in the vacuum chamber

Figure 4.16 below illustrates the new design for limiting the vibrations that occur when moving the gas jet. The mount simply consists of a nitrile o-ring around the tubing to the gas jet which is clamped by a set of screws concentric of the enclosing

metal mount. This is held in place by an optical post which is affixed to the mount by a grub screw. The structure is stably held by two angle clamps and optical posts perpendicular to the post supporting the mount. These posts are bolted to the breadboard of the HHG chamber. This construction limits lateral vibrations of the jet whilst still permitting it to be moved up and down with minimal backlash.

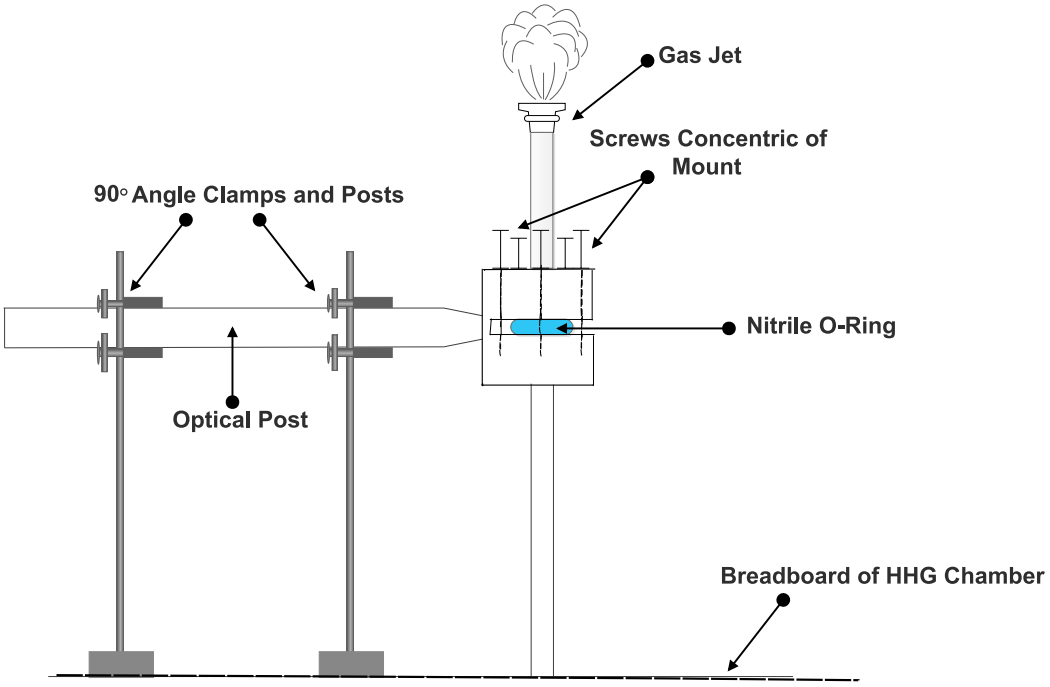


Figure 4.16: The redesign of the mount to dampen vibrations and backlash arising from the translation of the gas jet laterally and transversally

4.3 Other modifications for working with organic molecules

In order to work with the organic molecules in the vapour phase a number of their characteristics must be considered and accommodated to prevent damage to the vacuum chamber and its components. Since the organic molecules are in the liquid phase at room temperature, it is important to keep the delivery lines heated to prevent con-

densation. Since dry scroll or rotary vane pumps are not suited to pumping corrosive or liquid phase molecules the vacuum pumping must also be adapted accordingly. This section will discuss each of the modifications in turn and detail their importance to the system.

4.3.1 Pumping system

We have used turbomolecular pumps backed by scroll pumps with condensers and cold traps for the chamber when handling the organic vapours. To justify this arrangement I will now survey the main types of primary pumps and how they are suited to dealing with the vapours. The backing pumps used on the experimental chamber previously have been generic dry scroll pumps or rotary-vane pumps. Rotary pumps have the advantage of requiring very little maintenance and their pump oil is multi-purpose [172]. Figure 4.17 is a schematic of the operation of a rotary pump. The pump oil acts to lubricate all the moving parts in the pump and serves as a heat transfer medium to prevent overheating. As the rotor of the pump revolves, it divides the working chamber into two separate spaces. Gas flows into the suction chamber until it is sealed off by the second vane of the rotor. The volume of gas sealed off is then compressed before the outlet valve opens against atmospheric pressure expelling the gas through the outlet valve.

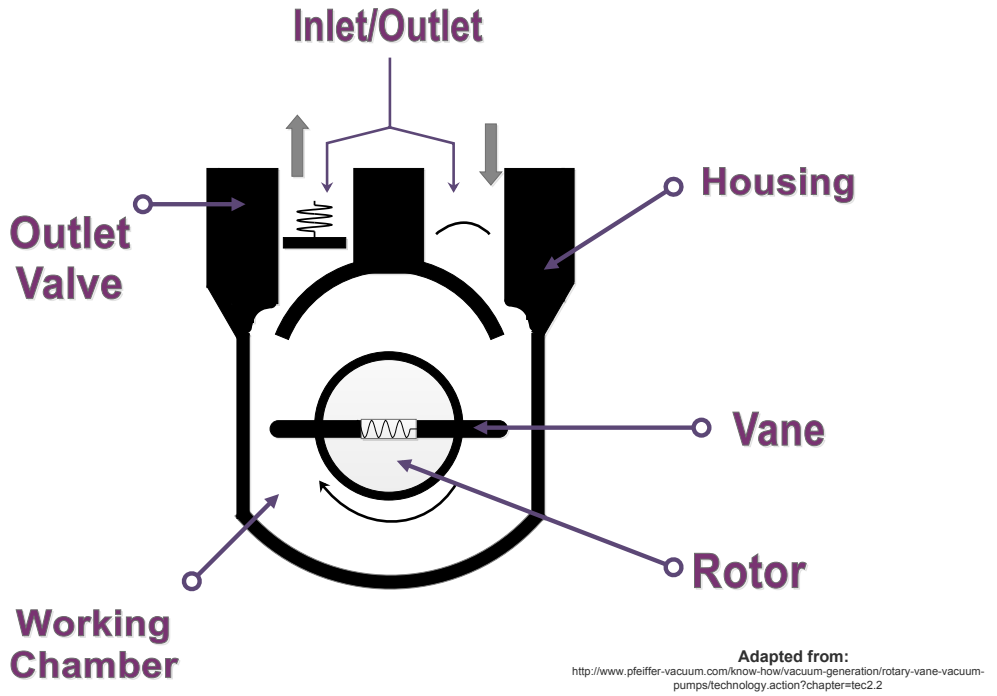


Figure 4.17: Main components involved in the operation of a rotary vane pump

Whilst rotary-vane pumps are credited for their longevity and reliability, their advantages are compromised by the potential contamination that can result from the pump oil. Backflow contamination from the pump to the vacuum chamber can occur due to a number of factors. "Suck back" involves the displacement of oil from the pump into the rest of the vacuum lines and chamber under the influence of atmospheric pressure [172]. This is most likely to occur in the event of a power failure whilst the system connected to the pump is still under vacuum. As the experimental chamber is housing an MCP which needs to be kept under a vacuum, a rotary-vane pump would be operating continuously and the oil would gradually heat up due to mechanical energy heat transfer. As the oil temperature increases, the vapour pressure also increases which can migrate back into the vacuum chamber and bellows lines. This usually occurs when low quality oil is being used. The use of more expensive oil with a lower vapour pressure at elevated temperatures will reduce the likelihood of back streaming but does add an additional cost to the upkeep of the pump.

There are a number of effective methods to minimise the backflow contamination.

Activated alumina is highly porous and can be used as a foreline trap to absorb back migrating oil. As practical an option as it may seem, foreline traps need to be regularly inspected as they eventually do become saturated with oil. Whilst they can be refreshed by baking the housing basket this is a time consuming process.
A less expensive method for reducing backflow contamination is using a gas ballast. This consists of simply leaking dry nitrogen into the foreline. Dry nitrogen is purged into the system at such a rate that the pressure in the foreline is in the viscous flow regime. Under these conditions, molecule-molecule collisions dominate the flow process such that the nitrogen molecules act as a barrier to the oil moving upstream.

Although oil pumps are undoubtedly a well established technology, they do have the downside of requiring considerable maintenance and incorporations for preventing backwards oil migration. As there is no definitive solution to completely preventing backstreaming it is more time and cost effective to use a dry pump in place of a rotary where oil must be completely eliminated from the system.
Whilst there are an abundance of oil free primary pumps, only scroll pumps will be discussed here as they are the variety of roughing pump that has been used on the vacuum chamber under discussion. Typically two Archimedes spirals made from Teflon are used: one is static, the other orbiting the stator. The orbiting spiral traps air pockets and compresses inward flowing gas to generate a vacuum. The only form of maintenance required for this type of pump is the replacement of the tip seals. Wearing of the tip seals can be detected when either the time taken to achieve the specified vacuum level, or the ability of the pump to even reach this value, becomes problematic or difficult.

In order to employ scroll pumps to the pumping of the Volatile Organic Compounds (VOC's) vapours a few modifications need to be made to both the interior of the pump and to the vacuum lines. Chemically resistant scroll pumps are available and differ from regular dry scrolls in the wetted parts they contain; PTFE or fluorinated plastics are resistant to chemical degradation and thus enable the pump to handle aggressive vapours. Whilst wetted parts enable the pump to handle organic vapours they do not prevent the vapour from condensing in the pump. If a significant volume of vapour is being pumped, the condensed liquid can solidify on the PTFE heads in the pump which can cause corrosion and pump failure. A dry nitrogen ballast can

prevent the vapour from condensing in the pump body. The pump is compressing the vapour as it passes through and if the vapour is dense enough the compression can cause it to condense. If ballast is used to purge some dry nitrogen into the compression chamber then atmospheric pressure is reached at a lower compression ratio and hence, less vapour condenses.

Naturally it is more sensible to mitigate the problems of a vapour condensing before it reaches the scroll pump. For this thesis, a condensate separator and a cold trap were used in conjunction. A condensate separator simply sits before the intake to the pump and prevents liquid droplets from entering the pump; it also serves to prevent the collection of liquid in the pumping lines [173]. By far the most effective means for protecting the pump from vapours is by using a cold trap. A cold trap was installed after the condensate separator in the set-up used for this thesis. The trap is filled with liquid nitrogen which is at -187 °C at atmospheric pressure. The trap rapidly solidifies any liquid that is exposed to it. The only downside to using cold traps is that they must be constantly filled with liquid nitrogen while the vapour is being pumped. For this reason, in the apparatus constructed, a bypass line has been made whereby the cold trap and condenser assembly can be isolated from the vacuum chamber and scroll pump by two vacuum valves and a direct line between the pump and the chamber can be used when the vapour is not flowing.

4.3.2 Moving flange for MCP detector and CCD

Due to the small size of the MCP detector (40 mm), we are unable to record a full HHG spectrum (plateau and cut-off) with a stationary MCP now that we are using the longer wavelength (near-IR 1200-2000 nm) source to extend the cut-off of the spectrum. To overcome this limitation we have developed a moving flange for the MCP and CCD. This allows us to record the whole spectrum that can be stitched together by noting the various positions of the MCP for data collection.

A schematic of the flange design is shown in Figure 4.18. A vernier callipers has been attached to the flange enabling us to note an arbitrary position for the MCP. Following from spectral calibration of the harmonics we then know what MCP positions correspond to the plateau and cut-off of our spectrum. Calibration of the spectrum can be performed by using a target with strong emission lines that can be distinguished from tables of the data. The drawbacks of this method include the appearance of emission lines that can be attributed to impurities in the sample and failure to identify first from second order diffracted peaks. The method that is used for the spectral calibration in this thesis is to use spectral filters. The spectrometer is calibrated by recording an image of the harmonics with a thin aluminium, zinc or germanium filter in the beam path. For example, from the CRXO plots, aluminium shows a steep drop in transmission at its L−edge at 72.7 eV. In conjunction with the grating equation, this allows for a spectral calibration of the spectrometer.

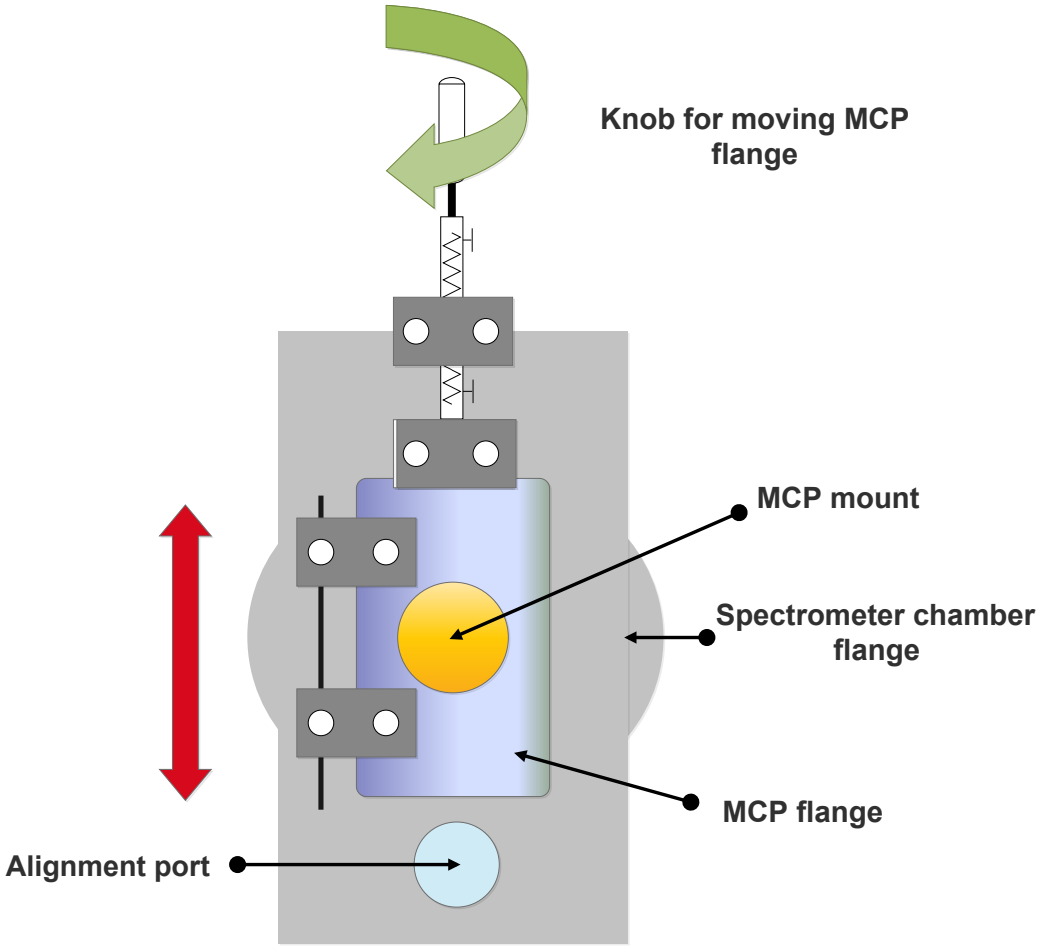


Figure 4.18: Moving MCP flange with main components labelled

4.3.3 Jet orientation

Preliminary experiments were carried out with the gas jet manipulator flanged to the port on top of the chamber. Whilst this has been the normal mode of operation previously it led to drawbacks when working with the organic vapours. Since benzene is an excellent solvent it had the effect of detaching any dirt or burrs from the inner walls of the delivery tubing. These particulates ended up clogging the gas jet, as it was observed that the vapour pressure reaching the interaction region was periodically compromised. Inspection of the jet under a microscope showed the build up of small particles in the 100 μm nozzle. To solve this problem, the jet orientation was changed so that it was flanged to the bottom of the chamber. In this configuration gravity

works in our favour as any loose particles stay in the tubing and cannot block the gas jet during experiments.

4.3.4 Cold traps on vacuum chamber

It was also observed during the initial experiments that the optical elements were becoming coated with condensed vapour, which was contributing to the rapid degradation of the mirrors in the chamber. No damage was observed on the flat field grating or the MCP detector which we suspected was due to the differential pumping gradient. This pumping arrangement inhibits the volume of vapour that can seep into the spectrometer chamber. Nevertheless, a cold trap filled with liquid nitrogen was installed on both the generation and spectrometer chambers to prevent any vapour being deposited on the optics. One could also bake the chamber to prevent the vapour from condensing but this is both a dangerous and impractical task as it requires having the entire outer walls of the chamber covered in heater tape and at an elevated temperature. Whilst this is a standard procedure in a lot of laboratories it was not implemented to prevent the vapour from condensing in this apparatus as it would necessitate the entire chamber being covered in heater tape at $\approx 200°C$. This would not only be very expensive to implement due to the size of the vacuum chamber but also it is more dangerous than using the cold traps as one could get burned, especially if components such as the moving flange, described in section 4.3.2, have to be heated at an elevated temperature and need to be adjusted by hand.

4.3.5 Spectrometer chamber material

As has been stated previously, the original housing for the flat field spectrometer was an anodized aluminium chamber. Anodizing aluminium is advantageous for the durability of the metal when compared to using raw aluminium. The deposited Al_2O_3 is a non−conductive, amorphous, transparent layer which is typically tens of nanometres in thickness. A major drawback of anodizing aluminium is that the aluminium oxide layer is highly porous. High porosity consequently results in a high outgassing rate [172]. The outgassing rate of a material specifies the amount of gas leaving a surface under vacuum in unit time. Outgassing rates are commonly quoted either by Torr x Litres per Squared Centimetre per Second or in units of Watts per Metre Squared (W/m^2) [174].

Table 4.1: Outgassing rates of anodized aluminium and stainless steel after 1 hour and 10 hours of pumping under similar conditions [175]

Material	K_1 torr $\frac{l}{s}/cm^2$ $(\times 10^{10})$	K_{10} torr $\frac{l}{s}/cm^2$ $(\times 10^{10})$
Al, anodized (2μm pores)	2760	322
SS304, mechanically polished	17.1	4.6

Permeation occurs with virtually every material but it is highly elevated in Al_2O_3. Pore size can vary widely depending on the nature of the anodizing procedure but is typically in the micron range. The oxide layer absorbs large quantities of organic vapour and then slowly desorbs them back into the vacuum space. This is disastrous for the spectrometer chamber as it needs to reach a vacuum level below 1×10^{-6} mbar to enable us to operate the MCP whilst there is a gas load present. The time taken for the chamber to reach this level drastically increased from a matter of hours to in excess of 24 hours. Not much improvement was made on this by baking out the chamber. A stainless steel detection chamber was designed and installed in 2013 and has been the detection chamber for all the experimental data presented in this thesis.

Table 4.1 illustrates the outgassing rate of anodized aluminium compared to mechanically polished stainless steel for both 1 and 10 hour pumping times. The outgassing rate in the aluminium is higher than that of stainless steel by a factor of 160 after 1 hour of pumping [175]. It must be kept in mind that there are numerous conditions in which the outgassing rate can be measured and it is dependent on the condition of the surface so these numbers are merely an example of how poor anodized aluminium is compared to stainless steel.

4.4 Working apparatus for vapour phase molecular HHG

The preceding sections of this chapter have discussed the previous methods used to perform HHG in organic molecules that are liquid phase at room temperature. The modifications which had to be made to the original HHG chamber in our laboratory in order for us to perform experiments without compromising the health of the vacuum system have also been outlined. Figure 4.19 illustrates the complete apparatus that

has been developed. These developments have resulted in a number of milestones for us in performing molecular HHG in a wider range of liquid phase targets:

- Moving the MCP flange increases the spectral range of data collection.
- Baratron to measure to backing pressure behind the gas−jet to three significant figures. The baratron power supply has been constructed in house to communicate with the data acquisition program to log the backing pressure over time.
- Ability to perform comparative measurements between molecules without having to disrupt the experiment.
- Choice of continuous flow gas jet will minimise the propagation length for phase−matching and self−absorption.
- Apparatus has been upgraded to ensure there is no degradation of components due to exposure to organic molecules.

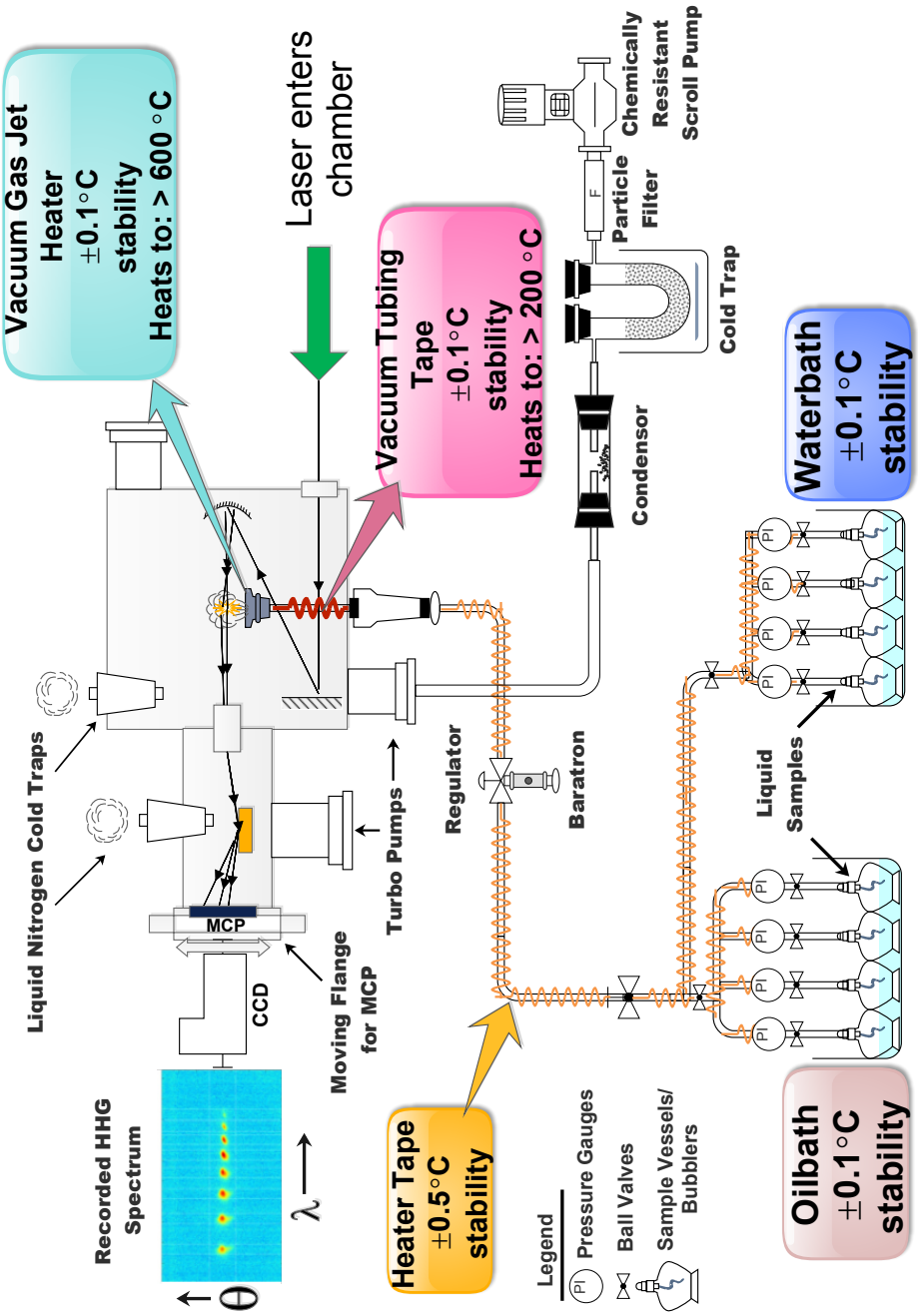


Figure 4.19: The complete apparatus that has been used for the experiments performed in this thesis.

4.5 Supplementary information on vacuum heater

This section lists the parts illustrated in Figure 4.20 that were used to construct the heater and controller inhouse. Parts list is valid as of March 2015.

Solid State Relay (x2)
Manufacturer: CRYDOM
Order Code: 1846111
Manufacturer Part No: EL240A10-24
http://www.farnell.com/datasheets/1598967.pdf

IEC Filter
IEC 1 fuse SP inlet filter w/red LED,6A
RS Stock No. 214-6158
Brand: Bulgin

K Type Thermocouple Connectors
Manufacturer: LABFACILITY
Farnell Order Code: 7087937
Manufacturer Part No: IS-K-F (IEC)

Manufacturer: B+B THERMO-TECHNIK
Farnell Order Code: 4691362
Manufacturer Part No: 0220 0005

Manufacturer: B+B THERMO-TECHNIK
Farnell Order Code: 4691325
Manufacturer Part No: 0220 0001

Mains Rated Connectors for Connection of Heaters
Manufacturer: NEUTRIK
Farnell Order Code: 892385
Manufacturer Part No: NAC3MPB-1

Manufacturer: NEUTRIK
Farnell Order Code: 892361
Manufacturer Part No: NAC3FCB.

Dual Loop PID Controller
Manufacturer: Watlow
Watlow EZ ZONE PM Integrated Controller
100 - 240 Volts AC supply
Product Code: PM9C1CH-ACCHAAA

Mineral Insulated Band Heater
Manufacturer: Watlow
1 1/2" Internal Diameter, 1" wide
240 Volt,300 Watts
12" type B leads
Product Code: MB1J1AN1-B12

Silicone Rubber Heater
Manufacturer: Watlow
Pre-formed for 1/4" Diameter Pipework
240 Volts, 0.09 Amps, 22 Watts
15" Straight Length @ 80"%" Coverage
Product Code: 005220501

Shim Style Thermocouple for Sensing Band Heater Temperature
Manufacturer: Watlow
K Calibration, Grounded Junction
12" Stainless Steel Braided Leads
Product Code: 75XKSGA012A

Thermocouple for Sensing Silicone Heater Temperature
Manufacturer: Watlow
K Calibration Assembly with Mini Plug, 12" Long Leads
Product Code: Z5639

Controller Drawing.pdf

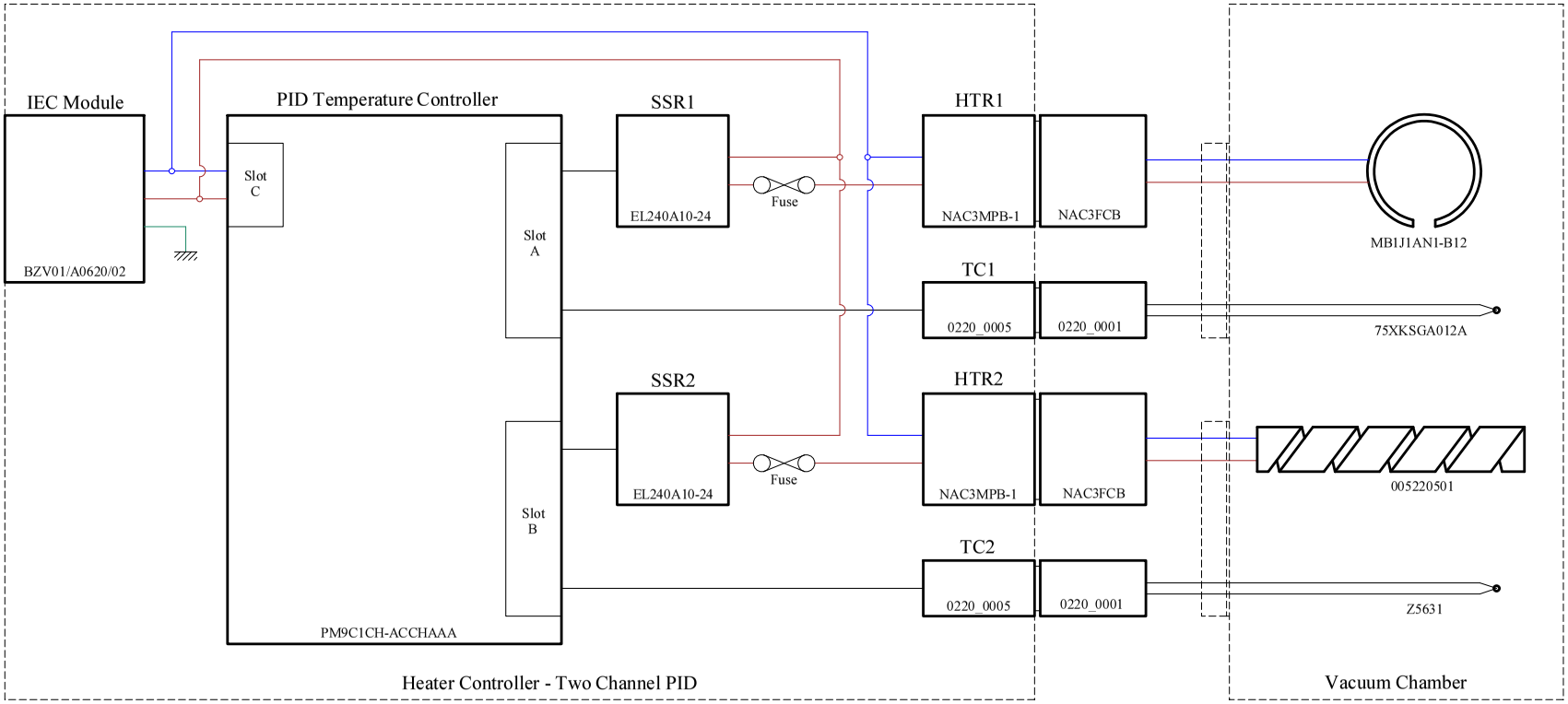


Figure 4.20: Detailed wiring diagram of the vacuum heating system including the part numbers of the components used. SSR is solid state relay, TC is thermocouple, HTR is heater power connector.

Chapter 5

Methodology

This chapter will concentrate on the issues associated with acquiring stable and reproducible HHG spectra from the substituted benzene molecules. The issues shall be addressed chronologically starting with those encountered in the 2013 data acquisition campaign, which was largely concerned with recording preliminary data, and then presenting the issues identified when the 2015 data run was in progress.

5.1 Safety

This use of carcinogenic molecules, class 4 lasers, elevated temperatures, cryogenics and high voltage electronics makes the running of the experiments concerned in this thesis quite hazardous. Every effort has been made to ensure all procedures involved in the experiments are as safe as possible. The preparation of the vessels, each containing ≈ 100 mL of one of the carcinogenic molecules was done in a fume cupboard with adequate personal protective equipment (PPE) in the form of safety glasses, lab coats and gloves. All waste associated with the handling of these molecules was disposed by a specialist hazardous waste contractor located on campus. A gas detector was also purchased and set-up in the vicinity of the experiment. The detector was set to alarm if any vapours from the molecules could be detected. Detailed procedures for the scenario of a leak in the vacuum lines causing lab members to be exposed to vapours was documented and approved by the colleges safety department. People on site have been trained on the use of the breathing apparatus equipment in the unlikely event that someone would have to enter the laboratory to shut off the lines causing the leak of vapour into the atmosphere. Any time the vacuum lines needed

to be changed, respirators were worn by those in the vicinity of the experiment. Any equipment which was exposed to any vapours that was removed from the apparatus went through a rigorous decontamination procedure of being washed in a specialist ultrasonic bath and flushed with a solvent such as high purity acetone, followed by water.

Since the water and oil baths used for the heating of the vessels containing the liquids are operated at temperatures up to 80°C and 140°C respectively, precautions were also taken to ensure no-one could be exposed to the extremely hot liquids. A kick guard was installed around the baths and special covers for the baths were made to ensure that no-one could get in direct contact with the bath liquids. Similarly, for the cases where the cold traps on the vacuum chamber and on the vacuum pump lines needed to be filled routinely with liquid nitrogen (198°C at room temperature) lab members also had to be equipped to deal with a lower temperature extremity. Participants on the experiment received specialist training and PPE for the handling of cryogenic liquids. A splash guard box was also made that could be placed over the cold traps on the vacuum chamber to ensure no splashes of liquid nitrogen could hit lab members or get in contact with the liquids in the water and oil baths.

Since the experiment has been designed to be as safe as possible it was only necessary for the laser protective eyewear to be worn whilst the experiment was running, unless liquid nitrogen needed to be used to top up the cold traps, in which case, the person doing so would wear the gauntlet gloves and splash goggles. Thorough leak testing of the vapour delivery lines with nitrogen before the attachment of the vessels containing the liquids ensured that there were no significant vapour leaks into the laboratory. Very strict checks of the apparatus had to be performed daily to ensure there were no flammable materials in the vicinity of the water and oil baths and the heating tapes on the vapour delivery lines that could ignite. These strict safety measures have ensured that there have been no serious incidents or accidents concerning this experiment throughout the course of this PhD work.

5.2 2013 data run

5.2.1 Spectral calibration

The moving flange was used to record spectra which could then be stitched together using the images acquired at three different MCP positions. Spectral calibration was performed by fitting the grating equation to the harmonics using the MCP vertical offset and the incident angle upon the grating as free parameters. These parameters were measured and the fit to the grating equation was optimised. The results of the fitting procedure are shown in Figure 5.1.

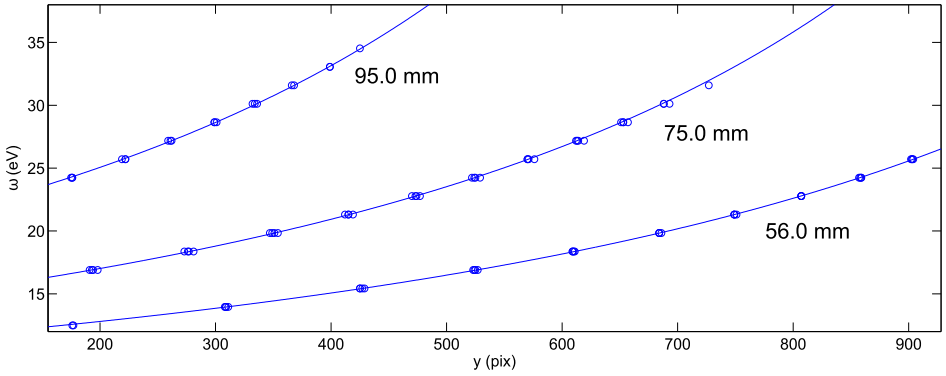


Figure 5.1: Results for the calibration of the energy scale of the spectrum.

Each circle represents the observed position of a harmonic and its assigned photon energy. The three lines each represent an MCP position − two cover the plateau region and one covers the cut−off region of the spectrum. As shown in Figure 5.1, the MCP positions are labelled as 56.0 mm, 75.0 mm and 95.0 mm; these MCP positions represent the distance the MCP flange is moved from an arbitrary offset.

5.2.2 2013 halogenated benzene data

As shown in Figure 5.2, the overall amplitudes for the curves obtained for the three different MCP positions are clearly different. It is evident that it is meaningless to compare absolute harmonic intensities if we get different results for the same molecule.

Spectra were therefore normalized to obtain the best agreement between different MCP positions. Although absolute intensity information is lost, the normalization

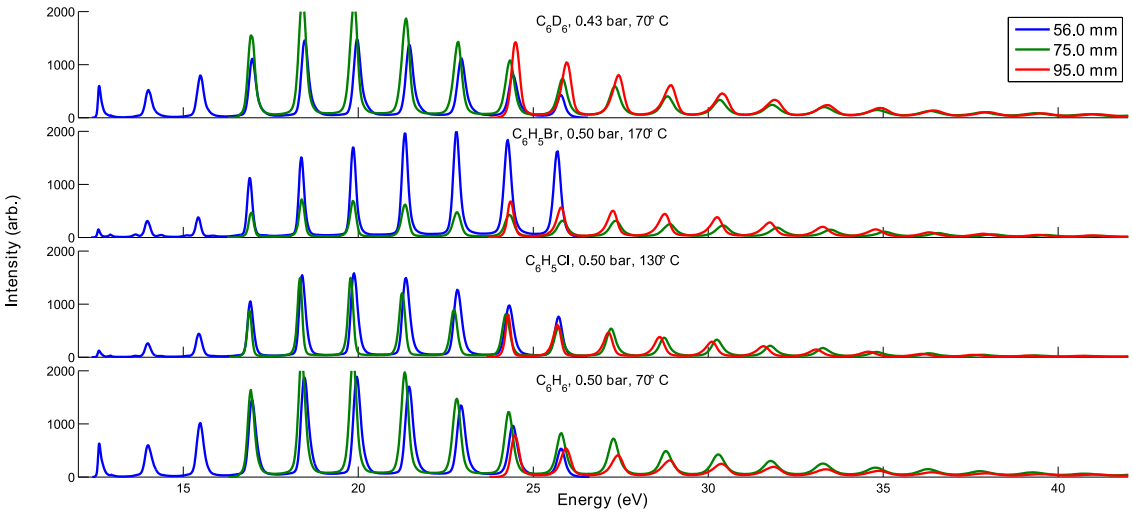


Figure 5.2: Unscaled spectra for deuterated benzene, bromobenzene, chlorobenzene and benzene for the three different MCP flange positions (50 images at 1s exposure time). The individual plot captions also show the backing pressure and the oil bath temperature required to obtain that value.

allows us to compare the shapes of the spectra between different molecules across the full range of MCP positions. Normalization was done by summing the area under each harmonic to get a discrete rather than a continuous spectrum. The discrete spectrum from the first MCP position is then normalized by its total area. The spectra from subsequent MCP positions were then scaled to ensure the same area of the spectrum in the overlapping region that is common with the previous MCP position.

The results of this normalization technique are shown in Figure 5.3 below with the harmonic peaks extracted.

There is reasonable consistency between the different MCP positions now with the exception of the C_6H_5Br spectrum at 270 μJ per pulse on the lowest energy MCP position (the leftmost part of the spectrum). This discrepancy can be attributed to a blip in the laser power. These plots show an enhancement in the higher harmonic orders for the halobenzenes (>25 eV) and a suppression at the lower orders (< 17 eV).

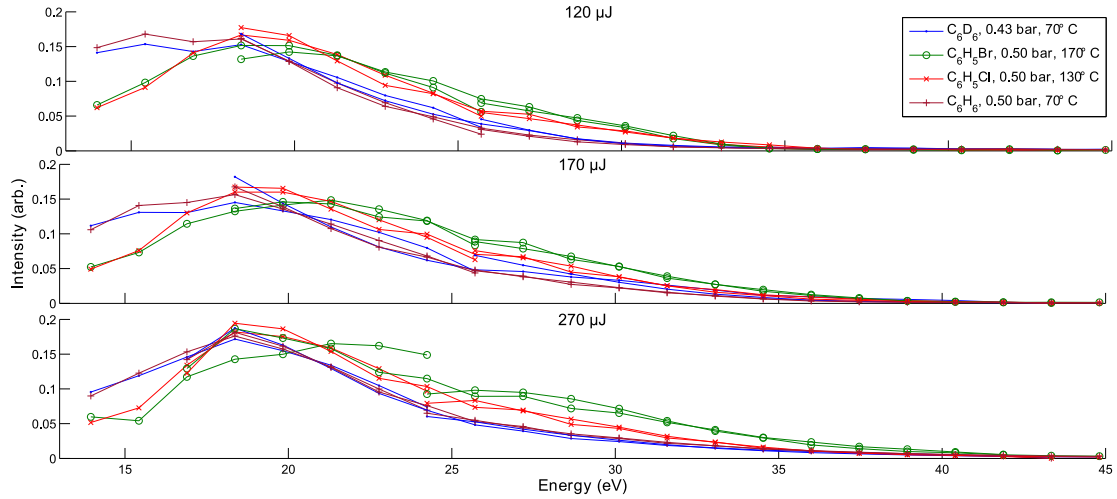


Figure 5.3: Normalised plots for the data shown in Figure 5.2 as a function of beam energy per pulse. 50 images were taken with a 1 s exposure time.

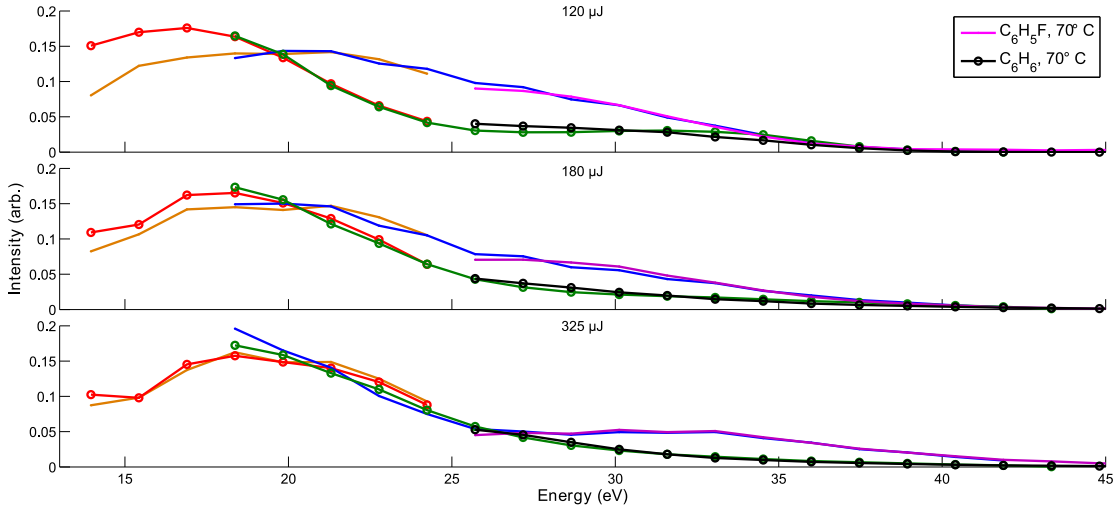


Figure 5.4: Comparison of the spectra for benzene and fluorobenzene as a function of energy per pulse. 50 images were taken with a 1 s exposure time. The straight lines are flourobenzene traces at MCP positions 56mm (brown), 75mm (blue), 95mm (pink), and the lines with circles are benzene at MCP positions 56mm (red), 75mm (green), 95mm (black)

We then switched to performing a comparison between benzene and fluorobenzene. Normalized spectra for C_6H_6 and C_6H_5F are shown in Figure 5.4. This data was taken when the nozzle diameter was 200 μm and for three different laser powers. In a similar manner to the spectra in Figure 5.3, the halogenated molecule exhibits more of a shoulder at the higher harmonic orders and lower signal at lower harmonic orders.

However on a separate day the same comparison between benzene and fluorobenzene was made, the difference between that and those displayed in Figure 5.4 is that the backing pressure for the fluorobenzene was 1.5 bar and that of benzene was 0.5 bar. The reason for the pressure discrepancy was that the oil bath was set to a temperature which gave 0.5 bar of benzene and this temperature was not lowered for fluorobenzene as this would have been extremely time consuming.

The attenuation of the laser beam using a half−wave plate and polariser combination enabled finer power scans to be performed. The enhancement that was observed in Figure 5.4 for the higher harmonic orders in fluorobenzene has disappeared.

This could be attributed to the pressure discrepancy but also could be due to fluctuations from the laser. These finer step intensity plots are displayed in Figure 5.5. The backing pressure for fluorobenzene was 0.75 bar and 1.5 bar at 70° and 110° respectively. A number of factors can contribute to the discrepancies between the fluorobenzene spectra in Figure 5.4 and Figure 5.5. Laser power instabilities and the precision in controlling the backing pressure of the vapour are both key contributors.

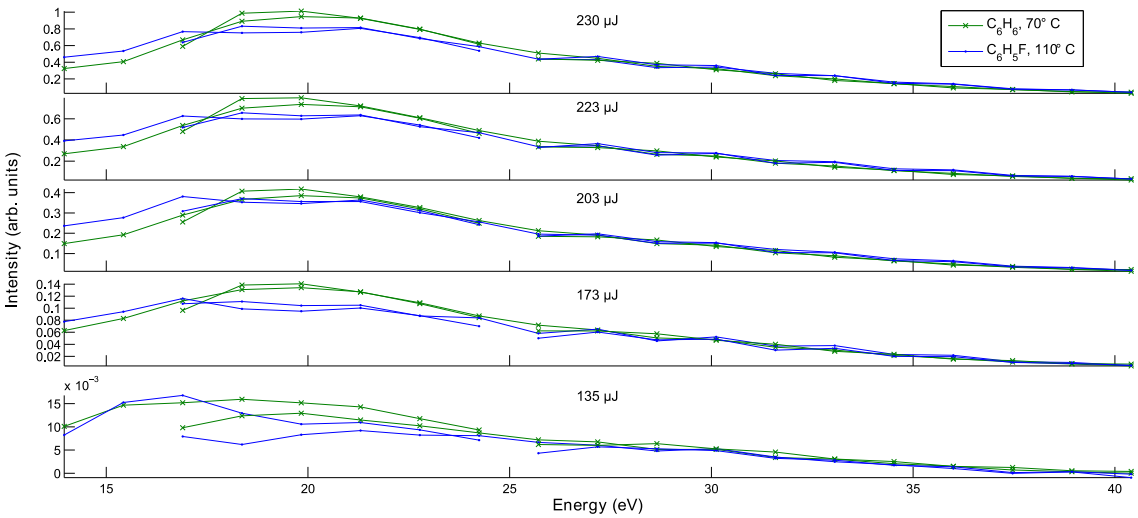


Figure 5.5: Intensity scans comparing the spectra from benzene and fluorobenzene under similar HHG conditions. For each scan 50 images were taken with a 1 s exposure time.

Figure 5.6 shows the unscaled spectra recorded in benzene with a beam energy of 320 μJ per pulse and the 200 μm nozzle as a function of backing pressure for benzene. Note that position of the lowest energy harmonic for the 0.5 bar differs from that of the lowest energy harmonics for the 1.4 and 3.5 bar spectra as it was recorded at an MCP position of 75 mm. The spectra for 1.4 and 3.5 bar were recorded at an MCP position of 83.3 mm. There is a significant variation in the shapes of the spectra for the different backing pressures. The lowest harmonic order (20 eV) intensity is nearly equal for the three spectra whereas the highest differ by almost a factor of two. There is a shift in the harmonic peaks which is possibly due to spectral shifting of the fundamental. To test if this is a physical effect or an artefact of fluctuations in the beam energy the reproducibility of the spectra must be verified. This pressure scan illustrates a clear pressure dependence on the shape of the spectrum. In order to avoid the regime where clustering becomes dominant this indicates that we should operate at the lowest possible backing pressure which still gives us reasonable signal to work with. Naturally, there is a higher HHG signal from the 3.5 bar backing pressure as the number of emitters contributing to the signal is dramatically higher than that of the lower pressure cases. Clusters are formed in the high pressure gas-jet due to the rapid cooling by the adiabatic expansion of the molecules into the vacuum. The harmonic yield scales as the square of the backing pressure in atoms and molecules. It has been observed that for clusters the scaling of harmonic signal with backing pressure is a cubic relationship [176].

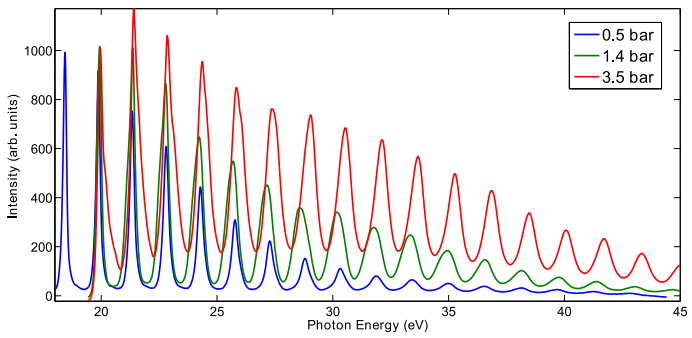


Figure 5.6: Pressure scan in benzene using spectra taken at different times during the data collection day. The time is shown in the legend alongside the backing pressure. There is also clear evidence of spectral shifting of the fundamental which is indicative of instabilities with the laser. 50 images were taken for each scan with a 1 s exposure time.

5.2.3 2013 PACER data

In Figure 5.7, the background subtracted peak heights are plotted as a function of peak number for both molecules. The red crosses represent one data set from C_6D_6 that was recorded at the middle MCP position (MCP d = 75.0 mm) which is a clear outlier when plotted against the other traces. Spectra were recorded at the three MCP positions and the molecules were alternated twice at each MCP position with the exception of C_6D_6 which was accidentally skipped at the middle MCP position.

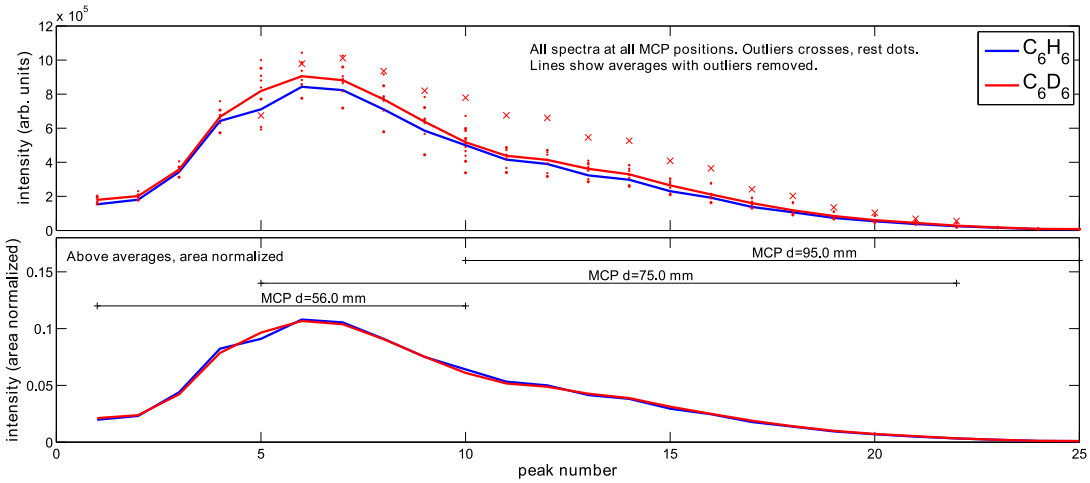


Figure 5.7: Background subtracted peak heights are plotted as a function of peak number for both molecules (top). The area normalised average peak heights are plotted for the three MCP positions (bottom).

In the bottom panel of Figure 5.7, the area normalised average peak heights are plotted for the three MCP positions. The benzene and deuterated benzene spectra are identical from this result.

A slight increase in the ratio was observed in the data that was acquired on a different day during the experimental campaign; this is displayed in Figure 5.8. Four pairs of spectra were acquired at MCP position d = 76.0 mm and 3 pairs were acquired at MCP d = 91.7 mm. The top panel shows the average peak intensity as a function of peak number for both molecules. The middle panel is the area normalised average peak height from the top panel. The bottom panel is the ratio of C_6D_6 to C_6H_6. There is an increase in the magnitude of the ratio with harmonic order. The sudden decrease at peak 19 is attributed to the position where the second MCP position ends. In contrast to Figure 5.7, this result is dubious. Monitoring the harmonic spatial mode throughout the data acquisition would be a useful test to check which results are physical and which are artefacts of the laser fluctuations.

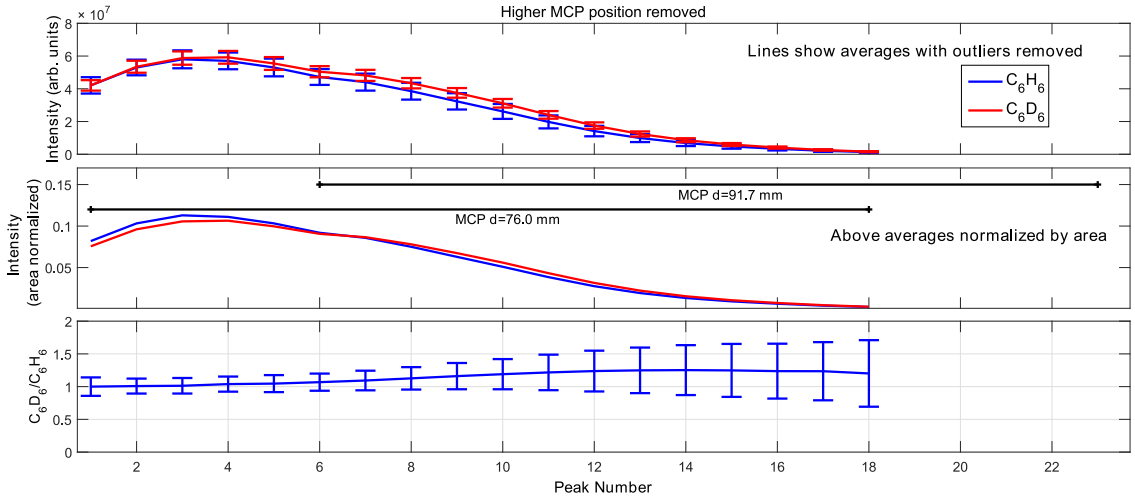


Figure 5.8: The average peak intensity as a function of peak number for both molecules (top). Area normalised average peak height from the top panel (middle). Ratio of C_6D_6 to C_6H_6 (bottom).

5.2.4 Pacer 2013 discussion

The PACER data acquired in the 2013 experimental campaign implies that there is no change in the ratio between the protonated and deuterated species. The discrepancy in the ratio between Figures 5.7 and 5.8 can be substantiated by looking at the stability of the harmonic spatial mode for both data sets as shown in Figures 5.9 and 5.10 respectively.

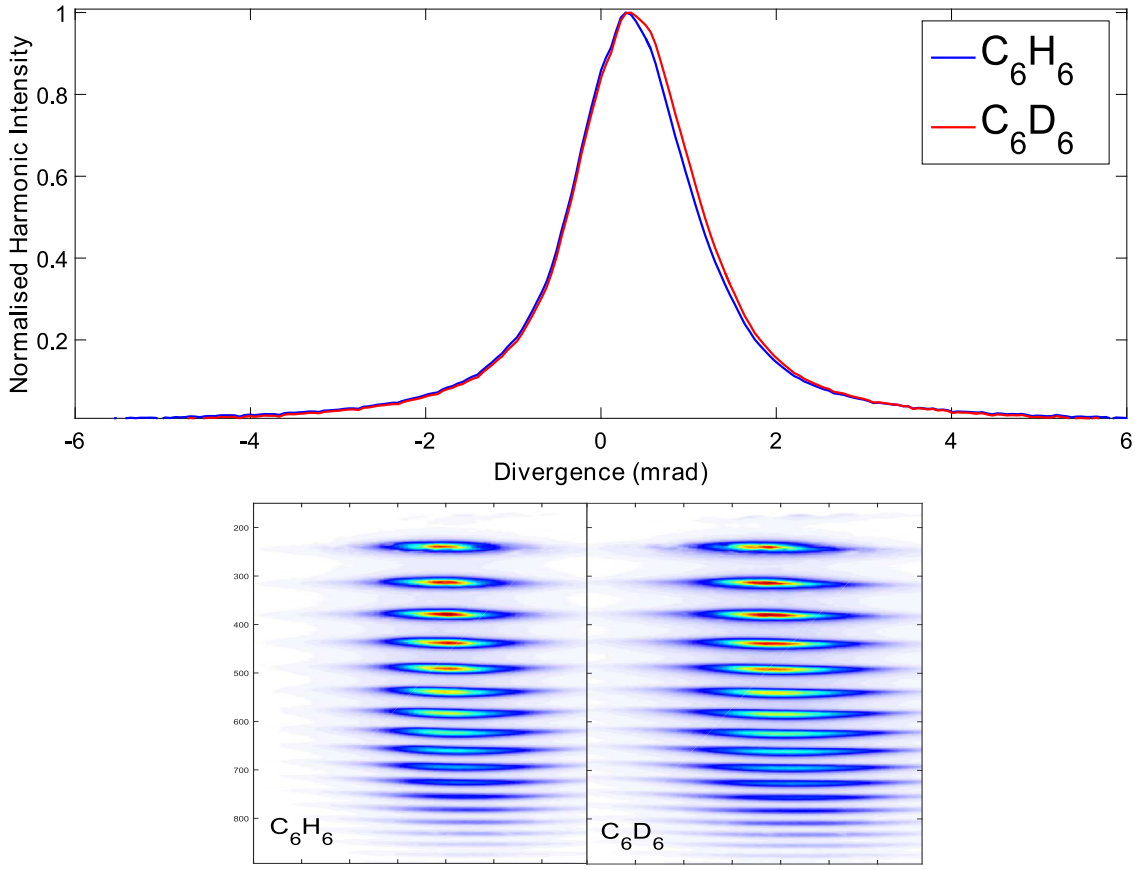


Figure 5.9: Stability of the harmonic spatial mode for the data shown in Figure 5.7

Figures 5.7 and 5.8 represent the spatial modes for benzene and deuterated benzene at two different times during the data acquisition period for the day that the data was taken. These plots were made by taking the mean value of the integrated image of the harmonics, normalising this value to 1 and converting the pixel scale to mrad. The conversion factor from pixels to mrad can be extracted from the plot made for determining the energy calibration, as in Figure 5.1. The bottom panels of both fig-

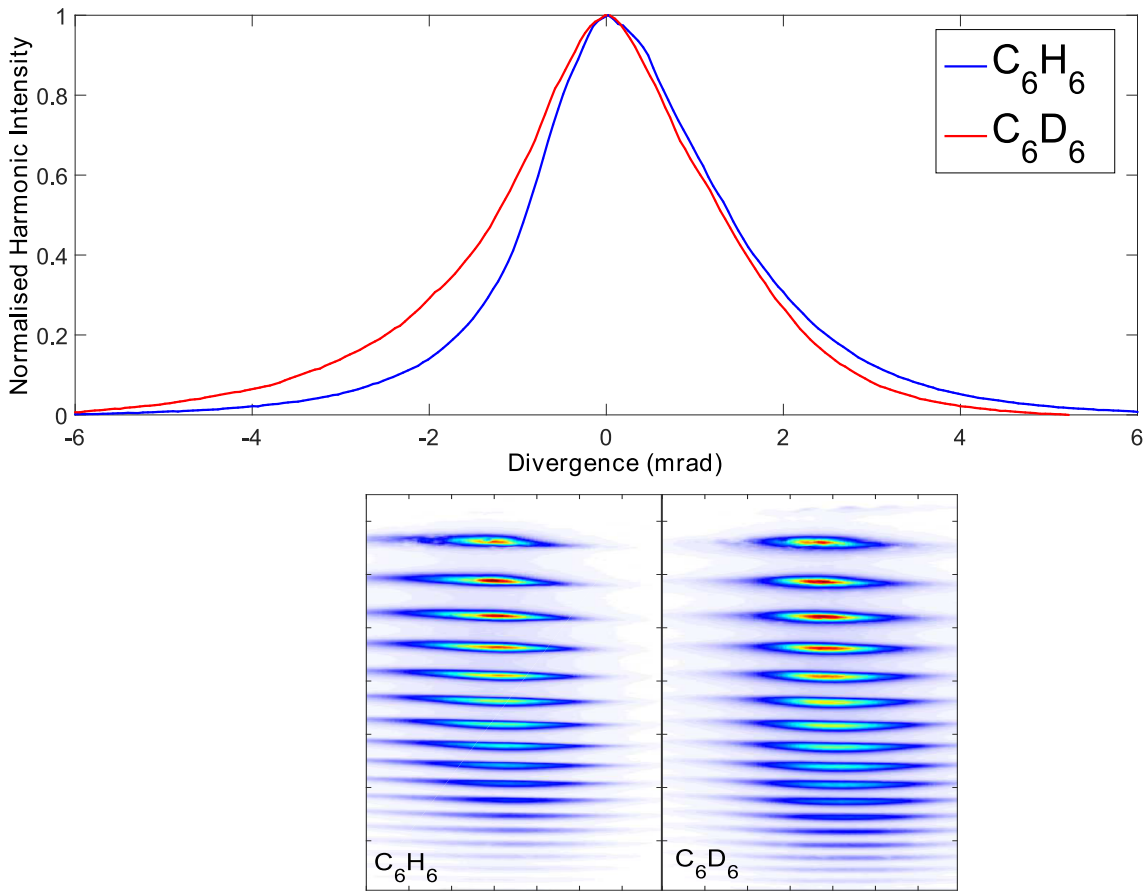


Figure 5.10: Stability of the harmonic spatial mode for the data shown in Figure 5.8

ures show the raw HHG images for the benzene and deuterated benzene spectra.

We can infer from this data that the data shown in Figure 5.8 is misleading as the fluctuations in the harmonic spatial mode have manifested as a contribution to the harmonic signal which has impacted upon the measurement of the ratio between the protonated and deuterated species. The stability of the harmonic spatial mode pertaining to the data shown in Figure 5.7 is excellent in contrast with no significant changes in the harmonic divergence that is exhibited in the bottom panel.

This check of the spatial mode stability was a necessary check to confirm if the ratio observed in Figure 5.7 was a real physical effect or a bogus result. The comparison of the deuterated and protonated species has further highlighted the importance of

confirming that any enhancements or suppressions observed in the data are not an artefact of fluctuations in the laser power or gas jet stability.

5.3 2013 data: Conclusions and actions taken

The 2013 data was a milestone for the progress on this project. We have demonstrated that we can perform HHG on a range of substituted benzene molecules using the heated continuous flow gas−jet. As a preliminary run though it highlighted a number of issues with the apparatus that needed to be addressed. These issues have been discussed in depth in the previous chapter. The implementation of a baratron pressure gauge allowed for finer tuning of the backing pressure. As opposed to solely relying on the readings off the Swagelok pressure gauges, the installation of the baratron close to the vacuum chamber enabled us to get a backing pressure value stably within tens of millibars accuracy.

To make the sample swapping procedure easier, two key modifications were made. First of all we installed the water bath alongside the oil bath such that we have 8 samples on the apparatus at any one time; four that can be sufficiently heated by the water bath to generate the required vapour pressure (i.e. benzene, deuterated benzene, fluorobenzene) and four that require the elevated heating capabilities offered by the oil bath to generate sufficient vapour pressure (i.e. the three xylene isomers, toluene, bromo, chloro and iodobenzene). The second change made to the apparatus was to install a copper tubing framework inside the oil bath such that cold water could be flowed through it so the oil would cool down quicker for when we are cycling through the series of molecules.

It was also decided to change the focusing conditions for the experiment from the 30 cm focal length spherical mirror to a 50 cm focal length CaF_2 lens. This switch of focusing optic was made as it was noted that the spectra tended to saturate under the previous focusing conditions and focusing looser is easier to implement than attenuation of the beam. This focusing geometry eliminates the need for a flat mirror in the chamber to send the beam to the focusing optic before it is focused over the vapour jet.

A filter wheel has also been installed in the spectrometer chamber to be used for the

spectral calibration. Filters such as Al and Zr with known transmission curves in the energy range of interest to us were used in conjunction with the previously outlined grating equation calibration method to improve the accuracy of the spectral calibration of the harmonics. The moving flange which is used to translate the MCP detector has also had a micrometer attached so there can be reproducibility in the movement of the MCP. The anti−vibration apparatus as shown in Figure 4.16 was also installed to mitigate fluctuations that emerged from the movement of the gas−jet manipulator.

Dr. Dane Austin also constructed a scanning FROG for the measurement of the pulse duration which is less cumbersome to make a measurement with in comparison to the SEA−SPIDER. To mitigate the laser stability issues encountered in the previous experimental run, Dr. Austin also implemented a number of diagnostics for the laser system. A stabilisation set−up consisting of two cameras and two motorised mirrors has been installed in the first amplification stage of the Red Dragon laser system at the ring. A camera is also in place at the output of the laser to lock the beam pointing. At the output of the laser there is also a photodiode monitoring a pick off from the main beam which records the output power of the laser. An actuator has also been installed onto one of the translation stages of the grating compressor in the second amplification stage of the Red Dragon laser system. Feedback from the SPIDER was also implemented in order to keep the chirp of the 800 nm beam stable. These modifications resulted in the chirp fluctuations going from ± 50 fs^2 to ± 10 fs^2. There is also a photodiode monitoring the output of the hollow core fibre.

Following all of these modifications, the 2015 data collection commenced. Iodobenzene was intentionally excluded from the data sets due to problems it caused with the Swagelok pressure gauges. Above a certain temperature we noticed that the readings on the pressure gauges were inconsistent with what we know from the temperature−vapour pressure curves i.e. in one instance we noticed that at a bath temperature of 140°C the gauge was reading a pressure of 8 bar which is not feasible. In light of these complications and the health hazards associated more so with this molecule than the other halogenated benzenes we decided to terminate data acquisition with this molecule. Following clarification from Sigma Aldrich that the main impurity in o-xylene was water which would evaporate at the temperatures required to generate ≈ 0.5 bar vapour pressure it was included in the 2015 data run.

5.4 2015 data run: benzene

This section will go through the second experimental run results with a focus on the reproducibility of the data as a function of time; first of all within the same day and then comparing data acquired with similar experimental parameters but collected on different days. The dependence of the shape of the spectrum on backing pressure is also investigated. Intensity scans were also performed to see both the extension of the cut−off and the saturation of the spectrum. In table 5.1, we show the relationship between the bath temperatures and the vapour pressure generated in the molecules of interest.

Table 5.1: Bath temperature and vapour pressure of molecules. WB stands for molecules that were heated using the waterbath. OB indicates those heated using the oil bath

Molecule	Temperature (°C) for 0.3 bar	Temperature (°C) for 0.5 bar
Benzene	45 (WB)	61 (WB)
Deuterated Benzene	36 (WB)	56 (WB)
Toluene	78 (OB)	91.5 (OB)
Fluorobenzene	50 (WB)	61 (WB)
M-Xylene	108 (OB)	119 (OB)
P-Xylene	107 (OB)	117 (OB)
O-Xylene	119 (OB)	129.6 (OB)
Chlorobenzene	98 (OB)	N/A
Bromobenzene	119 (OB)	N/A

The experimentally recorded vapour pressure curve for benzene is shown in Figure 5.11. The vapour pressure of a particular molecule is only temperature dependent − for example, it does not depend on the amount of liquid in the confining container. As shown in Figure 5.11, the vapour pressure has the expected exponential relationship with increasing temperature. The relationship between the temperature of a liquid and its vapour pressure is described by the Clausius−Clapeyron equation:

$$\ln \frac{P_2}{P_1} = \frac{\Delta H_{vap}}{R} \left(\frac{1}{T_1} - \frac{1}{T_2} \right) \tag{5.1}$$

where P_1 is the partial pressure of the liquid at T_1 and P_2 is the partial pressure of the liquid at T_2. $R = 8.3145$ J/mol/K is the ideal gas constant and ΔH_{vap} is the enthalpy of vapourization in units of J/mol.

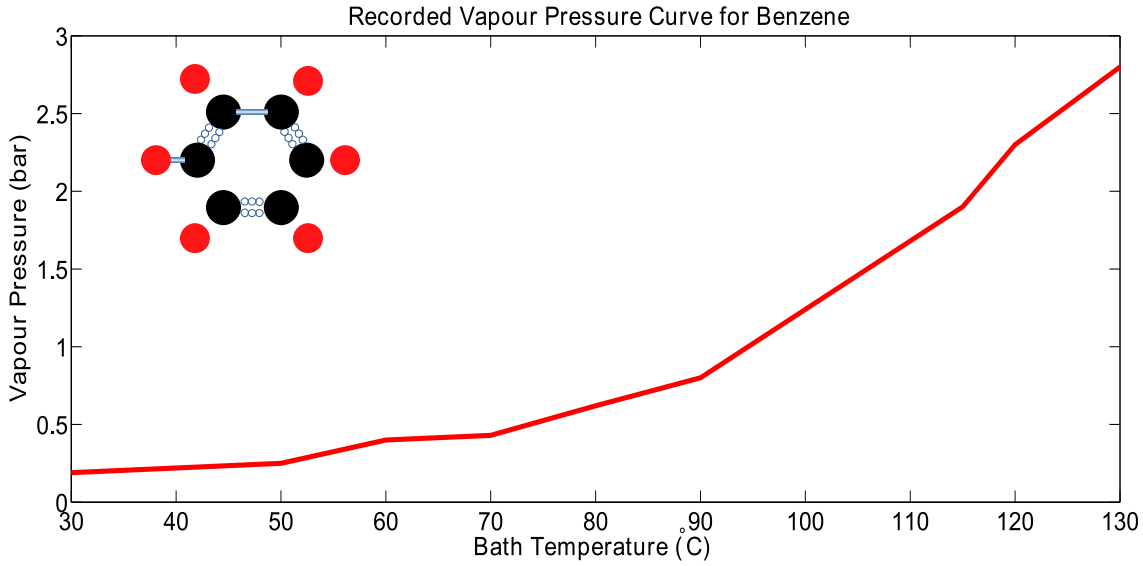


Figure 5.11: Vapour pressure curve recorded for benzene

5.4.1 Intensity measurements

To estimate the peak laser intensity at the focus of the laser we calculate the power from the simple relation: $P = E/t$ where E is the laser energy per pulse, which is recorded on a power meter before the entrance to the vacuum chamber, and t is the pulse duration which we measure from the FROG. We get an estimate of the beam waist using $\omega = \omega_{fibre} \times 0.64 \times f_1/f_2$, where ω_{fibre} is the measure of the beam waist at the exit of the hollow core fibre, f_1 is the focal length of the lens before the vacuum chamber and f_2 is the focal length of the collimating mirror at the output of the hollow core fibre. Optimal coupling into the lowest order mode occurs when the ratio of the focused spot size to the fibre inner diameter, ID, is: $2\omega/(ID) = 0.64$. The focal spot size area is then calculated using $area = \pi \times \omega^2/2$. We then simply use $I = P/area$ to calculate the intensity of the beam at the focus. This is the method that is used for peak intensity at the focus measurements throughout this thesis.
It is experimentally quite difficult to accurately measure the peak laser intensity at the laser focus. The approach we use here, as outlined above, is to estimate the focal spot size based on the near−field laser beam size. This tends to be an overestimate of the intensity due to the fact that it does not account for imperfections in the mode quality.

One *in situ* method for measuring the laser intensity at the focus of the beam in a gas−jet is to use an ionization gauge. A full description of the design and operation of an ionization gauge is given in the work by Shiner *et.al* [177] which discusses the measurement of the laser intensity in the focus of a gas−jet by recording the ion yield. Briefly, this paper states that due to the ion signal being proportional to the number of ions in the laser focus, the dependence of the ionization probability on the pulse energy can be measured. A single atom ionization rate model is then applied and integrated over the focal volume. In this work, the model developed by Yudin and Ivanov [20] is used to calculate the dependence of the field ionization rate on the laser intensity.

The intensity at which the maximum photon energy is produced can be simply calculated from the classical cut−off law: $E_{cut-off} = 3.17U_p + I_p$ where $U_p = E^2/(4\omega_0^2)$. However, we must bear in mind that the experimentally observed cut−off position is usually less than that given by the cut−off law. This can be attributed to poor phase matching of higher harmonic orders. For longer drive laser wavelengths (> 800 nm), the higher harmonic orders, which have shorter wavelengths, will be more sensitive to subtle changes of the phase of the drive laser field.

The efficiency of the harmonic generation process scales up rapidly with increasing laser intensity up to a certain value and plateaus off beyond that value − the *saturation intensity*. At this intensity, all of the emitters in the interaction volume are ionized and the number of electrons which contribute to the HHG process cannot increase further [178].

We will use the method outlined at the start of this section, which depends on the pulse energy, pulse duration and spot size, to calculate the intensity at the laser focus. It is important to note that in cases where the intensity of the cut−off position is calculated that the value for the laser intensity at the focus may exceed the saturation intensity value due to it being an overestimate as it does not account for inhomogeneities in the beam profile or phase matching.

5.4.2 Reproducibility of the spectra from benzene

Figure 5.12 shows the normalised harmonic spectra from benzene recorded over a period of 40 minutes on a particular day. The MCP was not moved during the data acquisition and the backing pressure recorded from the baratron was 0.55 bar throughout the collection. The beam energy randomly fluctuated between 0.34 and 0.38 μJ per pulse from the 1750 nm, 40 fs TOPAS beam. The pulse duration was measured to be 56.3 fs and the average pulse energy was 0.36 mJ per pulse. The calculated intensity at the focus was determined to be 5.7×10^{13} W/cm^2. The 200 μm nozzle was positioned with respect to the laser focus for the optimal phasematching conditions. The diameter of the iris before the entrance to the vacuum chamber was 10 mm.

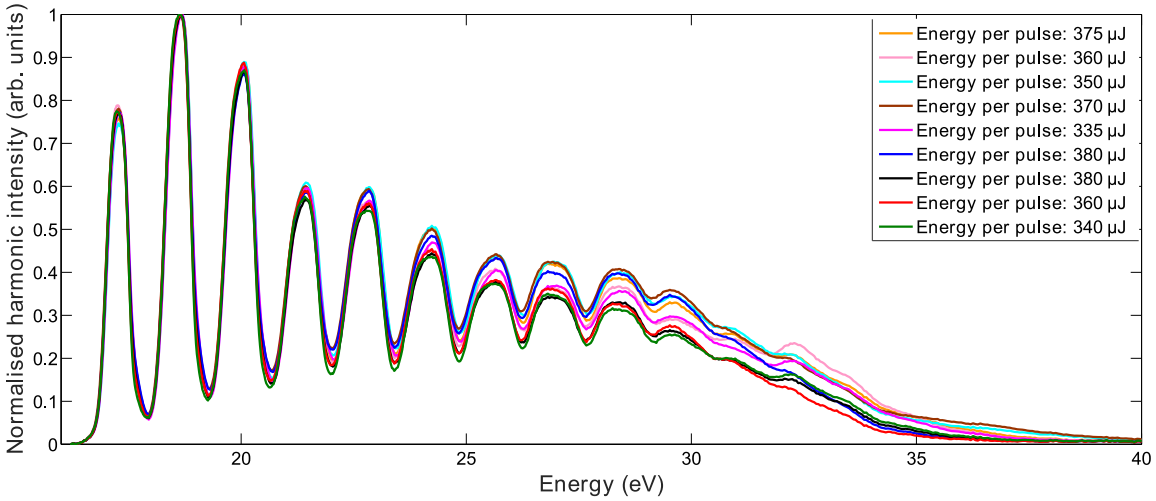


Figure 5.12: HHG spectra from benzene recorded with a backing pressure of 0.55 bar and beam energies per pulse are shown in the legend of the Figure. 10 images were taken for each spectrum with a 1 s exposure time.

This plot illustrates that over a short period of time the shape of the spectrum remains consistent despite the fluctuations in the beam power. Plotting the spectra from benzene acquired under similar conditions on two different days it is evident that reproducibility of the data is an issue in the data acquisition.

Data taken on two separate days is shown in Figure 5.13. The average peak intensity at the focus was 5.7×10^{13} W/cm^2.

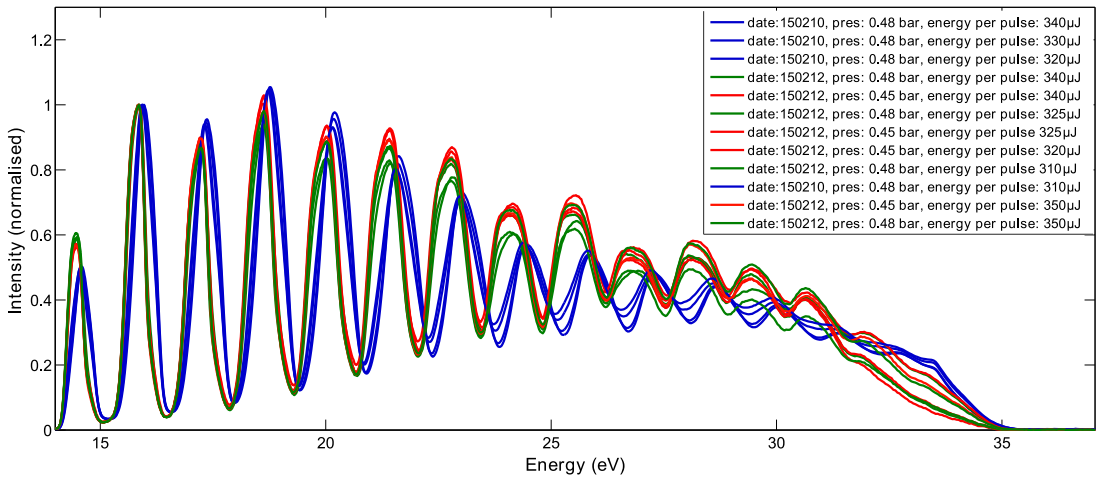


Figure 5.13: Spectra recorded in benzene for two different days where the generating conditions are not the same. The blue traces were taken on one day and the red and green traces represent a different day with similar laser parameters and backing pressures. On both days, there were 10 images taken for each data set witha 1 s exposure time.

The blue curves in Figure 5.13 retain a similar shape to one another. The data acquired on the other day is however different. A shift of the harmonic orders is noticeable; this can be an artefact of the spectral shifting of the fundamental. For example instabilities in the laser system can lead to higher order dispersion terms becoming significant which can cause the spectral position of the fundamental to shift to lower wavelengths (blue shifting) or to higher wavelengths (red shifting). Whilst the shape of the spectra in the red and green curves are comparable there are a few discrepancies between them and those taken on the other day of the data acquisition.

If we compare spectra acquired on three different days as shown in Figure 5.14 we see a similar result. The average peak intensity at the focus was 6.5×10^{13} W/cm^2.

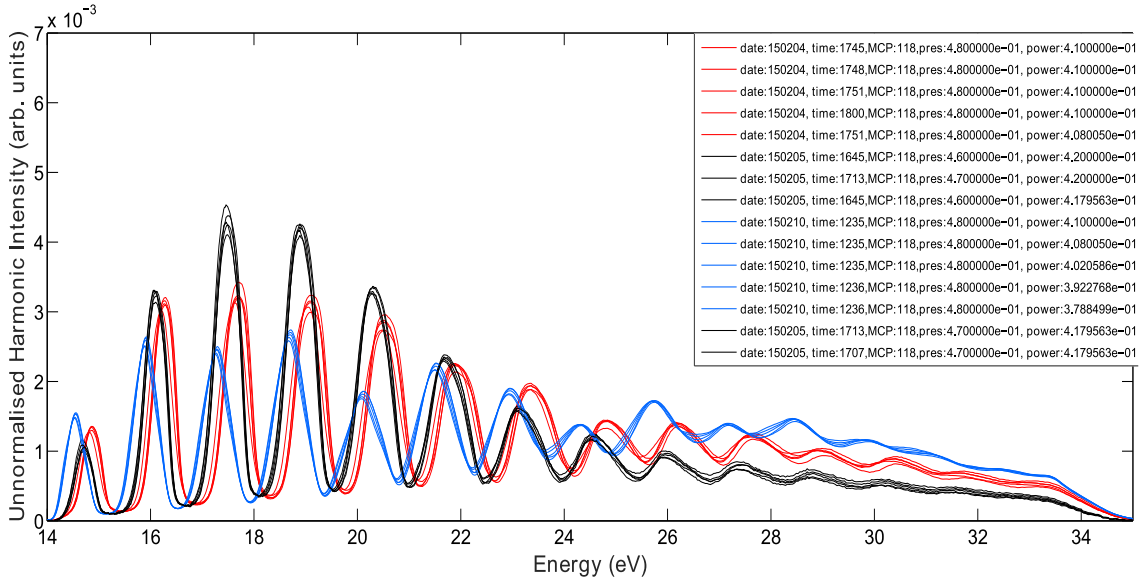


Figure 5.14: Unnormalised HHG spectra from benzene taken on three different days with similar backing pressures and laser parameters. For each data set 10 images were recorded with a 1 s exposure time.

The red plots are one day, the black plots a consecutive day and the blue plots are a third day that spectra from benzene were acquired under similar conditions. The shapes and relative harmonic intensities of the lime green and dark green curves are similar if the shifting of the harmonic orders is discounted. The blue data set does exhibit some interesting features such as reductions in the harmonic intensities of the harmonics at ≈ 20 eV and ≈ 24 eV.

Taking the ratios of benzene, deuterated benzene and fluorobenzene to benzene allows us to check the reproducibility of the shapes of the spectra too. Fluorobenzene is included in these plots to reinforce the result that the harmonic intensity from this molecule is suppressed across the recorded spectrum. In Figure 5.15, the ratio of benzene to benzene for two separate runs is plotted along with three different deuterated benzene spectra whose ratio is taken to the first benzene run too. The peak intensity at the focus is 7.8×10^{13} W/cm^2. Analogous to the deuterated benzene case, three distinct flurobenzene runs are also divided by a common benzene spectrum. The spectra are normalised to their first harmonic visible on the MCP before taking the ratio to benzene which enables easy comparison of the shape of the spectra but the magnitude of the ratio should be neglected.

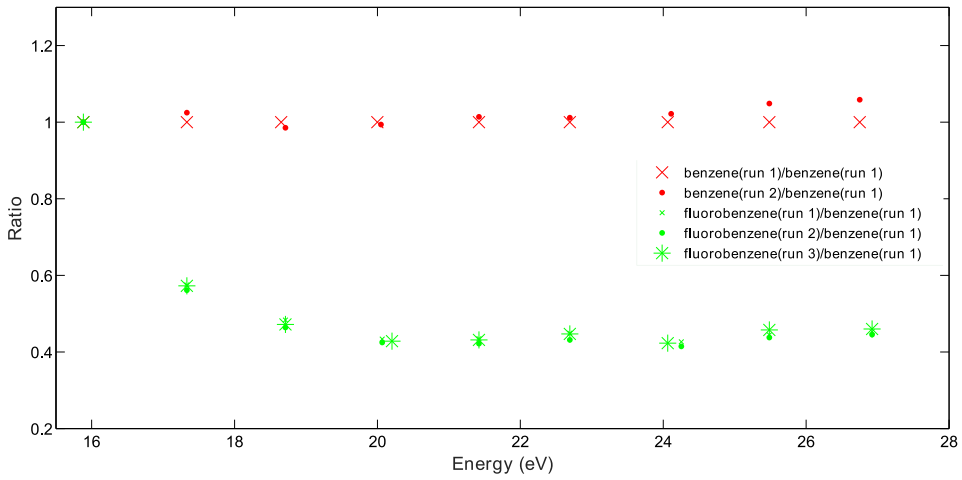


Figure 5.15: Ratios of spectra for different runs to the first benzene run. Different colours denote different molecules and different markers represent different data acquisition runs. Spectra are normalized to the first harmonic to appear on the MCP image. In all cases the backing pressure was 0.5 bar and the beam energy was 490 μJ per pulse. For each run, a sequence of 50 images were acquired with a 1 s exposure time.

The different runs shown in Figure 5.15 clearly follow similar shapes which is a positive result for the reproducibility of the spectra, especially as it is valid for three separate molecules on the apparatus. To accurately represent the error for this plot, the data from all the runs for a given molecule were collected into one data set with the associated error from the variation over the whole set. This does give quite large errors but it does allow us to see the ratios with absolute values. The data with error bars is shown in Figure 5.16. It is important to note that in Figure 5.16 it is

immediately clear that within the error bars the ratio of the deuterated to protonated benzene is one and does not change.

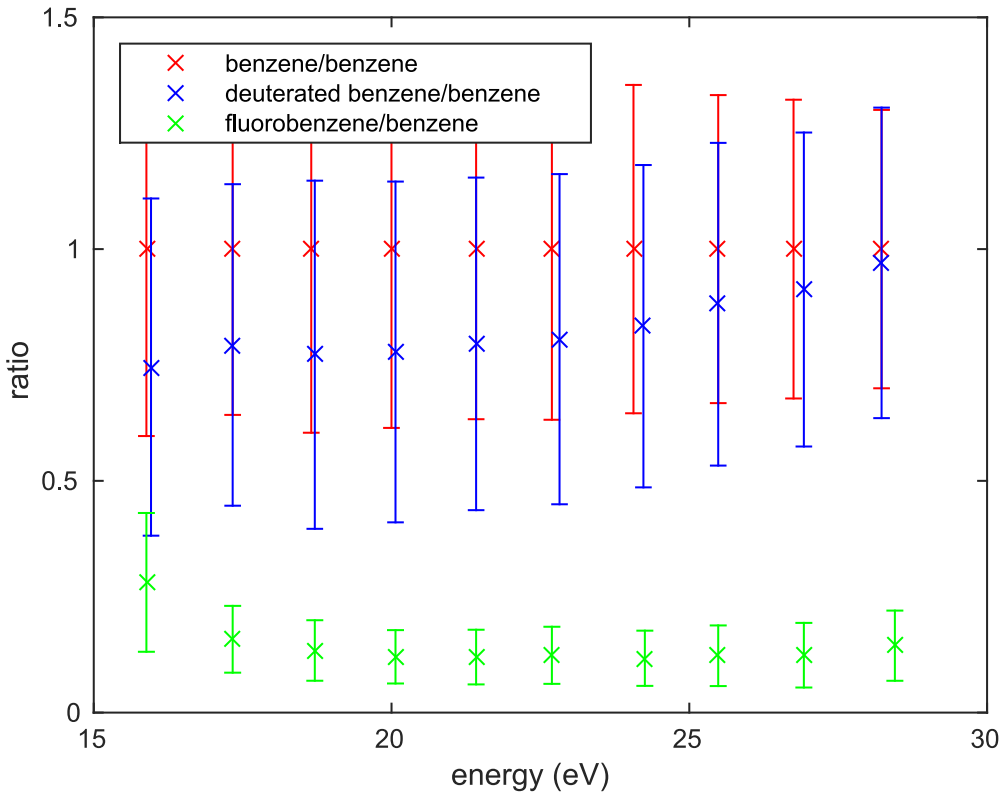


Figure 5.16: Ratios of benzene, fluorobenzene and deuterated benzene to benzene with associated errors.

With such large errors it is difficult to make any solid claims about the ratios but there is, for example, an increase in the deuterated benzene to benzene ratio which is consistent to what was observed in the 2013 run. What is striking is the significantly lower signal levels in fluorobenzene across the whole spectrum compared with the other molecules.

The shape of the spectrum is also sensitive to the vertical position of the gas−jet. It was noticed that when the cold trap on the generation vacuum chamber was being refilled that the signal had dropped by a factor of three suddenly. When the jet was being realigned to re−optimise the signal level, it was evident that the shape of the spectrum was changing significantly.

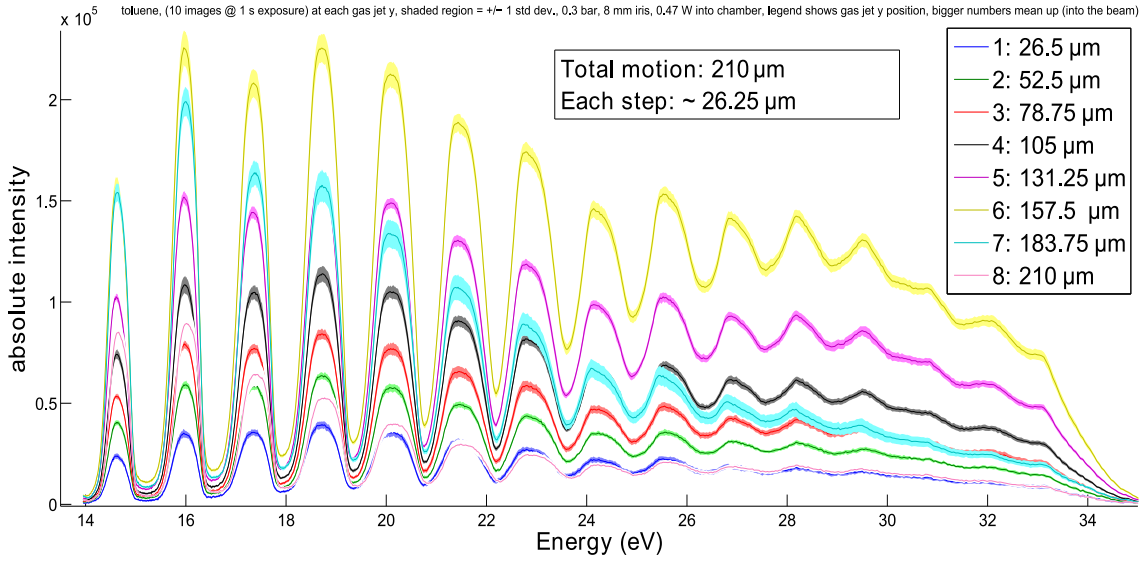


Figure 5.17: Unnormalised plots of the HHG spectra from toluene recorded as a function of the vertical position of the gas−jet. The total motion of the jet was 210 μm so each of the 8 steps was $\approx 26\mu$m. For this data 10 images were taken with a 1 s exposure time for each height increment.

The effect of the vertical height of the gas−jet was investigated in toluene for 8 different jet positions. The jet was set to a reference where there was no harmonic signal before being moved up such that position 1 corresponds to the first position where harmonics were detected. The lowest position for the gas−jet starts at a height where the signal is about a fifth of the maximum. The jet is then moved up towards the focus of the beam such that the highest position of the jet is where the beam focus is just grazing the gas−jet. The backing pressure was 0.3 bar and the beam energy was 470 μJ per pulse. The average peak intensity at the focus was 7.4×10^{13} W/cm^2. As shown in the Figure 5.17 of the unnormalized spectra, it is evident that the variation in the signal level is systematic with the signal increasing from the lowest position of the jet below the focus, 1, to position 6. At positions 7 and 8 the signal begins to dramatically decrease. It was noticed on the camera that images the gas−jet onto a CRT screen that the plasma plume was very bright.

Figure 5.18 is a plot of the normalized spectra displayed in Figure 5.17. It is clear that there is a variation in the shape of the spectrum at each height increment but the discrepancies are smallest for positions $1-3$. As the jet is moved closer to the focus of the beam the spectrum appears to shift to relatively higher harmonic orders until the jet is very close to the laser focus such that it is skimming it (positions 7

and 8). The spectra taken at these two positions show the spectrum shifting to lower harmonic orders. These results demonstrate that the gas−jet should be kept in the vicinity of positions $1-3$ to mitigate any significant reshaping of the spectrum.

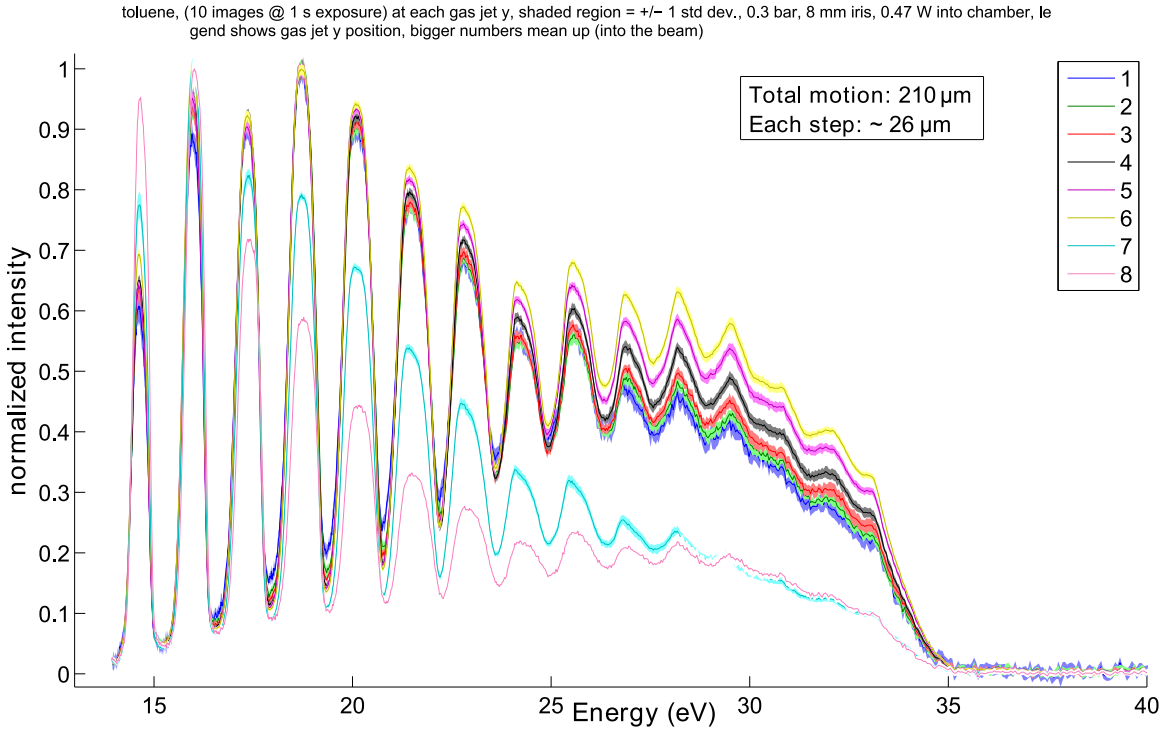


Figure 5.18: Normalised plots of the HHG spectra from toluene recorded as a function of the vertical position of the gas−jet. The total motion of the jet was 210 μm so each of the 8 steps was $\approx 26\mu$m.

5.4.3 Pressure dependence of harmonic spectra in benzene and substituted benzenes

The pressure dependence on the shape of the harmonic spectrum was also investigated. Figure 5.19 shows the raw lineouts of HHG spectra from benzene acquired at different backing pressures between 0.1 and 0.83 bar.

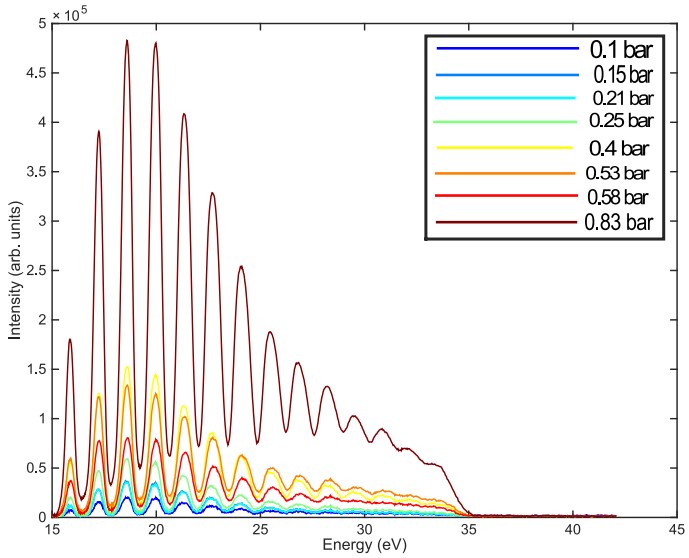


Figure 5.19: Unnormalised plot of a pressure scan in benzene going from 0.83 − 0.1 bar. This data was acquired as a sequence of 50 images with a 200 ms exposure time.

The shape of the spectrum is not drastically different as a function of the pressures investigated. The input beam energy was 490 μJ per pulse throughout the duration of the pressure scan. The average peak intensity at the focus was 8.7×10^{13} W/cm^2. The method of background subtraction used was to take an MCP image with the laser beam blocked but the gas going into the chamber. It is time consuming and laborious to take a background image with the laser in and the gas off as it takes time for the gas in the delivery lines to be evacuated through the 200 μm nozzle.

Figure 5.20 shows the harmonic peak intensities from Figure 5.19 normalised to the maximum peak in each spectrum.

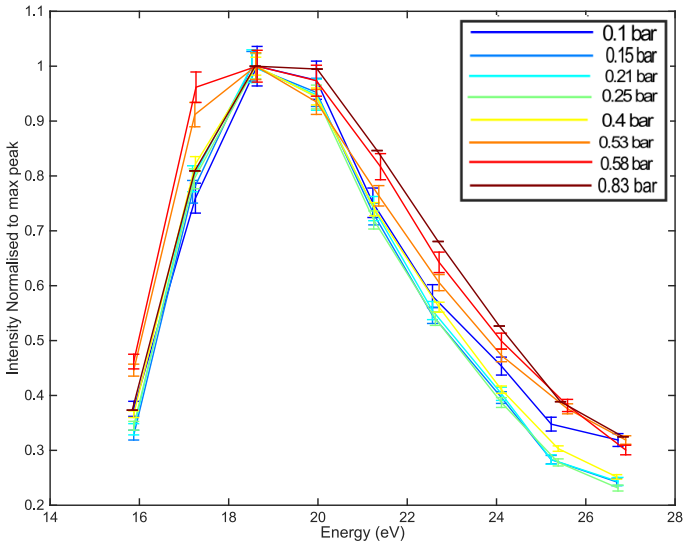


Figure 5.20: Harmonic peak intensities of the pressure scan shown in Figure 5.19 normalised to the maximum intensity peak of each spectrum.

There is a consistent trend in the lineouts in Figure 5.20. The number density in the gas−jet, N, is proportional to the backing pressure. The density dependence of the harmonics should be ultimately dependent upon propagation effects provided that the response of the individual molecules is independent of the density. A quadratic increase in the harmonic signal as a function of increasing backing pressure is expected as a regime for phasematched HHG is proportional to N^2.
In the Figures 5.21 and 5.22, the normalised and unnormalised pressure scans are presented. The average peak intensity at the focus was 7.5×10^{13} W/cm^2.

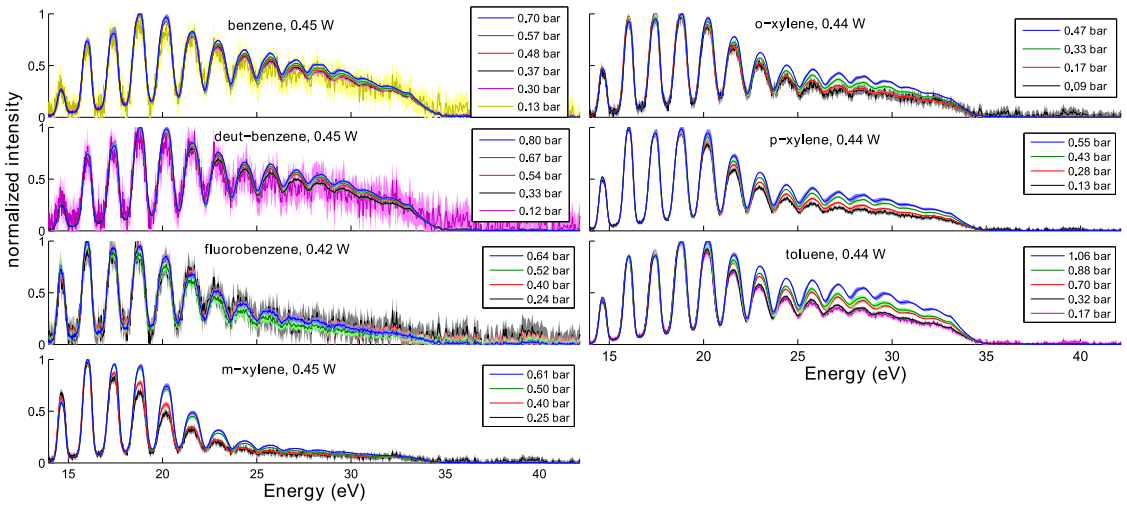


Figure 5.21: Area normalised HHG spectra as a function of backing pressure. In all molecules except fluorobenzene, higher harmonics become relatively stronger at higher pressures. The effect may be masked by the low signal in fluorobenzene. The effect is more pronounced in the xylenes and toluene but there in the benzene and deuterated benzene spectra. For each scan 30 images were recorded with a 1 s exposure time.

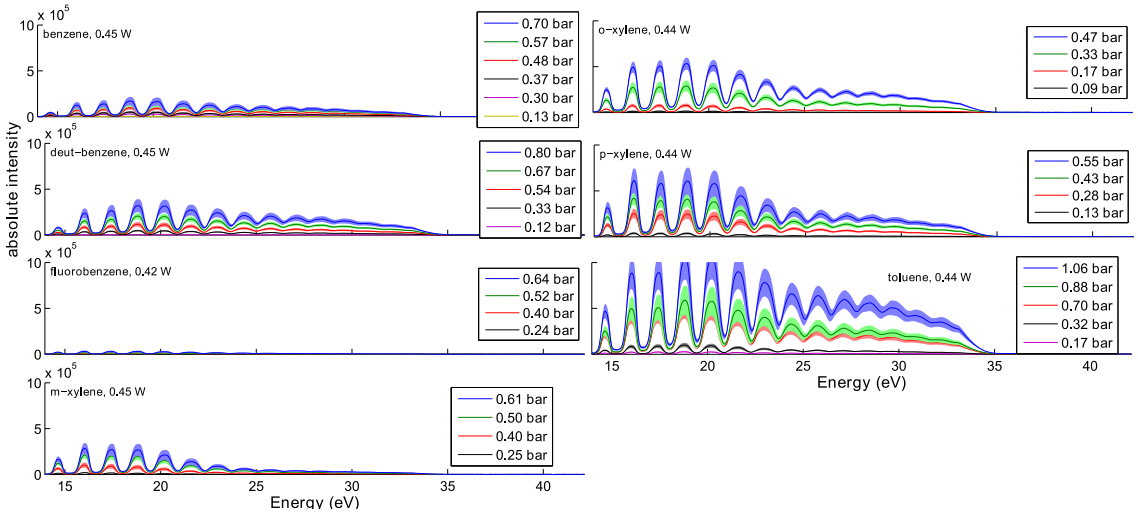


Figure 5.22: Unnormalized HHG spectra recorded as a function of backing pressure.

In Figure 5.23, spectra for benzene, toluene, fluorobenzene and the three xylene isomers are plotted unnormalised. The backing pressure varies from 0.26 to 0.31 bar for each species and the beam energy per pulse is 620 μJ. The average peak intensity at the focus was 1.1×10^{14} W/cm^2. There was a small ($\approx 5\%$) drift of the hollow core fibre output which was traced back to drift in the compressor of the Red Dragon

laser system when this data was taken. This plot substantiates that working with lower backing pressures keeps spectra self-similar. Reverting back to the 2013 data pressure scan in Figure 5.6 we see that the shape and magnitude of the spectrum changes as a function of backing pressure. Consistency in the spectral shape and ensuring local fluctuations in density or phenomena such as the formation of clusters are circumvented are of utmost importance to acquiring reliable and meaningful data on the molecules relevant to this thesis.

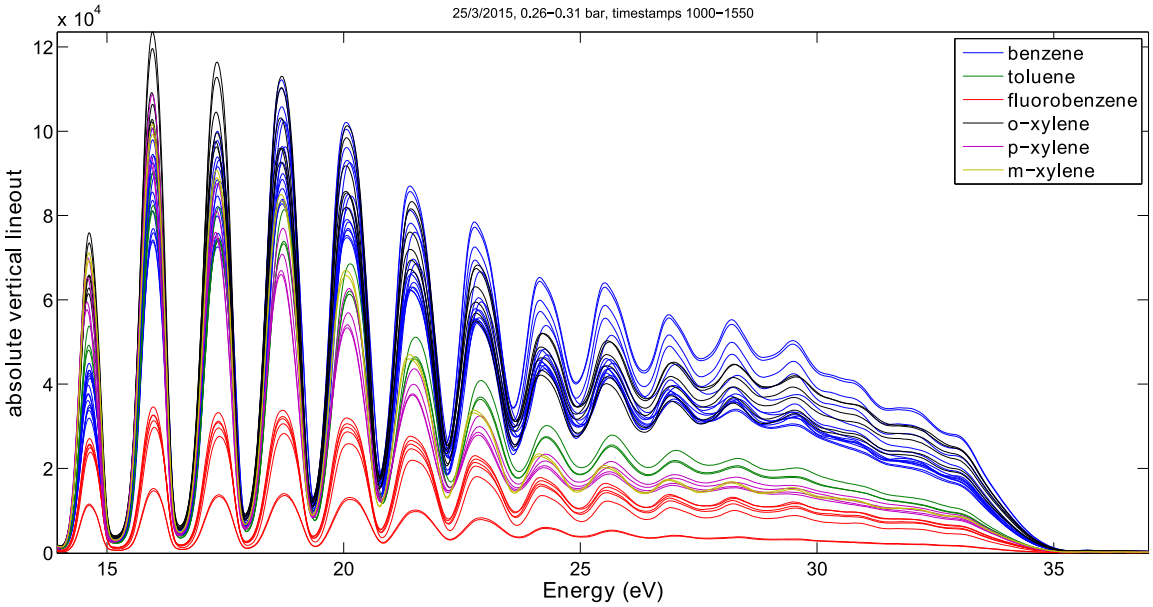


Figure 5.23: Spectra for benzene, toluene, fluorobenzene and the three xylene isomers are plotted unnormalised. For this data, each spectrum was acquired as a sequence of 15 images with a 1 s exposure time.

This chapter has focused on the issued related to acquiring stable and reproducible HHG spectra from the molecules on the apparatus. As the entire apparatus has been constructed in house, and is designed to generate a vapour jet from molecules that are in the liquid phase at room temperature, it is important to address these issues. Checking the dependence and reproducibility of the harmonic spectra on backing pressure, gas jet translation and switching between molecules has enabled us to establish the optimal working conditions for acquiring reliable data which shall be presented in chapter 6.

Chapter 6

Results

This chapter will present the data acquired and processed throughout this PhD project. The results were obtained in two campaigns - one in December 2013 (henceforth 2013) and one from February to April 2015 (2015). 2013 yielded preliminary data and highlighted some problems with the experiment. These issues were addressed in the 2015 data collection.

I will first present the data that was acquired in December 2013 with the apparatus. The data will be presented in chronological order. I will then the discuss the data acquired during 2015. The idler from the HE−TOPAS at a wavelength of 1.7 μm, duration of 40 fs (measured using the SEA−SPIDER) and repetition rate of 1 kHz was used. The beam was passed through an evacuated 1 m long, 400 μm hollow core fibre for mode cleaning. As shown in Figure 4.19, the beam was focused into the target gas by a $f = 30$ cm spherical mirror. The harmonics passed into the spectrometer which contained the 1200 lines/mm grating and the MCP detector. The gas−jet diameter was either 100 or 200 μm - it shall be explicitly stated which jet diameter was used for each data set presented. This apparatus only consisted of the oil bath for this run so only four samples could be used at one time. The backing pressure in the delivery lines was adjusted by changing the temperature of the oil bath. The pressure was monitored using the Swagelok pressure gauges, one of which was attached to each individual sample vessel. The data shall be split into three classes based on the molecules used; PACER, methylated benzenes and the halogenated benzenes.

Raw harmonic spectra for benzene, toluene, m-xylene and p-xylene are shown in Figure 6.1. The backing pressure was recorded as being 0.5 bar for benzene, toluene and m−xylene but was 0.4 bar for p−xylene. The energy per pulse was $\approx 255\mu$ J per pulse.

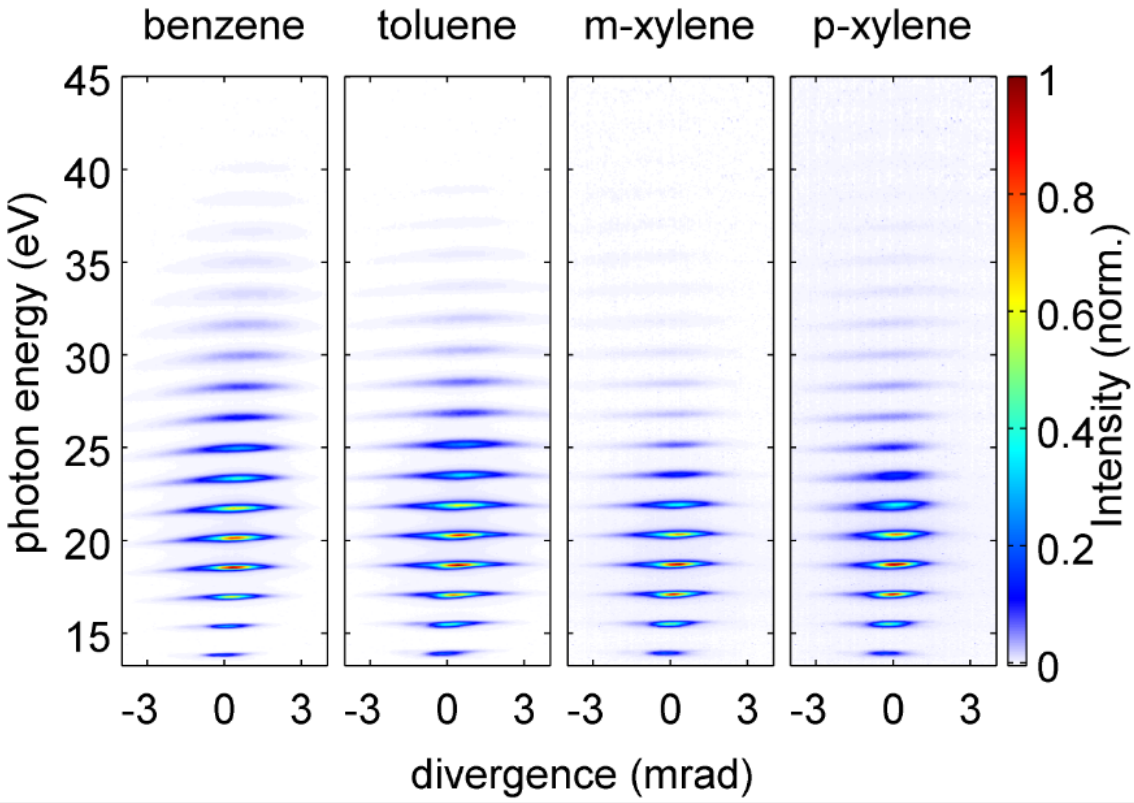


Figure 6.1: Raw harmonic spectra recorded in benzene, toluene, m-xylene and p-xylene.

As shown in Figure 6.2, we have recorded harmonic spectra from benzene, deuterated benzene, bromobenzene, chlorobenzene, iodobenzene and fluorobenzene. To the best of our knowledge these are the first recorded HHG spectra from these molecules and to be performed using both the continuous flow gas−jet and the 1700 nm drive wavelength. The 200 μm nozzle was used for the generation of the vapour and the long pulse idler (1750nm, 40 fs duration) was the drive laser.

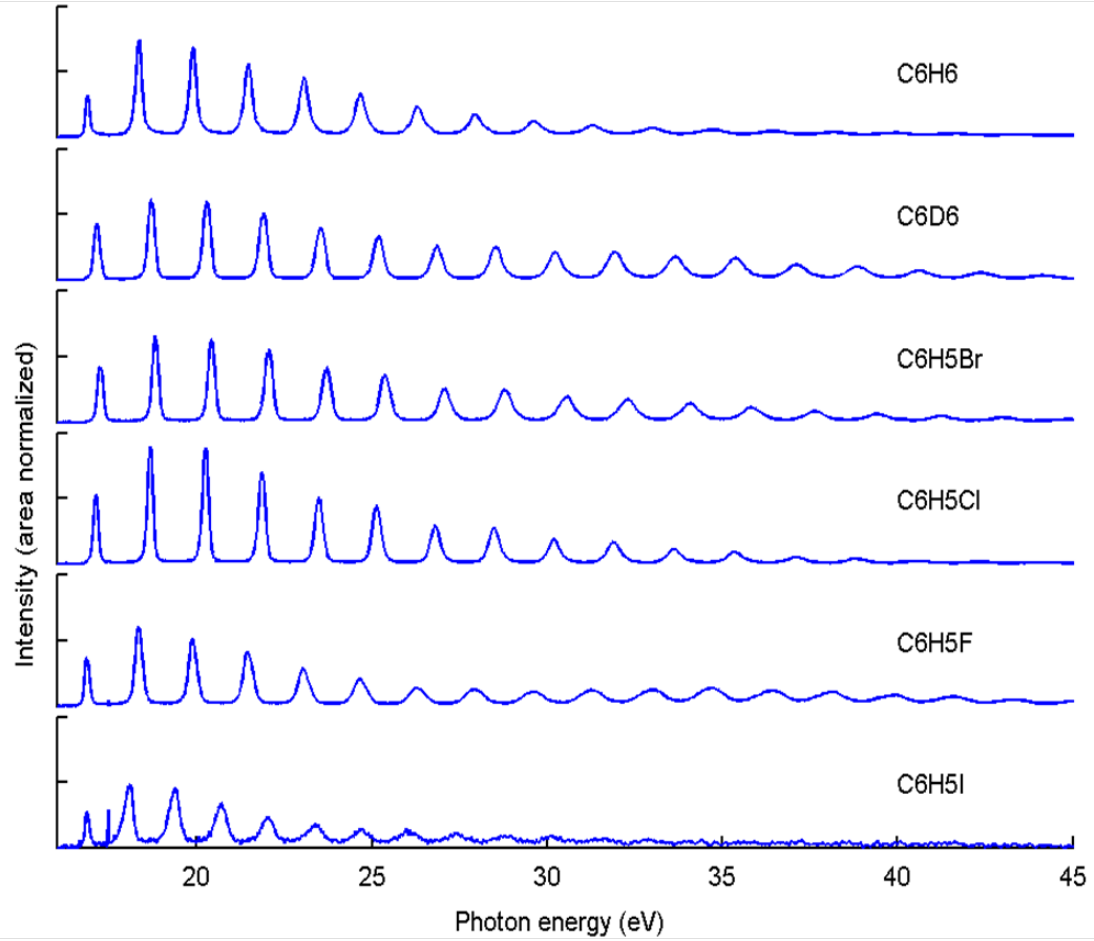


Figure 6.2: Spectra recorded in benzene, deuterated benzene and all of the mono halo substituted benzenes. The backing pressure is 0.4 bar for all molecules with the exception of iodobenzene where the backing pressure was 0.2 bar.

6.1 Comparison of benzene to deuterated benzene HHG spectra: December 2013 data

The PACER experiment as described in section 3.3 has been extended to benzene and deuterated benzene. The first attempt at performing PACER in benzene and deuterated benzene was also carried out during the 2013 data run.

On each day of data taking, four pairs of spectra were acquired for benzene and deuterated benzene. The four pairs of scans are shown plotted together in Figure 6.3. The spectra are area normalised to enhance the comparison between both species.

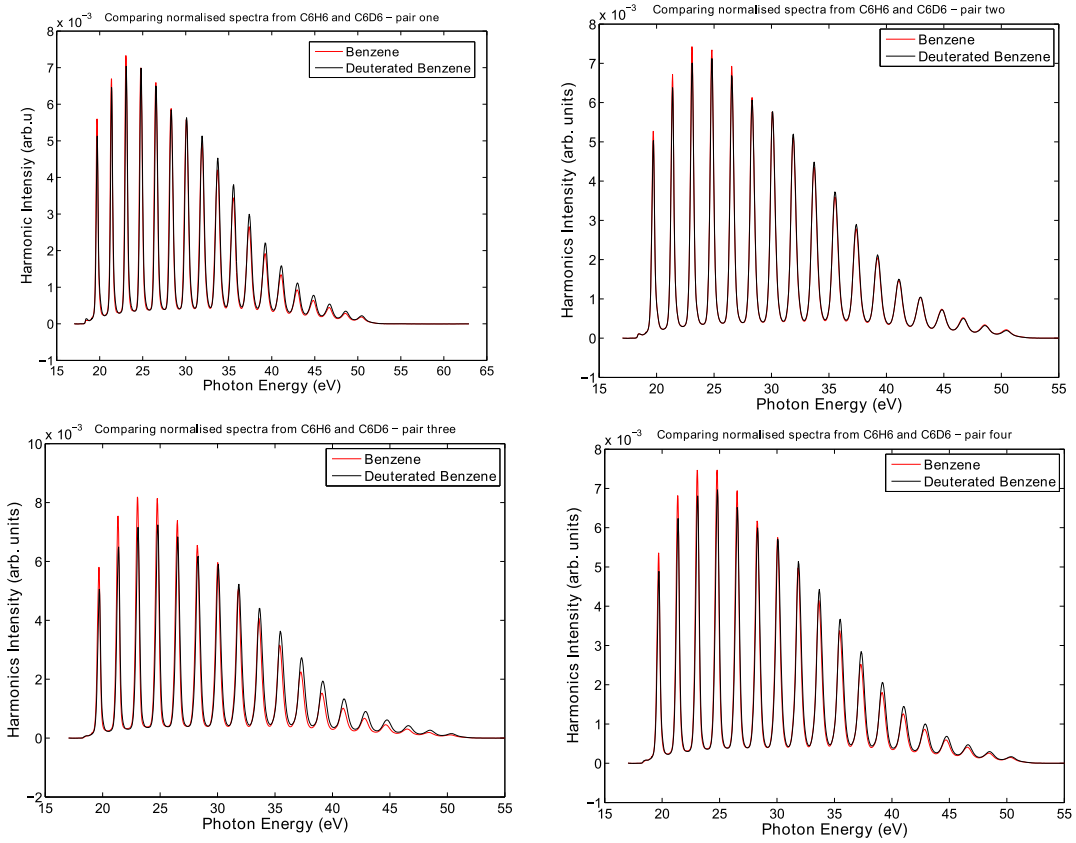


Figure 6.3: Area normalised spectra for benzene and deuterated benzene displayed as four pairs of data for the PACER comparison. For each data set 50 images were acquired with a 300 ms exposure time.

The laser beam input energy was fixed at 290 μJ per pulse and the backing pressures used were 0.55 bar and 0.50 bar for deuterated benzene and benzene respectively. The two samples were heated in the oil bath and measurements were taken at the same bath temperature for both molecules which yielded a discrepancy in backing pressure which would have been time consuming to adjust for as it would have relied on allowing the bath to cool by a few degrees to adjust the temperature which was an impractical procedure.

A third data set was acquired for the comparison of the protonated to deuterated benzenes. In Figure 6.4, four pairs of spectra are plotted for three intensity values; 63%, 79% and 100% of the input beam power. Each spectrum is normalised by the area All four data sets follow a similar trend and show that the ratio between deuterated benzene and benzene is the same. Since the variation between measurements exceeds the shot to shot variation from the laser, the individual measurements can be shown without error bars to give a sense of the overall uncertainty to the data. Since the stability of the mode was found to be very stable for this data set this further substantiates the claim that the spectra recorded for benzene and deuterated benzene are very similar.

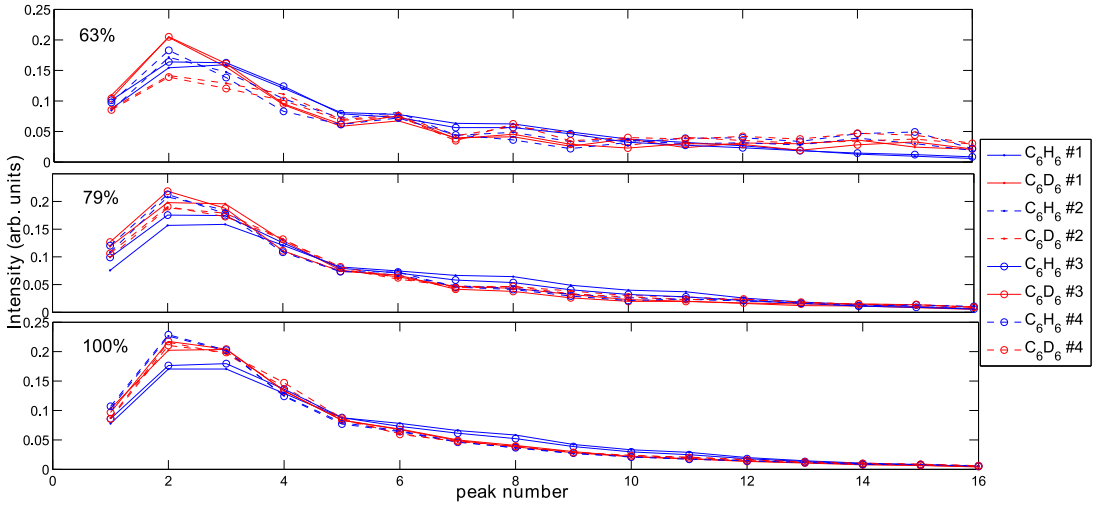


Figure 6.4: Four pairs of spectra plotted for three intensity values; 63%, 79% and 100% of the input beam power

6.2 Comparison of benzene to methylated benzene HHG spectra: December 2013 data

To investigate the effect of multiple substitutions on the benzene ring and the influence of the positions of the substituents we performed HHG in benzene, toluene and two of the three xylene isomers; meta and para−xylene which were presented in 1.7.5. The third of the isomers, ortho−xylene was excluded from this data run as it was thought to contain impurities according to the information from the supplier Sigma Aldrich. The exact classification of these impurities was not made available to us when the experiment commenced. We excluded o−xylene as it was feared that the impurities may be very efficient at HHG and would lead us to draw false conclusions from comparisons between the other xylene isomers.

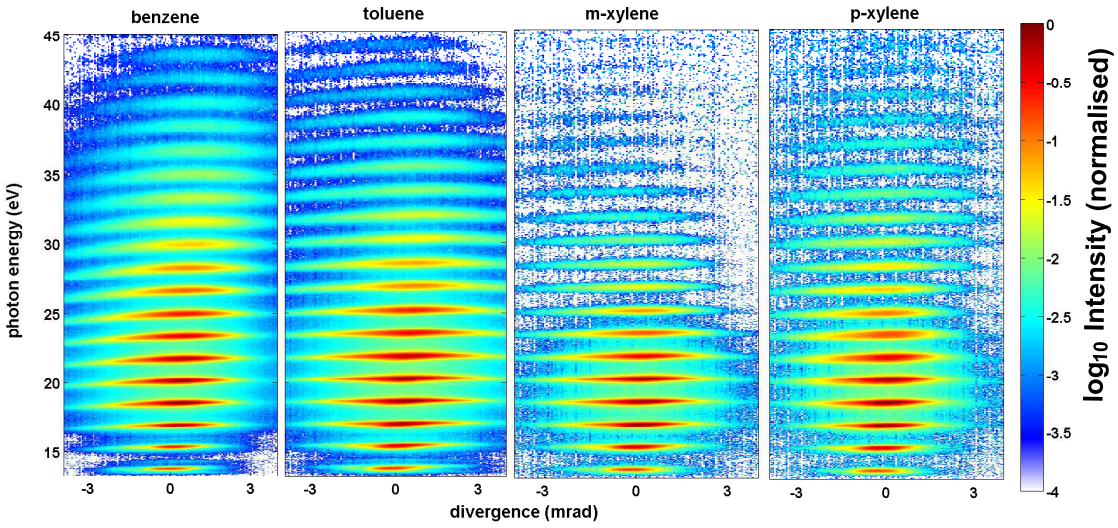


Figure 6.5: HHG spectra acquired in benzene, toluene, m−xylene and p−xylene.For each data set 50 images were taken with a 1 s exposure time.

Figure 6.5 shows the harmonic spectra from the four molecules: benzene, toluene, m−xylene and p−xylene. Both of the xylene isomers have smaller cut−off energies than benzene and toluene. M−xylene has the smallest cut−off energy of the four molecules. The backing pressure was recorded as being 0.5 bar for benzene, toluene and m−xylene but was 0.4 bar for p−xylene. The discrepancy in backing pressure arose from the fact that the two xylene isomers were placed in the oil bath at a temperature of 130°C which equated to 0.5 bar and 0.4 bar for m−xylene and p−xylene

respectively. Due to the fact that it took a considerable amount of time for the 7 L of silicone oil in the bath to cool down, it was inefficient to fine tune the temperature to the requirements of each molecule. The beam energy was ≈255 μJ per pulse for the four data sets. The goal of this experimental run was to record HHG spectra from benzene, toluene and the xylene isomers in order to take ratios of the substituted benzenes to benzene in order to elucidate if the nuclear dynamics are faster in the isomers as predicted by Mendive-Tapia *et.al* [125].

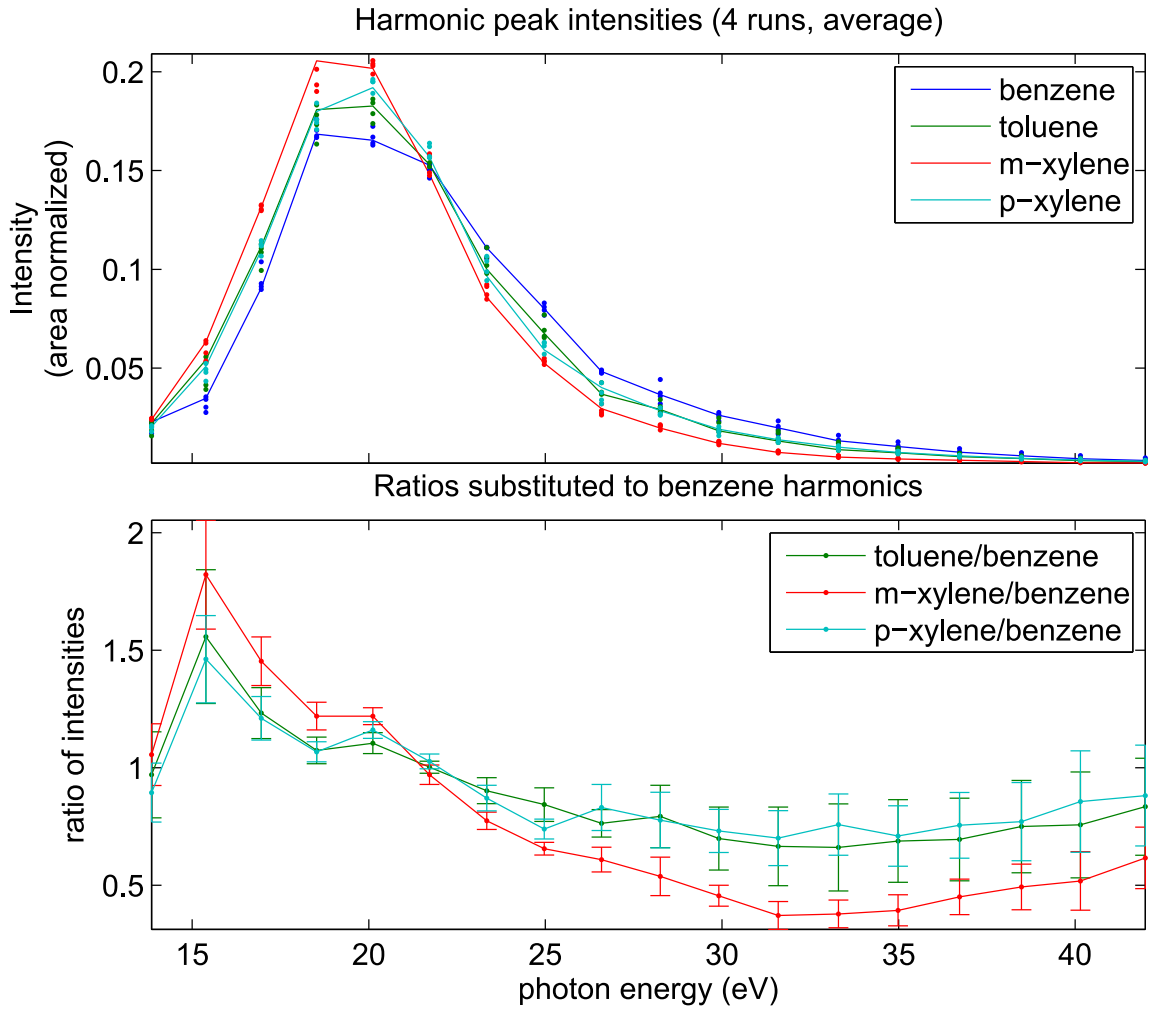


Figure 6.6: Area normalised harmonic peak intensities for benzene, toluene, m−xylene and p−xylene (top panel). Ratios of toluene, m−xylene and p−xylene to the benzene reference (bottom panel). The backing pressure was 0.5 bar for each molecule.

Figure 6.6 shows the ratios of the methylated benzenes to benzene. On the day these HHG spectra were recorded it was decided to start with the molecule with the low-

est temperature to vapour pressure requirement to achieve 0.5 bar backing pressure unlike the previous methylated benzene data. The backing pressure was $\approx$ 0.5 bar for each of the molecules and the beam energy was $\approx$ 260 μJ per pulse. The spectra were area normalised before the ratios were taken to facilitate better comparisons.

Also plotted in Figure 6.7 is the ratios of the substituted benzenes to benzene along with the ratio of m−xylene to p−xylene. For this experiment we used benzene as the reference molecule which is analogous to the PACER experiment. It is evident in Figures 6.5 and 6.6 that the substituted benzene harmonics decrease faster with harmonic order. This decrease is also faster in m−xylene than in p−xylene. Possible explanations for these trends are both rapid nuclear motion arising from the methyl groups although contributions from multiple electronic states must also be considered.

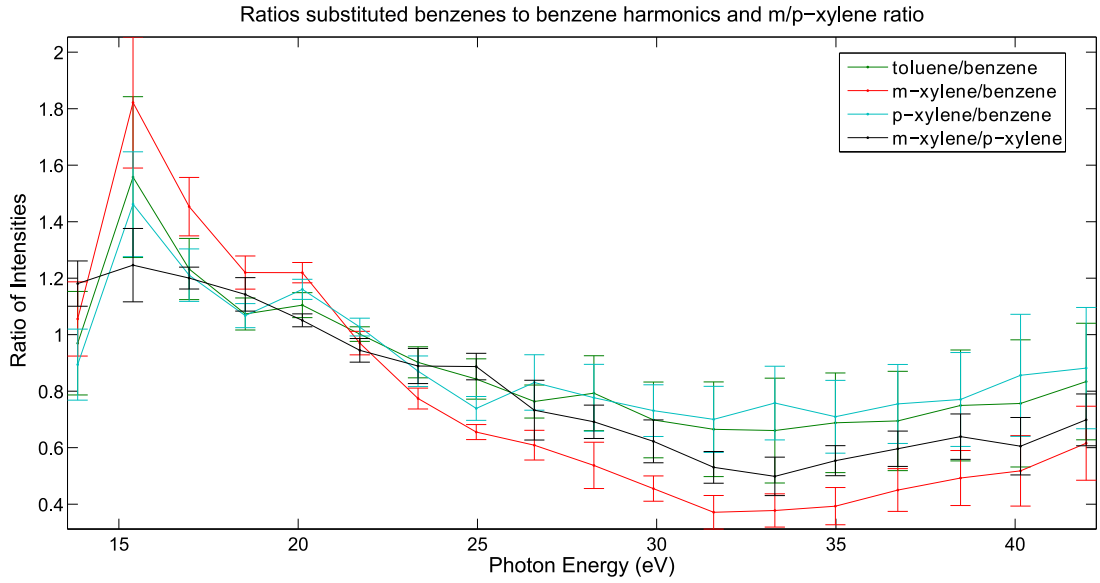


Figure 6.7: This plot is identical to that of the bottom panel in Figure 6.6 but with the addition of the ratio of m−xylene to p−xylene.

6.3 Intensity dependence of HHG in benzene and substituted benzenes

Recording HHG spectra as a function of laser intensity is important for ensuring we are acquiring data under conditions where the spectra are not saturated. In Figure 6.8 the harmonic intensity as a function of power fraction and the harmonic energy is plotted. The pulse energy was 420 μJ and this was varied using a half−wave plate and polariser combination such that spectra can also be recorded as a function of power fractions. The average peak intensity at the focus was 7.4×10^{13} W/cm^2.

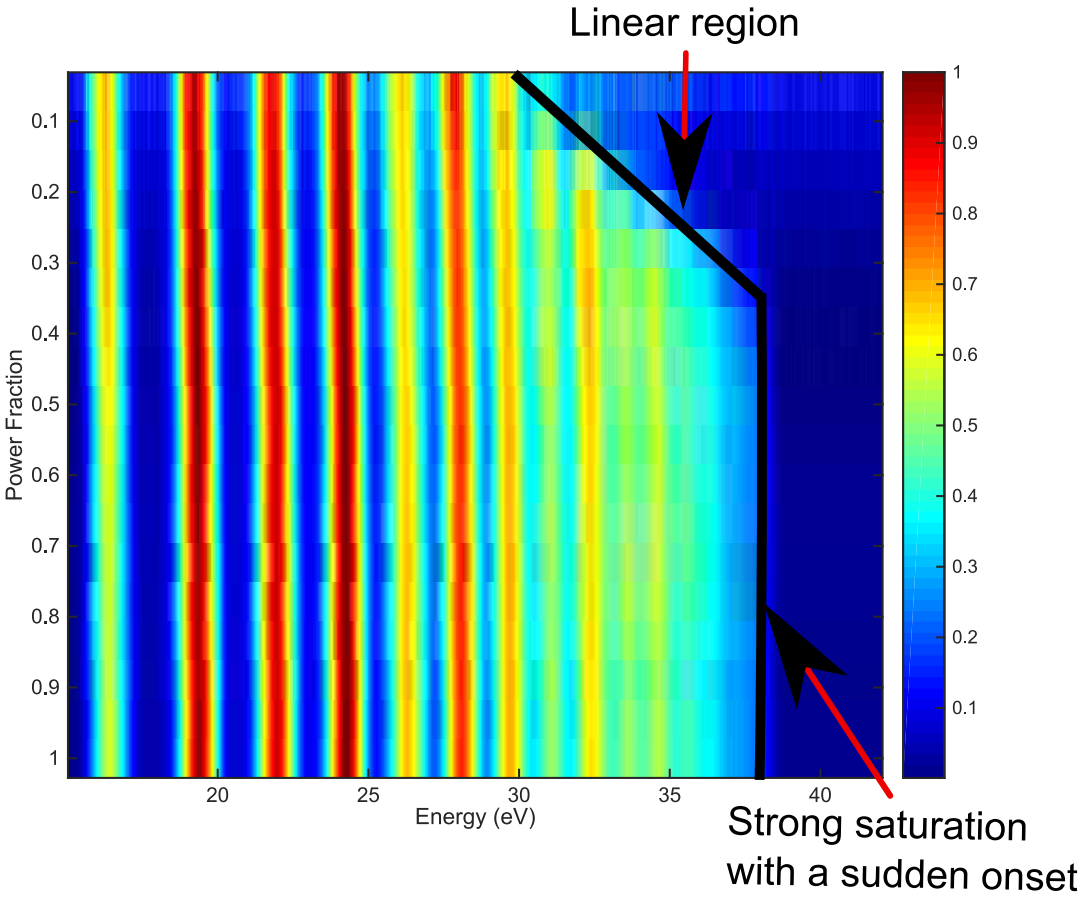


Figure 6.8: Intensity scan in benzene. The maximum energy per pulse was 420 μJ per pulse which corresponds to a power fraction of 1. The backing pressure was 0.48 bar for benzene. A sequence of 20 images was taken with a 1 s exposure time.

A clear linear dependence of the harmonic cut−off energy on the driving laser power is evident as shown in Figure 6.8, as is expected from the classical cut−off law. The

cut−off shifts to successively higher photon energies as the pulse energy is increased until it saturates at ≈ 150 μJ (power fraction of 0.35). The power fraction, which is seen as the right hand vertical scale in Figure 6.8, is recorded as the fraction of the maximum pulse energy measured using a power meter at the entrance of the vacuum chamber. This immediately tells us that we need to operate with pulse energies below ≈150 μJ to avoid saturating the spectra in benzene. As mentioned in section 5.3.1, this value is focus dependent though and as a result, it is difficult to determine. It is also inaccurate as phasematching conditions and imperfections in the mode quality are not accounted for. In the linear region of the plot the cut−off intensity dependence can be investigated by using the cut−off law $E_{co} = I_p + 3.17U_p$ where $U_p \propto I\lambda^2$. Using the classical cut−off law allows us to approximate the relationship between the angle of the polariser and the intensity of the laser field. The following equation is particularly suited to approximating the intensity which corresponds to the ponderomotive energy at the cut−off:

$$U_p[eV] \simeq 9 \times 10^{-14} I\lambda^2 \tag{6.1}$$

where I is in units of W/cm^2 and λ is in microns. For example we can estimate the saturation intensity in Figure 6.8 to be 1.3×10^{15} W/cm^2 since the spectrum saturates at 38 eV and the wavelength is 1.7 μm. This is two orders of magnitude larger than the expected value of 2.9×10^{13} W/cm^2 which highlights the difficulties inherent to making a measurement of the saturation intensity. The intensity dependence of the harmonic spectra of benzene and fluorobenzene was investigated as shown in Figures 6.9 and 6.10. For this data the pulse energy was 380 μJ.

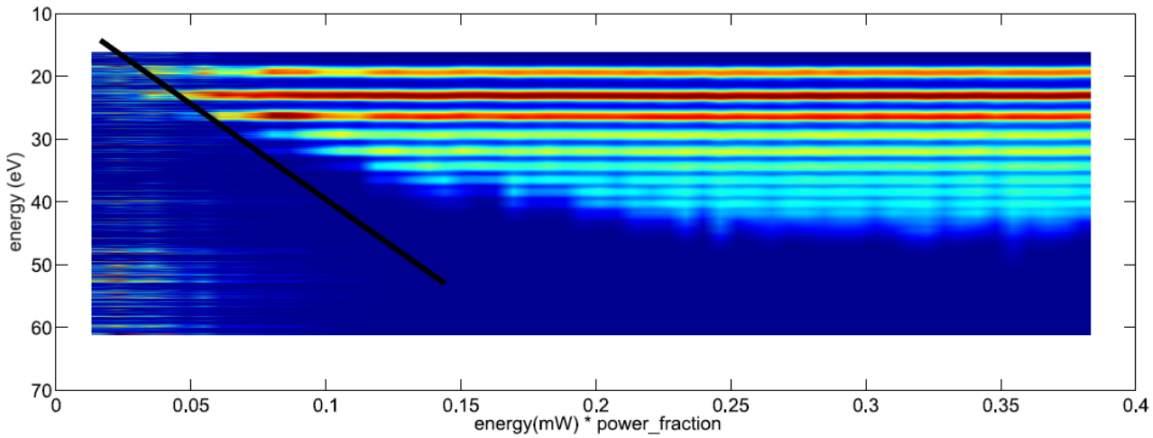


Figure 6.9: Intensity dependence of the cut−off position in the HHG spectrum from benzene. The black line represents the predicted cut−off position from the classical cut−off law. For this data set a sequence of 10 images were recorded with a 1 s exposure time.

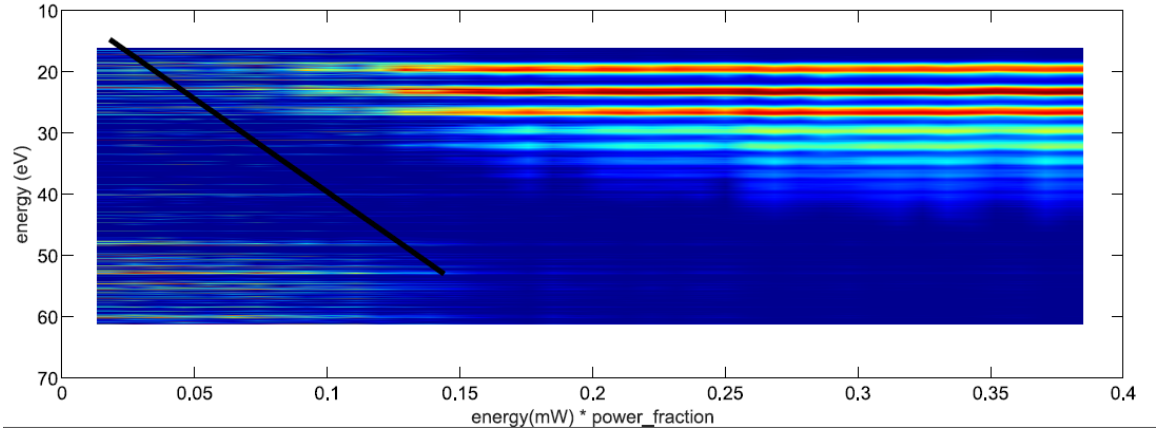


Figure 6.10: Intensity dependence of the cut−off position in the HHG spectrum from fluorobenzene. The black line represents the predicted cut−off position from the classical cut−off law. For this data set a sequence of 10 images were recorded with a 1 s exposure time.

Intensity scans were also performed on benzene, fluorobenzene and the methylayed benzenes. Intensity scan sets of 20 images, each of 1 s exposure were taken at each intensity for the aforementioned molecules. The maximum beam energy was 420 μJ per pulse which corresponds to a power fraction of 1. Each molecule had a backing pressure in the range $0.48 - 0.52$ bar. In Figure 6.11, the logarithm of the spectra is plotted as a false colour image as a function of intensity. An approximately linear extension of the cut−off is seen at low intensities before becoming saturated. Due to the plots being shown on a log scale, only changes in relative high harmonic

amplitudes are seen. It may appear that the signal is higher for lower power fractions for m-xylene, p-xylene and toluene, however this is a false interpretation of the data. Since the spectra are already well above the saturation limit, the amplitudes of any harmonics ≥ 35 eV decrease as a consequence of the normalisation done on the data.

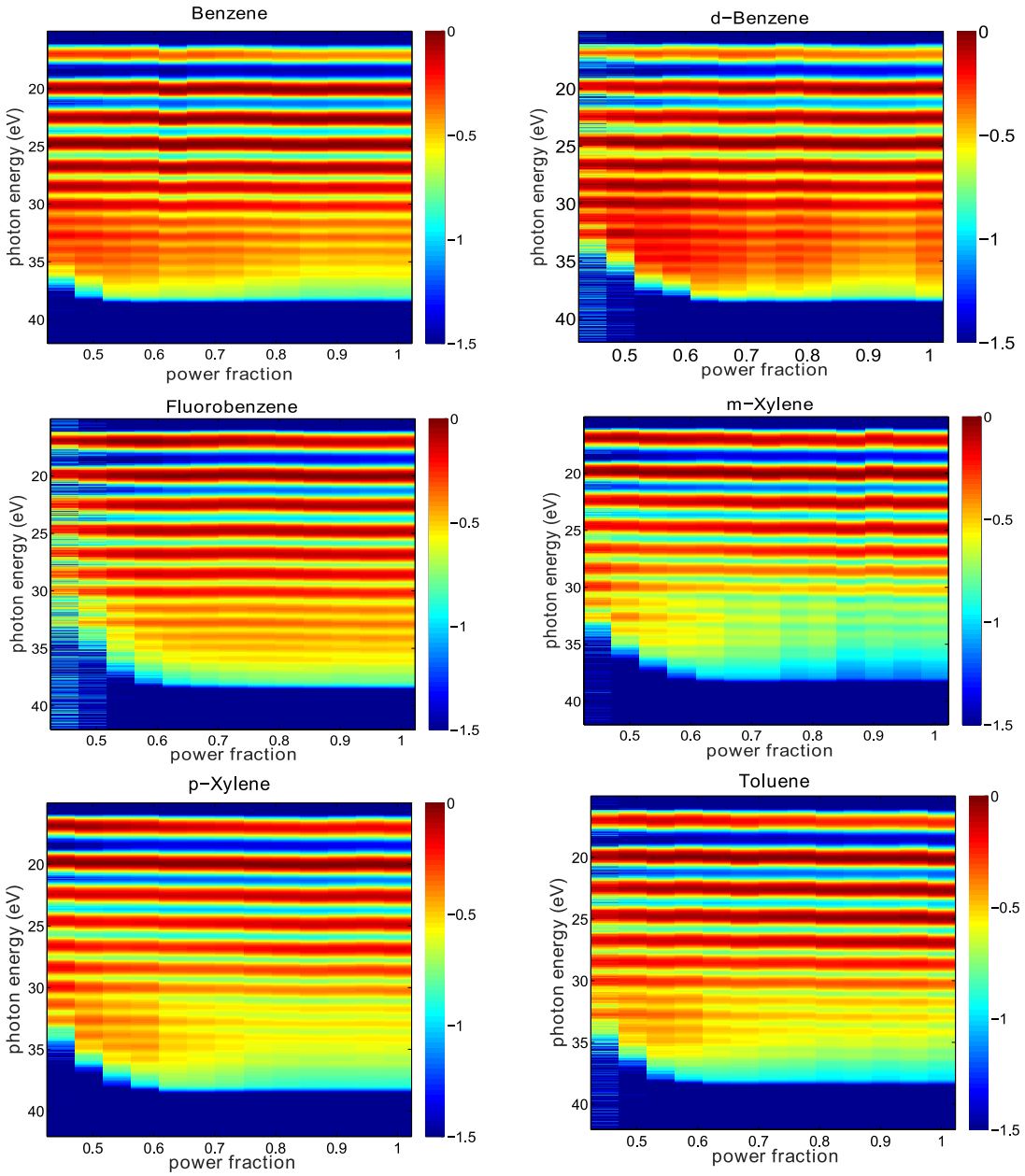


Figure 6.11: Intensity scans recorded in benzene, deuterated benzene, toluene, fluorobenzene and m and p−xylene. These plots indicate the power fraction of the maximum beam energy, 420 μJ per pulse, that will lead to saturation of the HHG spectra. The pulse duration for these scans was 44 fs and the data was acquired as a sequence of 10 images with a 1 s exposure time for each molecule.

There is also an evident cut−off shift as a function of iris diameter plotted in Figure 6.12 for toluene. The backing pressure in this case was 0.30 bar and the maximum

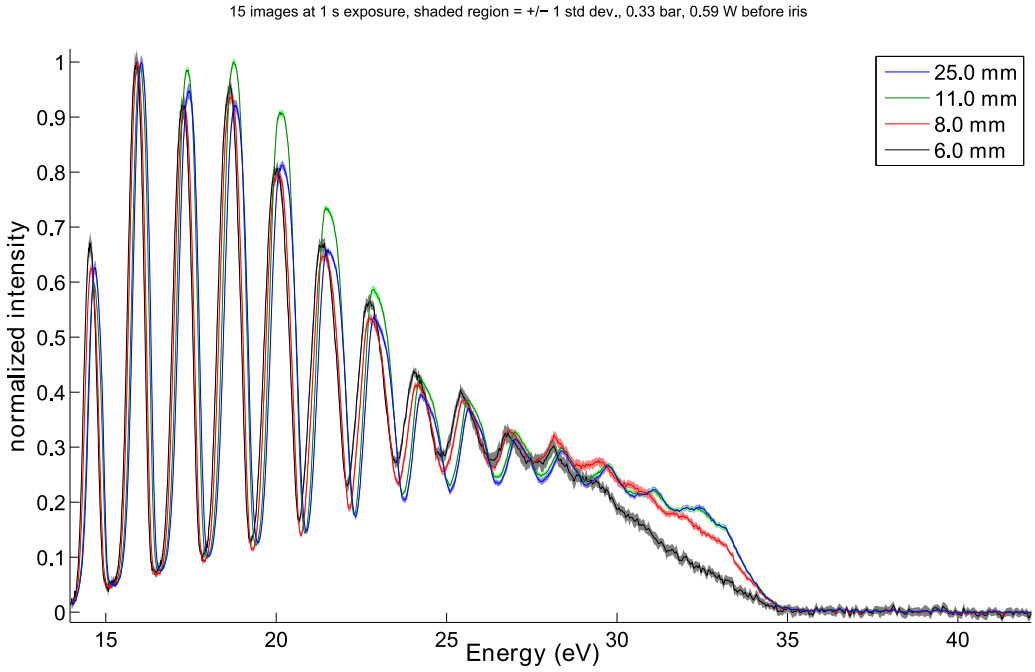


Figure 6.12: Normalized HHG spectra from toluene as a function of varying iris diameter. A shift in the cut−off position of the spectra is clearly evident with increasing iris diameter.

beam energy was 420 μJ per pulse. The peak intensity at the focus was 1.0×10^{14} W/cm^2.

As the iris diameter, and hence the input beam power, is increased the cut−off visibly shifts until it is saturated at the last two iris diameters. This method was just trialled without the half wave plate and polariser combination. Adjustments of the iris diameter are not precise enough to be reproducible as they are done by hand. Once the iris is set it cannot be touched which means it cannot be rechecked later. It was decided that the wave plate and polariser are the best means of adjusting the input beam power. The effect of these optics on the pulse duration of the idler does need to be investigated though. It was later found that the thin film polarizers we have been using degrade within seconds when in the blocking position. Once degraded, their extinction drops significantly. This implies that the intensity scans we took before are probably incorrectly calibrated, since $\cos^2(\theta)$ behaviour was assumed. However for the data in Figure 6.11 which was recorded using the wave-plate and polariser combination the cut-off is $\approx$ 37 eV for each of the molecules. For the case where the iris is used to adjust the input beam energy, as shown in Figure 6.12, the cut-off

for the case of the iris being fully open, which implies the maximum beam energy is used, the cut-off position is ≈ 35 eV. Since there is only a minor difference in the cut-off positions for the spectra using both beam energy adjustment methods we can infer that the calibration is not drastically affected by the degradation of the thin film polarizers. A variable ND filter or possibly a motorised iris could be implemented as alternatives.

6.3.1 Halogenated benzenes 2015

The main focus of this subsection is the comparison of fluorobenzene to benzene at the same backing pressure which implies the density of molecules in the interaction region is comparable. As shown in Figure 6.13 it is evident that the average signal level from fluorobenzene is ≈ a factor of three less than that of benzene.

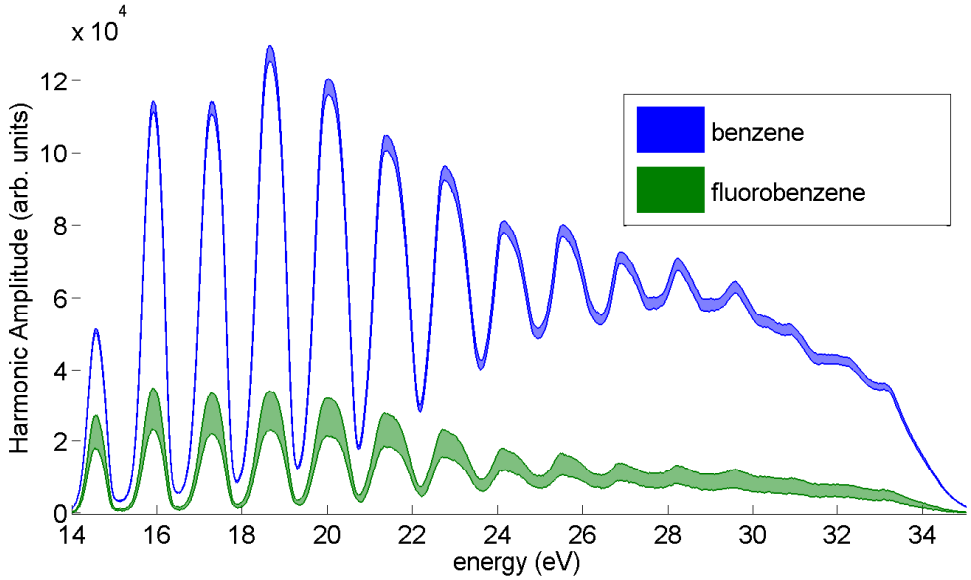


Figure 6.13: Comparison of high harmonic spectra taken in benzene and fluorobenzene under identical conditions (0.3 bar backing pressure - comparable densities in the interaction region - and 490 μJ per pulse beam energy). The line width indicates minimum and maximum harmonic amplitudes observed. For each data set a sequence of 50 images was recorded with a 1 s exposure time.

This result is further substantiated by comparing the unnormalised spectra from fluorobenzene and benzene acquired on the same day as shown in Figure 6.14 and 6.15 respectively.

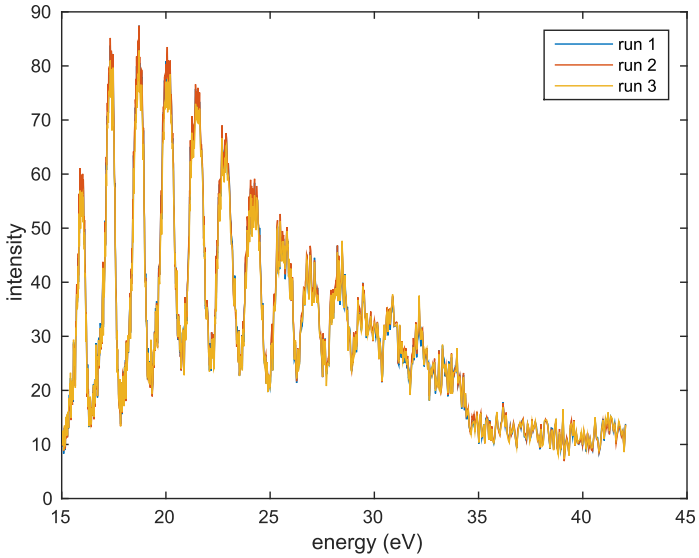


Figure 6.14: Unnormalised HHG spectra from fluorobenzene for three data runs. For each run the data was acquired as a sequence of 50 images with a 1 s exposure time. The beam energy was 490 μJ per pulse and the pulse duration was 56 fs.

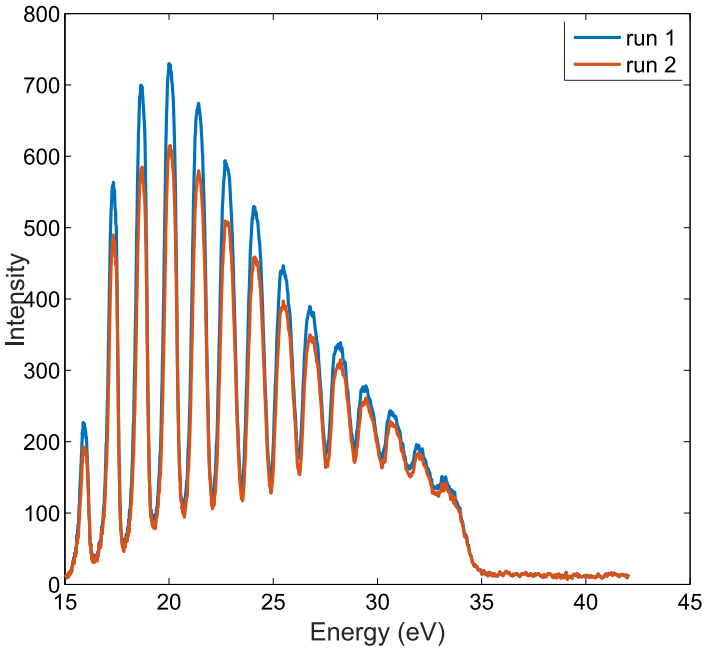


Figure 6.15: Unnormalised HHG spectra from benzene for two data runs.

These results confirm what we see in Figure 6.13. The unnormalised harmonic intensity counts for benzene reach ≈ 700 at a maximum whereas they reach a maximum count level of 90 for the fluorobenzene spectra. Both sets of data were acquired under near identical conditions; each with 0.5 bar backing pressure and $\approx 480\mu$J per pulse beam energy. The sets of spectra were acquired within an hour of each other on this particular day.

Figures 6.16 and 6.17 further confirm this anomaly of signal levels between benzene and fluorobenzene. For both data sets, the pulse duration was measured to be 56 fs. The average peak intensity at the focus was $\approx 7.6 \times 10^{13}$ W/cm^2 The data was acquired as a sequence of 10 images with a 1 s exposure time.

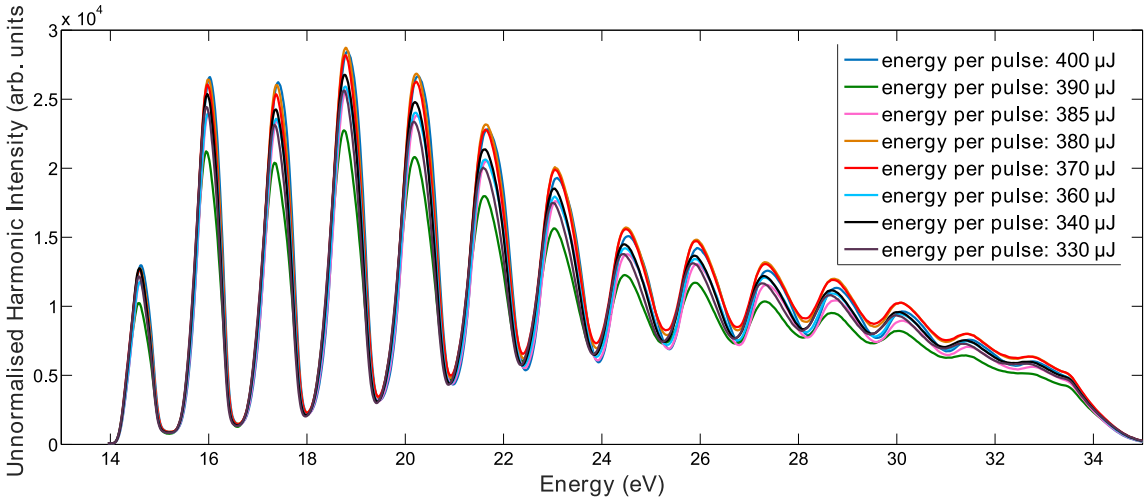


Figure 6.16: Unnormalised HHG spectra recorded in benzene at a backing pressure of 0.48 bar. The signal level minimum is $\approx 1 \times 10^4$ counts.

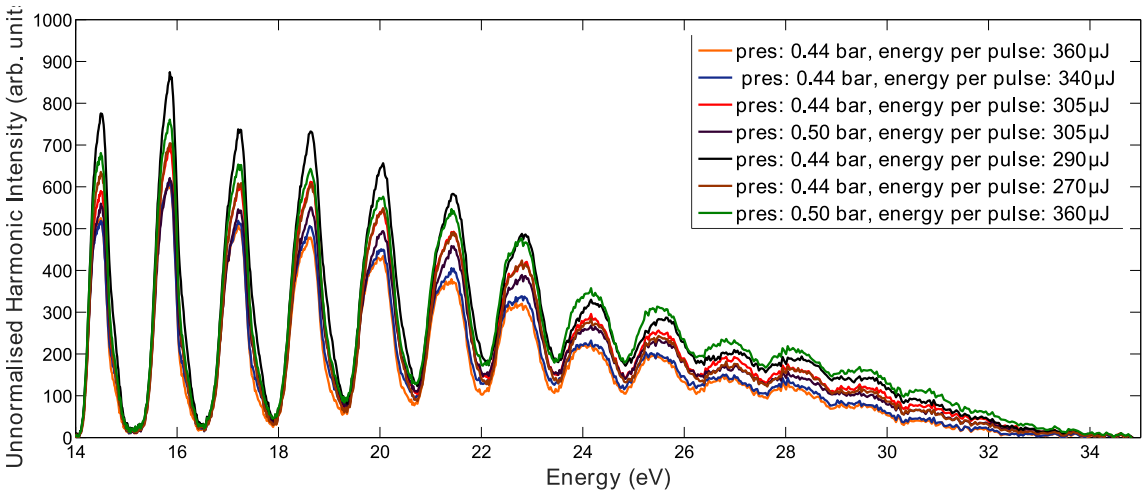


Figure 6.17: Unnormalised HHG spectra recorded from fluorobenzene. The minimum signal level is ≈ 200 counts and the maximum signal level is just above 900 counts.

Shown in Figure 6.18 are spectra recorded in benzene and the three halogenated benzene molecules we are studying. The beam energy for this data set was consistently 440 μJ per pulse and the iris diameter was set to 5.5 mm. Due to the irising of the beam and the lowering and raising of the gas−jet to search for self similarity between the spectra, the signal was low enough such that the laser−on−gas−off background was significant. Due to this, backgrounds with the gas turned off were taken after each measurement. It was noticed that the background appeared to change and was dependent on the positioning of the gas−jet. Background measurements were not taken for each gas−jet height as this would have been very time consuming. To circumvent this issue in future, a background was taken by closing the iris before the vacuum chamber entrance for each of the different jet positions and/or backing pressures. Backing pressures differ for this data set due to uncertainties in getting the necessary relationship between bath temperature and backing pressure as this was the first run where the three halogenated benzene molecules were on the apparatus together. Since adjusting the temperature was time consuming, the pressure range accuracy was relaxed. Instead, for each molecule the gas−jet was moved up and down and the self similarity of the spectrum was monitored. In general it was never perfectly self similar but for low gas−jet positions it was quite close − within 5% change in normalised spectral intensity. The spectra shown in Figure 6.18 were acquired at some compromise between the signal intensity and self similarity of the spectra. The

average peak intensity at the focus was 7.5×10^{13} W/cm^2.

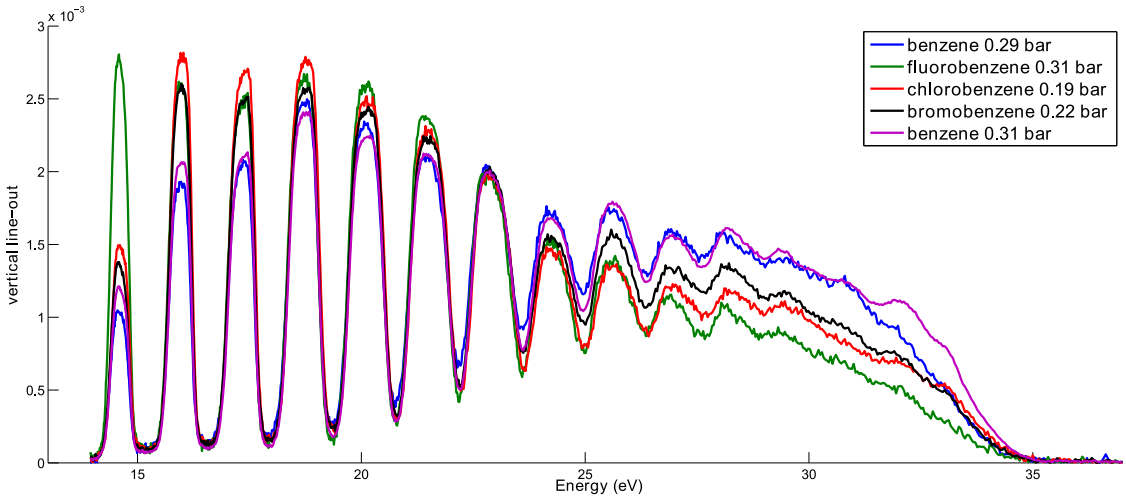


Figure 6.18: Area normalised HHG spectra recorded in benzene and the halogenated benzenes. For each data set a sequence of 10 images was recorded with a 1 s exposure time. This data may be affected by the change in the background taken which is dependent upon the vertical position of the gas-jet that was changed to ensure similarity in the shapes of the spectra for each molecule.

6.4 2015 PACER data

The PACER data was also retaken in this experimental run to determine if the evolution of the ratios between deuterated benzene and protonated benzene is reproducible. As previously discussed, discrepancies in the backing pressure between the two molecules or instabilities in the laser beam can both contribute to markedly different generating conditions for both molecules even if the data acquisitions are closely spaced in time.

Figure 6.19 shows three sets of spectra recorded in deuterated benzene on one particular day. The laser beam energy was 480 μJ per pulse and the backing pressure was 0.54 bar in all cases. The peak intensity at the focus was 8.5 $\times 10^{13}$ W/cm^2. The spectra are area normalised. There is excellent reproducibility in the shapes of the spectra. The actions taken to improve the laser stability have been discussed in chapter 5.

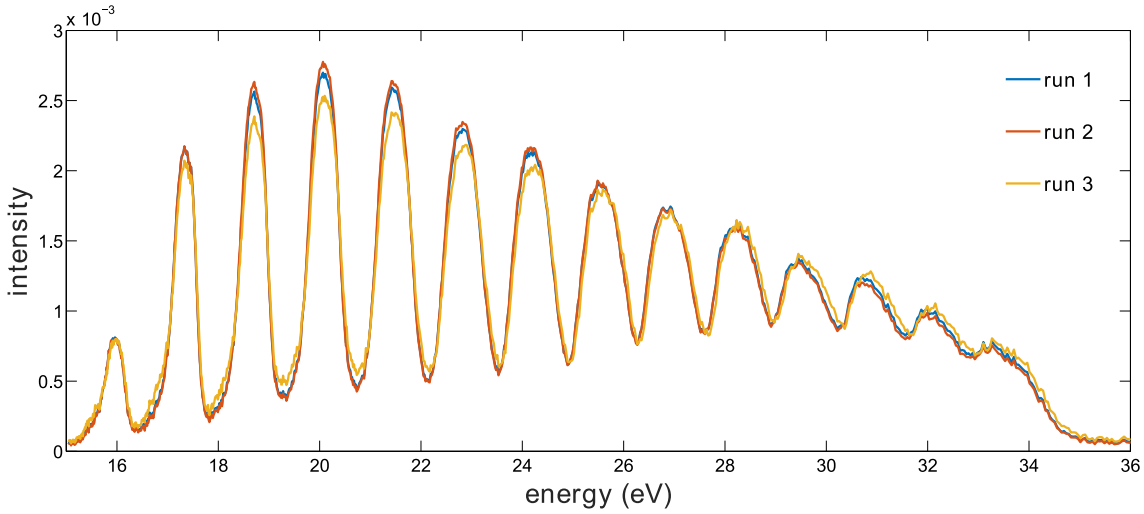


Figure 6.19: Area normalised HHG spectra from deuterated benzene. Three spectra are displayed on this plot. The data was acquired as a sequence of 50 images with a 1 s exposure time. The pulse duration was 50 fs.

The improved stability of the experiment as a whole is reflected in the pressure scan performed in deuterated benzene as shown in Figure 6.20. The peak intensity at the focus was 6.1 $\times 10^{13}$ W/cm^2. The pressure is varied from 0.58 to 0.1 bar and the shape of the spectrum is consistent. Features such as the dip in the spectrum at $\approx$ 27 eV is present in all of the spectra which is indicative of near identical phase matching conditions.

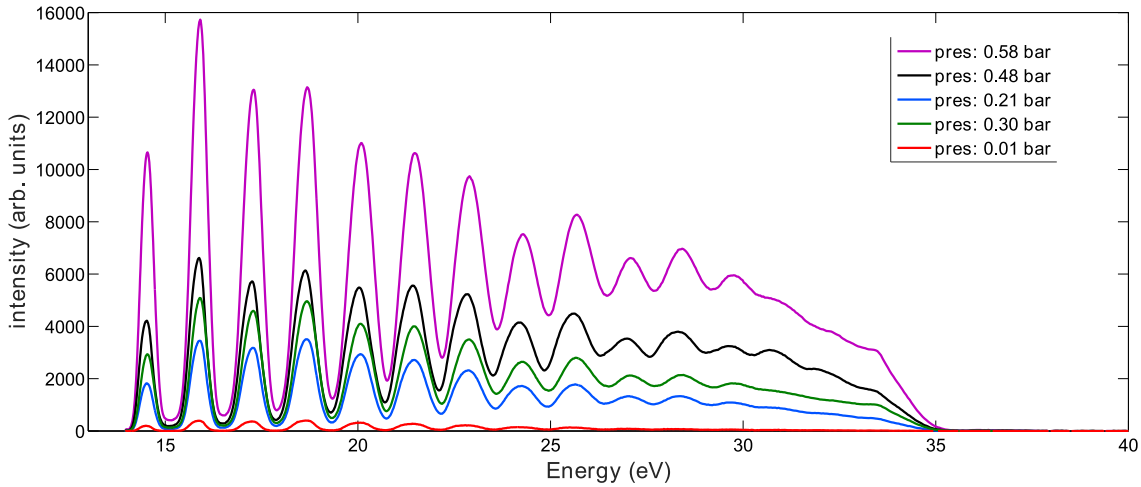


Figure 6.20: Pressure scan recorded from deuterated benzene. For this data set the pulse duration was 56 fs, the energy per pulse was 380 μJ and the data was acquired as a sequence of 15 images with a 1 s exposure time for each pressure displayed in the legend.

In Figure 6.21, normalised spectra of benzene and deuterated benzene are plotted. The peak intensity at the focus was 6.9 $\times 10^{13}$ W/cm^2. As was observed with the data recorded in 2013, we still see that there is very little difference between the spectra of the two molecules. Note that the blue benzene trace has a higher cut−off position which is consistent with the fact that the power was higher for this measurement.

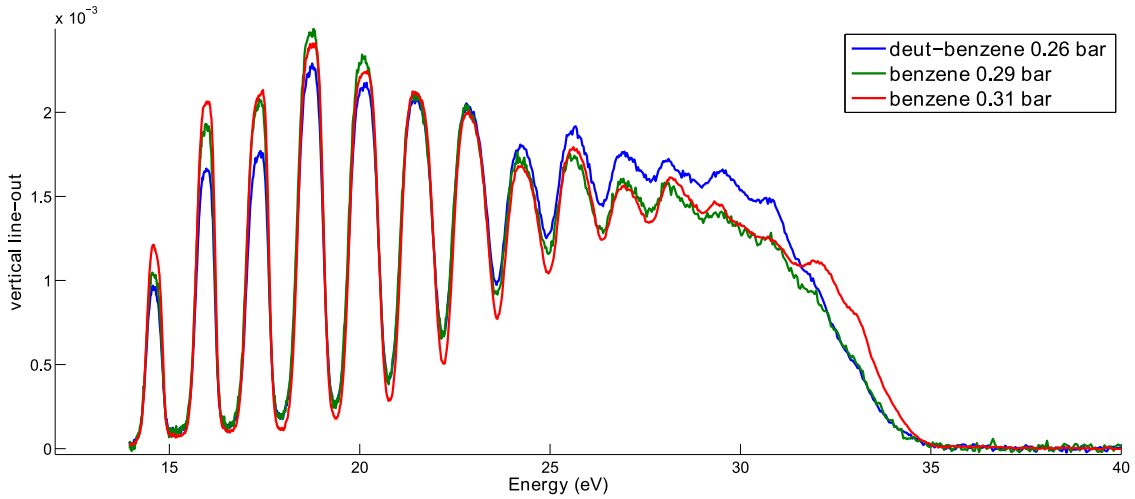


Figure 6.21: Comparison of HHG spectra in benzene and deuterated benzene under similar generating conditions. The blue trace was recorded with a higher input beam energy which is reflected in its higher energy cut−off position. The data was acquired as series of 20 images with a 1 s exposure time. The pulse duration was 44 fs.

The ratio of deuterated benzene to benzene to plotted in Figure 6.22. Note that the vertical axis has been constrained to ratio values between 0.93 and 1 to emphasise the $< 10\%$ change in the ratio which is insignificant. Within the error bars it is conclusive that there is no change in harmonic signal level between the deuterated and protonated benzenes. The data plotted is averaged over 3 sets of data acquired at different times on the same day.

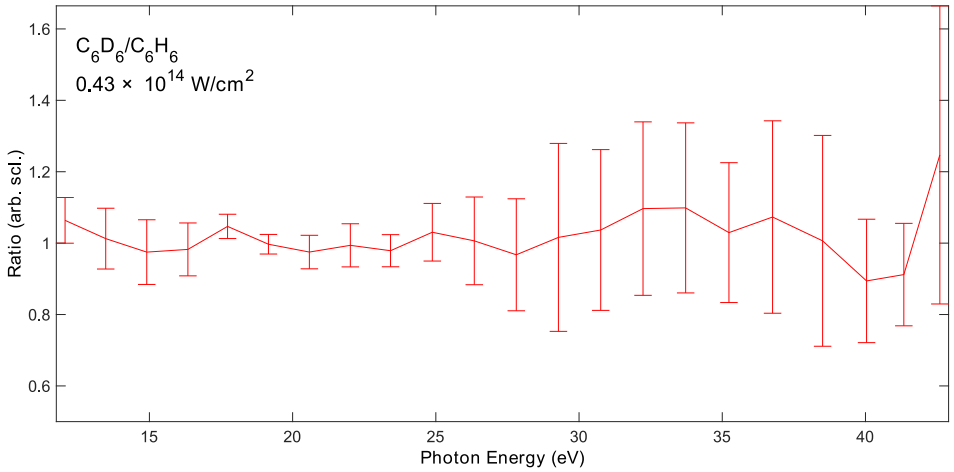


Figure 6.22: Ratio of deuterated benzene to benzene

6.5 Methylated benzene molecules

We have also successfully performed HHG on the family of methylated benzene molecules. These include the mono−substituted toluene and the di−substituted structural isomers of xylene. We initially did not work with ortho−xylene as it was known to contain impurities (2013 data). It was later discovered through correspondence with Sigma Aldrich Ltd. that these impurities largely consist of water and since we must heat the sample in excess of 100°C this will not be a potential contributor to the HHG spectrum recorded from ortho−xylene as the water impurity will have evaporated at the elevated temperatures required to generate $\approx>$ 0.3 bar of ortho−xylene. We begin by analysing the spectra from benzene and toluene, which is mono−substituted with a methyl group. Figure 6.23 below is a pressure scan in toluene illustrating that the shape of the spectrum is similar at the different pressures. The peak intensity at the focus was 6.2 $\times 10^{13}$ W/cm^2.

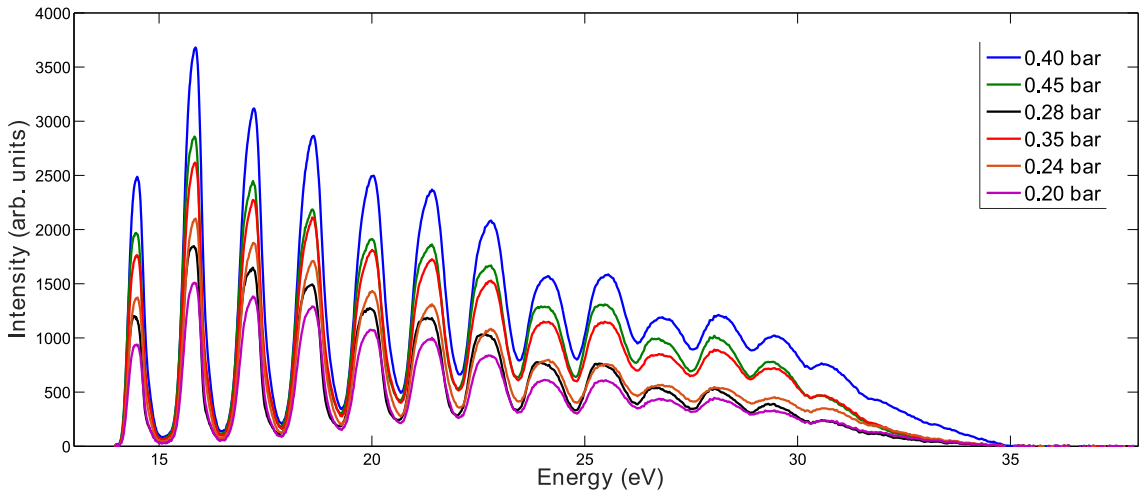


Figure 6.23: Pressure scan recorded from toluene. The backing pressure was varied from 0.45 − 0.2 bar. The beam power was 390 mW, the pulse duration was 56 fs and the iris diameter before the chamber was 10 mm. This data was acquired as as sequence of 10 images with a 1 s exposure time.

A comparison of the spectral intensities was made between benzene and toluene. Figure 6.24 shows four benzene spectra and one toluene spectrum, all normalised, which clearly illustrates that the signal at higher photon energies is stronger in benzene than in toluene. In all cases the beam energy was 470 μJ per pulse and the backing pressure was 0.21 bar for both species. The peak intensity at the focus was 8.4 $\times 10^{13}$ W/cm^2.

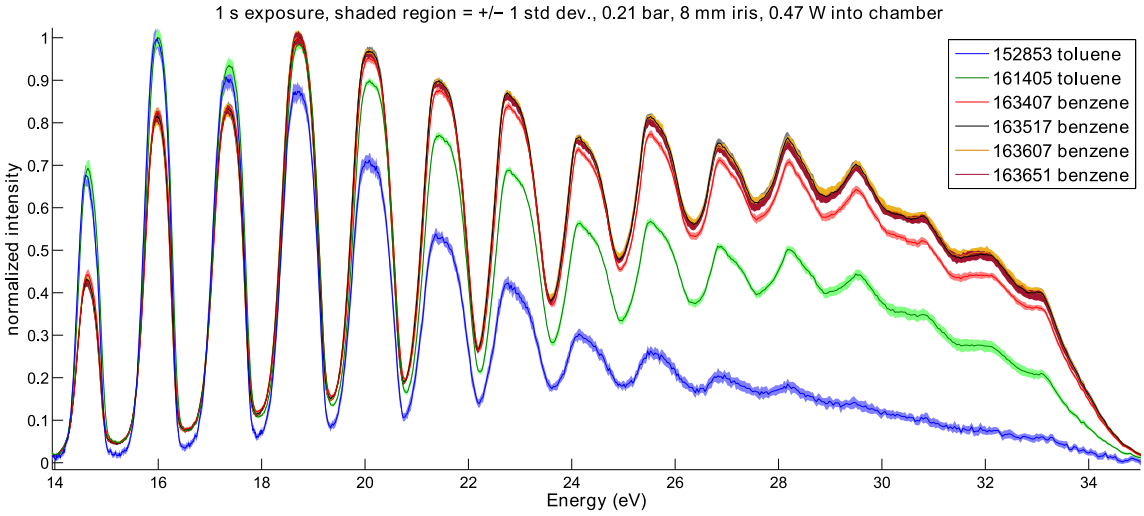


Figure 6.24: Comparison of HHG spectra recorded in benzene and toluene which illustrates the lower intensity of the cut−off harmonics in toluene compared to benzene using similar backing pressures and laser parameters.

The average ratio of toluene to benzene for twelve pairs of spectra are shown in Figure 6.25. The peak intensity at the focus was 9.4 $\times 10^{13}$ W/cm^2.

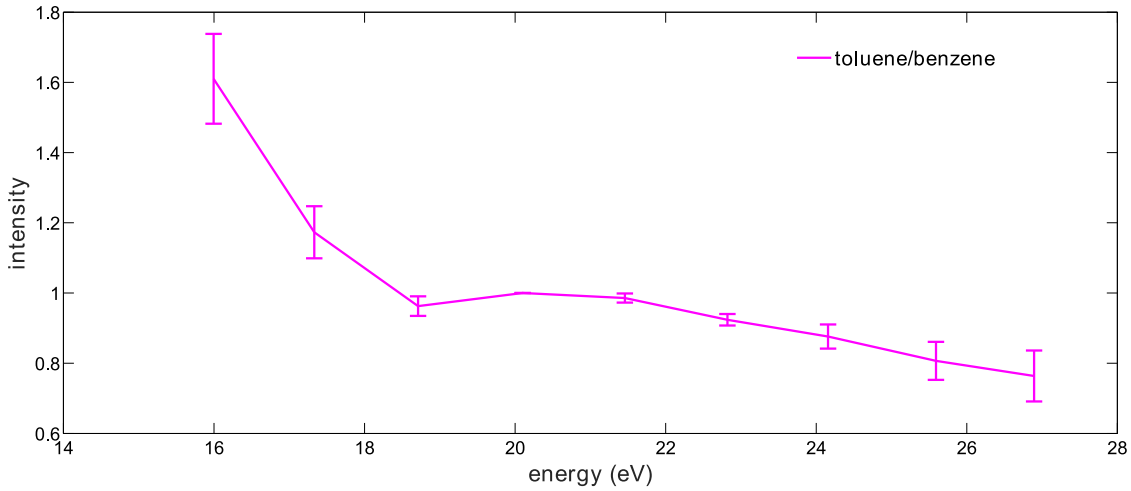


Figure 6.25: Ratio of toluene to benzene. Spectra were normalised to the fourth peak visible on the MCP image. The data is averaged over the twelve pairs of benzene−toluene spectra to compute the error bars. The pulse duration was 34.8 fs and the data was acquired as a sequence of 50 images with a 1 s exposure time.

The ratios of toluene to benzene have also been recorded as a function of power fraction as shown in Figure 6.26. The maximum energy was 410 μJ per pulse and the backing pressure was 0.48 bar for both molecules.

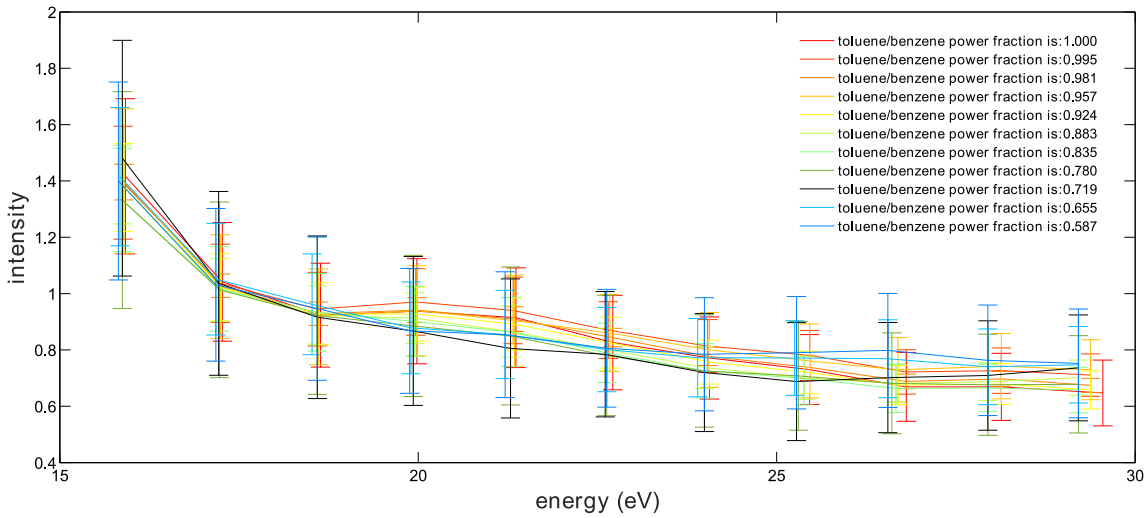


Figure 6.26: Ratios of toluene to benzene harmonics as a function of input beam power. The general trend of the ratio decrease is similar to that in Figure 6.24 which is a further indicator of the improved stability of the apparatus to generate more consistently reproducible spectra. For each power the data was acquired as a series of 20 images with a 1 s exposure time.

Spectra from all three of the xylene isomers were also recorded during this run. In Figures, 6.27, 6.28 and 6.29 spectra from the three xylene isomers are plotted, normalised to the intensity of the harmonic at ≈ 17 eV which is the most intense for all spectra. The purpose of this panel of spectra is to inspect the subtle differences in the shapes of the spectra for the three xylene isomers. For o−xylene, there is a clear sharp decrease for the lower harmonic orders before there is a well defined plateau from $\approx 25 - 30$ eV and then a decline preceding the cut−off. For p−xylene there are a few intricate details such as reduction in signal for the harmonic at ≈ 25 eV. M−xylene has a somewhat similar shape to o−xylene but has a less pronounced plateau region.

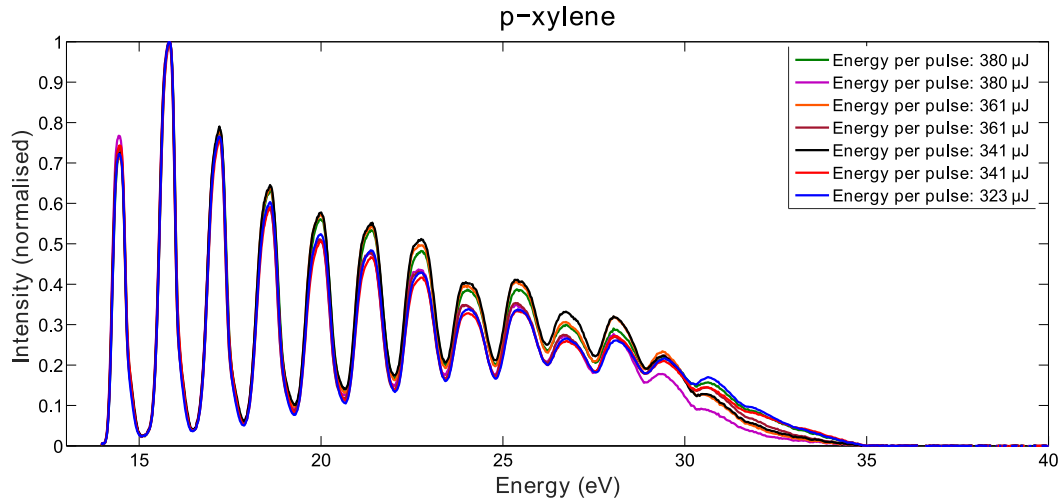


Figure 6.27: HHG spectra recorded in the para-xylene isomer to allow for a comparison of the differing shapes of the spectra between isomers. The data was acquired as a sequence of 50 images with a 1 s exposure time. The pulse duration was 34.8 fs and the backing pressure was 0.52 bar.

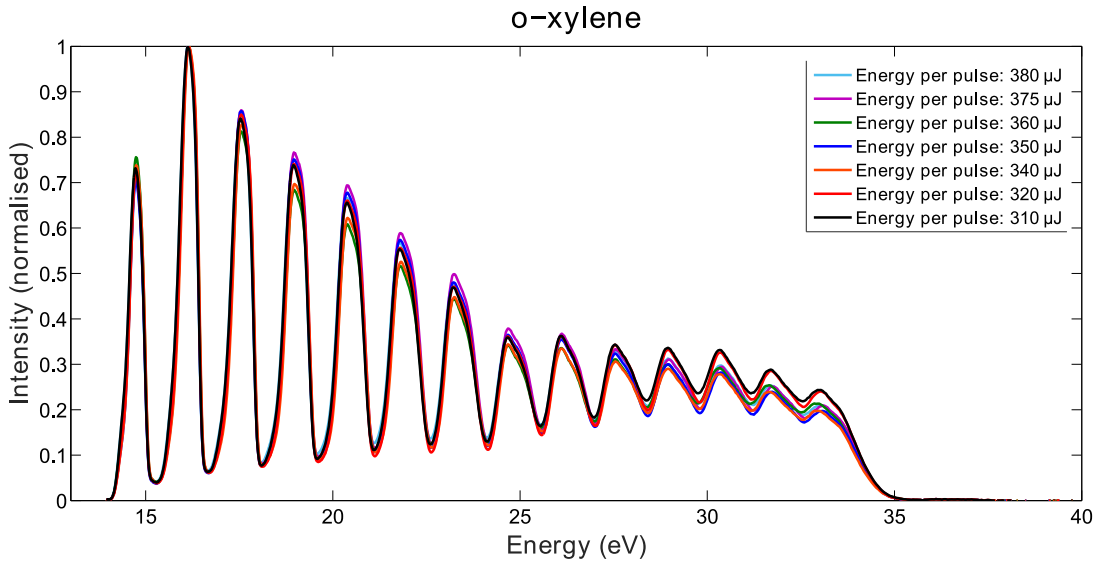


Figure 6.28: HHG spectra recorded in the ortho-xylene isomer to allow for a comparison of the differing shapes of the spectra between isomers. The data was acquired as a sequence of 50 images with a 1 s exposure time. The pulse duration was 34.8 fs.

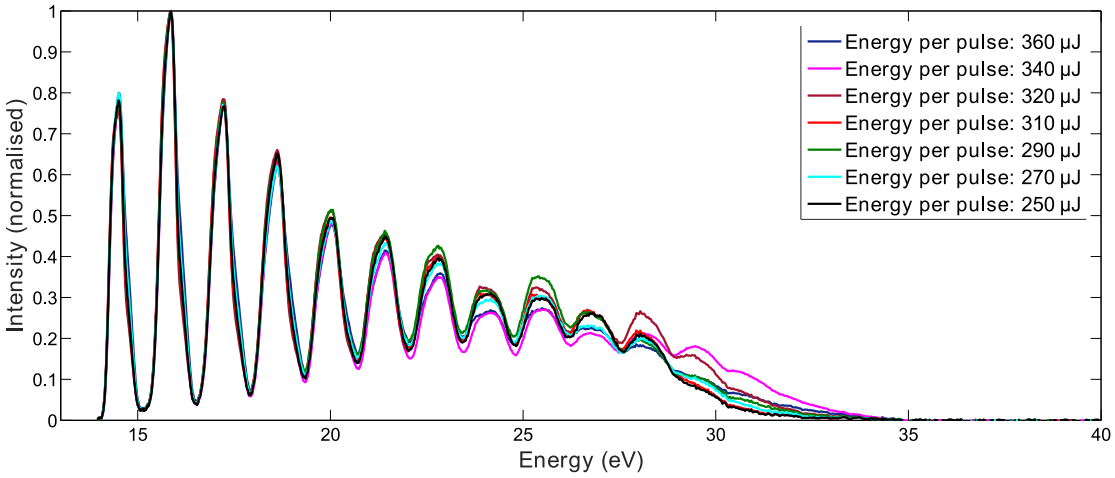


Figure 6.29: HHG spectra recorded in the meta-xylene isomer to allow for a comparison of the differing shapes of the spectra between isomers. The data was acquired as a sequence of 50 images with a 1 s exposure time. The pulse duration was 34.8 fs and the backing pressure was 0.50 bar.

In Figure 6.30 we show the ratios of p−xylene to m−xylene and the ratios of o−xylene to m−xylene. For each molecule, sets of 50 images, each of one second exposure, were taken at several times during the data collection day. Four sets of spectra were recorded for p−xylene and m−xylene and three sets were recorded for o−xylene.

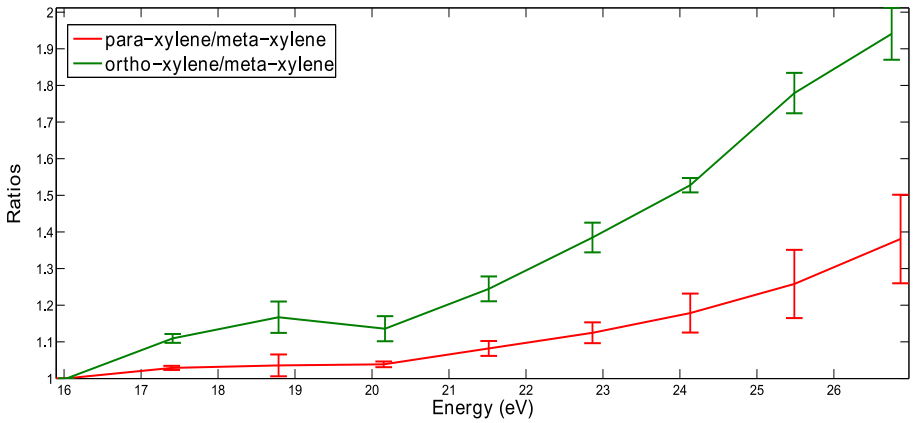


Figure 6.30: Ratios of p−xylene and o−xylene to m−xylene. The data is averaged over four data sets for each ratio shown. The beam energy was 440 μJ per pulse. The data was acquired as a sequence of 20 images witha 1 s exposure time.

The combined signal for all combinations of runs is shown in Figure 6.31. The error is taken from the spread of the data at each harmonic order as opposed to taking the individual errors into account as these are a lot smaller than the spread that is seen from run to run. These ratios are normalised to the second harmonic on the screen. This is the maximum intensity harmonic order for each data set as the first harmonic visible is on the edge of the MCP. The ratios plotted only represent the shape of the ratio with photon energy, not the absolute value. The effect of taking the absolute value of a number is to strip away the minus sign if the number is negative and to leave the number unchanged if it is non-negative. The ratios plotted in Figure 6.31 takes negative values into account thus just representing the shape of the ratio as a function of photon energy.

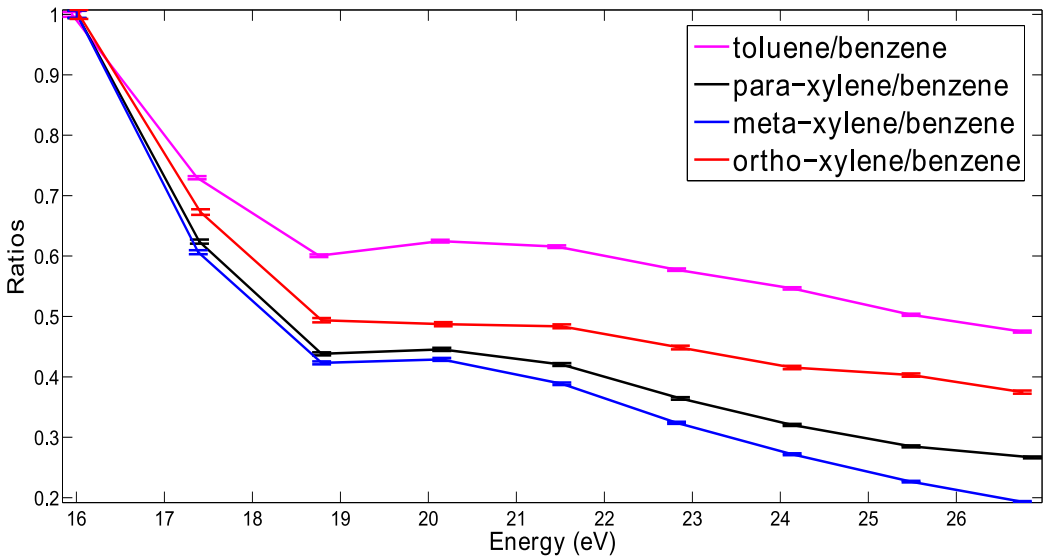


Figure 6.31: Ratios of toluene, m−xylene p−xylene and o−xylene to benzene. The data is averaged over four data sets for each ratio shown. The beam energy was 440 μJ per pulse. The data was acquired as a sequence of 20 images with a 1 s exposure time.

Shown in Figure 6.32 are the unnormalised harmonic spectra of benzene, o−xylene and m−xylene. It is clear that o−xylene is very similar to benzene whereas m−xylene has a lower signal magnitude at higher harmonic orders. The peak intensity at the focus was 1.2 $\times 10^{14}$ W/cm^2.

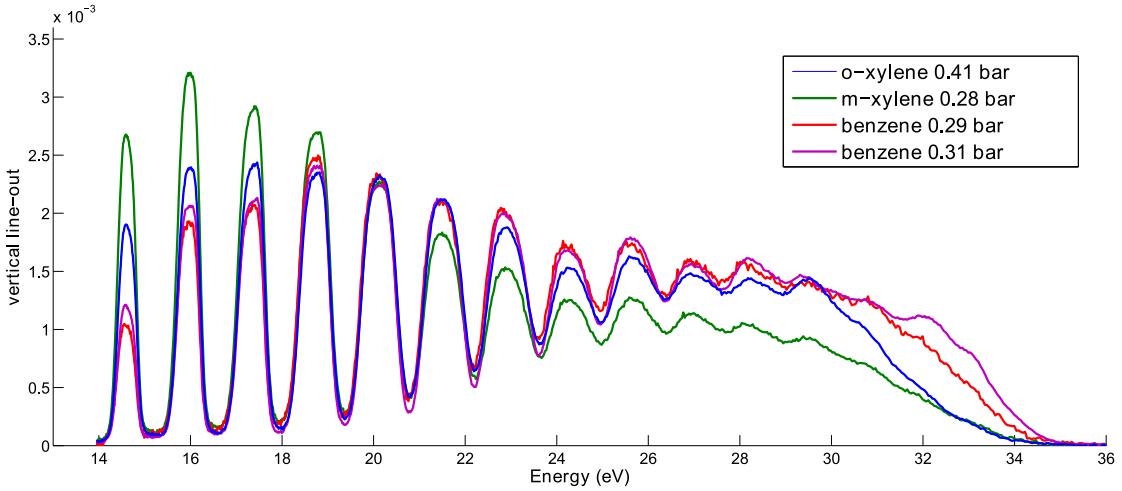


Figure 6.32: Unnormalised HHG spectra from benzene, o−xylene and p−xylene plotted to facilitate a comparison of the shapes of the spectra between molecules. The beam energy was 620 μJ per pulse, pulse duration was 45.6 fs and the backing pressure was $\approx$ 0.30 bar for each molecule. The data was acquired as a sequence of 10 images with a 1 s exposure time.

In order to elucidate the effect of the methyl substitutions on the benzene ring, ratios of the methyl substituted benzenes to benzene were also taken as shown in Figure 6.33. The backing pressure for the five molecules was ≈ 0.30 bar and the beam energy per pulse was 620 μJ. The spectra are area normalised. Using benzene as a reference molecule, we see that the slowest to fastest ratio decrease goes from o−xylene, toluene, p−xylene and finally m−xylene in the cut−off region of the spectrum. In contrast to the data shown in Figure 6.31, the absolute values of the ratios are plotted.

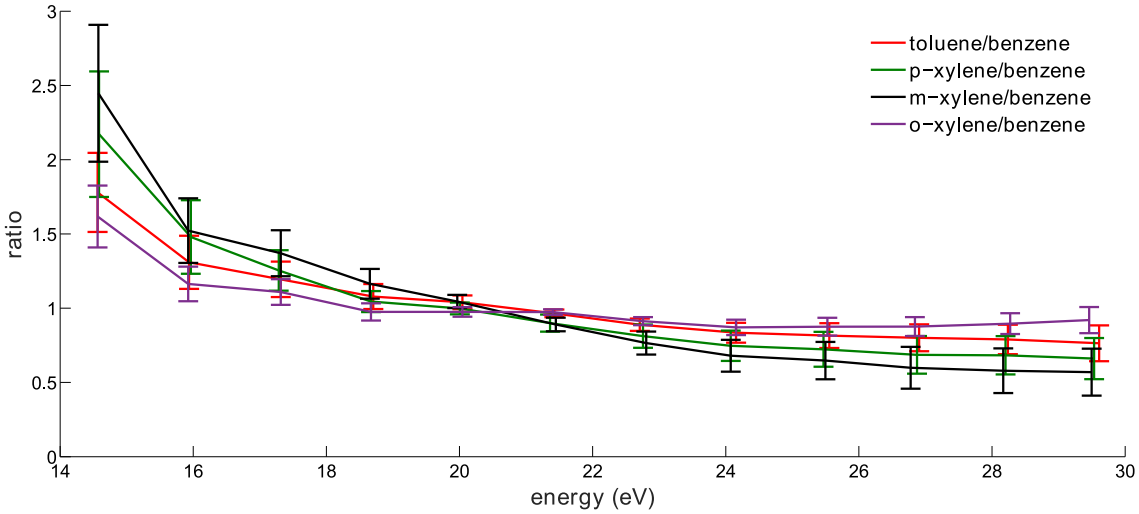


Figure 6.33: Ratios of methylated benzene molecules to the reference benzene.

6.6 Molecular SFA calculations

Strong Field Approximation (SFA) calculations have also been performed by Dr. Ricardo Torres and myself on the molecules of interest to this thesis. The methodology behind these calculations has been presented in section 1.8. The molecular orbital coefficients are calculated using a 3-21G basis set in the GAUSSIAN computational chemistry package.

An SFA code has been developed to investigate the effects of the contribution of the HOMO-1 orbital to the harmonic spectra of the halogenated and methylated benzenes. The HHG spectra are averaged over all possible orientations of the molecules in an isotropic distribution. For these calculations we have used the following parameters - a drive wavelength of 1700 nm, a pulse duration of 30 fs and a laser intensity of 5×10^{13} W/cm^2. Only short trajectories are taken into account to reflect the phase matching conditions we have in the experiments performed.

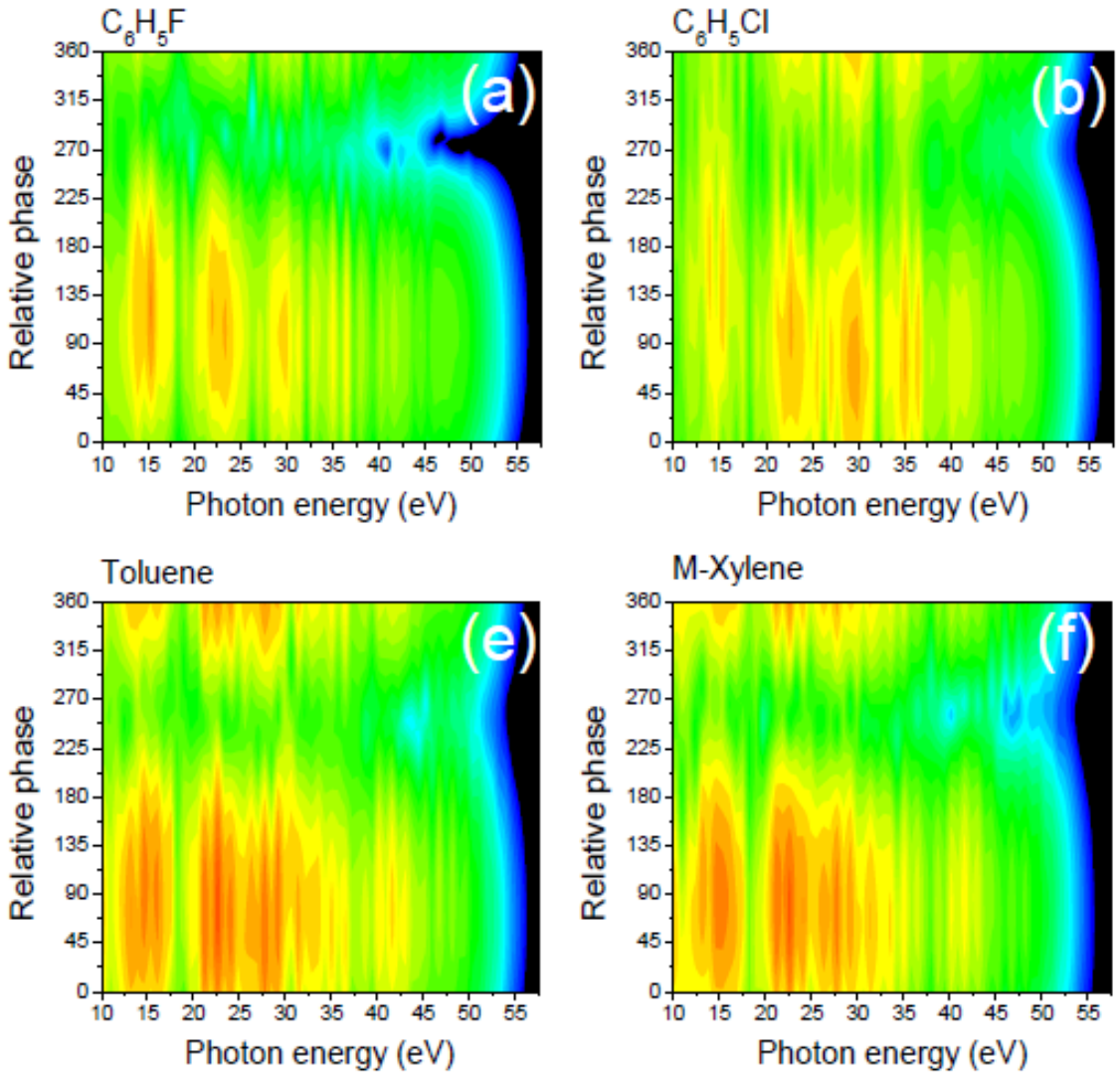


Figure 6.34: SFA simulation results of the harmonic intensity as a function of the relative phase between HOMO and HOMO-1, for different molecules (a) fluorobenzene, (b) chlorobenzene, (c) toluene, (d) m-xylene. I = 5×10^{13} W/cm^2, $\lambda = 1700$ nm, cos^2 pulse of $\tau = 30$ fs, short trajectories only.

Figures 6.34 and 6.35 show the harmonic intensity as a function of the relative phase between the HOMO and HOMO-1. A higher contrast on the colourmaps for different relative phases is obtained when the energy difference between the HOMO and HOMO-1 is smaller. For instance, iodobenzene shows the highest harmonic intensity but has the weakest dependence on the relative phase which is what is expected as the energy difference between the HOMO and HOMO-1 is 0.81 eV. In the case of the

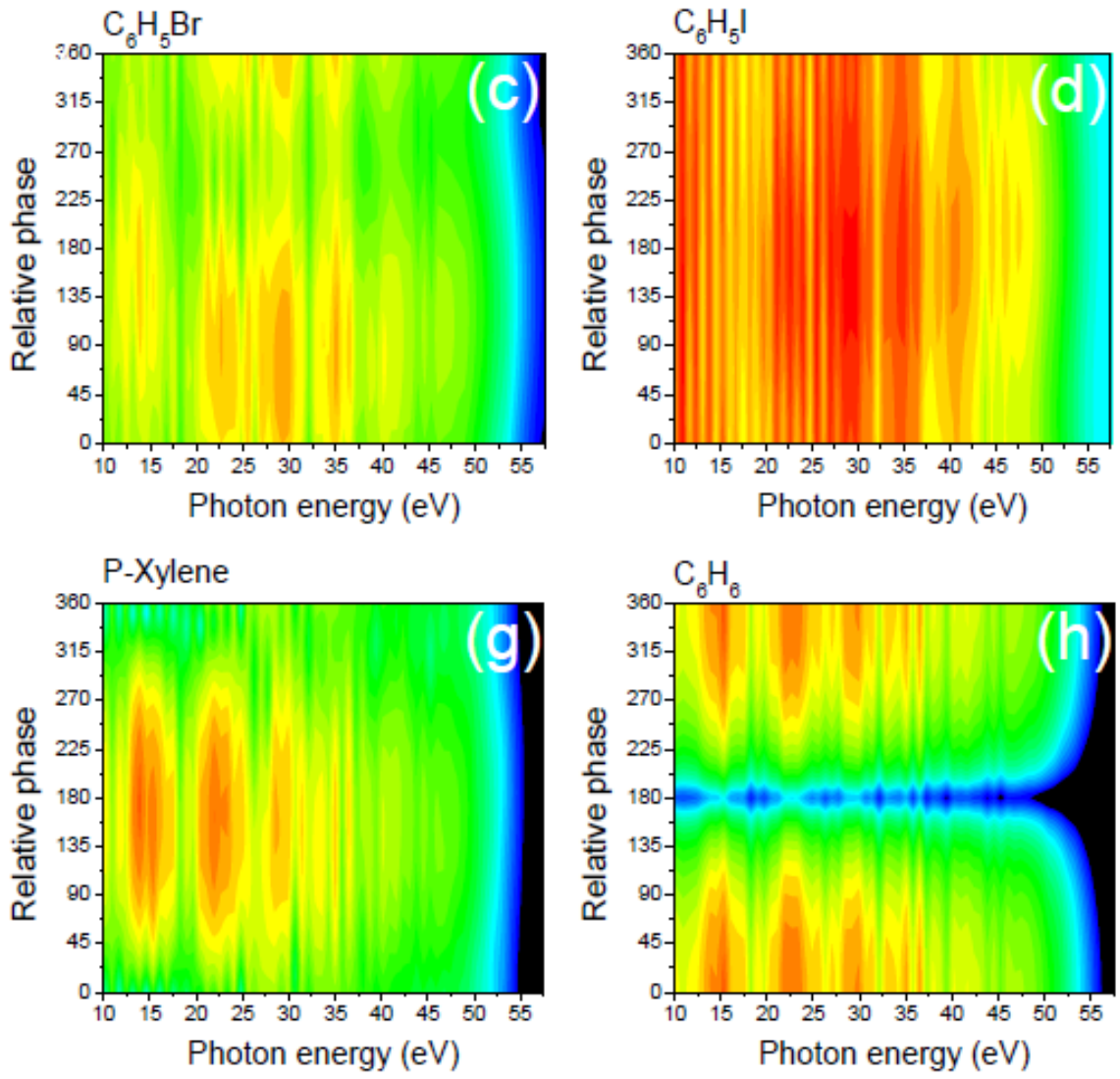


Figure 6.35: SFA simulation results of the harmonic intensity as a function of the relative phase between HOMO and HOMO-1, for different molecules (a) Bromobenzene, (b) iodobenzene, (c) p-xylene, (d) benzene. I = 5×10^{13} W/cm^2, $\lambda = 1700$ nm, cos^2 pulse of τ = 30 fs, short trajectories only.

colourmap for benzene the relative phase between the two degenerate HOMO orbitals cannot be fixed and is thus the harmonic intensity spectra of benzene are averaged over the relative phase of the orbitals which is equivalent to incoherently adding the contributions from each degenerate orbital.

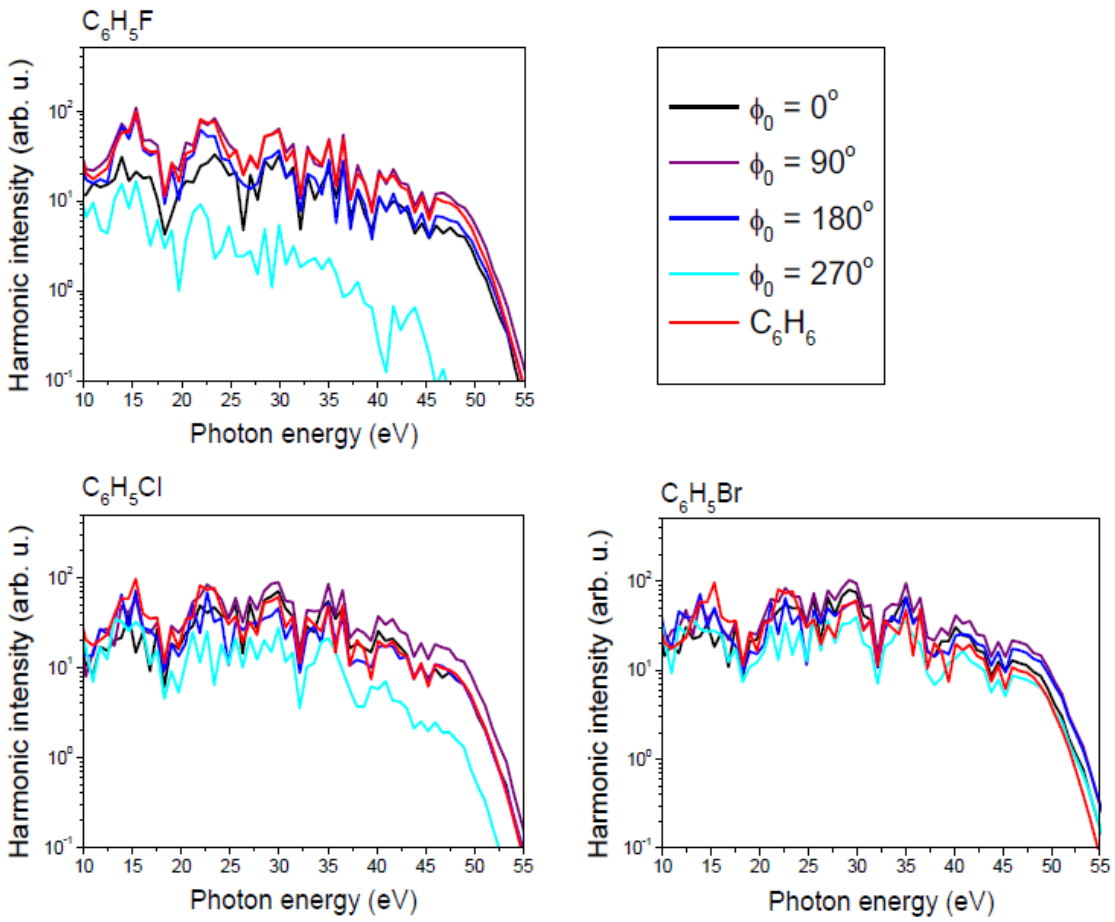


Figure 6.36: SFA simulation results of the harmonic spectra for different molecules and relative phases between HOMO and HOMO-1, compared with benzene. I = 5×10^{13} W/cm^2, $\lambda = 1700$ nm, cos^2 pulse of $\tau = 30$ fs, short trajectories only.

Shown in Figures 6.36 and 6.37 are comparisons of benzene with the other aromatic molecules as a function of four values of the relative phase between the HOMO and HOMO-1. We can see for both fluorobenzene and chlorobenzene that a phase difference of 270° produces a spectrum which is much weaker than that of benzene, in bromobenzene the spectrum with 270° phase difference is only slightly weaker; in iodobenzene all the phases give a stronger harmonic signal than benzene; in toluene and meta-xylene the weakest spectrum is obtained again with 270°, and para-xylene yields the weakest spectrum when the phase is 0°.

In terms of comparing these results to what we observe experimentally, there is little to no agreement between the experiment and calculations. Comparing the spectra of

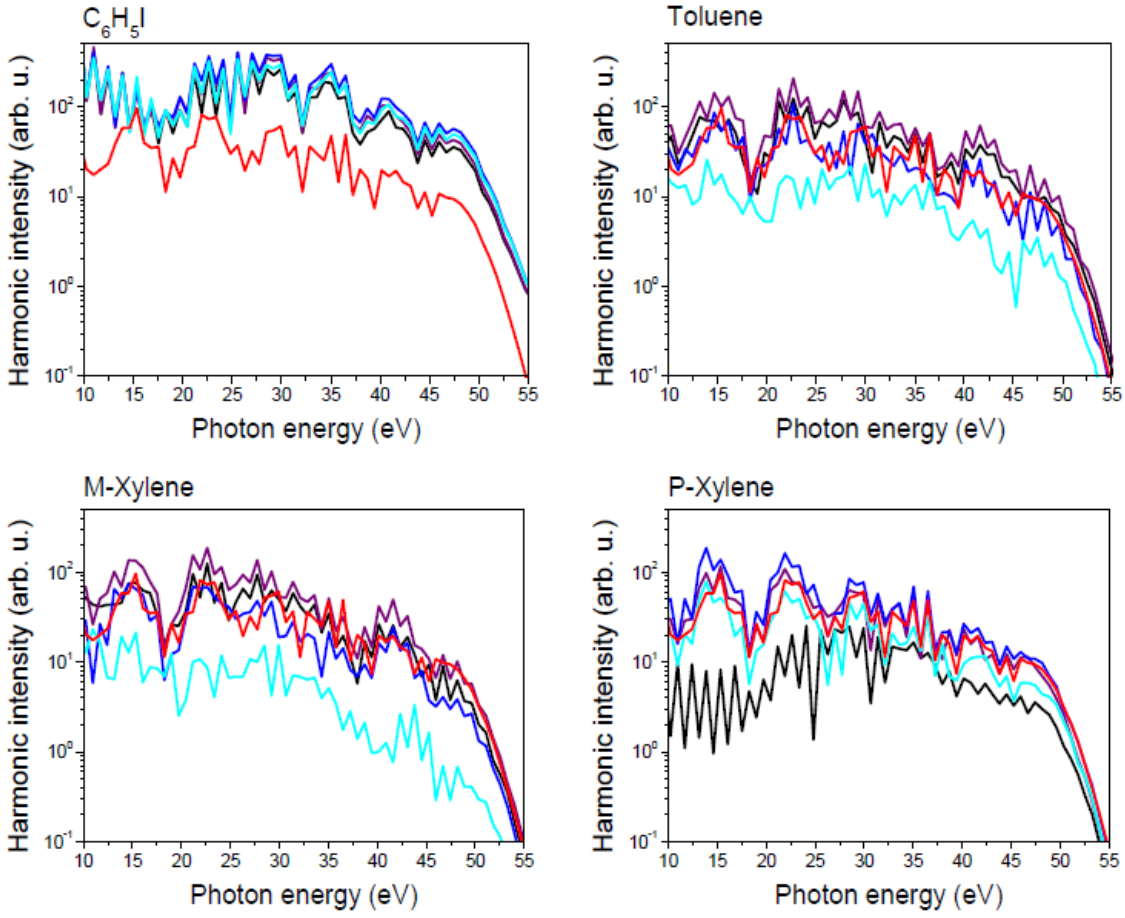


Figure 6.37: SFA simulation results of the harmonic spectra for different molecules and relative phases between HOMO and HOMO-1, compared with benzene. I = 5×10^{13} W/cm^2, $\lambda = 1700$ nm, cos^2 pulse of $\tau = 30$ fs, short trajectories only.

chlorobenzene and bromobenzene at $\varphi_0 = 90°$ with the spectrum of benzene, we see a behaviour which is the exact opposite of what we observe in the experimental data in Figure 6.18, that is, the signal for the halogenated benzenes is less intense than benzene for low harmonic orders (< 20 eV) and more intense for higher harmonic orders (> 20 eV approximately). One notable result is the signal level for fluorobenzene at $\varphi_0 = 270°$ which is suppressed in comparison to that of benzene and is consistent with what we have observed in the experiments.

The SFA code used for these calculations has some significant drawbacks which include the use of a basis set which is not particularly accurate for heavy atoms such as bromine and iodine, the lack of ground state depletion and propagation effects and no inclusion of exchange correlations. However it does demonstrate the dependence of the harmonic spectra to the relative phase between the HOMO and HOMO-1 which is very sensitive to the energy gap between these participating orbitals.

Chapter 7

Discussion of results

7.1 Discussion of halogenated benzenes data

The importance of the stability of the laser and the vapour generation was highlighted by the data comparing benzene and fluorobenzene from 2013 and 2015. The data from 2013 (Figure 5.4) would lead one to believe that fluorobenzene exhibited an enhancement at higher harmonic orders. In contrast the 2015 data repeatedly showed that the harmonic signal from fluorobenzene was suppressed across the whole recorded spectrum. The suppressed harmonic intensity could be explained in terms of the slower change in the nuclear autocorrelation function in halo-substituted species. The evidence of additional temporal modulation in fluorobenzene may indicate an additional interference from the HOMO/HOMO-1 that have a 0.6 eV separation as can be seen from the photoelectron spectroscopy (PES) spectrum for this molecule [49].

The relative intensities of the cut−off harmonics for the halogenated species is consistent with what one would deduce from looking at the polarizabilities of the substitutions. In both Figure 5.3 from 2013 and Figure 6.18 from the 2015 data, the more polarizable species have higher cut−off harmonic intensities. The polarizability generally increases down the columns on the periodic table This is consistent with bromobenzene exhibiting the highest cut−off harmonic intensities followed by chlorobenzene and lastly fluorobenzene. Since iodobenzene were not recorded in the 2015 data set there is one final piece of evidence for this argument missing.

The stability of the laser has proven to be a significant contributor to the repro-

ducibility and quality of the data recorded. The stability monitors installed at the exit of the 800 nm laser and the output of the hollow core fibre, in conjunction with the box placed over the compressor in the 800 nm laser, have impacted upon the reliability of the PACER data. The data recorded in 2013 in which an increase in harmonic signal in the ratio between deuterated and protonated benzene has proven to be a false result. This was reinforced by monitoring the stability of the harmonic spatial mode as shown in Figures 5.9 and 5.10.

What is striking is the significantly lower signal levels in fluorobenzene across the whole spectrum compared with the other molecules. This is examined further by comparing raw spectra from benzene and fluorobenzene as shown in Figure 6.13. This strong suppression at otherwise identical conditions is unique to fluorobenzene amongst the molecules studied, and is not observed in methyl−substituted benzenes like toluene and xylene. As the suppression is consistent across all harmonic orders, and does not show a dynamical effect, it is inconsistent with nuclear dynamics. As defined in [59] and [56] minima in HHG spectra can not only arise from molecular structure but also from the motion of the hole. The creation of a multielectron wavepacket is visualized as the motion of a hole after the ionization process. The motion of the hole is manifested as a time dependent interference between the contributions from the different HHG channels associated with the different populated ionic states.

This can be verified by measuring how much the recombination time varies in the energy range of interest (18-28 eV in this case) which can be done via changing the wavelength of the drive laser. It is however suggestive of interference from multiple electronic states, and could be related to structural differences in the electronic states. Other factors that can contribute to the observed suppression also include the polarizability of the molecule where fluorobenzene may be less polarizable than benzene or the other molecules under study. Calculations on the nuclear autocorrelation function for benzene and fluorobenzene are currently under improvement by Patchkovskii *et.al* [179] to determine if the phase of the nuclear wavepacket has signatures of dynamics associated with multi-orbital HHG present.

7.2 PACER

Nuclear dynamics in benzene were studied by comparing the harmonic spectra from benzene and deuterated benzene taken under similar conditions. As discussed in section 3.3, this experiment would enable us to deduce the origin of the electron wavepacket from the molecule; if it is from the pi or sigma orbitals of the molecule. Using the 1750 nm drive wavelength enables us to track nuclear dynamics up to 4 fs post ionization. As observed in the case of the PACER experiment on methane and deuterated methane where there is no ambiguity to the origin of the electron wavepacket. Since it is also a C-H system a change in the ratio of deuterated methane to methane was observed in the time window available. Thus we would expect to see a change in the ration between deuterated benzene and benzene if the electron originated from the sigma orbital of the molecule. However, from the experiments performed in both the 2013 and 2015 data runs, we see no change in the ratio between the two molecules. This is indicative that the origin of the electron wavepacket is from the C-C pi system since no change in the ratio has been observed over 4 fs and that the C-C bond vibrational period is longer than this at 35 fs.

This result is substantiated by the checks done on the stability of the harmonic spatial mode as discussed in chapter 5. The baratron used to monitor the backing pressure to the gas-jet was also configured to make live recordings of the pressure whilst the data was being taken. Along with the harmonic spatial mode check, the backing pressure monitoring and testing the reproducibility of the spectra, we have confidence that the results obtained are displaying a physical effect and that fluctuations in the laser beam profile and pulse energy or density of the jet are not affecting the data.

The main result shown in Figure 6.22 is the ratio of deuterated benzene to benzene averaged over four independent data runs. Within the error bars we can conculde that the ratio between the two molecules does not change. This result is a milestone in field of HHG spectroscopy as it has now been extended to larger multielectron systems using a longer drive wavelength.

7.3 Methylated benzenes

Electron coupled nuclear dynamics were investigated using benzene as a reference molecule and taking the ratios of the methyl substituted benzenes to benzene. For the 2013 data shown in Figure 6.7, the slowest ratio change relative to benzene is from p-xylene followed by toluene and then m-xylene. As a preliminary result this verified that the dynamics were faster in toluene than in benzene.

Using benzene as a reference molecule, we see that the slowest to fastest ratio decrease goes from o−xylene, toluene, p−xylene and finally m−xylene in the cut−off region of the spectrum. From the electron dynamics point of view, taking into account ionization from the HOMO/HOMO−1 predicts faster dynamics in para-xylene than in toluene and therefore larger "damping" of the higher order harmonics intensity which is what we see in Figure 6.33.

The electron dynamics in ortho−xylene and meta−xylene should be similar to the toluene case according to the preliminary calculations of Vacher *et.al* [126]. It matches for ortho−xylene but not for meta−xylene but more accurate calculations are being performed. It is encouraging that we do see some reproducibility in the data between the 2013 and 2015 experimental campaigns. In both cases, the m−xylene to benzene ratio decreases the fastest of all the molecules ratios. In the cut-off region of the spectrum we have an agreement between the theory and the experiment that the coupled electronic and nuclear dynamics are faster in p-xylene than in toluene.
There are a number of shortcomings to the methodology behind the theoretical calculations which shall be briefly addressed here:

- The use of the sudden approximation is incompatible with tunnel ionization that is associated with HHG spectroscopy.
- The energy gaps used in the calculations for toluene and p-xylene are calculated theoretically using a CASSCF method starting with a 6-31G* basis set. These gaps are different to what is observed experimentally from photoelectron spectra for these molecules. The incorporation of the experimental energy gaps would be a stepping stone towards modelling more experimentally relevant situations.

- The Ehrenfest method does not include electronic decoherence - both populated electronic eigenstates share the same nuclear geometry as a consequence of the ansatz for the total wavefunction including electronic and nuclear dynamics. This can lead to non physical results on the > 1 fs timescale.

- A classical approach for modelling the nuclear dynamics is also inadequate. It does not account for more significant dynamical effects which can occur when nuclei move in different directions on a potential energy surface. Currently the nuclear dynamics follows a single trajectory - what would be more suitable would be using a wavepacket representation of the nuclear motion which can incorporate these inevitable motions of the nuclei.

7.4 Linking photoelectron spectroscopy to high harmonic generation spectroscopy

Theoretical and experimental work by Kraus *et.al* [180] has established a link between photoelectron spectroscopy and high harmonic generation spectroscopy. This work shows how the nuclear autocorrelation function can be determined from knowing the vibrational energy level structure of the cation and the Franck-Condon factors. These quantities can be calculated by determining the Born-Oppenheimer potential energy surfaces for the neutral and ionic species, as was done by Lein *et.al* [127] for probing the vibrational dynamics in H_2 and D_2 and was fitted to the PACER data presented by Baker *et.al* [7]. However, accurate calculations to allow us to extract these quantities are quite challenging for polyatomic molecules. The information required can, however, be extracted from experimental photoelectron spectra as has been done for the ammonia cation [180]. This approach involves taking the inverse Fourier transform of the photoelectron band which corresponds to ionization from the vibrational ground state of the neutral to the electronic ground state of the cation, which is multiplied by the strong field ionization amplitude.

The width of the spectral envelope of the photoelectron band of the electronic ground state determines the energy bandwidth of the nuclear wavepacket that is launched and can thus be used to measure its early temporal evolution. Certainly, this method circumvents the complications inherent to calculating the Franck-Condon factors and the Born-Oppenheimer potential energy surfaces, which is particularly difficult for larger polyatomic molecules such as benzene where phenomena such as the Jahn-Teller effect need to be accounted for. In a crude estimation of the attosecond nuclear dynamics in fluorobenzene we have attempted to extract the width of the photoelectron band for the electronic ground states of benzene and fluorobenzene. The PES were taken from [49] and the data was extracted using the DataTheif software program.

As shown in Figure 7.1, the data is plotted with the area under the curves normalised to facilitate a better visual comparison. The flurobenzene ground state photoelectron band is wider by inspection which implies that the motion on the ring will be faster compared to benzene despite it having a greater weight in the F atom as opposed to

a H atom.

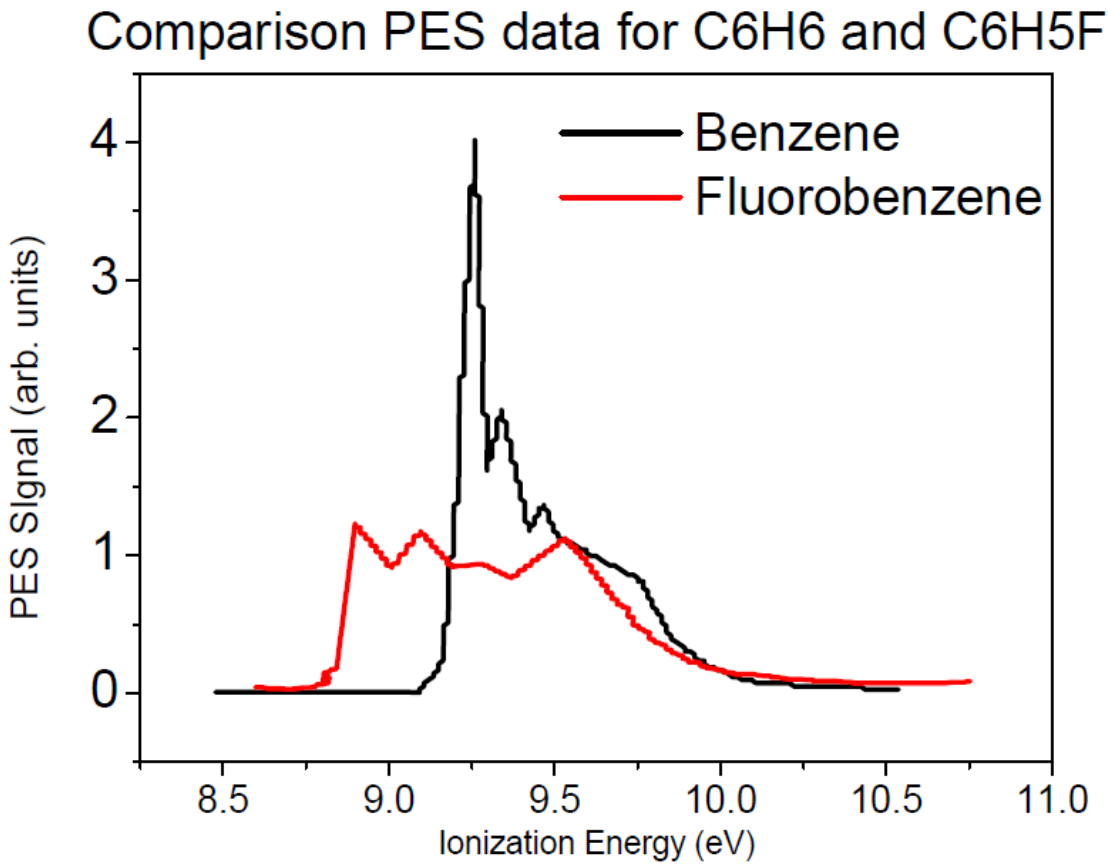


Figure 7.1: Estimation of widths of ground state photoelectron bands for benzene and fluoroebenzene. Data is extracted from [49].

7.5 Future work: improvements to intensity scan method

The implementation of the half-wave plate and polariser combination for performing intensity scans was found to be impractical for our purpose. After all the data that is presented in this thesis was recorded it was found that after some time with the half-wave plate and polarizer in the beam path it was not possible to see the shift of the cut-off as a function of increasing beam power anymore. This was in contrast to data that was recorded using this set-up in which the cut-off shift was clearly visible. It was decided to use the iris before the entrance to the chamber as an attenuator instead. Of course, this was trialled manually in this thesis but it was decided to design an iris mount that could be used to adjust the iris diameter via a computer program. The new set-up is shown in Figure 7.2 below.

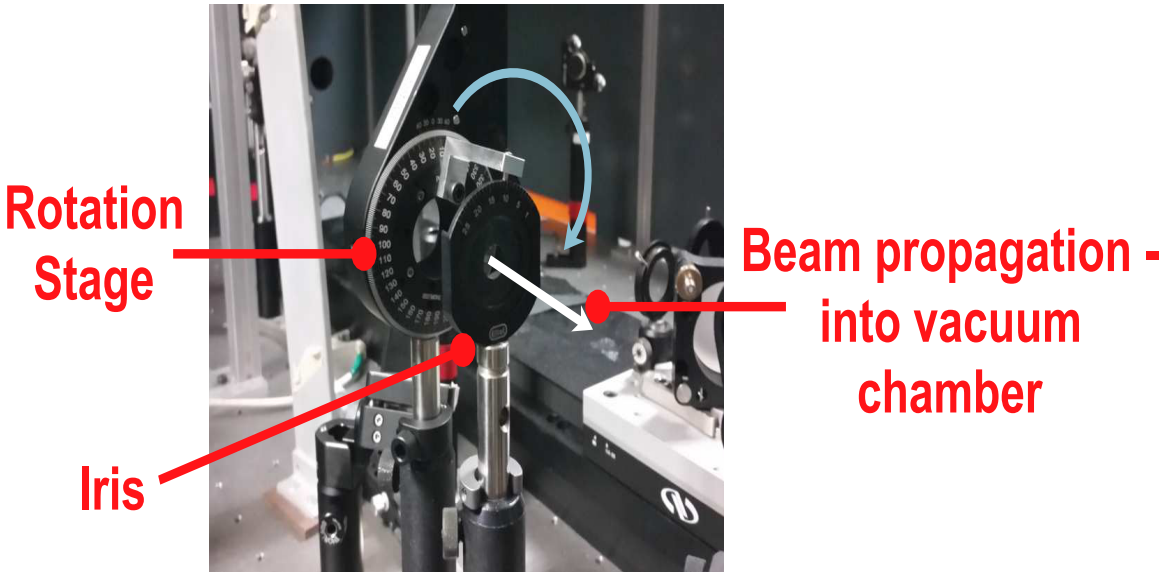


Figure 7.2: Iris scan intensity adjustment set-up

A bracket was attached to a rotation stage which is used to control the dial for setting the iris diameter. This is more beneficial than using the half-wave plate and polarizer combination as there are no losses of beam energy from reflections off the optical surfaces and the size of the focal spot size gets bigger as the intensity is decreased. Careful calibration of the focus size and iris diameter is required. The set-up is calibrated such that a relationship can be found between the angle of the rotation stage

and the iris diameter. For example, setting the stage to 45° was found to correspond to the case where the iris is shut and an angle of 315° means the iris is fully open.

An example of an iris scan performed on toluene is shown in Figure 7.3. The shift in cut-off position with increasing harmonic photon is clear. This method is still being optimised at the time of writing this thesis. This method removes the possibility of the half-wave and polarizer introducing distortions the beam profile which make the determination of the saturation intensity more difficult.

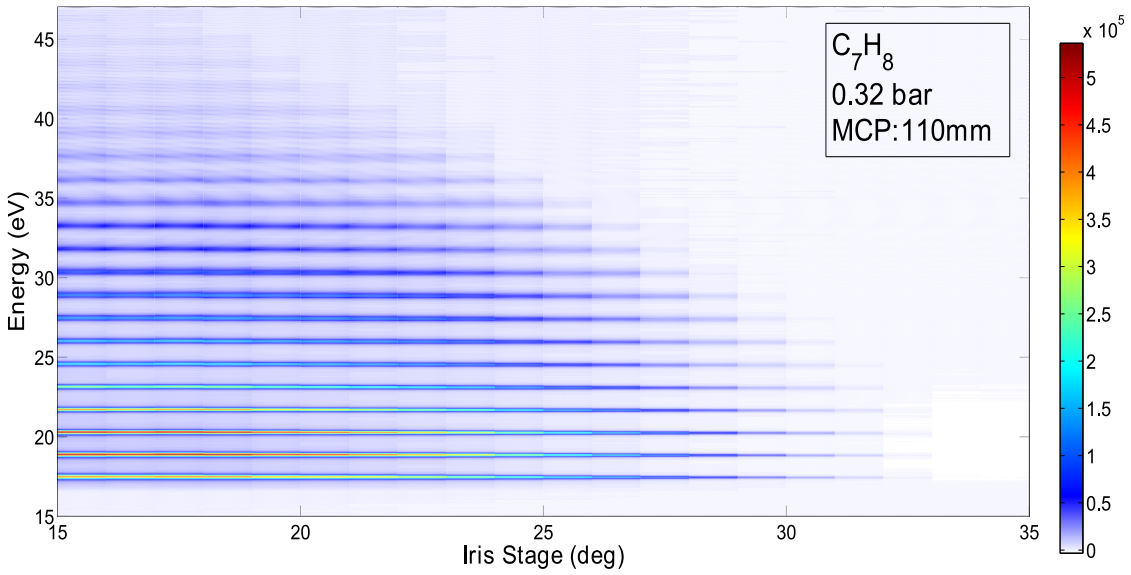


Figure 7.3: Intensity scan in toluene showing clear cut-off shift using new iris adjustment method

7.6 Conclusions and outlook

A number of milestones have been arrived at in the development of this project and shall be listed here as a summary of the highlights of this thesis and the impact they have upon future work in the field of HHG spectroscopy and indeed other ultrafast molecular imaging techniques:

An apparatus has been designed and developed from scratch inhouse to produce a stable vapour from a range of molecules existing in the liquid phase at room temperature. The apparatus is centred around using a thin (200μm) diameter nozzle to minimise phasematching effects such that the recorded HHG spectra are resemblant of the single molecule response as much as possible.

HHG spectra have been acquired in low I_p ($\leq$10 eV) organic molecules using the $\approx$ 35 fs, 1735 nm OP-CPA laser source which has extended the time window for observing dynamics up to 4 fs using short trajectory emission.

HHG spectra have been successfully and reproducibly acquired in benzene, methylated benzenes and halogenated benzenes demonstrating a capability of this apparatus which has not been previously inherent to other vapour generation methods - the ability to switch reliably between up to 8 different samples quickly and non-invasive of the apparatus. This is a necessary requirement for experiments involving the comparison of spectra under similar generating conditions.

The PACER experiment has yielded two milestone results. Firstly, obtaining a reproducible ratio of 1 for the comparison of the deuterated to protonated benzene is indicative that the ionization of benzene must originate from the C-C system; if it were to arise from the C-H bonds then we would anticipate some nuclear dynamics to have manifested in the 4 fs observation time window. Secondly, we have also demonstrated by achieving a ratio of 1 that, since the electronic structure is similar in both molecules, that the IR field is not perturbing the dynamics to a detrimental degree. This implies that the IR field is not introducing significant Stark shifts to the electronic states of the molecule.

Although it is not a fundamental result, the demonstration of impulsive alignment in benzene using the continuous flow gas jet and an 800 nm alignment and 800 nm generation interferometer proves the versatility of the design of the apparatus. The ability to obtain reproducible spectra in a range of molecules without having to stop the system to change samples which are installed in the vacuum chamber along with the demonstration of pressure tunability, impulsive alignment capability and compatibility with the components of the vacuum system has not ever been previously demonstrated in one independent apparatus design.

The ratios of the methylated benzene to benzene obtained experimentally compare very well with the coupled electronic-nuclear dynamics calculated by our collaborators in the Theoretical Chemistry group at Imperial College. Improvements to the calculations are under-way, including a quantum mechanical description of the nuclear motion. Again, bearing in mind that the calculations do not account for the presence of the IR laser field which ionizes the sample, the good agreement between the theory and experiment further substantiates our claim that the IR field does not perturb the dynamics in the molecules to a great extent.

As demonstrated for the result of the simple molecular SFA calculations and the estimate of the width of the photoelectron bands for benzene and fluorobenzene, two things are clear. First of all, both simple calculations show that dynamical interferences are observable in the HHG photon energy range measured experimentally. Secondly, it is also important to note that it is not just full calculations that can give us an insight into electronic and nuclear dynamics.

The data from the halogenated benzenes has primarily produced the interesting result of the significantly suppressed harmonic signal in fluorobenzene compared to benzene, and indeed the other molecules in this study. The consistent presence of this effect in fluorobenzene independent of backing pressure and to a lesser extent laser intensity at the focus imply that fluorobenzene is exhibiting a structural or dynamical suppression. More precise intensity scans will support the claim that this signal is due to contributions from a lower lying orbital. Scans of the drive wavelength would indicate if it is a dynamical effect. This result will no doubt encourage theorists to investigate the nature of this suppression.

This PhD has resulted in important developments for the field of ultrafast science with an emphasis on attosecond chemistry. Not only has this work contributed to high harmonic generation spectroscopy experiments on organic molecules but has produced a versatile apparatus with cross compatibility to other experiments in mind. For example, X-ray initiated HHG (XiHHG) [181] and attosecond transient absorption (ATA) [182] experiments are being pioneered in our laboratory also using continuous flow gas-jets.

The integration of the experimental technology, and even knowledge on handling organic vapours in a vacuum system, can be readily applied to these new technologies in our laboratory. HHG spectroscopy has the limitation of only being able to probe dynamics arising from the ionization of the outer valence electron of a target molecule. XiHHG enables us to probe lower lying electronic states with negligible distortion to the electronic structure of the molecule as the probe field is weaker in comparison to single colour HHG spectroscopy which has been the focus of this thesis.

Due to saturation of the harmonic spectra of bromobenzene and chlorobenzene we were unable to reach the cut-off photon energies required to observe Cooper minima in these molecules HHG spectra - a problem that could be circumvented by XiHHG. Single photon XUV ionization is also more compatible with the sudden approximation which is a foundation for many theoretical calculations; for example those presented in this thesis on coupled electron-nuclear dynamics. Indeed, theoretical studies focusing on hole migration in benzene which would be observable in an XUV-pump, IR-probe scheme have recently been published [183]. The advancements of high harmonic spectroscopy, especially the experiments performed by Wörner *et.al* on following a chemical reaction using high harmonic interferometry [184] can be used in conjunction with the technology developed in this thesis to track chemical reactions in more complex molecules. The fusion of these two capabilities will facilitate core electron ionization in the substituted benzenes which will invariably advance attochemistry towards more insightful experiments on the electronic and nuclear dynamics in biologically relevant and topical molecules [121].

Appendix A: Physical properties of the molecules studied

Table 7.1: Ionization potentials for substituted benzenes (in units of eV)

Molecule		HOMO	HOMO-1	HOMO-2
Benzene [49]	Experimental	9.24	11.53	12.38
	Theoretical	9.03	13.22	13.54
Toluene [49]	Experimental	8.83	9.36	11.43
	Theoretical	8.68	8.99	12.74
Fluorobenzene [49]	Experimental	9.20	9.81	12.24
	Theoretical	9.29	9.57	13.66
m-Xylene [185]	Experimental	8.71	9.03	11.24
	Theoretical	-	-	-
Chlorobenzene [49]	Experimental	9.10	9.69	11.32
	Theoretical	-	-	-
Bromobenzene [49]	Experimental	9.02	9.65	10.63
	Theoretical	-	-	-
Iodobenzene [49]	Experimental	8.79	9.52	9.78
	Theoretical	-	-	-
p-Xylene [185]	Experimental	8.44	-	-
	Theoretical	-	-	-
o-Xylene [185]	Experimental	8.56	-	-
	Theoretical	-	-	-

"-" indicates no reliable data was available for these orbitals.

Table 7.2: Other physical properties of substituted benzenes

Molecule	BP (°C)	MP (°C)	Dipole moment (Debyes)
Benzene	80	5.5	0
Toluene	111	-93	0.36
Fluorobenzene	85	-42	1.66
Bromobenzene	156	-31	1.55
Chlorobenzene	132	-45	1.54
Iodobenzene	188	-29	1.70
m-Xylene	138	-48	0.35
p-Xylene	138	12	0.07
o-Xylene	143	-26	0.64

Boiling (BP) and melting points (MP) taken from MSDS sheets for the molecules from the Sigma Aldrich website. Dipole moments from [185].

Table 7.3: Temperature and vapour pressures for substituted benzenes.

Molecule	Temp. for 0.1 bar (°C)	Temp. for 1.0 bar (°C)
Benzene	83	155
Toluene	45	110
Fluorobenzene	24	84
Bromobenzene	83	155
Chlorobenzene	63	131
Iodobenzene	110	187
m-Xylene	70	139
p-Xylene	69	138
o-Xylene	67	144

Data taken from [185]

Permissions

The images taken from other publications which have been used in this thesis have been granted permission to be used in this work. Listed below are all the publications from which images and figures were used. The date on which permission was granted, the title of the article, publisher of the journal and licence number are listed below. Where a licence number is listed, this permission was acquired through the Copyright Clearance Centre Rightslink online.

- **Date:** 06/06/2015
  Article title: High Harmonic Generation from Multiple Orbitals in N_2
  Publication: Science
  Licence number: 3643080336809

- **Date:** 03/06/2015
  Article title: Electron dynamics upon ionization: Control of the timescale through chemical substitution and effect of nuclear motion
  Publication: Journal of Chemical Physics
  Licence number: 3640891210985

- **Date:** 29/05/2015
  Article title: Generating single attosecond pulses via spatial filtering
  Publication: Optics Letters
  Licence number: N/A - permission granted via email - see Figure 6.11

- **Date:** 29/05/2015
  Article title: Characterization of high-intensity sub-4-fs laser pulses using spatially encoded spectral shearing interferometry
  Publication: Optics Letters
  Licence number: N/A - permission granted via email - see Figure 6.12

- **Date:** 29/05/2015
  Article title: A photoabsorption, photodissociation and photoelectron spectroscopy study of C_6H_6 and C_6D_6
  Publication: Chemical Physics
  Licence number: 3638370598682

- **Date:** 26/05/2015
  Article title: Nonadiabatic tunnel ionization: Looking inside a laser cycle
  Publication: Physical Review A
  Licence number: 3636520753408

- **Date:** 26/05/2015
  Article title: Generation of Optical Harmonics
  Publication: Physical Review Letters
  Licence number: 3636520645607

- **Date:** 26/05/2015
  Article title: Tracking individual electron trajectories in a high harmonic spectrum
  Publication: Optics Communications
  Licence number: 3633041328982

- **Date:** 26/05/2015
  Article title: High-order harmonic generation in cyclic organic molecules
  Publication: Physical Review A
  Licence number: 3636520857848

- **Date:** 19/05/2015
  Article title: Intense few-cycle laser fields: Frontiers of nonlinear optics
  Publication: Reviews of Modern Physics
  Licence number: 3636521009278

- **Date:** 19/05/2015
  Article title: Recent developments in compact ultrafast lasers
  Publication: Nature
  Licence number: 3632450120656

- **Date:** 19/05/2015
  Article title: High-order harmonic generation from organic molecules in ultrashort pulses
  Publication: The European Physical Journal D - Atomic, Molecular, Optical and Plasma Physics
  Licence number: 3632440643784

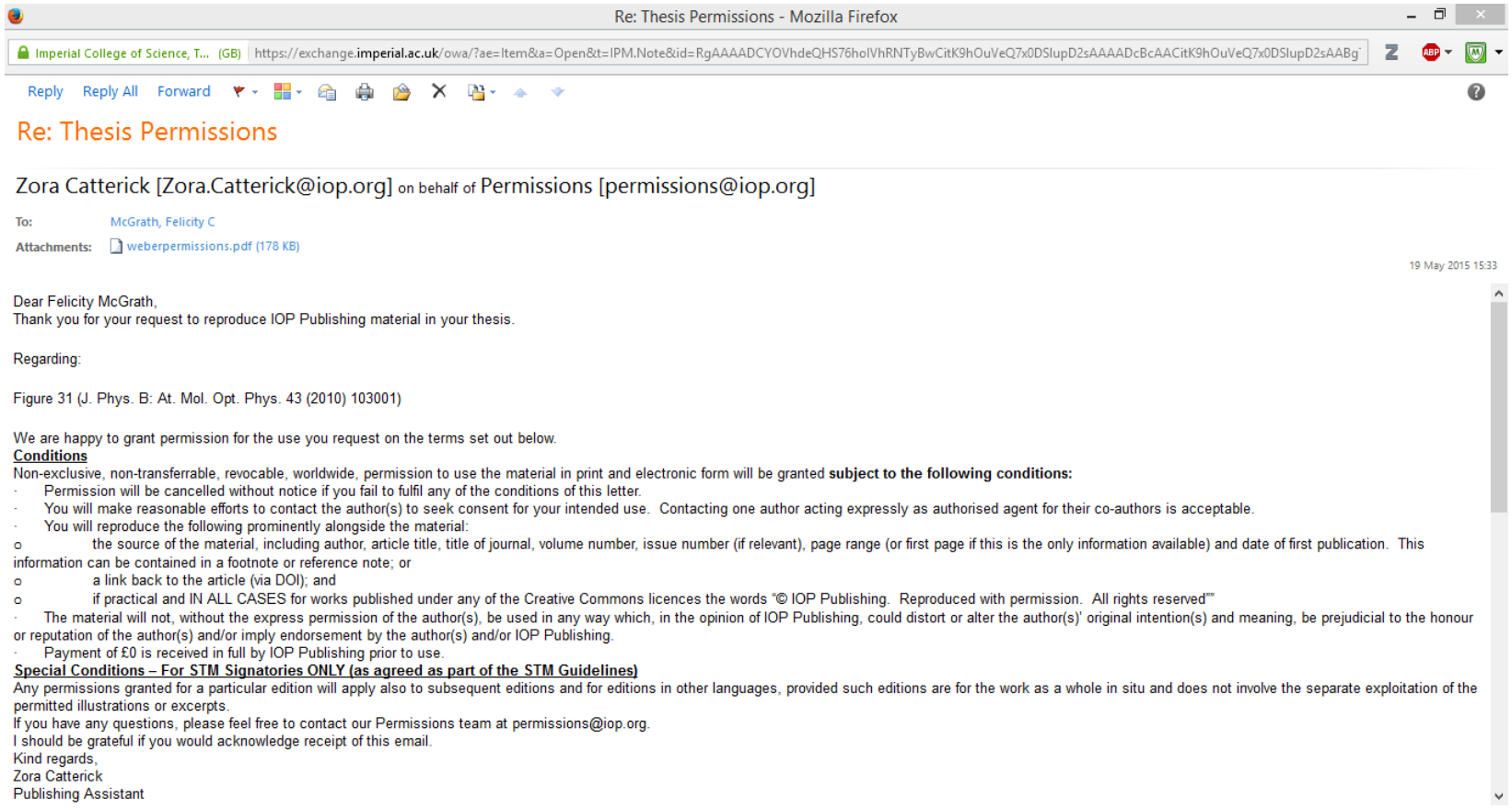
- **Date:** 19/05/2015
  Article title: Ionization and fragmentation dynamics of benzene in intense laser fields by tandem mass spectroscopy
  Publication: Journal of Chemical Physics
  Licence number: 3632440354858

- **Date:** 19/05/2015
  Article title: Coupled electron-nuclear dynamics: Charge migration and charge transfer initiated near a conical intersection
  Publication: Journal of Chemical Physics
  Licence number: 3632640990658

- **Date:** 19/05/2015
  Article title: Probing Proton Dynamics in Molecules on an Attosecond Time Scale
  Publication: Science
  Licence number: 3632640630504

- **Date:** 19/05/2015
  Article title: Nuclear Dynamics in Polyatomic Molecules and High-Order Harmonic Generation
  Publication: Physical Review Letters
  Licence number: 3632640509805

- **Date:** 19/05/2015
  Article title: A newcomer's guide to ultrashort pulse shaping and characterization
  Publication: Journal of Physics B: Atomic, Molecular and Optical Physics
  Licence number: please see attached email on following page - Figure 6.10



Re: Thesis Permissions - Mozilla Firefox

Imperial College of Science, T... (GB) https://exchange.imperial.ac.uk/owa/?ae=Item&a=Open&t=IPM.Note&id=RgAAAADCYOVhdeQHS76holVhRNTyBwCitK9hOuVeQ7x0DSlupD2sAAAADcBcAACitK9hOuVeQ7x0DSlupD2sAABg

Reply Reply All Forward

Re: Thesis Permissions

Zora Catterick [Zora.Catterick@iop.org] on behalf of Permissions [permissions@iop.org]

To: McGrath, Felicity C

Attachments: weberpermissions.pdf (178 KB)

19 May 2015 15:33

Dear Felicity McGrath,
Thank you for your request to reproduce IOP Publishing material in your thesis.

Regarding:

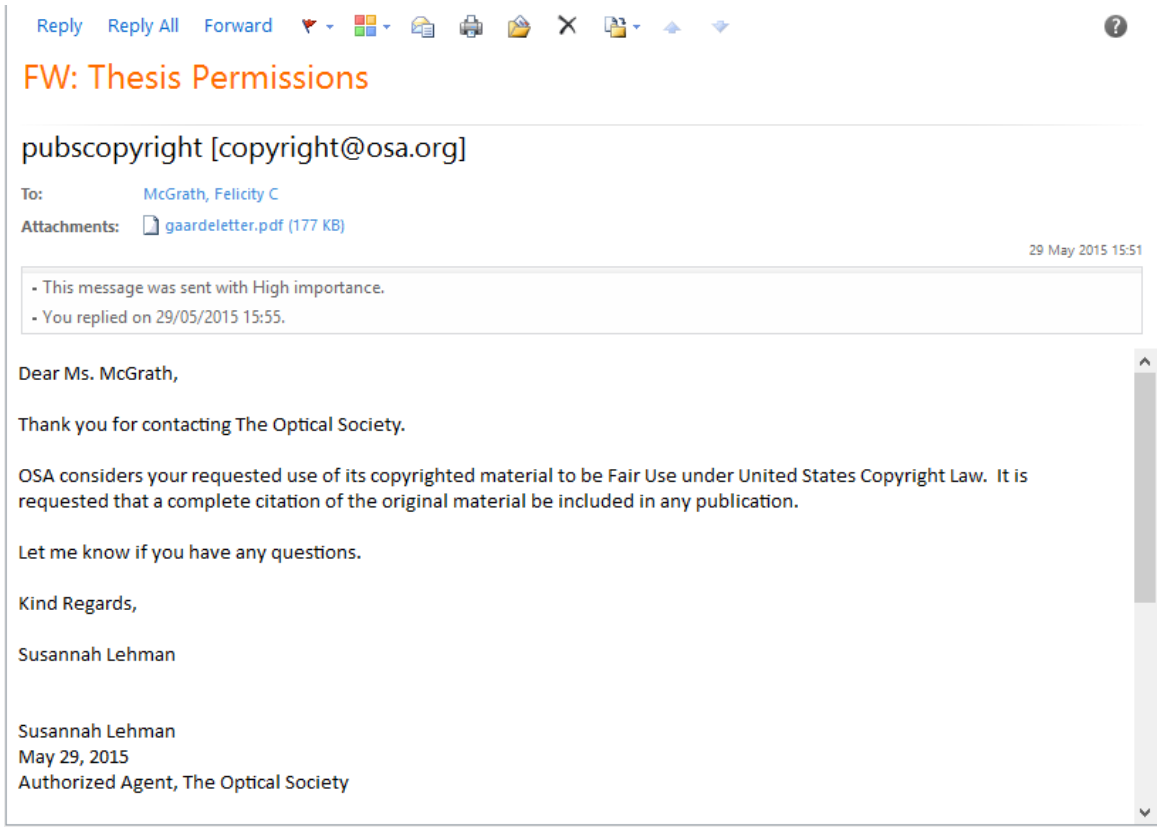
Figure 31 (J. Phys. B: At. Mol. Opt. Phys. 43 (2010) 103001)

We are happy to grant permission for the use you request on the terms set out below.
Conditions
Non-exclusive, non-transferrable, revocable, worldwide, permission to use the material in print and electronic form will be granted **subject to the following conditions:**

- Permission will be cancelled without notice if you fail to fulfil any of the conditions of this letter.
- You will make reasonable efforts to contact the author(s) to seek consent for your intended use. Contacting one author acting expressly as authorised agent for their co-authors is acceptable.
- You will reproduce the following prominently alongside the material:
  - the source of the material, including author, article title, title of journal, volume number, issue number (if relevant), page range (or first page if this is the only information available) and date of first publication. This information can be contained in a footnote or reference note; or
  - a link back to the article (via DOI); and
  - if practical and IN ALL CASES for works published under any of the Creative Commons licences the words "© IOP Publishing. Reproduced with permission. All rights reserved""
- The material will not, without the express permission of the author(s), be used in any way which, in the opinion of IOP Publishing, could distort or alter the author(s)' original intention(s) and meaning, be prejudicial to the honour or reputation of the author(s) and/or imply endorsement by the author(s) and/or IOP Publishing.
- Payment of £0 is received in full by IOP Publishing prior to use.

Special Conditions – For STM Signatories ONLY (as agreed as part of the STM Guidelines)
Any permissions granted for a particular edition will apply also to subsequent editions and for editions in other languages, provided such editions are for the work as a whole in situ and does not involve the separate exploitation of the permitted illustrations or excerpts.
If you have any questions, please feel free to contact our Permissions team at permissions@iop.org.
I should be grateful if you would acknowledge receipt of this email.
Kind regards,
Zora Catterick
Publishing Assistant

Figure 7.4: Permission email response from the IOP for reference [90]



Reply Reply All Forward

FW: Thesis Permissions

pubscopyright [copyright@osa.org]

To: McGrath, Felicity C

Attachments: gaardeletter.pdf (177 KB)

29 May 2015 15:51

- This message was sent with High importance.
- You replied on 29/05/2015 15:55.

Dear Ms. McGrath,

Thank you for contacting The Optical Society.

OSA considers your requested use of its copyrighted material to be Fair Use under United States Copyright Law. It is requested that a complete citation of the original material be included in any publication.

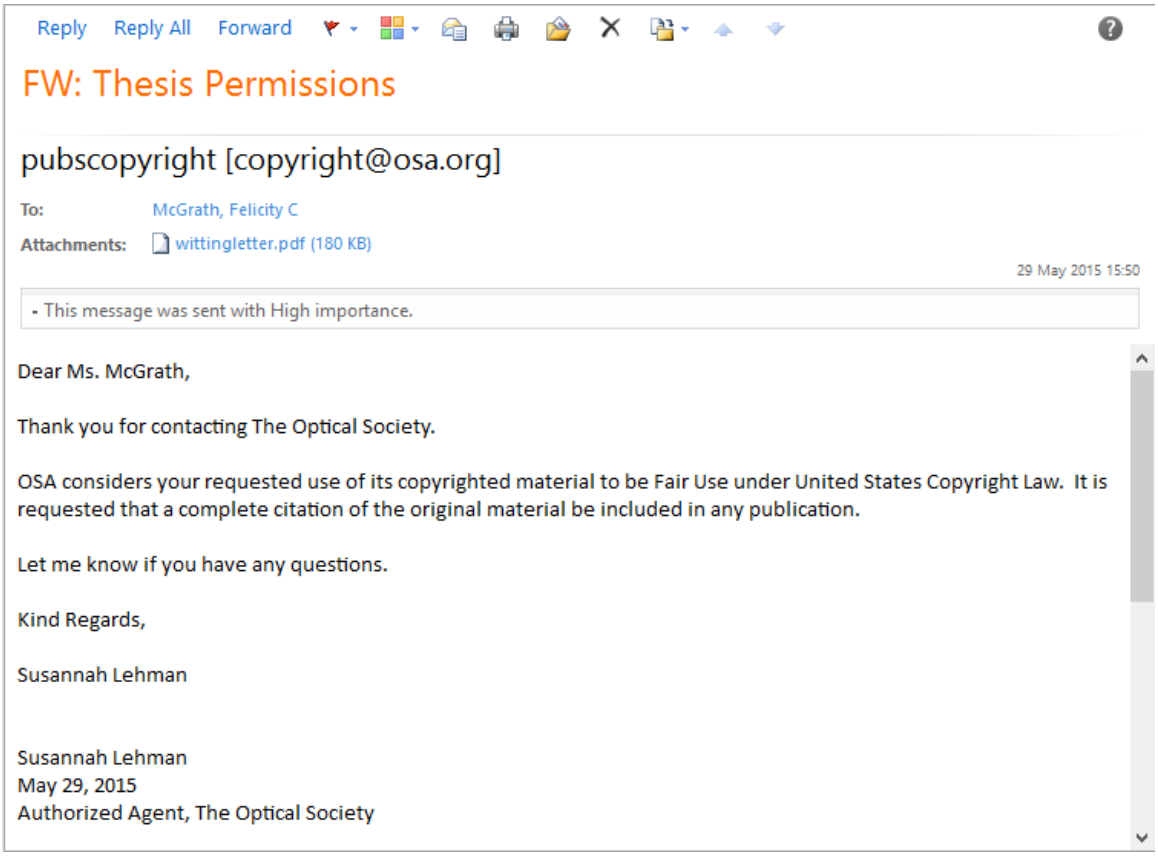
Let me know if you have any questions.

Kind Regards,

Susannah Lehman

Susannah Lehman
May 29, 2015
Authorized Agent, The Optical Society

Figure 7.5: Permission email response from the OSA for reference [168]



Reply Reply All Forward

FW: Thesis Permissions

pubscopyright [copyright@osa.org]

To: McGrath, Felicity C

Attachments: wittingletter.pdf (180 KB)

29 May 2015 15:50

- This message was sent with High importance.

Dear Ms. McGrath,

Thank you for contacting The Optical Society.

OSA considers your requested use of its copyrighted material to be Fair Use under United States Copyright Law. It is requested that a complete citation of the original material be included in any publication.

Let me know if you have any questions.

Kind Regards,

Susannah Lehman

Susannah Lehman
May 29, 2015
Authorized Agent, The Optical Society

Figure 7.6: Permission email response from the OSA for reference [109]

Bibliography

[1] T. H. Maiman. 'Stimulated Optical Radiation in Ruby'. *Nature*, vol. 187(4736), pp. 493–494 (1960). doi:10.1038/187493a0.

[2] M. Protopapas, C. H. Keitel & P. L. Knight. 'Atomic physics with super-high intensity lasers'. *Reports on Progress in Physics*, vol. 60(4), p. 389 (1997). doi:10.1088/0034-4885/60/4/001.

[3] A. McPherson, G. Gibson, H. Jara et al. 'Studies of multiphoton production of vacuum-ultraviolet radiation in the rare gases'. *Journal of the Optical Society of America B*, vol. 4(4), pp. 595–601 (1987). doi:10.1364/JOSAB.4.000595.

[4] S. Haessler, J. Caillat & P. Saliéres. 'Self-probing of molecules with high harmonic generation'. *Journal of Physics B: Atomic, Molecular and Optical Physics*, vol. 44(20), p. 203001 (2011). doi:10.1088/0953-4075/44/20/203001.

[5] C. Altucci, R. Velotta & J. P. Marangos. 'Ultra-fast dynamic imaging: an overview of current techniques, their capabilities and future prospects'. *Journal of Modern Optics*, vol. 57(11), pp. 916–952 (2010). doi:10.1080/09500340.2010.493621.

[6] A. Barty. 'Time-resolved imaging using x-ray free electron lasers'. *Journal of Physics B: Atomic, Molecular and Optical Physics*, vol. 43(19), p. 194014 (2010). doi:10.1088/0953-4075/43/19/194014.

[7] S. Baker, J. S. Robinson, C. A. Haworth et al. 'Probing Proton Dynamics in Molecules on an Attosecond Time Scale'. *Science*, vol. 312(5772), pp. 424–427 (2006). doi:10.1126/science.1123904.

[8] R. Boyd. *Nonlinear Optics*. Academics Press, 2008, 3rd edn. ISBN 978-0-12-369470-6.

[9] P. A. Franken, A. E. Hill, C. W. Peters & G. Weinreich. 'Generation of Optical Harmonics'. *Physical Review Letters*, vol. 7(4), pp. 118–119 (1961). doi:10.1103/PhysRevLett.7.118.

[10] G. New. *Introduction to Nonlinear Optics*. Cambridge University Press, 2011, 1st edn. ISBN 978-0-521-87701-5.

[11] L. A. Lomprê, A. L'Huillier, G. Mainfray & C. Manus. 'Laser-intensity effects in the energy distributions of electrons produced in multiphoton ionization of rare gases'. *Journal of the Optical Society of America B*, vol. 2(12), p. 1906 (1985). doi:10.1364/JOSAB.2.001906.

[12] F. Fabre, G. Petite, P. Agostini & M. Clement. 'Multiphoton above-threshold ionisation of xenon at 0.53 and 1.06μm'. *Journal of Physics B: Atomic and Molecular Physics*, vol. 15(9), p. 1353 (1982). doi:10.1088/0022-3700/15/9/012.

[13] L. Keldysh. 'Ionization in the field of a strong electromagnetic wave'. *Sov. Phys - JETP*, vol. 20(5), pp. 1307–14 (1965).

[14] G. Mainfray & G. Manus. 'Multiphoton ionization of atoms'. *Reports on Progress in Physics*, vol. 54(10), p. 1333 (1991). doi:10.1088/0034-4885/54/10/002.

[15] P. Agostini, F. Fabre, G. Mainfray et al. 'Free-Free Transitions Following Six-Photon Ionization of Xenon Atoms'. *Physical Review Letters*, vol. 42(17), pp. 1127–1130 (1979). doi:10.1103/PhysRevLett.42.1127.

[16] M. Ammosov, N. Delone & V. Krainov. 'Tunnel ionization of complex atoms and of atomic ions in an alternating electromagnetic field'. *Zh. Eksp. Teor. Fiz.*, vol. 91(6), p. 2008 (1986).

[17] J. P. Marangos, S. Baker, N. Kajumba et al. 'Dynamic imaging of molecules using high order harmonic generation'. *Physical chemistry chemical physics: PCCP*, vol. 10(1), pp. 35–48 (2008). doi:10.1039/b714126m.

[18] P. B. Corkum. 'Plasma perspective on strong field multiphoton ionization'. *Physical Review Letters*, vol. 71(13), pp. 1994–1997 (1993). doi:10.1103/PhysRevLett.71.1994.

[19] K. J. Schafer, B. Yang, L. F. DiMauro & K. C. Kulander. 'Above threshold ionization beyond the high harmonic cutoff'. *Physical Review Letters*, vol. 70(11), pp. 1599–1602 (1993). doi:10.1103/PhysRevLett.70.1599.

[20] G. L. Yudin & M. Y. Ivanov. 'Nonadiabatic tunnel ionization: Looking inside a laser cycle'. *Physical Review A*, vol. 64(1), p. 013409 (2001). doi:10.1103/PhysRevA.64.013409.

[21] B. E. Schmidt, A. D. Shiner, P. Lassonde et al. 'CEP stable 1.6 cycle laser pulses at 1.8 μm'. *Optics Express*, vol. 19(7), p. 6858 (2011). doi:10.1364/OE.19.006858.

[22] X. M. Tong, Z. X. Zhao & C. D. Lin. 'Theory of molecular tunneling ionization'. *Physical Review A*, vol. 66(3), p. 033402 (2002). doi:10.1103/PhysRevA.66.033402.

[23] T. K. Kjeldsen, C. Z. Bisgaard, L. B. Madsen & H. Stapelfeldt. 'Influence of molecular symmetry on strong-field ionization: Studies on ethylene, benzene, fluorobenzene, and chlorofluorobenzene'. *Physical Review A*, vol. 71(1) (2005). doi:10.1103/PhysRevA.71.013418. ArXiv: physics/0409150.

[24] R. Murray, M. Spanner, S. Patchkovskii & M. Y. Ivanov. 'Tunnel Ionization of Molecules and Orbital Imaging'. *Physical Review Letters*, vol. 106(17), p. 173001 (2011). doi:10.1103/PhysRevLett.106.173001.

[25] J. Wu, L. P. H. Schmidt, M. Kunitski et al. 'Multiorbital Tunneling Ionization of the CO Molecule'. *Physical Review Letters*, vol. 108(18), p. 183001 (2012). doi:10.1103/PhysRevLett.108.183001.

[26] B. Sheehy, J. D. D. Martin, L. F. DiMauro et al. 'High Harmonic Generation at Long Wavelengths'. *Physical Review Letters*, vol. 83(25), pp. 5270–5273 (1999). doi:10.1103/PhysRevLett.83.5270.

[27] B. Shan & Z. Chang. 'Dramatic extension of the high-order harmonic cutoff by using a long-wavelength driving field'. *Physical Review A*, vol. 65(1), p. 011804 (2001). doi:10.1103/PhysRevA.65.011804.

[28] A. D. Shiner, C. Trallero-Herrero, N. Kajumba et al. 'Wavelength Scaling of High Harmonic Generation Efficiency'. *Physical Review Letters*, vol. 103(7), p. 073902 (2009). doi:10.1103/PhysRevLett.103.073902.

[29] M. D. Perry & J. K. Crane. 'High-order harmonic emission from mixed fields'. *Physical Review A*, vol. 48(6), pp. R4051–R4054 (1993). doi:10.1103/PhysRevA.48.R4051.

[30] Z. Chang, A. Rundquist, H. Wang et al. 'Temporal phase control of soft-x-ray harmonic emission'. *Physical Review A*, vol. 58(1), pp. R30–R33 (1998). doi:10.1103/PhysRevA.58.R30.

[31] Y. Mairesse, A. d. Bohan, L. J. Frasinski et al. 'Attosecond Synchronization of High-Harmonic Soft X-rays'. *Science*, vol. 302(5650), pp. 1540–1543 (2003). doi:10.1126/science.1090277.

[32] J. Mauritsson, P. Johnsson, E. Gustafsson et al. 'Attosecond Pulse Trains Generated Using Two Color Laser Fields'. *Physical Review Letters*, vol. 97(1), p. 013001 (2006). doi:10.1103/PhysRevLett.97.013001.

[33] G. Sansone, E. Benedetti, F. Calegari et al. 'Isolated Single-Cycle Attosecond Pulses'. *Science*, vol. 314(5798), pp. 443–446 (2006). doi:10.1126/science.1132838.

[34] A. Zaïr, T. Siegel, S. Sukiasyan et al. 'Molecular internal dynamics studied by quantum path interferences in high order harmonic generation'. *Chemical Physics*, vol. 414, pp. 184–191 (2013). doi:10.1016/j.chemphys.2012.12.022.

[35] P. Balcou, P. Sali'eres, A. L'Huillier & M. Lewenstein. 'Generalized phase-matching conditions for high harmonics: The role of field-gradient forces'. *Physical Review A*, vol. 55(4), pp. 3204–3210 (1997). doi:10.1103/PhysRevA.55.3204.

[36] A. L'Huillier. 'Atoms in strong laser fields'. *Europhysics News*, vol. 33(6), pp. 205–207 (2002). doi:10.1051/epn:2002606.

[37] L. A. Lomprê, A. L'Huillier, M. Ferray et al. 'High-order harmonic generation in xenon: intensity and propagation effects'. *Journal of the Optical Society of America B*, vol. 7(5), pp. 754–761 (1990). doi:10.1364/JOSAB.7.000754.

[38] S. Feng & H. G. Winful. 'Physical origin of the Gouy phase shift'. *Optics Letters*, vol. 26(8), pp. 485–487 (2001).

[39] M. B. Gaarde, J. L. Tate & K. J. Schafer. 'Macroscopic aspects of attosecond pulse generation'. *Journal of Physics B: Atomic, Molecular and Optical Physics*, vol. 41(13), p. 132001 (2008). doi:10.1088/0953-4075/41/13/132001.

[40] C. Corsi, A. Pirri, E. Sali et al. 'Direct Interferometric Measurement of the Atomic Dipole Phase in High-Order Harmonic Generation'. *Physical Review Letters*, vol. 97(2), p. 023901 (2006). doi:10.1103/PhysRevLett.97.023901.

[41] M. Lewenstein, P. Saliéres & A. L'Huillier. 'Phase of the atomic polarization in high-order harmonic generation'. *Physical Review A*, vol. 52(6), pp. 4747–4754 (1995). doi:10.1103/PhysRevA.52.4747.

[42] L. E. Chipperfield, P. L. Knight, J. W. G. Tisch & J. P. Marangos. 'Tracking individual electron trajectories in a high harmonic spectrum'. *Optics Communications*, vol. 264(2), pp. 494–501 (2006). doi:10.1016/j.optcom.2006.03.078.

[43] M. Born & R. Oppenheimer. 'Zur Quantentheorie der Molekeln'. *Annalen der Physik*, vol. 389(20), pp. 457–484 (1927). doi:10.1002/andp.19273892002.

[44] H. Haken & H. C. Wolf. *Molecular Physics and Elements of Quantum Chemistry: Introduction to Experiments and Theory*. Springer Science & Business Media, 2004. ISBN 9783540407928.

[45] Atkins & de Paula. *Elements of Physical Chemistry*. W.H. Freedman and Company, 2006, 4th edn. ISBN 0716773295.

[46] Eisberg & Resnick. *Quantum Physics of Atoms, Molecules, Solids, Nuclei and Particles*. John Wiley and Sons Inc., 1985, 2nd edn. ISBN 0-471-87373-X.

[47] J. B. Foresman, A. Frisch & G. Inc. *Exploring chemistry with electronic structure methods*. Gaussian, Inc., 1996. ISBN 9780963676931.

[48] M. Lewenstein, P. Balcou, M. Y. Ivanov et al. 'Theory of high-harmonic generation by low-frequency laser fields'. *Physical Review A*, vol. 49(3), pp. 2117–2132 (1994). doi:10.1103/PhysRevA.49.2117.

[49] K. Kimura. *Handbook of HeI photoelectron spectra of fundamental organic molecules: ionization energies, ab initio assignments, and valence electronic structure for 200 molecules*. Japan Scientific Societies Press, 1981.

[50] K. C. Molloy. *Group Theory for Chemists: Fundamental Theory and Applications*. Elsevier, 2010. ISBN 9780857092410.

[51] M. H. Smith. *HarperCollins College Outline Organic Chemistry*. HarperCollins, 1993. ISBN 9780064671262.

[52] M. Smith. *Organic Chemistry*. HarperCollins, 1993, 1st edn. ISBN 0-06-467126-7.

[53] T. Kanai, S. Minemoto & H. Sakai. 'Quantum interference during high-order harmonic generation from aligned molecules'. *Nature*, vol. 435(7041), pp. 470–474 (2005). doi:10.1038/nature03577.

[54] C. Vozzi, F. Calegari, E. Benedetti et al. 'Controlling Two-Center Interference in Molecular High Harmonic Generation'. *Physical Review Letters*, vol. 95(15), p. 153902 (2005). doi:10.1103/PhysRevLett.95.153902.

[55] H. J. Wörner, J. B. Bertrand, P. Hockett et al. 'Controlling the Interference of Multiple Molecular Orbitals in High-Harmonic Generation'. *Physical Review Letters*, vol. 104(23), p. 233904 (2010). doi:10.1103/PhysRevLett.104.233904.

[56] R. Torres, T. Siegel, L. Brugnera et al. 'Revealing molecular structure and dynamics through high-order harmonic generation driven by mid-IR fields'. *Physical Review A*, vol. 81(5), p. 051802 (2010). doi:10.1103/PhysRevA.81.051802.

[57] B. K. McFarland, J. P. Farrell, P. H. Bucksbaum & M. Guehr. 'High Harmonic Generation from Multiple Orbitals in N2'. *Science*, vol. 322(5905), pp. 1232–1235 (2008). doi:10.1126/science.1162780.

[58] M. Negro, M. Devetta, D. Faccialá et al. 'High-order harmonic spectroscopy for molecular imaging of polyatomic molecules'. *Faraday Discuss.*, vol. 171, pp. 133–143 (2014). doi:10.1039/C4FD00033A.

[59] O. Smirnova, Y. Mairesse, S. Patchkovskii et al. 'High harmonic interferometry of multi-electron dynamics in molecules'. *Nature*, vol. 460(7258), pp. 972–977 (2009). doi:10.1038/nature08253.

[60] Z. Diveki, A. Camper, S. Haessler et al. 'Spectrally resolved multi-channel contributions to the harmonic emission in N2'. *New Journal of Physics*, vol. 14(2), p. 023062 (2012). doi:10.1088/1367-2630/14/2/023062.

[61] A.-T. Le, R. R. Lucchese & C. D. Lin. 'Uncovering multiple orbitals influence in high harmonic generation from aligned N2'. *Journal of Physics B: Atomic, Molecular and Optical Physics*, vol. 42(21), p. 211001 (2009). doi:10.1088/0953-4075/42/21/211001.

[62] C. Jin, J. B. Bertrand, R. R. Lucchese et al. 'Intensity dependence of multiple orbital contributions and shape resonance in high-order harmonic generation of aligned N_2 molecules'. *Physical Review A*, vol. 85(1), p. 013405 (2012). doi:10.1103/PhysRevA.85.013405.

[63] Y. Mairesse, J. Higuet, N. Dudovich et al. 'High Harmonic Spectroscopy of Multichannel Dynamics in Strong-Field Ionization'. *Physical Review Letters*, vol. 104(21), p. 213601 (2010). doi:10.1103/PhysRevLett.104.213601.

[64] C. C. Chirilă & M. Lein. 'Strong-field approximation for harmonic generation in diatomic molecules'. *Physical Review A*, vol. 73(2), p. 023410 (2006). doi:10.1103/PhysRevA.73.023410.

[65] A. Gordon & F. X. Kaertner. 'First-order strong field approximation for high-order harmonic generation'. *arXiv:physics/0607088* (2006). ArXiv:physics/0607088.

[66] I. V. Litvinyuk, K. F. Lee, P. W. Dooley et al. 'Alignment-Dependent Strong Field Ionization of Molecules'. *Physical Review Letters*, vol. 90(23), p. 233003 (2003). doi:10.1103/PhysRevLett.90.233003.

[67] M. Y. Ivanov, M. Spanner & O. Smirnova. 'Anatomy of strong field ionization'. *Journal of Modern Optics*, vol. 52(2-3), pp. 165–184 (2005). doi:10.1080/09500340420002753 60.

[68] M. Lewenstein, K. C. Kulander, K. J. Schafer & P. H. Bucksbaum. 'Rings in above-threshold ionization: A quasiclassical analysis'. *Physical Review A*, vol. 51(2), pp. 1495–1507 (1995). doi:10.1103/PhysRevA.51.1495.

[69] X. Zhou, X. M. Tong, Z. X. Zhao & C. D. Lin. 'Alignment dependence of high-order harmonic generation from N_2 and O_2 molecules in intense laser fields'. *Physical Review A*, vol. 72(3), p. 033412 (2005). doi:10.1103/PhysRevA.72.033412.

[70] S. Patchkovskii, Z. Zhao, T. Brabec & D. M. Villeneuve. 'High Harmonic Generation and Molecular Orbital Tomography in Multielectron Systems: Beyond the Single Active Electron Approximation'. *Physical Review Letters*, vol. 97(12), p. 123003 (2006). doi:10.1103/PhysRevLett.97.123003.

[71] B. Shan, S. Ghimire & Z. Chang. 'Effect of orbital symmetry on high-order harmonic generation from molecules'. *Physical Review A*, vol. 69(2), p. 021404 (2004). doi:10.1103/PhysRevA.69.021404.

[72] Z. B. Walters & O. Smirnova. 'Attosecond correlation dynamics during electron tunnelling from molecules'. *Journal of Physics B: Atomic, Molecular and Optical Physics*, vol. 43(16), p. 161002 (2010). doi:10.1088/0953-4075/43/16/161002.

[73] O. Smirnova, M. Spanner & M. Ivanov. 'Analytical solutions for strong field-driven atomic and molecular one- and two-electron continua and applications to strong-field problems'. *Physical Review A*, vol. 77(3), p. 033407 (2008). doi:10.1103/PhysRevA.77.033407.

[74] A. DiChiara, S. Ghimire, C. Blaga et al. 'Scaling of High-Order Harmonic Generation in the Long Wavelength Limit of a Strong Laser Field'. *IEEE Journal of Selected Topics in Quantum Electronics*, vol. 18(1), pp. 419–433 (2012). doi:10.1109/JSTQE.2011.2158391.

[75] B. E. Schmidt, A. D. Shiner, M. Giguére et al. 'High harmonic generation with long-wavelength few-cycle laser pulses'. *Journal of Physics B: Atomic, Molecular and Optical Physics*, vol. 45(7), p. 074008 (2012). doi:10.1088/0953-4075/45/7/074008.

[76] R. Itakura, J. Watanabe, A. Hishikawa & K. Yamanouchi. 'Ionization and fragmentation dynamics of benzene in intense laser fields by tandem mass spectroscopy'. *The Journal of Chemical Physics*, vol. 114(13), pp. 5598–5606 (2001). doi:doi:10.1063/1.1352619.

[77] M. Castillejo, S. Couris, E. Koudoumas & M. Martín. 'Ionization and fragmentation of aromatic and single-bonded hydrocarbons with 50 fs laser pulses at 800 nm'. *Chemical Physics Letters*, vol. 308(5-6), pp. 373–380 (1999). doi:10.1016/S0009-2614(99)00636-3.

[78] D. J. Smith, K. W. D. Ledingham, R. P. Singhal et al. 'Time-of-flight mass spectrometry of aromatic molecules subjected to high intensity laser beams'. *Rapid Communications in Mass Spectrometry*, vol. 12(13), pp. 813–820 (1998). doi:10.1002/(SICI)1097-0231(19980715)12:13⟨813::AID-RCM241⟩3.0.CO;2-X.

[79] N. Hay, R. de Nalda, T. Halfmann et al. 'Pulse-length dependence of high-order harmonic generation in dissociating cyclic organic molecules'. *Physical Review A*, vol. 62(4), p. 041803 (2000). doi:10.1103/PhysRevA.62.041803.

[80] C. Altucci, R. Bruzzese, C. d. Lisio et al. 'Features of high-order harmonic generation in the 30 fs and the sub-10 fs regimes'. *Journal of Optics A: Pure and Applied Optics*, vol. 2(4), p. 289 (2000). doi:10.1088/1464-4258/2/4/308.

[81] T. Brabec & F. Krausz. 'Intense few-cycle laser fields: Frontiers of nonlinear optics'. *Reviews of Modern Physics*, vol. 72(2), pp. 545–591 (2000). doi:10.1103/RevModPhys.72.545.

[82] A. M. Müller, C. J. G. J. Uiterwaal, B. Witzel et al. 'Photoionization and photofragmentation of gaseous toluene using 80-fs, 800-nm laser pulses'. *The Journal of Chemical Physics*, vol. 112(21), pp. 9289–9300 (2000). doi:doi:10.1063/1.481550.

[83] X. P. Tang, A. Becker, W. Liu et al. 'Self-action effects in ionization and fragmentation of toluene by femtosecond laser pulses'. *Applied Physics B*, vol. 80(4-5), pp. 547–557 (2005). doi:10.1007/s00340-005-1760-2.

[84] M. Castillejo, S. Couris, E. Koudoumas & M. Martín. 'Subpicosecond ionization and dissociation of benzene and cyclic alkanes at 800 and 400 nm'. *Chemical Physics Letters*, vol. 289(3-4), pp. 303–310 (1998). doi:10.1016/S0009-2614(98)00442-4.

[85] N. Hay, M. Castillejo, R. de Nalda et al. 'High-order harmonic generation in cyclic organic molecules'. *Physical Review A*, vol. 61(5), p. 053810 (2000). doi:10.1103/PhysRevA.61.053810.

[86] N. Kajumba. 'Angular dependence of high harmonic generation from impulsively aligned molecules'. Ph.D. thesis, Imperial College London (2007).

[87] C. Gohle, T. Udem, M. Herrmann et al. 'A frequency comb in the extreme ultraviolet'. *Nature*, vol. 436(7048), pp. 234–237 (2005). doi:10.1038/nature03851.

[88] R. J. Jones, K. D. Moll, M. J. Thorpe & J. Ye. 'Phase-Coherent Frequency Combs in the Vacuum Ultraviolet via High-Harmonic Generation inside a Femtosecond Enhancement Cavity'. *Physical Review Letters*, vol. 94(19), p. 193201 (2005). doi:10.1103/PhysRevLett.94.193201.

[89] J. Rothhardt, M. Krebs, S. Hädrich et al. 'Absorption-limited and phase-matched high harmonic generation in the tight focusing regime'. *New Journal of Physics*, vol. 16(3), p. 033022 (2014). doi:10.1088/1367-2630/16/3/033022.

[90] A. Monmayrant, S. Weber & B. Chatel. 'A newcomer's guide to ultrashort pulse shaping and characterization'. *Journal of Physics B: Atomic, Molecular and Optical Physics*, vol. 43(10), p. 103001 (2010). doi:10.1088/0953-4075/43/10/103001.

[91] S. Hooker & C. Webb. *Laser Physics*. OUP Oxford, 2010. ISBN 9780198506928.

[92] E. Hecht. *Optics*. Pearson Education, 2008. ISBN 9788131718070.

[93] U. Keller. 'Recent developments in compact ultrafast lasers'. *Nature*, vol. 424(6950), pp. 831–838 (2003). doi:10.1038/nature01938.

[94] A. H. Zewail. 'Femtochemistry: Atomic-Scale Dynamics of the Chemical Bond'. *The Journal of Physical Chemistry A*, vol. 104(24), pp. 5660–5694 (2000). doi:10.1021/jp001460h.

[95] A. Maria, D. Stetser & H. Heynau. 'Self mode-locking of lasers with saturable absorbers'. *Appl. Phys. Lett.*, vol. 8, pp. 174–176 (1966).

[96] R. L. Fork, C. H. B. Cruz, P. C. Becker & C. V. Shank. 'Compression of optical pulses to six femtoseconds by using cubic phase compensation'. *Optics Letters*, vol. 12(7), p. 483 (1987). doi:10.1364/OL.12.000483.

[97] Wilson & Hawkes. *Lasers: Principles and Applications*. Prentice Hall, 1987, 1st edn. ISBN 0-13-523705-X.

[98] J. Wilson & J. F. B. Hawkes. *Optoelectronics: an introduction*. Prentice Hall Europe, 1998. ISBN 9780131039612.

[99] Y. Ishida, N. Sarukura & N. Nakano. In 'Ultrafast Phenomena', OSA, California, 1990.

[100] D. E. Spence, P. N. Kean & W. Sibbett. '60-fsec pulse generation from a self-mode-locked Ti:sapphire laser'. *Optics Letters*, vol. 16(1), p. 42 (1991). doi:10.1364/OL.16.000042.

[101] S. Backus, C. G. D. Iii, M. M. Murnane & H. C. Kapteyn. 'High power ultrafast lasers'. *Review of Scientific Instruments*, vol. 69(3), pp. 1207–1223 (1998). doi:10.1063/1.1148795.

[102] G. Steinmeyer, D. H. Sutter, L. Gallmann et al. 'Frontiers in Ultrashort Pulse Generation: Pushing the Limits in Linear and Nonlinear Optics'. *Science*, vol. 286(5444), pp. 1507–1512 (1999). doi:10.1126/science.286.5444.1507.

[103] D. Strickland & G. Mourou. 'Compression of amplified chirped optical pulses'. *Optics Communications*, vol. 55(6), pp. 447–449 (1985). doi:10.1016/0030-4018(85)90151-8.

[104] C. Iaconis & I. Walmsley. 'Spectral phase interferometry for direct electric-field reconstruction of ultrashort optical pulses'. *Optics Letters*, vol. 23(10), p. 792 (1998). doi:10.1364/OL.23.000792.

[105] F. X. Kärtner. *Few-Cycle Laser Pulse Generation and Its Applications*. Springer Science & Business Media, 2004. ISBN 9783540201151.

[106] C. Dorrer, B. de Beauvoir, C. Le Blanc et al. 'Characterization of chirped-pulse amplification systems with spectral phase interferometry for direct electric-field

reconstruction'. *Applied Physics B*, vol. 70(S1), pp. S77–S84 (2000). doi:10.1007/s003400000334.

[107] L. Conversion. 'HE-TOPAS users manual' (2011).

[108] M. Nisoli, S. De Silvestri & O. Svelto. 'Generation of high energy 10 fs pulses by a new pulse compression technique'. *Applied Physics Letters*, vol. 68(20), pp. 2793–2795 (1996). doi:10.1063/1.116609.

[109] T. Witting, F. Frank, C. A. Arrell et al. 'Characterization of high-intensity sub-4-fs laser pulses using spatially encoded spectral shearing interferometry'. *Optics Letters*, vol. 36(9), pp. 1680–1682 (2011).

[110] M. E. Anderson, A. Monmayrant, S.-P. Gorza et al. 'SPIDER: A decade of measuring ultrashort pulses'. *Laser Physics Letters*, vol. 5(4), p. 259 (2008). doi:10.1002/lapl.200710129.

[111] F. Frank. 'Generation and Application of Ultrashort Laser Pulses on Attosecond Science'. Ph.D. thesis, Imperial College London (2011).

[112] R. Trebino. *Frequency-Resolved Optical Gating: The Measurement of Ultrashort Laser Pulses*. Springer Science & Business Media, 2012. ISBN 9781461511816.

[113] D. J. Fraser, M. H. R. Hutchinson, J. P. Marangos et al. 'High harmonic generation in butane and butadiene'. *Journal of Physics B: Atomic, Molecular and Optical Physics*, vol. 28(23), pp. L739–L745 (1995). doi:10.1088/0953-4075/28/23/006.

[114] C. Trallero-Herrero, B. E. Schmidt, A. D. Shiner et al. 'High harmonic generation in ethylene with infrared pulses'. *Chemical Physics*, vol. 366(1-3), pp. 33–36 (2009). doi:10.1016/j.chemphys.2009.10.014.

[115] C. Vozzi, R. Torres, M. Negro et al. 'High harmonic generation spectroscopy of hydrocarbons'. *Applied Physics Letters*, vol. 97(24), p. 241103 (2010). doi:10.1063/1.3526752.

[116] A.-T. Le, R. R. Lucchese & C. D. Lin. 'High-order-harmonic generation from molecular isomers with midinfrared intense laser pulses'. *Physical Review A*, vol. 88(2), p. 021402 (2013). doi:10.1103/PhysRevA.88.021402.

[117] T. Siegel, R. Torres, D. J. Hoffmann et al. 'High harmonic emission from a superposition of multiple unrelated frequency fields' (2010).

[118] H. Stapelfeldt & T. Seideman. 'Colloquium: Aligning molecules with strong laser pulses'. *Reviews of Modern Physics*, vol. 75(2), pp. 543–557 (2003). doi: 10.1103/RevModPhys.75.543.

[119] R. Torres, R. de Nalda & J. P. Marangos. 'Dynamics of laser-induced molecular alignment in the impulsive and adiabatic regimes: A direct comparison'. *Physical Review A*, vol. 72(2), p. 023420 (2005). doi:10.1103/PhysRevA.72.023420.

[120] M. D. Morse, F. Dunning & R. Hulet. *Methods of Experimental Physics: Atomic, Molecular, and Optical Physics*, vol. II. Atoms and Molecules. Academics Press, Orlando, Florida, 1996.

[121] F. Lépine, M. Y. Ivanov & M. J. J. Vrakking. 'Attosecond molecular dynamics: fact or fiction?' *Nature Photonics*, vol. 8(3), pp. 195–204 (2014). doi:10.1038/nphoton.2014.25.

[122] F. Remacle & R. D. Levine. 'An electronic time scale in chemistry'. *Proceedings of the National Academy of Sciences*, vol. 103(18), pp. 6793–6798 (2006). doi: 10.1073/pnas.0601855103.

[123] S. Lünnemann, A. I. Kuleff & L. S. Cederbaum. 'Ultrafast charge migration in 2-phenylethyl-N,N-dimethylamine'. *Chemical Physics Letters*, vol. 450(4-6), pp. 232–235 (2008). doi:10.1016/j.cplett.2007.11.031.

[124] M. J. Paterson, M. J. Bearpark, M. A. Robb et al. 'Conical intersections: A perspective on the computation of spectroscopic Jahn-Teller parameters and the degenerate 'intersection space''. *Physical Chemistry Chemical Physics*, vol. 7(10), p. 2100 (2005). doi:10.1039/b416538a.

[125] D. Mendive-Tapia, M. Vacher, M. J. Bearpark & M. A. Robb. 'Coupled electron-nuclear dynamics: Charge migration and charge transfer initiated near a conical intersection'. *The Journal of Chemical Physics*, vol. 139(4), p. 044110 (2013). doi:10.1063/1.4815914.

[126] M. Vacher, D. Mendive-Tapia, M. J. Bearpark & M. A. Robb. 'Electron dynamics upon ionization: Control of the timescale through chemical substitution

and effect of nuclear motion'. *The Journal of Chemical Physics*, vol. 142(9), p. 094105 (2015). doi:10.1063/1.4913515.

[127] M. Lein. 'Attosecond Probing of Vibrational Dynamics with High-Harmonic Generation'. *Physical Review Letters*, vol. 94(5), p. 053004 (2005). doi:10.1103/PhysRevLett.94.053004.

[128] S. Baker. 'Dynamic Two-Center Interference in High-Order Harmonic Generation from Molecules with Attosecond Nuclear Motion'. *Physical Review Letter*, vol. 101, pp. 053901–1 (2008). doi:10.1103/PhysRevLett.101.053901.

[129] H. Niikura, F. Légaré, R. Hasbani et al. 'Sub-laser-cycle electron pulses for probing molecular dynamics'. *Nature*, vol. 417(6892), pp. 917–922 (2002). doi:10.1038/nature00787.

[130] S. Patchkovskii. 'Nuclear Dynamics in Polyatomic Molecules and High-Order Harmonic Generation'. *Physical Review Letters*, vol. 102(25), p. 253602 (2009). doi:10.1103/PhysRevLett.102.253602.

[131] S. Baker, J. S. Robinson, C. A. Haworth et al. 'Probing fast nuclear wavepackets in light molecules: monitoring structural rearrangement on an attosecond timescale'. *Journal of Modern Optics*, vol. 54(7), pp. 1011–1017 (2007). doi:10.1080/09500340601022516.

[132] J. Farrell, B. K. McFarland, L. S. Spector et al. 'Isotope Effect in the High Harmonics of Water'. p. QMC4. OSA, 2011. ISBN 978-1-55752-910-7. doi:10.1364/QELS.2011.QMC4.

[133] M. FORD, R. LINDNER & K. MÜLLER-DETHLEFS. 'Fully rotationally resolved ZEKE photoelectron spectroscopy of C6H6 and C6D6: photoionization dynamics and geometry of the benzene cation'. *Molecular Physics*, vol. 101(4-5), pp. 705–716 (2003). doi:10.1080/0026897021000054916.

[134] R. Lindner, H. Sekiya, B. Beyl & K. Müller-Dethlefs. 'Structure and Symmetry of the Benzene Cation'. *Angewandte Chemie International Edition in English*, vol. 32(4), pp. 603–606 (1993). doi:10.1002/anie.199306031.

[135] J. W. Cooper. 'Photoelectron-angular-distribution parameters for rare-gas subshells'. *Physical Review A*, vol. 47(3), pp. 1841–1851 (1993). doi:10.1103/PhysRevA.47.1841.

[136] T. A. Carlson, A. Fahlman, M. O. Krause et al. 'Systematic investigation of the Cooper minimum for the hydrogen halides'. *The Journal of Chemical Physics*, vol. 81(12), pp. 5389–5394 (1984). doi:doi:10.1063/1.447683.

[137] J. Higuet, H. Ruf, N. Thiré et al. 'High-order harmonic spectroscopy of the Cooper minimum in argon: Experimental and theoretical study'. *Physical Review A*, vol. 83(5), p. 053401 (2011). doi:10.1103/PhysRevA.83.053401.

[138] J. P. Farrell, L. S. Spector, B. K. McFarland et al. 'Influence of Phase Matching on the Cooper Minimum in Ar High Harmonic Spectra'. arXiv e-print 1011.1297 (2010). Phys. Rev. A 83, 023420 (2011).

[139] M. C. H. Wong, A.-T. Le, A. F. Alharbi et al. 'High harmonic spectroscopy of the Cooper minimum in molecules'. *Physical review letters*, vol. 110(3), p. 033006 (2013).

[140] D. M. P. Holland, D. Edvardsson, L. Karlsson et al. 'A systematic investigation of the influence of Cooper minima on the photoionisation dynamics of the monohalobenzenes'. *Chemical Physics*, vol. 253(1), pp. 133–155 (2000). doi:10.1016/S0301-0104(99)00383-3.

[141] S. T. Manson, A. Msezane, A. F. Starace & S. Shahabi. 'Photoionization of chalcogen and halogen atoms: Cross sections and angular distributions'. *Physical Review A*, vol. 20(3), pp. 1005–1018 (1979). doi:10.1103/PhysRevA.20.1005.

[142] D. Holland, I. Powis, G. Öhrwall et al. 'A study of the photoionisation dynamics of chloromethane and iodomethane'. *Chemical Physics*, vol. 326(2-3), pp. 535–550 (2006). doi:10.1016/j.chemphys.2006.03.017.

[143] A. D. Shiner, B. E. Schmidt, C. Trallero-Herrero et al. 'Observation of Cooper minimum in krypton using high harmonic spectroscopy'. *Journal of Physics B: Atomic, Molecular and Optical Physics*, vol. 45(7), p. 074010 (2012). doi:10.1088/0953-4075/45/7/074010.

[144] M. Lein, N. Hay, R. Velotta et al. 'Interference effects in high-order harmonic generation with molecules'. *Physical Review A*, vol. 66(2), p. 023805 (2002). doi:10.1103/PhysRevA.66.023805.

[145] M. Lein, N. Hay, R. Velotta et al. 'Role of the Intramolecular Phase in High-Harmonic Generation'. *Physical Review Letters*, vol. 88(18), p. 183903 (2002). doi:10.1103/PhysRevLett.88.183903.

[146] J. P. Farrell, B. K. McFarland, M. Guehr & P. H. Bucksbaum. 'Relation of high harmonic spectra to electronic structure in N2'. *Chemical Physics*, vol. 366(1-3), pp. 15–21 (2009). doi:10.1016/j.chemphys.2009.10.015.

[147] K. Kato, S. Minemoto & H. Sakai. 'Suppression of high-order-harmonic intensities observed in aligned CO_2 molecules with 1300-nm and 800-nm pulses'. *Physical Review A*, vol. 84(2), p. 021403 (2011). doi:10.1103/PhysRevA.84.021403.

[148] R. Torres, T. Siegel, L. Brugnera et al. 'Extension of high harmonic spectroscopy in molecules by a 1300 nm laser field'. *Optics Express*, vol. 18(3), pp. 3174–3180 (2010).

[149] R. d. Nalda, E. Heesel, M. Lein et al. 'Role of orbital symmetry in high-order harmonic generation from aligned molecules'. *Physical Review A*, vol. 69(3), p. 031804 (2004). doi:10.1103/PhysRevA.69.031804.

[150] R. Torres, N. Kajumba, J. G. Underwood et al. 'Probing Orbital Structure of Polyatomic Molecules by High-Order Harmonic Generation'. *Physical Review Letters*, vol. 98(20), p. 203007 (2007). doi:10.1103/PhysRevLett.98.203007.

[151] M. C. H. Wong, J. P. Brichta & V. R. Bhardwaj. 'High-harmonic generation in H_2O'. *Optics Letters*, vol. 35(12), p. 1947 (2010). doi:10.1364/OL.35.001947.

[152] J. P. Farrell, S. Petretti, J. Förster et al. 'Strong Field Ionization to Multiple Electronic States in Water'. *Physical Review Letters*, vol. 107(8), p. 083001 (2011). doi:10.1103/PhysRevLett.107.083001.

[153] N. Hay. 'The interaction of organic molecules and atomic clusters with ultrashort high intensity laser pulses'. PhD Thesis, Imperial College London, London (2001).

[154] R. Gratings. 'Technical Note 3 CONCAVE GRATINGS'.

[155] N. Nakano, H. Kuroda, T. Kita & T. Harada. 'Development of a flat-field grazing-incidence XUV spectrometer and its application in picosecond XUV spectroscopy'. *Applied Optics*, vol. 23(14), pp. 2386–2392 (1984). doi:10.1364/AO.23.002386.

[156] H. H. Technologies. 'Hitachi Aberration-Corrected Concave Gratings for Flat-Field Spectrographs' (2015).

[157] T. Kita, T. Harada, N. Nakano & H. Kuroda. 'Mechanically ruled aberration-corrected concave gratings for a flat-field grazing-incidence spectrograph'. *Applied Optics*, vol. 22(4), pp. 512–513 (1983). doi:10.1364/AO.22.000512.

[158] J. Ladislas Wiza. 'Microchannel plate detectors'. *Nuclear Instruments and Methods*, vol. 162(1-3), pp. 587–601 (1979). doi:10.1016/0029-554X(79)90734-1.

[159] P. USA. 'Storage, Handling and Operation of Microchannel Plates'.

[160] V. R. Bhardwaj, D. M. Rayner, D. M. Villeneuve & P. B. Corkum. 'Quantum Interference in Double Ionization and Fragmentation of C_6H_6 in Intense Laser Fields'. *Physical Review Letters*, vol. 87(25), p. 253003 (2001). doi:10.1103/PhysRevLett.87.253003.

[161] M. C. H. Wong, J.-P. Brichta & V. R. Bhardwaj. 'Signatures of symmetry and electronic structure in high-order harmonic generation in polyatomic molecules'. *Physical Review A*, vol. 81(6), p. 061402 (2010). doi:10.1103/PhysRevA.81.061402.

[162] M. C. H. Wong, J.-P. Brichta, M. Spanner et al. 'High-harmonic spectroscopy of molecular isomers'. *Physical Review A*, vol. 84(5), p. 051403 (2011). doi:10.1103/PhysRevA.84.051403.

[163] J.-P. Brichta, M. C. H. Wong, J. B. Bertrand et al. 'Comparison and real-time monitoring of high-order harmonic generation in different sources'. *Physical Review A*, vol. 79(3), p. 033404 (2009). doi:10.1103/PhysRevA.79.033404.

[164] E. Constant, D. Garzella, P. Breger et al. 'Optimizing High Harmonic Generation in Absorbing Gases: Model and Experiment'. *Physical Review Letters*, vol. 82(8), pp. 1668–1671 (1999). doi:10.1103/PhysRevLett.82.1668.

[165] U. Even, J. Jortner, D. Noy et al. 'Cooling of large molecules below 1 K and He clusters formation'. *The Journal of Chemical Physics*, vol. 112(18), pp. 8068–8071 (2000). doi:10.1063/1.481405.

[166] J. Sutherland, E. Christensen, N. Powers et al. 'High harmonic generation in a semi-infinite gas cell'. *Optics Express*, vol. 12(19), pp. 4430–4436 (2004). doi:10.1364/OPEX.12.004430.

[167] D. S. Steingrube, T. Vockerodt, E. Schulz et al. 'Phase matching of high-order harmonics in a semi-infinite gas cell'. *Physical Review A*, vol. 80(4), p. 043819 (2009). doi:10.1103/PhysRevA.80.043819.

[168] M. B. Gaarde & K. J. Schafer. 'Generating single attosecond pulses via spatial filtering'. *Optics Letters*, vol. 31(21), pp. 3188–3190 (2006). doi:10.1364/OL.31.003188.

[169] J. Peatross, J. R. Miller, K. R. Smith et al. 'Phase matching of high-order harmonic generation in helium- and neon-filled gas cells'. *Journal of Modern Optics*, vol. 51(16-18), pp. 2675–2683 (2004). doi:10.1080/09500340408231826.

[170] 'Even Lavie Valve webpage: https://sites.google.com/site/evenlavievalve/' (2015).

[171] N. Hay, R. d. Nalda, T. Halfmann et al. 'High-order harmonic generation from organic molecules in ultra-short pulses'. *The European Physical Journal D - Atomic, Molecular, Optical and Plasma Physics*, vol. 14(2), pp. 231–240 (2001). doi:10.1007/s100530170221.

[172] I. R. Walker. *Reliability in Scientific Research: Improving the Dependability of Measurements, Calculations, Equipment, and Software*. Cambridge University Press, 2011. ISBN 9781139493352.

[173] D. W. Umrath. *Fundamentals of Vacuum Technology*. Oerlikon Leybold Vacuum, 2007.

[174] K. J. Lesker. 'Outgassing - Measuring Outgassing Rates' (2015).

[175] R. J. Elsey. 'Outgassing of vacuum materials-II'. *Vacuum*, vol. 25(8), pp. 347–361 (1975).

[176] J. Posthumus. *Molecules and Clusters in Intense Laser Fields*. Cambridge University Press, 2009. ISBN 9780521120272.

[177] A. D. Shiner, C. Trallero-Herrero, N. Kajumba et al. 'High harmonic cutoff energy scaling and laser intensity measurement with a 1.8 μm laser source'. *Journal of Modern Optics*, vol. 60(17), pp. 1458–1465 (2013). doi:10.1080/09500340.2013.765067.

[178] M. M. Shakya. *Generation of Intense High Harmonics: (i) To Test and Improve Resolution of Accumulative X-ray Streak Camera; (ii) To Study the Effects of Carrier Envelope Phase on XUV Super Continuum Generation by Polarization Gating*. ProQuest, 2007. ISBN 9780549654384.

[179] S. Patchkovskii & M. S. Schuurman. 'Short-Time Dynamics at a Conical Intersection in High-Harmonic Spectroscopy'. *The Journal of Physical Chemistry A*, vol. 118(51), pp. 12069–12079 (2014). doi:10.1021/jp5090444.

[180] P. M. Kraus & H. J. WÃűrner. 'Attosecond Nuclear Dynamics in the Ammonia Cation: Relation between High-Harmonic and Photoelectron Spectroscopies'. *ChemPhysChem*, vol. 14(7), pp. 1445–1450 (2013). doi:10.1002/cphc.201201022.

[181] G. Gademann, F. Kelkensberg, W. K. Siu et al. 'Attosecond control of electron-ion recollision in high harmonic generation'. *New Journal of Physics*, vol. 13(3), p. 033002 (2011). doi:10.1088/1367-2630/13/3/033002.

[182] E. Goulielmakis, Z.-H. Loh, A. Wirth et al. 'Real-time observation of valence electron motion'. *Nature*, vol. 466(7307), pp. 739–743 (2010). doi:10.1038/nature09212.

[183] V. Despré, A. Marciniak, V. Loriot et al. 'Attosecond Hole Migration in Benzene Molecules Surviving Nuclear Motion'. *The Journal of Physical Chemistry Letters*, vol. 6(3), pp. 426–431 (2015). doi:10.1021/jz502493j.

[184] H. J. Wörner, J. B. Bertrand, D. V. Kartashov et al. 'Following a chemical reaction using high-harmonic interferometry'. *Nature*, vol. 466(7306), pp. 604–607 (2010). doi:10.1038/nature09185.

[185] D. R. Lide. *CRC Handbook of Chemistry and Physics, 85th Edition*. CRC Press, 2004. ISBN 9780849304859.